

UNIVERSITÉ DU QUÉBEC À TROIS-RIVIÈRES

ÉTUDE DE LA MICROSTRUCTURE ET DES PROPRIÉTÉS D'HYDROGÉNATION DES
ALLIAGES À HAUTE ENTROPIE À BASE DE TiHfZrNbV ET DE $Ti_{0.3}V_{0.3}Mn_{0.2}Fe_{0.1}Ni_{0.1}$
ET EFFET DE LA DÉFORMATION MÉCANIQUE
SUR L'ALLIAGE $Ti_1V_{0.9}Cr_{1.1}$ POUR L'ABSORPTION D'HYDROGÈNE

STUDY THE MICROSTRUCTURE AND HYDROGENATION PROPERTIES OF
HIGH ENTROPY ALLOYS OF TiHfZrNbV-BASED AND $Ti_{0.3}V_{0.3}Mn_{0.2}Fe_{0.1}Ni_{0.1}$
AND EFFECT OF MECHANICAL DEFORMATION ON
 $Ti_1V_{0.9}Cr_{1.1}$ ALLOY FOR HYDROGEN ABSORPTION

THÈSE PRÉSENTÉE
COMME EXIGENCE PARTIELLE DU
DOCTORAT EN SCIENCES DE L'ÉNERGIE ET DES MATÉRIAUX

PAR
SALMA SLEIMAN

AVRIL 2023

Université du Québec à Trois-Rivières

Service de la bibliothèque

Avertissement

L'auteur de ce mémoire, de cette thèse ou de cet essai a autorisé l'Université du Québec à Trois-Rivières à diffuser, à des fins non lucratives, une copie de son mémoire, de sa thèse ou de son essai.

Cette diffusion n'entraîne pas une renonciation de la part de l'auteur à ses droits de propriété intellectuelle, incluant le droit d'auteur, sur ce mémoire, cette thèse ou cet essai. Notamment, la reproduction ou la publication de la totalité ou d'une partie importante de ce mémoire, de cette thèse et de son essai requiert son autorisation.

UNIVERSITÉ DU QUÉBEC À TROIS-RIVIÈRES

DOCTORAT EN SCIENCES DE L'ÉNERGIE ET DES MATÉRIAUX (PH. D.)

Direction de recherche :

Jacques Huot

Directeur de recherche

Jury d'évaluation de la thèse :

Jacques Huot

Directeur de recherche

Jacques Goyette

Président de jury

Cibian Mihaela

Évaluatrice externe

Dilson Silva dos Santos

Évaluateur externe

Thèse soutenue le 15 février 2023

Abstract

This thesis reports the investigation of the microstructure and first hydrogenation process of TiHfZrNbV-based and $Ti_{0.3}V_{0.3}Mn_{0.2}Fe_{0.1}Ni_{0.1}$ alloys for hydrogen storage. This work was carried out, under the supervision of Professor Jacques Huot, in the laboratories of the Hydrogen Research Institute, at the University of Quebec at Trois-Rivières.

In the context commercialization of the alloys, the first hydrogenation, the so-called "activation" is usually a step that is costly and time consuming. The first part of this thesis presents a systematic investigation of the effect of particle size, pressure and temperature on the first hydrogenation of TiHfZrNbV high entropy alloy. Three particle size ranges were selected: less than 0.5 mm, between 0.5 mm and 1 mm and between 1 mm and 2 mm. The hydrogen pressures applied during the first hydrogenation were 1, 2 and 20 bars. The temperature of the first hydrogenation was varied from 100 °C to 400 °C. It was found that the particle size is a factor in the activation; smaller particle size having faster hydrogenation kinetics. Under 2 bars and 20 bars of hydrogen pressure, the activation curves have the same features. The activation is strongly dependent on the temperature: higher temperature drastically reducing the incubation period. The important parameter for the activation is the temperature rather than the particle size. It was also found that the activation process obeys an Arrhenius relationship. Upon hydrogenation, the BCC phase is transformed to a (Body Centered Tetragonal) BCT phase. Also, an amorphous phase seems to be formed. This formation depends on the hydrogenation temperature and particle size.

The effect of the substitution of Nb by V on the microstructure and hydrogen storage properties of $TiHfZrNb_{1-x}V_{1+x}$ alloys ($x= 0.1, 0.2, 0.4, 0.6$ and 1) was also investigated. For $x=0$, the alloy is pure Body Centered Cubic (BCC) and upon the substitution of niobium by vanadium, the BCC was progressively replaced by a Hexagonal Closed Packed (HCP) and a Face Centered Cubic (FCC) phases. For $x= 0.6$, a Laves phase Strukturbericht type cubic C15 phase was also present and becomes the main phase for $x= 1$. The substitution greatly enhanced the first hydrogenation and makes it possible at room temperature under 20 bars of hydrogen. The hydrogen storage capacity of all substituted alloys was around 2 wt.%.

In a way to potentially increase the gravimetric hydrogen storage capacity, the heavy elements Hf, Zr and Nb were replaced by lighter ones of period 4 giving the composition $Ti_{0.3}V_{0.3}Mn_{0.2}Fe_{0.1}Ni_{0.1}$. The alloy was synthesized by arc melting and mechanical alloying, resulting in different microstructures. The as-cast alloy is multiphase, with a main Laves phase Strukturbericht type hexagonal C14 phase matrix along with a BCC phase and a

small amount of Ti_2Fe -type phase. The maximum hydrogen storage capacity of the alloy was 1.6 wt.%. We found that the air-exposed samples had the same capacity as the as-cast sample but with a longer incubation time. Synthesis by mechanical alloying for five hours resulted in an alloy with only BCC structure. The hydrogen capacity of the milled alloy was 1.2 wt.%, lower than the as-cast one. The effect of ball milling of the as-cast alloy was also studied. Ball milling for five hours produced a BCC structure similar to the one obtained by milling the raw materials for the same time.

Finally, we tried to solve the problem of impossible first hydrogenation of $Ti_1V_{0.9}Cr_{1.1}$ BCC alloy by mechanical deformation techniques. The $Ti_1V_{0.9}Cr_{1.1}$ alloy was processed using cold rolling (CR) and ball milling (BM). The first hydrogenation of the alloy at room temperature under 20 bars of hydrogen is practically impossible. However, the samples mechanically activated by CR or BM readily absorbed hydrogen. The sample cold-rolled for one pass exhibited faster kinetics than the sample ball-milled for five minutes, but both samples reached the same storage capacity of 3.6 wt.% hydrogen. Increasing the amount of rolling or the milling time decreased the hydrogen capacity. CR is considered the best and most efficient method for the activation of $Ti_1V_{0.9}Cr_{1.1}$ BCC alloy.

Résumé

Cette thèse porte sur l'étude de la microstructure et de la première hydrogénation des alliages à base de TiHfZrNbV et $Ti_{0.3}V_{0.3}Mn_{0.2}Fe_{0.1}Ni_{0.1}$ pour le stockage de l'hydrogène. Ces travaux ont été réalisés, sous la direction du professeur Jacques Huot, dans les laboratoires de l'Institut de recherche sur l'hydrogène, à l'Université du Québec à Trois-Rivières.

Dans le cadre de la commercialisation des alliages, la première hydrogénation dite « d'activation » est généralement une étape coûteuse et chronophage. La première partie de cette thèse présente une étude systématique de l'effet de la taille des particules, de la pression et de la température sur la première hydrogénation de l'alliage à haute entropie TiHfZrNbV. Trois gammes de granulométries ont été sélectionnées : moins de 0.5 mm, entre 0.5 mm et 1 mm et entre 1 mm et 2 mm. Les pressions d'hydrogène appliquées lors de la première hydrogénation étaient de 1, 2 et 20 bars. La température de la première hydrogénation a varié de 100°C à 400°C. Il a été constaté que la taille des particules est un facteur d'activation ; taille de particule plus petite ayant une cinétique d'hydrogénation plus rapide. Sous 2 bars et 20 bars de pression d'hydrogène, les courbes d'activation ont les mêmes caractéristiques. L'activation est fortement dépendante de la température : une température plus élevée réduit drastiquement la durée d'incubation. Le paramètre important pour l'activation est la température plutôt que la taille des particules. Il a également été constaté que le processus d'activation obéit à une relation d'Arrhenius. Lors de l'hydrogénation, la phase BCC est transformée en une phase BCT. De plus, une phase amorphe semble se former. Cette formation dépend de la température d'hydrogénation et de la taille des particules.

L'effet de la substitution de Nb par V sur la microstructure et les propriétés de stockage d'hydrogène des alliages $TiHfZrNb_{1-x}V_{1+x}$ ($x = 0,1, 0,2, 0,4, 0,6$ et 1) a également été étudié. Pour $x = 0$, l'alliage est purement cubique à corps centré (CC) et lors de la substitution du niobium par du vanadium, la structure CC a été progressivement remplacée par une phase hexagonale compacte (HC) et une structure cubique à face centrée (CFC). Pour $x = 0,6$, une phase C15 cubique de type Strukturbericht de Laves était également présente et devient la phase principale pour $x = 1$. La substitution améliore fortement la première hydrogénation et la rend possible à température ambiante sous 20 bars d'hydrogène. La capacité de stockage d'hydrogène de tous les alliages substitués était d'environ 2 % en poids.

De manière à augmenter potentiellement la capacité gravimétrique de stockage d'hydrogène, les éléments lourds Hf, Zr et Nb ont été remplacés par des éléments plus légers de période 4 donnant la composition $Ti_{0.3}V_{0.3}Mn_{0.2}Fe_{0.1}Ni_{0.1}$. L'alliage a été synthétisé par fusion à l'arc et broyage mécanique, ce qui a donné différentes microstructures. L'alliage brut de coulée est multiphasé, avec une matrice de phase principale hexagonale de type C14 Strukturbericht de Laves ainsi qu'une phase CC et une petite quantité de phase de type Ti_2Fe . La capacité maximale de stockage d'hydrogène de l'alliage était de 1,6 % en poids. Nous avons constaté que les échantillons exposés à l'air avaient la même capacité que l'échantillon brut de coulée, mais avec un temps d'incubation plus long. La synthèse par mécanosynthèse pendant cinq heures a conduit à un alliage à structure CC uniquement. La capacité en hydrogène de l'alliage broyé était de 1,2 % en poids, inférieur à celle de la coulée. L'effet du broyage à billes de l'alliage brut de coulée a également été étudié. Le broyage à billes pendant cinq heures a produit une structure CC similaire à celle obtenue en broyant les matières premières pendant le même temps.

Enfin, nous avons essayé de résoudre le problème de la première hydrogénation impossible de l'alliage $Ti_1V_{0.9}Cr_{1.1}$ CC par des techniques de déformation mécanique. L'alliage $Ti_1V_{0.9}Cr_{1.1}$ a été traité par laminage à froid et broyage à billes. La première hydrogénation de l'alliage à température ambiante sous 20 bars d'hydrogène est pratiquement impossible. Cependant, les échantillons activés mécaniquement par laminage ou broyage absorbaient facilement l'hydrogène. L'échantillon laminé à froid une fois a présenté une cinétique plus rapide que l'échantillon broyé à billes pendant cinq minutes, mais les deux échantillons ont atteint la même capacité de stockage de 3,6 % en poids d'hydrogène. L'augmentation du nombre de laminages ou du temps de broyage a diminué la capacité en hydrogène. Le laminage est considéré comme la méthode la meilleure et la plus efficace pour l'activation de l'alliage $Ti_1V_{0.9}Cr_{1.1}$ CC.

Acknowledgements

My profound gratitude to God Almighty. He was, He is, and He shall be with me all days of my life.

I would like to acknowledge and give my deepest thanks to my thesis director and supervisor Professor Jacques Huot (Institut Recherche Hydrogène, UQTR) for his brilliant comments and fruitful guidance during this work.

I would like to thank Dr. Agnes. Lejeune for SEM analysis.

Thanks to Dr. Amol Kamble, Dr. Peng Lv and Dr. Viney Dixit for the useful discussions. Thanks to Dr. Jingjing Liu for her constructive suggestions. Many thanks to Anis Aliouat and Maria Moussa for their unparalleled enthusiasm that gave a new energy to our lab. Thank you, Chourouk, Francia, Priyanka and Ravi, I had memorable moments with all of you. I am grateful to be part of Jacques group and having you all in my life. I am thankful for Dr. Khalil and his wife Dr. Zainab for being a family to me in Canada.

Special thanks to my wonderful sister Mariam, I hope I have achieved your dream. I will never forget those coffee cups that we had together. That was so effective in the tough times. I would like to express my deepest appreciation to my soul mate Sanaa for her continuous moral support.

All the thanks to my beloved husband Mohamad for his unwavering motivation and understanding. To my sons Hussein, Ibrahim and Jad thank you all for encouraging me to finish my PhD.

Finally, I owe my deepest gratitude to my parents Ibrahim and Zahra for their love, prayers and sacrifices.

I love you all and may the Almighty God richly bless all of you.

Table of contents

Abstract	iii
Résumé	v
Acknowledgements	vii
Table of contents.....	viii
List of Figures.....	xi
List of Tables.....	xiv
SECTION 1.....	1
Chapter 1.....	2
Introduction	2
1.1 Energy Transition.....	2
1.2 Hydrogen Energy	2
1.3 Hydrogen Storage	3
1.4 Metal Hydrides.....	4
1.5 High Entropy Alloys (HEAs)	5
1.5.1 Definition of HEAs	6
1.5.2 Basic factors affecting the phase stability of HEAs	6
1.6 Chemical reaction of metal hydride and its thermodynamics	11
1.7 Activation process	14
1.8 Choice of alloy composition.....	14
1.9 Research objective	16
1.10 Thesis structure	16
Chapter 2.....	17
Experimental Details	17
2.1 Synthesis of Materials.....	17
2.1.1 Arc Melting	18
2.1.2 Ball Milling	19
2.1.3 Cold Rolling	20
2.2 Characterization techniques	21
2.2.1 Scanning Electron Microscopy (SEM).....	21

2.2.2 X-Ray Diffraction	23
2.2.3 Sievert's Apparatus	24
Chapter 3.....	26
Effect of particle size, pressure, and temperature on first hydrogenation of TiVZrHfNb high entropy alloy	26
3.1 Overview	26
3.2 Microstructural Study.....	26
3.3 Crystal Structure	30
3.4 First Hydrogenation (Activation)	31
3.4.1 Effect of Particle size on activation behaviour.....	31
3.4.2 Effect of Temperature on activation behaviour	33
3.4.3 Effect of Pressure on first hydrogenation	40
3.4.4 Study of Stability of the hydrided phase	42
3.5 Conclusion.....	43
Chapter 4.....	45
Microstructure and hydrogen storage properties of TiHfZrNb _{1-x} V _{1+x} alloy for x=0, 0.1, 0.2, 0.4, 0.6 and 1.	45
4.1 Overview.....	45
4.2 Calculation of Parameters for Phase Formation Rules	46
4.3 Microstructural Study.....	46
4.4 Crystal Structure	50
4.5 First Hydrogenation	55
4.6 Conclusions	60
Chapter 5.....	61
Microstructure and Hydrogen Storage Properties of the multi-phase alloy Ti _{0.3} V _{0.3} Mn _{0.2} Fe _{0.1} Ni _{0.1}	61
5.1 Overview.....	61
5.2 Microstructural Study.....	62
5.3 Crystal Structure	65
5.4 First Hydrogenation Properties	67
5.5 Air Exposure Effect.....	69
5.6 Synthesis by Mechanical Alloying	71

5.7 Effect of Milling on As-cast Alloy	72
5.8 First Hydrogenation of the Milled Raw Powder and the Alloy	73
5.9 Conclusions	76
Chapter 6.....	77
Enhancement of first hydrogenation of $Ti_1V_{0.9}Cr_{1.1}$ BCC alloy by cold rolling and ball milling	77
6.1 Overview.....	77
6.2 Morphology	77
6.3 Crystal Structure	78
6.4 First Hydrogenation.....	80
6.5 Effect of ball milling on $Ti_1V_{0.9}Cr_{1.1}$ alloy	83
6.6 Conclusions	87
Chapter 7.....	89
Conclusion and Future Work.....	89
REFERENCES.....	91
SECTION 2.....	96
Publications.....	96
Article 1	97
Article 2	106
Article 3	121
Article 4.....	135

List of Figures

Figure 1.1 Volume of 4 kg of hydrogen compacted in different ways with size relative to car's size [11].	4
Figure 1.2 Crystal structures of the C14 MgZn ₂ -type and the C15 MgCu ₂ -type.	5
Figure 1.3 The relationship between the parameters Ω and δ [43].	10
Figure 1.4 Relationships between VEC and the FCC, BCC phase stability for some HEA systems. Note on the legend: fully closed symbols for only FCC phase; fully open symbols for only BCC phase; top-half-closed symbols for mixed BCC and FCC phases [44].	11
Figure 1.5 Schematic representation of ideal Pressure Composition Temperature "PCT" curve showing three absorption regions for hydride formation [45].	12
Figure 1.6 Pressure-composition temperatures (PCTs) at different temperatures and associated Van't Hoff graph [46].	13
Figure 1.7 Summary of the work.	15
Figure 2.1 Arc melter (Centorr Associates Inc, USA).	19
Figure 2.2 Ball miller Spex 8000.	20
Figure 2.3 Schematic of cold rolling.	20
Figure 2.4 Schematic of scanning electron microscope.	21
Figure 2.5 Mechanisms of emission of secondary electrons SEs, backscattered electrons BSE, and characteristic X-rays from atoms of the sample.	22
Figure 2.6 Schematic diagram of Bragg diffraction.	23
Figure 2.7 Basic schematic diagram of Sieverts-type apparatus.	25
Figure 3.1 Flow chart of synthesis & characterization of TiVZrHfNb alloy.	26
Figure 3.2 Backscattered electrons (BSE) micrograph of as-cast TiVZrHfNb alloy.	27
Figure 3.3 BSE micrograph of as-cast TiVZrHfNb alloy with magnification 2000 \times .	28
Figure 3.4 Line analysis of line A of Figure 3.3.	29
Figure 3.5 XRD patterns of the as-cast TiVZrHfNb alloy. The bottom curve is the difference between calculated and measured intensities.	30
Figure 3.6 Activation curves at 300 $^{\circ}$ C of TiVZrHfNb alloy for different particle size.	31
Figure 3.7 XRD patterns of different particle sizes hydrogenated at 300 $^{\circ}$ C under 20 bars.	32
Figure 3.8 Activation curves of as-crushed TiVZrHfNb alloy at 100 $^{\circ}$ C, 200 $^{\circ}$ C, 300 $^{\circ}$ C and 400 $^{\circ}$ C under 20 bars.	34
Figure 3.9 XRD patterns of as-crushed TiVZrHfNb alloy hydrogenated at 300 $^{\circ}$ C and 400 $^{\circ}$ C under 20 bars.	35
Figure 3.10 Activation curves at 200 $^{\circ}$ C, 225 $^{\circ}$ C, 250 $^{\circ}$ C, 275 $^{\circ}$ C and 300 $^{\circ}$ C of particle size less than 0.5 mm.	36

Figure 3.11 Graph of $\ln t$ as a function of $1000/T$ where t is the incubation period and T the temperature.	37
Figure 3.12 XRD patterns of particles of size less than 0.5 μm hydrogenated at 200°C, 225°C, 250°C, 275°C and 300°C.	38
Figure 3.13 Activation curves at 300°C under 1, 2 and 20 bars of hydrogen of particles of size less than 0.5 μm	40
Figure 3.14 XRD patterns of size less than 0.5 μm hydrogenated at 300°C under 1, 2 and 20 bars of hydrogen.	41
Figure 3.15 XRD patterns of particles of size less than 0.5 μm in the as-cast state and after dehydrogenation at 350°C under vacuum.	42
Figure 4.1 Flow chart of synthesis & characterization of $\text{TiHfZrNb}_{1-x}\text{V}_{1+x}$ alloys for $x=0.1, 0.2, 0.4, 0.6$ and 1	45
Figure 4.2 Backscattered electron (BSE) micrograph of $\text{TiHfZrNb}_{1-x}\text{V}_{1+x}$ alloys for $x=0, 0.1, 0.2, 0.4, 0.6$ and 1	47
Figure 4.3 BSE micrographs of $\text{TiHfZrNb}_{1-x}\text{V}_{1+x}$ alloys for $x=0, 0.1, 0.2, 0.4, 0.6$ and 1 with higher magnification.	48
Figure 4.4 X-ray diffraction patterns of as-cast $\text{TiHfZrNb}_{1-x}\text{V}_{1+x}$ alloys for $x=0, 0.1, 0.2, 0.4, 0.6$ and 1 . The bottom (red) line of each pattern is the residue of Rietveld refinement.	51
Figure 4.5 Activation curves of $\text{TiHfZrNb}_{1-x}\text{V}_{1+x}$ alloys for $x=0, 0.1, 0.2, 0.4, 0.6$ and 1	55
Figure 4.6 XRD patterns of $\text{TiHfZrNb}_{1-x}\text{V}_{1+x}$ alloys in the hydrogenated state for $x=0.1, 0.2, 0.4, 0.6$ and 1 . The bottom (red) line of each pattern is the residue of Rietveld refinement.	56
Figure 4.7 XRD pattern of TiHfZrV_2 alloy ($x=1$) dehydrided at 400 °C under vacuum.	60
Figure 5.1 Flow chart of synthesis & characterization of $\text{Ti}_{0.3}\text{V}_{0.3}\text{Mn}_{0.2}\text{Fe}_{0.1}\text{Ni}_{0.1}$ alloy.	62
Figure 5.2 Backscattered electron (BSE) micrograph of as-cast $\text{Ti}_{0.3}\text{V}_{0.3}\text{Mn}_{0.2}\text{Fe}_{0.1}\text{Ni}_{0.1}$ alloy.	62
Figure 5.3 BSE micrographs with elemental mappings of as-cast $\text{Ti}_{0.3}\text{V}_{0.3}\text{Mn}_{0.2}\text{Fe}_{0.1}\text{Ni}_{0.1}$ alloy.	64
Figure 5.4 X-ray diffraction patterns of as-cast $\text{Ti}_{0.3}\text{V}_{0.3}\text{Mn}_{0.2}\text{Fe}_{0.1}\text{Ni}_{0.1}$ alloy. The bottom curve is the difference between calculated and measured intensities.	65
Figure 5.5 Activation curve of as-cast $\text{Ti}_{0.3}\text{V}_{0.3}\text{Mn}_{0.2}\text{Fe}_{0.1}\text{Ni}_{0.1}$ alloy.	67
Figure 5.6 XRD patterns of the hydride sample.	68
Figure 5.7 Activation curves at room temperature under 20 bars of hydrogen of as-cast $\text{Ti}_{0.3}\text{V}_{0.3}\text{Mn}_{0.2}\text{Fe}_{0.1}\text{Ni}_{0.1}$ alloy crushed in argon and air. The sample crushed in air was further exposed for two and five days.	70
Figure 5.8 XRD patterns of Ti-V-Mn-Fe-Ni powders milled for 1, 5 and 10 h.	71
Figure 5.9 X-ray diffraction patterns of as-cast $\text{Ti}_{0.3}\text{V}_{0.3}\text{Mn}_{0.2}\text{Fe}_{0.1}\text{Ni}_{0.1}$ alloy after milling for 1, 5 and 10 h.	72
Figure 5.10 Activation curves of the milled raw powder for five hours, the as-cast alloy further milled for five hours, and the as-cast one.	74

Figure 5.11 XRD patterns of the milled raw powder and milled alloy in the hydrogenated state.....	75
Figure 6.1 Flow chart of synthesis & characterization of $Ti_1V_{0.9}Cr_{1.1}$ alloy.	77
Figure 6.2 Scanning electron microscopy (SEM) micrographs of hand crushed (a), CR-1× (b), CR-3× (c), and CR-6× (d) of $Ti_1V_{0.9}Cr_{1.1}$ alloy.	78
Figure 6.3 XRD patterns of the as-cast, CR-1×, CR-3×, and CR-6× of, $Ti_1V_{0.9}Cr_{1.1}$ alloy.	79
Figure 6.4 Activation curves of the as-cast, CR-1×, CR-3×, and CR-6× of $Ti_1V_{0.9}Cr_{1.1}$ alloy.	80
Figure 6.5 X-ray diffraction (XRD) patterns of hydrogenated of CR-1×, CR-3×, and CR-6× of $Ti_1V_{0.9}Cr_{1.1}$ alloy.	81
Figure 6.6 SEM micrographs of $Ti_1V_{0.9}Cr_{1.1}$ alloy before (a) and after 5 (b), 15 (c), 30 (d,e), and 60 min (f,g) of ball milling (BM).....	83
Figure 6.7 Diffraction patterns of $Ti_1V_{0.9}Cr_{1.1}$ alloy for different ball milling times.	84
Figure 6.8 Activation curves of $Ti_1V_{0.9}Cr_{1.1}$ alloy for different BM times as compared to the 1 cold-rolled sample.	85
Figure 6.9 Diffraction patterns of $Ti_1V_{0.9}Cr_{1.1}$ alloy for different BM times after hydrogenation.	86

List of Tables

Table 2.1 Raw elements.	17
Table 2.2 Summary of the compositions.	18
Table 3.1 EDX analysis showing the elemental composition of TiVZrHfNb alloy. Error on each value is 0.1 at.%.	28
Table 3.2 Crystal structure parameters and the R_{wp} value of the as-cast TiVZrHfNb alloy. Error on the last significant digit is indicated in parentheses.	30
Table 3.3 Crystal structure parameters of the BCT phase for different particle sizes hydrogenated at 300°C under 20 bars. Error on the last significant digit is indicated in parentheses.	32
Table 3.4 Crystal structure parameters of the BCT phase for as-crushed TiVZrHfNb alloy hydrogenated at 300°C and 400°C under 20 bars. Error on the last significant digit is indicated in parentheses.	35
Table 3.5 Crystal structure parameters of the BCT phase for particles of size less than 0.5 mm hydrogenated at different temperatures. Error on the last significant digit is indicated in parentheses.	39
Table 3.6 Crystal structure parameters of the BCT phase of the particles of size less than 0.5 mm hydrogenated at 300°C under 1, 2 and 20 bars of hydrogen. Error on the last significant digit is indicated in parentheses.	41
Table 3.7 Crystal structure parameters of particles of size less than 0.5 mm dehydrided at 350°C under vacuum as compared to the as-cast alloy. Error on the last significant digit is indicated in parentheses.	43
Table 4.1 The parameters ΔS_{mix} , ΔH_{mix} , Ω and δ for each alloy.	46
Table 4.2 EDX analysis showing the elemental composition of the matrix (point 1) of: TiHfZrNb _{1-x} V _{1+x} alloys for x= 0.1, 0.2, 0.4, 0.6 and 1. Error on all values is 1 at.%.	49
Table 4.3 EDX analysis showing the elemental composition of the bright phase (point 2) of: TiHfZrNb _{1-x} V _{1+x} alloys for x= 0.1, 0.2, 0.4, 0.6 and 1. Error on all values is 1 at %. 50	50
Table 4.4 EDX analysis showing the elemental composition of the dark phase (point 3) of: TiHfZrNb _{1-x} V _{1+x} alloys for x= 0.1, 0.2, 0.4 and 0.6. Error on all values is 1 at %. ...	50
Table 4.5 Abundance in wt.% of each phase in TiHfZrNb _{1-x} V _{1+x} alloys for x= 0, 0.1, 0.2, 0.4, 0.6 and 1. The number in parentheses is the error on the last significant digit. ...	51
Table 4.6 Crystal structure parameters of the BCC phase in TiHfZrNb _{1-x} V _{1+x} alloys for x= 0, 0.1, 0.2, 0.4, 0.6 and 1. Error on the last significant digit is indicated in parentheses.	53
Table 4.7 Crystal structure parameters of HCP phase in TiHfZrNb _{1-x} V _{1+x} alloys for x= 0.1, 0.2, 0.4 and 0.6. Error on the last significant digit is indicated in parentheses.	53
Table 4.8 The crystal structure parameters of the FCC phase in TiHfZrNb _{1-x} V _{1+x} alloys for x= 0.1 to 0.6. Error on the last significant digit is indicated in parentheses.	54

Table 4.9 Crystal structure parameters of the C15 phase in TiHfZrNb _{1-x} V _{1+x} alloys for x= 0.6 and 1. Error on the last significant digit is indicated in parentheses.	54
Table 4.10 The crystal parameters of each phase in the hydrogenated TiHfZrNb _{1-x} V _{1+x} alloys for x= 0.1, 0.2, 0.4, 0.6 and 1. Error on the last significant digit is indicated in parentheses.	57
Table 4.11 The variation of volume ΔV and the estimated range of hydrogen in each phase in the hydrogenated TiHfZrNb _{1-x} V _{1+x} alloys for x= 0.1, 0.2, 0.4, 0.6 and 1.....	58
Table 4.12 Estimated capacity of the phases in the hydrided samples.	59
Table 5.1 Bulk atomic abundance: nominal and as measured by EDX of as-cast Ti _{0.3} V _{0.3} Mn _{0.2} Fe _{0.1} Ni _{0.1} alloy. Error on the last significant digit is indicated in parentheses.	63
Table 5.2 EDX analysis showing the elemental composition of all the phases of as-cast Ti _{0.3} V _{0.3} Mn _{0.2} Fe _{0.1} Ni _{0.1} alloy. Error on all values is 1 at %.....	65
Table 5.3 Crystal parameters and abundance of each phase of as-cast Ti _{0.3} V _{0.3} Mn _{0.2} Fe _{0.1} Ni _{0.1} alloy. Error on the last significant digit is indicated in parentheses.	66
Table 5.4 Crystal structure parameters and abundance of each phase in the hydride sample. Error on the last significant digit is indicated in parentheses.....	68
Table 5.5 Estimated capacity of the phases in the hydride sample.	69
Table 5.6 Crystal parameters of the BCC phase of the samples milled for 5 and 10 h. Error on the last significant digit is indicated in parentheses.	71
Table 5.7 Crystal parameters and abundance of each phase in as-cast Ti _{0.3} V _{0.3} Mn _{0.2} Fe _{0.1} Ni _{0.1} alloy before and after milling. Error on the last significant digit is indicated in parentheses.....	73
Table 6.1 Crystal structure parameters and the R _{wp} values of the as-cast, CR-1×, CR-3×, and CR-6× of Ti ₁ V _{0.9} Cr _{1.1} alloy. Error on the last significant digit is indicated in parentheses.	79
Table 6.2 Crystal structure parameters and the R _{wp} values of all patterns after hydrogenation. Error on the last significant digit is indicated in parentheses.	82
Table 6.3 Crystal parameters and the R _{wp} values of Ti ₁ V _{0.9} Cr _{1.1} alloy for different ball milling times compared with the as-cast sample. Error on the last significant digit is indicated in parentheses.....	84
Table 6.4 Crystal parameters of Ti ₁ V _{0.9} Cr _{1.1} alloy for different ball milling times after hydrogenation. Error on the last significant digit is indicated in parentheses.	87

SECTION 1

Chapter 1

Introduction

1.1 Energy Transition

Many countries have been working towards reducing greenhouse gas emissions and transitioning to a cleaner and more sustainable energy system. To support this transition, they have implemented national strategies with a focus on increasing the use of renewable energy sources and reducing dependence on fossil fuels. One key area in these strategies is the development of hydrogen as a low-carbon energy source.

In Canada, the National Hydrogen Strategy outlined a plan to support the development and deployment of low-carbon hydrogen production, distribution, and end-use technologies. The strategy includes a combination of research and development, policy incentives and public-private partners. It traces a vision for Canada to become a global leader in hydrogen technologies with net-zero carbon emissions by 2050. Achieving this vision will bring a significant economic and environmental benefits to the country [1].

1.2 Hydrogen Energy

To meet the growing global energy demand, the utilization of renewable energies like wind and solar is now widely used [2]. However, these renewables are intermittent, and their production is usually not in phase with the demand. Thus, the use of these energies should be supported by an energy storage system. Hydrogen can be considered as an energy storage and energy vector for the renewable energies. Its gravimetric density is 120 MJ/kg which is nearly three times that of petroleum. The emission from hydrogen combustion is carbon-free which makes it environmentally friendly. Hydrogen is also used for heat storage [3], in heat actuators [4] and in Ni-MH batteries [5].

Hydrogen is the most abundant element in the universe. But on earth, it should be released from molecular compounds that contain it such as water and hydrocarbons. Currently, most of the hydrogen is produced by thermochemical processes such as natural gas reforming and gasification of coal [6]. These productions are responsible for the emission of greenhouse gases. The electrolytic process is a promising option to produce clean hydrogen provided that the electricity is coming from a green energy source such as solar, hydro and wind.

After production, hydrogen has to be stored. Because of its low volumetric energy density at atmospheric pressure and room temperature ($11 \text{ m}^3/\text{kg}$) and its wide flammability range, the storage of hydrogen safely and efficiently is an important challenge [7].

1.3 Hydrogen Storage

For mobile applications, high volumetric and gravimetric energy densities are preferable. Presently, hydrogen is mainly stored in three forms: gaseous hydrogen, liquid hydrogen, and in solid form through physisorption or chemisorption [8].

Storage of hydrogen in its gaseous state at room temperature is the most utilized technology [9]. Currently, pressurized cylinders are used in fuel-cell vehicles such as Toyota Mirai and Honda Clarity [10]. However, the specialized tanks that could support high pressure of up to 70 MPa are very expensive.

Liquid hydrogen is stored at very low temperature ($< -253^{\circ}\text{C}$) at ambient pressure in cryogenic tanks. This technique is used to transport large quantities of hydrogen for long distances, especially when pipelines of hydrogen are not available.

In physisorbed hydrogen storage materials, such as metal–organic frameworks (MOFs) and carbon-based materials, hydrogen molecules are adsorbed at low temperature on porous surfaces. The storage capacity is directly proportional to the specific surface area.

In metal hydrides, the atomic hydrogen is chemically bonded with the metal atoms in the bulk of the material. Hydrogen occupies interstitial sites of the crystal structure. Storing hydrogen in metal hydrides is a more compact and safer way than in high hydrogen pressure tanks and cryogenic reservoirs. The volumetric hydrogen density storage in metal hydrides at ambient conditions is higher than in the conventional compressed gas and liquid hydrogen storage methods. Figure 1.1 shows the volume needed to store hydrogen in various storage systems. It is clear that storing hydrogen in metal hydrides is a much more compact way than the other techniques. Moreover, there are no issues of high pressure (compressed hydrogen) or cryogenic temperatures (liquified hydrogen). Since the reduction in volume is important for many practical applications, the storage of hydrogen in metal hydrides could be promising.

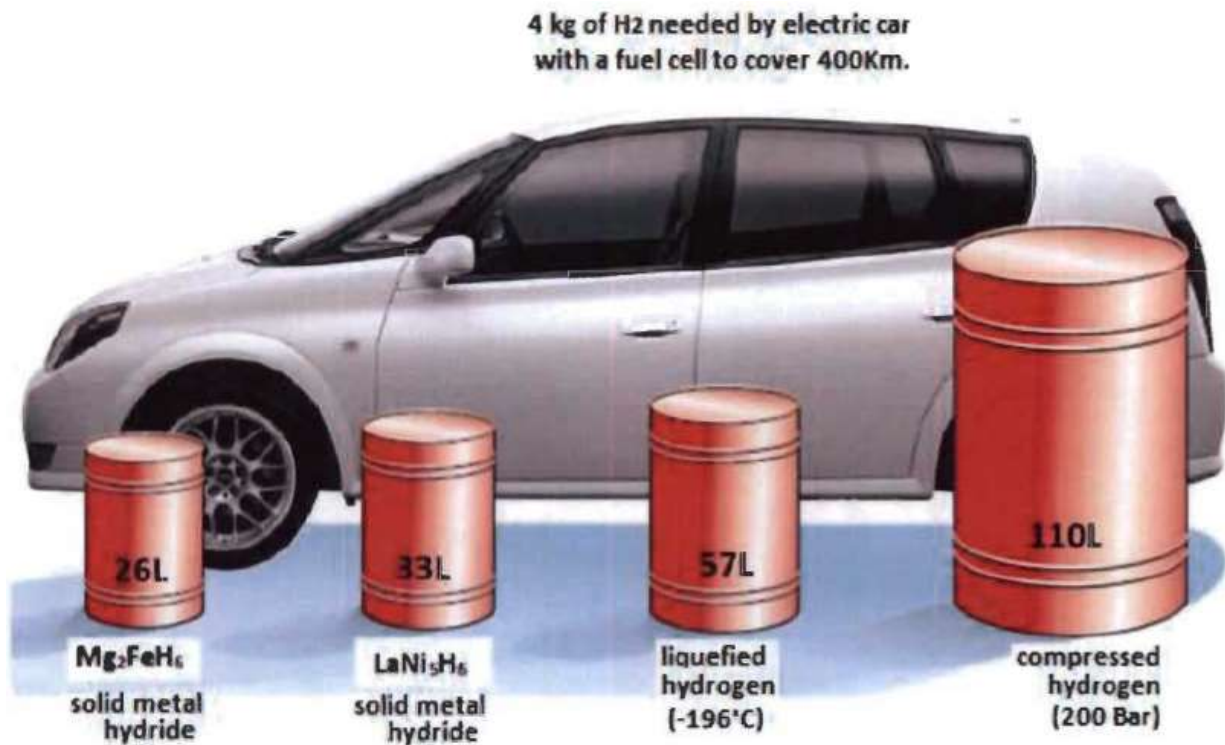


Figure 1.1 Volume of 4 kg of hydrogen compacted in different ways with size relative to car's size [11].

1.4 Metal Hydrides

Metal hydrides are a safe and cost-effective way to store hydrogen. They have a variety of chemical compositions and crystal structures. Some of the studied classes of metal hydrides are magnesium-based and intermetallic alloys.

Magnesium-based hydrides have been intensively studied as hydrogen storage materials. They are well known for their high theoretical hydrogen capacity of 7.6 wt.% and low cost. However, the absorption/desorption processes take place at a high temperature range (300-400°C) [12]. Ball milling preparation and adding catalysts have been shown to enhance the kinetics [12, 13].

Intermetallic hydrides are usually formed from alloys of type AB₅, AB, AB₂, etc. where A is a strong hydride forming element like Ti, V, Zr, Hf, Nb, La and B is a weak hydride forming element like Mn, Ni, Fe [14]. AB₅ alloy has prototype CaCu₅-type hexagonal structure. LaNi₅ is the main example of AB₅ type hydrogen storage alloys. AB₅-type

hydrides have reversible and fast hydrogen absorption/desorption kinetics at room temperature under low hydrogen pressure with about 1.5 wt.% theoretical hydrogen storage capacity [15]. They are mainly used in Ni/MH batteries.

AB_2 alloys crystallize in Laves phase structures. The three types of Laves phases are hexagonal C14 structure (prototype $MgZn_2$), hexagonal C36 structure (prototype $MgNi_2$) and cubic C15 structure (prototype $MgCu_2$) [16]. The crystallographic structures of the three polytypes are presented in Figure 1.2 [17]. Generally, C15 and C14 structures have better hydrogenation performance than the C36 structure [18]. Laves phase-based alloys are considered as promising active materials for the negative electrode of Ni/MH batteries [19]. The theoretical maximum hydrogen storage capacities are 6.33 and 6 H atoms per AB_2 formula unit for C14 and C15 respectively [20]. The reported storage capacity of AB_2 -type alloys is around 2 wt% [21].

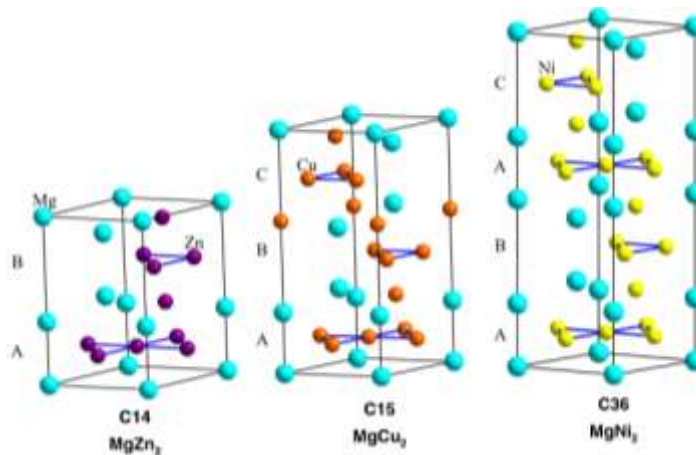


Figure 1.2 Crystal structures of the C14 $MgZn_2$ -type and the C15 $MgCu_2$ -type.

Solid solution alloys could have body centred cubic BCC, face centred cubic FCC or hexagonal close-packed HCP crystal structures. Here the metal atoms are randomly distributed over the sites of the crystal lattice. TiVCr system with BCC structure is extensively studied for hydrogen storage due to its high capacity up to 3.4 wt.% [22-24].

Recently, a novel class of alloy, the so-called high entropy alloys (HEAs) has been examined [25]. In the following section, the HEA will be presented in more details.

1.5 High Entropy Alloys (HEAs)

In 2004, the concept of HEA was introduced independently by Yeh [26], Cantor [27] and Ranganathan [28]. HEAs have broken the design concept of traditional alloys by having many principal elements with significant atomic fractions. They form a new class of

metallic alloys with interesting and outstanding mechanical properties such as strength, hardness, wear and corrosion resistance, softening resistance, etc. [29]. HEAs have been explored for potential industrial applications [30]. Recently, they have also been considered as hydrogen storage materials [31-35].

1.5.1 Definition of HEAs

There are no strict criteria for an alloy to be considered as high entropy alloy. Generally, the definition of HEAs is based on composition or configurational entropy. From the composition point of view, HEAs should contain at least five principal elements, each with an atomic percentage between 5 and 35 %. From the entropy point of view, HEAs are alloys having configurational entropy greater than or equal 1.5 R where R is the gas constant [25].

1.5.2 Basic factors affecting the phase stability of HEAs

Thermodynamics parameters, atomic size difference, and valence electron concentration play an important role in the phase stability of HEAs.

1.5.2.1 Thermodynamic parameters and atomic size difference

A single-phase HEAs is thermodynamically stabilized by its high mixing entropy [36]:

$$\Delta S_{mix} = \Delta S_{mix}^{conf} + \Delta S_{mix}^{ex} + \Delta S_{mix}^{vib} + \Delta S_{mix}^{elec} + \Delta S_{mix}^{mag} \quad (1.1)$$

where ΔS_{mix}^{conf} is the configurational mixing entropy, ΔS_{mix}^{ex} is the excess mixing entropy, ΔS_{mix}^{vib} is the vibrational mixing entropy of mixing, ΔS_{mix}^{elec} is the electronic mixing entropy and ΔS_{mix}^{mag} is the magnetic mixing entropy. The magnetic and electronic contributions are present only in a system that contains strong chemical interactions, such as transition metal alloys [37].

The main contribution of mixing entropy is the configurational mixing entropy:

$$\Delta S_{mix}^{conf} = -R \sum_{i=1}^N C_i \ln C_i \quad (1.2)$$

Where R is the gas constant, and C_i is the mole fraction of the i^{th} element.

" ΔS_{mix}^{conf} " is always positive. It is maximum for an equiatomic chemical composition with random distribution of the N elements on the lattice sites. For example, for equiatomic composition formed of five elements, we get:

$$\Delta S_{mix}^{conf} = -R \sum_{i=1}^5 \frac{1}{5} \ln \left(\frac{1}{5} \right) = R \ln 5 \approx 1.61 R \quad (1.3)$$

The concept of configurational entropy of mixing comes from the assumption that the atoms forming the alloy have the identical size and are freely packed. This assumption is similar to the case of the ideal gas whose configurational entropy of mixing depends only on positioning the constituent atoms. However, this is not true for real alloys, where the sizes of the constituent elements are not the same. Ye et al. proposed to add a negative excess entropy ΔS_{mix}^{ex} to the ideal ΔS_{mix}^{conf} , where " ΔS_{mix}^{ex} " takes into consideration the true atomic sizes and their packing fractions [38].

Generally, ΔS_{mix}^{ex} can be expressed as [39]:

$$\Delta S_{mix}^{ex} = \Delta S_{mix}^{ex} (d_i, C_i, \xi) \quad (1.4)$$

Where ξ is the atomic packing fraction of the N-element alloy ranging from 0.68 (BCC-like packing) to 0.74 (FCC-like packing), and d_i is the atomic diameter of the i^{th} element ($i = 1, 2, 3, \dots, N$) [39].

The vibrational or electronic entropy of mixing is determined as:

$$\Delta S_{mix} = S_{alloy} - \sum_{i=1}^N C_i S_i \quad (1.5)$$

where S_i is the entropy (vibrational or electronic) of the i^{th} element.

Note that the pure elements lack configurational entropy, and hence,

$$\Delta S_{mix}^{conf} = S_{alloy}^{conf} \quad (1.6)$$

" ΔS_{mix}^{vib} " could be positive or negative due to the difference between the atomic interaction potential in the pure elements and in the HEA, as well as on the changes in the vibrational density of states. The vibrational entropy S^{vib} is calculated from:

$$S^{vib} = 3k_B \int_0^\infty n^{vib} [(f_{BE} + 1) \ln(f_{BE} + 1) - f_{BE} \ln f_{BE}] d\varepsilon \quad (1.7)$$

Where n^{vib} is the phonon density of states, and f_{BE} is the Bose-Einstein distribution function [40].

" ΔS_{mix}^{elec} " comes from the change in the distribution of localized electrons and holes in the HEA as a result of mixing. Electronic excitation across the Fermi level by migrating from valance band to the conduction band gives rise to electronic entropy S^{elec} which can be determined by:

$$S^{elec} = -2k_B \int_{-\infty}^{\infty} n^{elec} [f_{FD} \ln f_{FD} + (1 - f_{FD}) \ln(1 - f_{FD})] d\varepsilon \quad (1.8)$$

Where n^{elec} is the electron density of states, and f_{FD} is Fermi-Dirac distribution function [40].

The magnetic entropy change " ΔS_{mix}^{mag} " is present when the atoms have a large magnetic moment such as some rare-earth elements. ΔS_{mix}^{mag} is associated with the H (magnetic field) variation can be calculated by integrating the Maxwell relation, i.e.,

$$\Delta S_{mix}^{mag} = \int_{H_{min}}^{H_{max}} \left(\frac{\partial M}{\partial T} \right)_H dH \quad (1.9)$$

Where H_{max} and H_{min} represent the initial and final value of the magnetic field respectively [41].

Due to its entropy stabilization, a HEA will be thermodynamically stable only above a given threshold temperature T for which the Gibbs free mixing energy is negative:

$$\Delta G_{mix} = \Delta H_{mix} - T \Delta S_{mix} < 0 \quad (1.10)$$

So that ΔH_{mix} is calculated using the expression:

$$\Delta H_{mix} = \sum_{i=1, i \neq j}^N 4 \Delta H_{AB}^{mix} C_i C_j \quad (1.11)$$

Where ΔH_{AB}^{mix} is the binary enthalpy of equiatomic AB alloy, taken from reference [42].

The stabilization occurs when: $|\Delta H_{mix}| < |T \Delta S_{mix}|$ and $\Delta S_{mix} > 0$.

Formation of intermetallic compounds is favoured when $|\Delta H_{mix}| > |T \Delta S_{mix}|$ and $\Delta H_{mix} < 0$. While a phase separation can happen for $\Delta H_{mix} > 0$ and $|\Delta H_{mix}| > |T \Delta S_{mix}|$. When $|\Delta H_{mix}|$ is not remarkably larger than $|T \Delta S_{mix}|$ and $\Delta H_{mix} < 0$, then an ordered substructure could be seen with some disorder on one or more sublattice sites [36].

Yang and Zhang proposed two dimensionless parameters Ω and δ to determine the phase formation of HEAs [43]. The parameter Ω combines the effects of entropy of mixing ΔS_{mix} and enthalpy of mixing ΔH_{mix} .

Ω is defined as:

$$\Omega = \frac{T_m \Delta S_{mix}}{\Delta H_{mix}} \quad (1.12)$$

where T_m is the melting temperature of the alloy, determined by the rule of mixtures:

$$T_m = \sum_{i=1}^N C_i (T_m)_i \quad (1.13)$$

with $(T_m)_i$ is the melting temperature of the i^{th} element.

The parameter δ is a quantitative parameter that describes the strained or distorted crystal lattice due to the difference of atomic radii of the elements. It is the lattice distortion or atomic size difference. δ is calculated using the equation:

$$\delta (\%) = 100 \sqrt{\sum_{i=1}^N C_i (1 - r_i/\bar{r})^2} \quad (1.14)$$

$$\text{and } \bar{r} = \sum_{i=1}^N C_i r_i \quad (1.15)$$

where r_i is the atomic radius of the i^{th} element.

Yang and Zhang suggested the formation of solid solution phases when $\Omega \geq 1.1$ and $\delta \leq 6.6\%$. In intermetallic compounds and bulk metallic glasses (amorphous phases) are favoured for larger δ values and smaller values of Ω as shown in Figure 1.3.

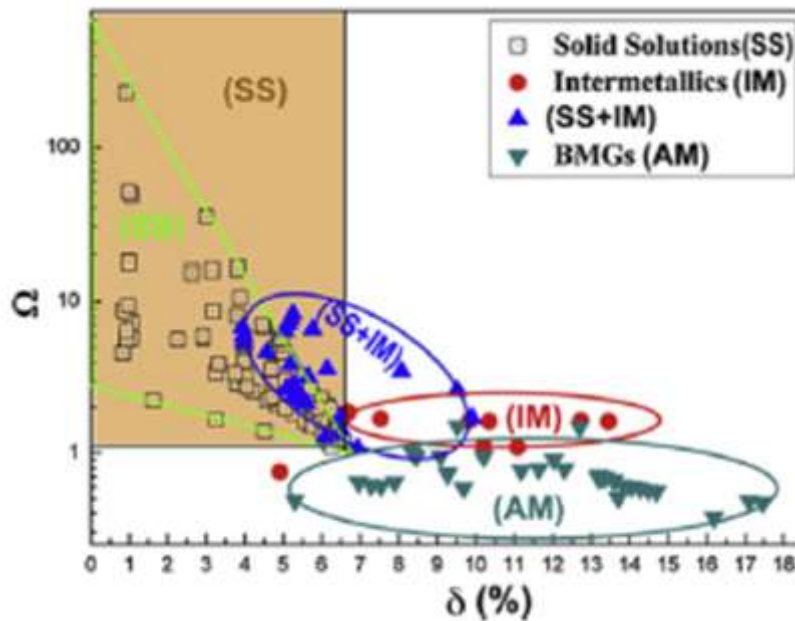


Figure 1.3 The relationship between the parameters Ω and δ [43].

1.5.2.2 Valence electron concentration VEC

The valence electron concentration VEC is the number of electrons in the valence band including d electrons. VEC is a critical parameter to identify the crystal structure of the solid solutions whether it is BCC and/or FCC [44]. It is defined by:

$$VEC = \sum_{i=1}^N C_i (VEC)_i \quad (1.16)$$

where $(VEC)_i$ is the VEC for the i^{th} element.

It was found by Guo et al. that FCC phases are stabilized at $VEC \geq 8$ whereas BCC phases are stabilized at $VEC < 6.87$ [44]. The FCC and BCC phases coexist in between as shown in Figure 1.4.

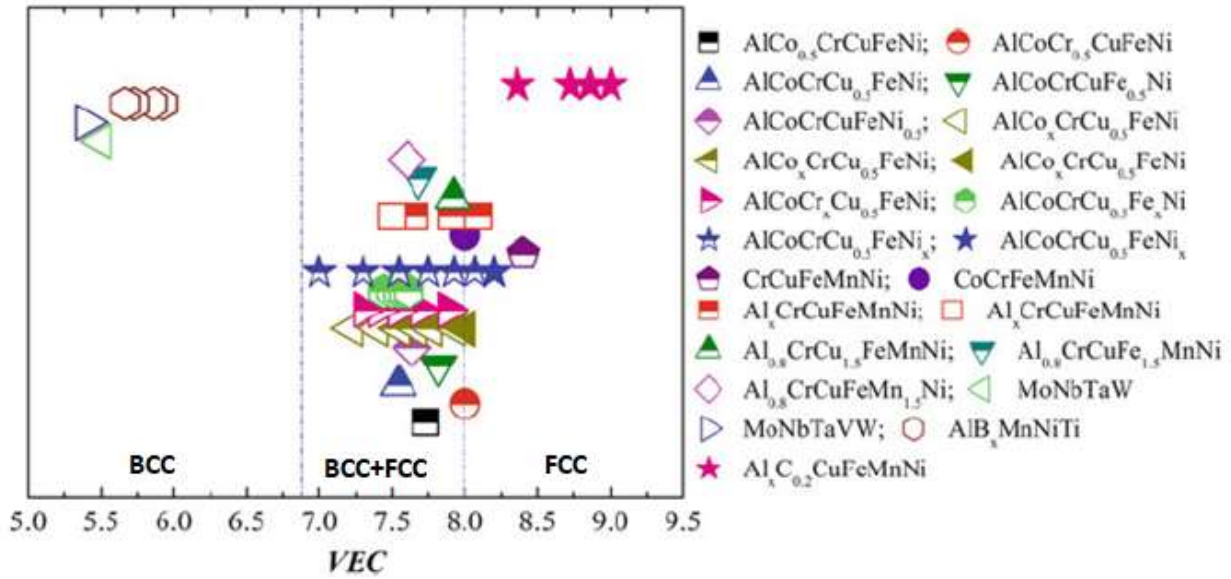
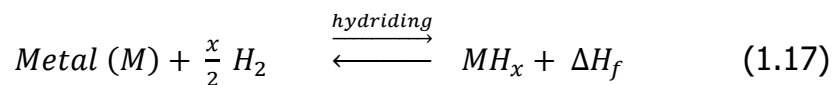


Figure 1.4 Relationships between VEC and the FCC, BCC phase stability for some HEA systems. Note on the legend: fully closed symbols for only FCC phase; fully open symbols for only BCC phase; top-half-closed symbols for mixed BCC and FCC phases [44].

The valence electron concentration rule has been applied successfully for the selection of BCC and FCC solid solution phases [36].

1.6 Chemical reaction of metal hydride and its thermodynamics

A metal hydride is chemically formed from the reaction of hydrogen gas with metal or alloy. The reaction is schematically given by (1.17):



where M is a metal, MH_x is the hydride and ΔH_f is the hydride heat of formation. The hydride formation is exothermic while its decomposition is endothermic. The thermodynamics and the kinetics of the metal-hydrogen system determine the temperature and pressure conditions.

The hydride formation could be divided into different steps. First, when hydrogen is in contact with a metal, the H_2 molecules are attracted to the metal surface by Van der Waals forces and physically adsorbed on it. Then, the H_2 molecules must be decomposed

into two H atoms. This decomposition occurs after overcoming an energy barrier that usually depends on the type of metal atoms at the surface. After the decomposition, the H atoms will be chemisorbed on the metal surface and bonded to the metal atoms. Finally, the chemisorbed H atoms move to the subsurface layers and diffuse into the bulk, producing a hydrogen-metal solid solution known as the α -phase. This is schematically shown in Figure 1.5 from point A to B.

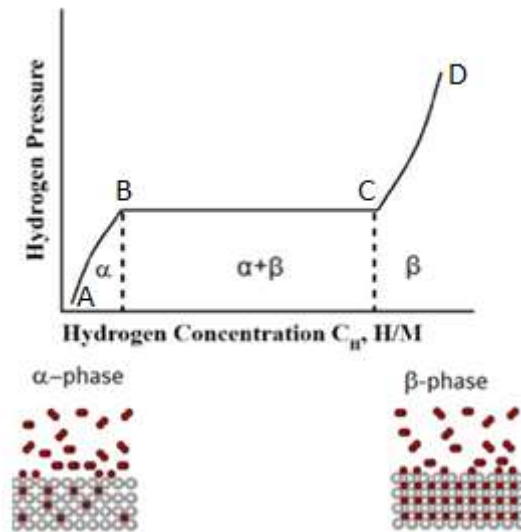


Figure 1.5 Schematic representation of ideal Pressure Composition Temperature “PCT” curve showing three absorption regions for hydride formation [45].

In this stage (from A to B), H atoms diffuse randomly into the interstitial sites (tetrahedral or octahedral) of the metal lattice with no structural change of the metal. At point B, the α -phase becomes saturated with hydrogen and the hydride phase (β -phase) starts to nucleate. From B to C, the β -phase grows, resulting in a decrease of α -phase until the complete transformation to the β -phase (point C). Ideally, this happens under constant pressure and is called the plateau pressure. The length of this plateau indicates the reversible capacity of the hydride. In this plateau region, α and β phases coexist, so the total number of phases is three (α , β and hydrogen gas).

According to Gibb's phase rule, the degree of freedom F at constant temperature in each region is determined by the equation:

$$F = C - P + 2 \quad (1.18)$$

Where C is the number of components and P is the number of phases in thermodynamic equilibrium with each other. F gives the number of possible variables that can change. There are two components: the metal and hydrogen, so $C = 2$.

Referring to Gibb's rule, where α and β phases coexist, there is only one degree of freedom thus giving rise to a plateau region. In the region of α (A to B) or region of β (C to D), $F = 2$, and hydrogen concentration increases with hydrogen pressure.

When new alloys are synthesized for hydrogen storage, it is important to determine the heat of formation of their hydrides. For this purpose, pressure composition temperatures "PCTs" should be carried at different temperatures. By changing the temperature, the plateau pressure changes. This gives rise to the Van't Hoff plot. The Van't Hoff relation is given by:

$$\ln \left(\frac{P_{eq}}{P_0} \right) = \frac{\Delta H}{RT} - \frac{\Delta S}{R} \quad (1.19)$$

where P_{eq} is the equilibrium pressure, P_0 is the standard atmospheric pressure (10^2 kPa), ΔH is the enthalpy change during the formation of the hydride (transition α and β), ΔS is the associated change in entropy, R is the gas constant and T is the temperature at which the experiment is carried out. The enthalpy of formation ΔH and the entropy ΔS can be derived from a plot of $\ln (P_{eq}/P_0)$ versus $1/T$ (Figure 1.6). The enthalpy and entropy are respectively the slope and intercept of the straight line.

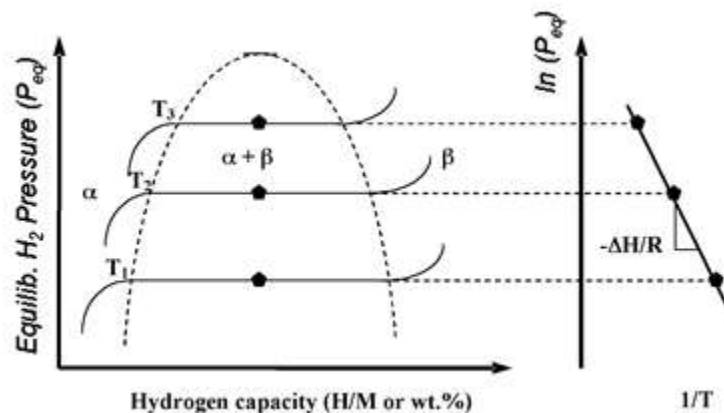


Figure 1.6 Pressure-composition temperatures (PCTs) at different temperatures and associated Van't Hoff graph [46].

1.7 Activation process

Activation process is the first exposure of metal alloy to hydrogen i.e., the “first hydrogenation”. Usually, before hydrogenation, the surface of the metal alloy is passivated by oxide layers. These layers may act as a barrier for hydrogen and should be cracked to get hydrogen in contact with the bare metal surfaces.

Generally, the activation process is done at high temperature and high hydrogen pressure. Under these conditions, hydrogen is compelled through the oxide layer to reach the fresh metal surface for direct hydrogen interaction. Once the alloy is activated, hydrogenation becomes easier and quicker. Activation is an essential step that should be taken into consideration in the utilization of metal hydrides.

1.8 Choice of alloy composition

HEAs are beneficial for hydride formation because of their distorted lattices. The difference in atomic radii of the constituent elements of a HEA could lead to an important degree of lattice strain distortion. This large distortion is particularly interesting for hydrogen absorption by offering large interstitial sites that might be useful for the insertion of a significant amount of hydrogen [47].

One of the first HEA studied for its hydrogen storage properties was the BCC alloy TiVZrHfNb [34]. Sahlberg et al. showed that this alloy can absorb hydrogen with a plateau pressure of 0.1 bar H₂ at 299 °C with 2.7 wt% maximum storage capacity. In their work, they ball milled the as-cast TiVZrHfNb alloy and afterward sieved it to obtain a powder of size less than 0.05 mm. This particle size was used for activation at 400 °C under 20 bar H₂ [34]. As activation may be affected by temperature, pressure and particle size, in our first investigation we studied the effect of these parameters on the activation process of TiVZrHfNb alloy.

After understanding the important parameters for activation, we substituted Nb by V in the TiHfZrNb_{1-x}V_{1+x} alloy. The reason for this substitution is that V is lighter than Nb but has the same chemistry. Thus, the hydride could potentially have a higher capacity.

A new multicomponent alloy of composition Ti_{0.3}V_{0.3}Mn_{0.2}Fe_{0.1}Ni_{0.1} was also investigated. The transition elements of period 4, Ti, V, Mn, Fe and Ni were selected. Even though not all of them are strong hydride forming elements, not using the heavier elements of periods 5 or 6 means that potentially the gravimetric hydrogen storage capacity may be

higher. The atomic compositions of the selected elements were chosen using the criteria Ω , δ and VEC.

It is well known that Ti-V-Cr BCC solid solution alloys are promising hydrogen storage materials for stationary applications [48, 49]. The $Ti_1V_{0.9}Cr_{1.1}$ BCC alloy was selected by looking at the ternary phase diagram of the Ti-V-Cr system. Its first hydrogenation is practically impossible at room temperature and under 20 bars of hydrogen [50]. In this work, we tried to treat this problem by mechanical deformation.

Figure 1.7 shows the summary of the work in this thesis.

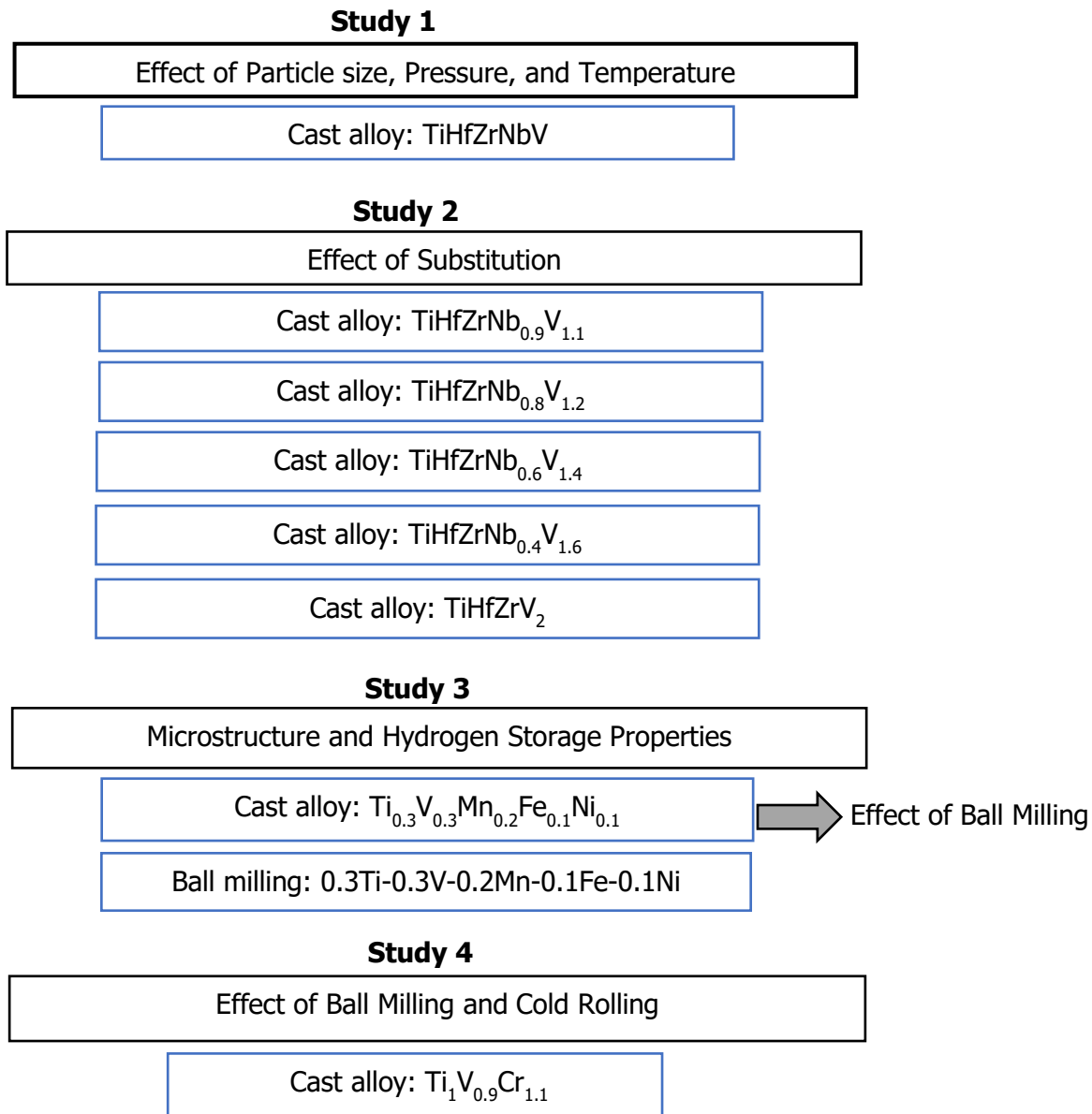


Figure 1.7 Summary of the work.

1.9 Research objective

The goal of this PhD was to explore the hydrogenation behaviour of HEAs. First, the effect of particle size, pressure, and temperature on the activation process of TiVZrHfNb HEA was investigated. Secondly, a systematic study on the composition variation of HEAs by substituting Nb by V in TiHfZrNb_{1-x}V_{1+x} alloy was performed. Thirdly, the heavy elements: Zr, Nb and Hf were replaced by lighter ones of period 4, in the composition Ti_{0.3}V_{0.3}Mn_{0.2}Fe_{0.1}Ni_{0.1}. The microstructure and the hydrogen storage properties of the Ti_{0.3}V_{0.3}Mn_{0.2}Fe_{0.1}Ni_{0.1} alloy were also studied. Finally, the effect of a mechanical treatment on the first hydrogenation of BCC alloy Ti₁V_{0.9}Cr_{1.1} was investigated.

1.10 Thesis structure

In this thesis, the experimental details are reported in chapter 2. Chapter 3 covers the effect of particle size, pressure and temperature on the activation process of hydrogen absorption in TiVZrHfNb high entropy alloy. The effect of the substitution of Nb by V on the microstructure and hydrogen storage properties of TiHfZrNb_{1-x}V_{1+x} alloy for x=0, 0.1, 0.2, 0.4, 0.6 and 1 is presented in chapter 4. Chapter 5 shows the microstructure and hydrogen storage properties of the multiphase Ti_{0.3}V_{0.3}Mn_{0.2}Fe_{0.1}Ni_{0.1} alloy. In chapter 6, the enhancement of the first hydrogenation of Ti₁V_{0.9}Cr_{1.1} BCC alloy by cold rolling and ball milling is discussed. The conclusion of this research and future work are in chapter 7.

Chapter 2

Experimental Details

2.1 Synthesis of Materials

All elements were purchased from Alfa Aesar and used without further purification. Table 2.1 presents all the raw elements used with their purity and physical appearance.

Table 2.1 Raw elements.

Element	Purity at. %	Description
Ti	99.95	sponge
V	99.7	pieces
Zr	99.5	sponge
Hf	99.6	sponge
Nb	99.8	pieces
Mn	99.9	pieces
Fe	99.9	Pieces
Ni	99	pieces
Cr	99	pieces

Ti-V-Zr-Hf-Nb, $Ti_{0.3}V_{0.3}Mn_{0.2}Fe_{0.1}Ni_{0.1}$ and $Ti_1V_{0.9}Cr_{1.1}$ alloys were prepared by arc melting in argon atmosphere. Each pellet was melted and turned over three times to ensure homogeneity.

Ball milling was used to synthesize the alloy $Ti_{0.3}V_{0.3}Mn_{0.2}Fe_{0.1}Ni_{0.1}$. Ball milling was also performed on as-cast $Ti_{0.3}V_{0.3}Mn_{0.2}Fe_{0.1}Ni_{0.1}$ and $Ti_1V_{0.9}Cr_{1.1}$ alloys. The samples were milled for different time intervals.

Cold rolling was performed in air on as-cast $Ti_1V_{0.9}Cr_{1.1}$ alloy for different numbers of rolling passes. Table 2.2 shows the summary of the compositions processed with different synthesizing techniques.

Table 2.2 Summary of the compositions.

Arc melting	Ball Milling	Cold Rolling
0.2Ti-0.2V-0.2Zr-0.2Hf-0.2Nb	0.3Ti-0.3V-0.2Mn-0.1Fe-0.1Ni	Cast(0.33Ti-0.3V-0.37Cr) rolled one, three and six times.
0.2Ti-0.2Hf-0.2Zr-0.18Nb-0.22V	milled for 1, 5 and 10 hours.	
0.2Ti-0.2Hf-0.2Zr-0.16Nb-0.24V		
0.2Ti-0.2Hf-0.2Zr-0.12Nb-0.28V		
0.2Ti-0.2Hf-0.2Zr-0.8Nb-0.32V	Cast (0.3Ti-0.3V-0.2Mn-0.1Fe 0.1Ni), milled for 1, 5 and 10 hours.	
0.2Ti-0.2Hf-0.2Zr-0.4V		
0.33Ti-0.3V-0.37Cr		
0.3Ti-0.3V-0.2Mn-0.1Fe-0.1Ni	Cast (0.33Ti-0.3V-0.37Cr), milled for 5, 15, 30, and 60 minutes.	

2.1.1 Arc Melting

Arc melting is a conventional and simple technique, typically used for the synthesis of alloys of electrically conductive materials. In our laboratory, a Centorr Associates Inc, USA arc melter is used and its setup is shown in Figure 2.1. This arc melting machine is made of a melting chamber, electric arc welder, vacuum pump, inert gas delivery system and water cooling.

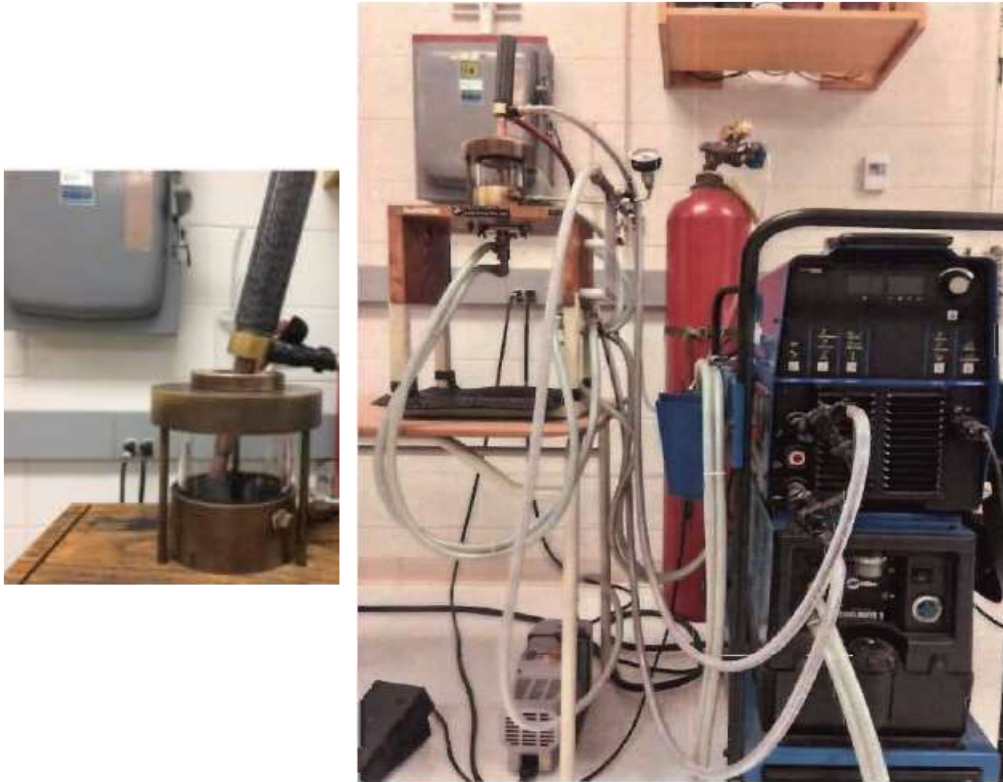


Figure 2.1 Arc melter (Centorr Associates Inc, USA).

The sample of desired stoichiometry is placed on a water-cooled copper crucible. The arc melting chamber is evacuated via a rotary pump and then refilled by argon gas of 0.7 bars pressure. To ensure homogeneity, the pellet is turned over three times and remelted.

2.1.2 Ball Milling

Ball milling process is used for mechanical alloying (MA) and to pulverize alloys into powder. In the present investigation ball milling was used to synthesize alloys (mechanical alloying) and to study its effect on arc-melted alloys.

In this work, ball milling was carried out on a Spex 8000M high energy ball mill (SPEX SamplePrep, Metuchen, NJ, USA) in a hardened 55 cc stainless steel crucible and balls with a powder-to-ball mass ratio of 1/10. All loadings and unloading of powder in the crucible were performed in an argon-filled glove box. The shaking frequency was 1060 cycles per minute. The ball miller is shown in Figure 2.2.



Figure 2.2 Ball miller Spex 8000.

2.1.3 Cold Rolling

Rolling is a process where the sample is introduced between two rollers where it is compressed and rolled. If the sample temperature is higher than its recrystallization temperature, then the process is called hot rolling (HR). If the sample temperature is below its recrystallization temperature, the term cold rolling (CR) is used.

In this research work, only cold rolling was done. The CR apparatus used was a Durston DRM 130 (High Wycombe, UK) that was modified so the powder samples could be rolled vertically (Figure 2.3). Rolling experiments were performed in the air by inserting the powder obtained from hand crushing between two 316 stainless steel plates. The plates were used to prevent contamination from the rolls. Rolling was performed one, three, and six times.

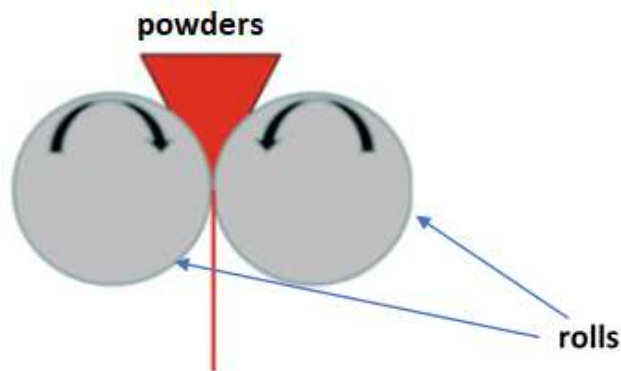


Figure 2.3 Schematic of cold rolling.

2.2 Characterization techniques

The microstructure and chemical analysis were performed using a JEOL JSM-5500 scanning electron microscopy (SEM) equipped with an EDX (Energy Dispersive X-ray) apparatus from Oxford Instruments. Image J software was used to analyze the percentage area of different phases in SEM micrographs [51]. The crystal structure of the samples was determined by X-ray diffraction (XRD; Bruker D8 Focus; Cu K α radiation). Crystal structure parameters were evaluated from Rietveld's method using TOPAS software [52]. The hydrogen storage properties were measured by using a home-made Sieverts-type apparatus.

2.2.1 Scanning Electron Microscopy (SEM)

SEM is a technique used to produce high-resolution images of a sample by scanning its surface with a focused beam of electrons. Because of the large depth of field, these images have a 3-dimensional appearance.

A SEM is typically formed of an electron gun, electromagnetic lenses and detectors. The electron gun generates high energy electrons, and these electrons are accelerated and focused on the sample using the electromagnetic lenses. The interaction of the electrons with atoms in the sample occur at different depths. This interaction produces secondary and backscattered electrons and other radiations such as X-rays. Each signal is measured with a dedicated detector. The schematic for scanning electron microscope is shown in Figure 2.4 [53].

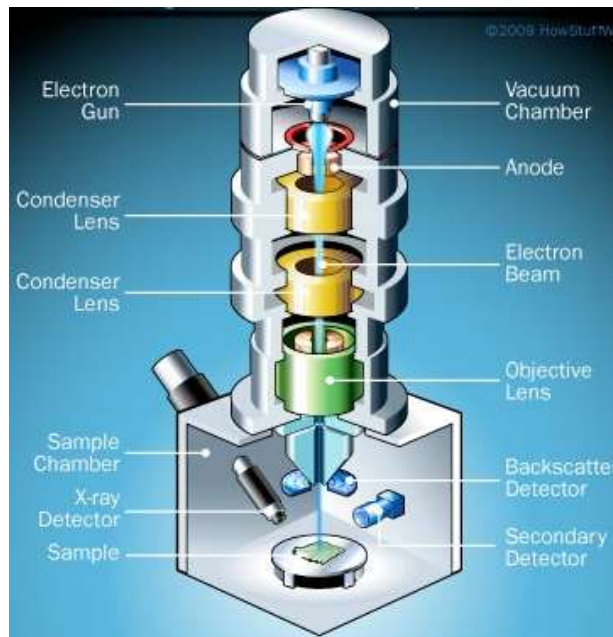


Figure 2.4 Schematic of scanning electron microscope.

Figure 2.5 shows the interactions of the primary electrons with atoms in the sample.

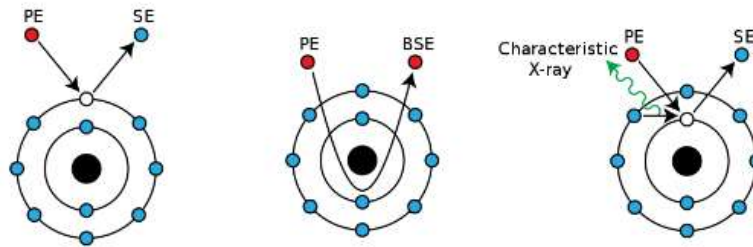


Figure 2.5 Mechanisms of emission of secondary electrons SEs, backscattered electrons BSE, and characteristic X-rays from atoms of the sample.

The secondary electrons "SE" are emitted by inelastic scattering from the atoms on the surface or the near-surface regions of the sample. The SEs give a high-resolution image of the sample surface.

Back scattered electrons "BSE" are the incident electrons reflected or back scattered by the atoms in the sample by elastic scattering. The intensity of BSE is directly proportional to the atomic number Z of the elements probed. Thus, elements with different atomic numbers could be easily distinguished. Heavy elements backscatter electrons more strongly than light elements, and thus appear brighter in the image. BSE provides images showing the contrast between regions with different chemical compositions but without identifying the elements.

The X-rays are emitted when the incident electrons interact with an atom and cause an inner shell electron to be ejected. The ejection of the electron creates a vacancy in the inner shell. This vacancy is then filled by the transition of an electron from a higher energy shell. The transition is accompanied by emitting radiation with energy equal to the energy difference between the higher and the lower energy shells. This emitted radiation is in the form of X-ray known as the characteristic X-ray since each element produces X-rays with a unique wavelength. It is these "characteristic X-ray lines" that the EDX uses to identify and quantify the elements present in the sample. The number and energy of the X-rays are measured by an energy-dispersive spectrometer.

2.2.2 X-Ray Diffraction

X-ray diffraction is a common technique used to characterize and identify the crystalline phases in a material. X-ray diffraction is based on constructive interference of monochromatic X-rays. The wavelength of the X-rays should be of the same order as the spacing between atoms in the crystal lattice. When the X-ray beam hits the crystal, a constructive interference between elastically scattered X-ray beams occurs at the Bragg's angle. Bragg's law is expressed as:

$$2d_{hkl} \sin \theta_{hkl} = n \lambda \quad (2.1)$$

Where, d_{hkl} is the interplanar spacing of crystallographic planes hkl , θ_{hkl} is Bragg's angle, n is an integer, the order of the reflection (normally equal to 1) and λ is the wavelength of the X-rays. Figure 2.6 presents the schematic diagram of Bragg diffraction [54].

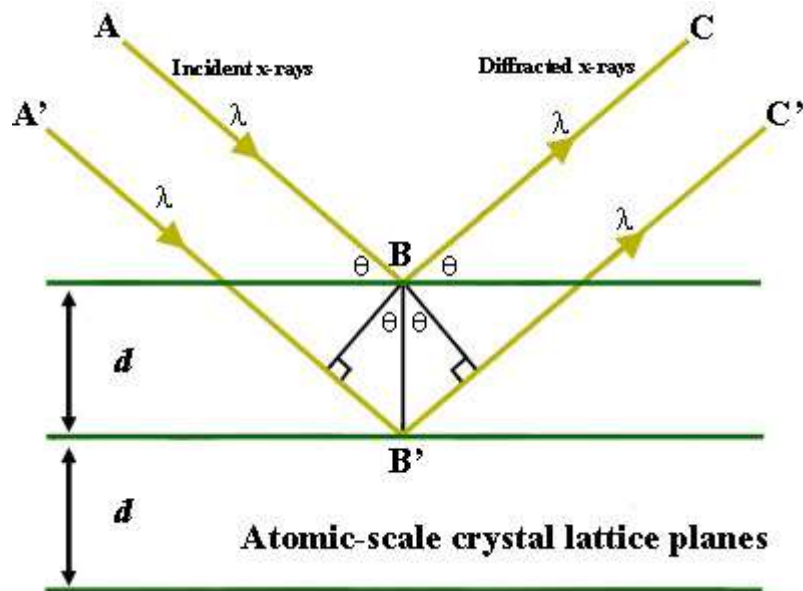


Figure 2.6 Schematic diagram of Bragg diffraction.

The interplanar spacing d_{hkl} depends on the crystal structure. For each crystal system, there is a formula relating this distance d_{hkl} to the Miller indices (hkl) and the lattice parameters of the crystal lattice. The Equation 2.2 for a cubic system is:

$$d_{hkl} = \frac{a}{\sqrt{h^2 + l + k^2}} \quad (2.2)$$

Where a is the lattice parameter of the cubic crystal and h , k , and l are the Millers indices of the Bragg's plane.

For phase identification, the "fingerprint" of a diffraction pattern can be compared to a database such as the International Powder Diffraction File (PDF) database compiled by the Joint Committee for Powder Diffraction Standards (JCDs) [55].

The quantitative analysis of the diffraction patterns was carried out by a Rietveld refinement using the TOPAS software [56]. Rietveld's method is a complete pattern analysis where the experimental pattern is compared to a calculated diffraction pattern. Based on crystallographic data provided by the user together with instrumental parameters, the calculated pattern is generated. The theoretical crystal structure information includes the crystal chemical formula, space group, unit cell parameters, atomic positions, thermal factors and occupancy of atomic positions. A least square method is used to minimize the difference between the calculated pattern and the observed one. The refinement is done by changing structural parameters of the calculated pattern one by one. When Rietveld refinement confirms the theoretical crystal structure, unit cell parameters, crystallite size, and microstrain could be extracted. It can also determine the weight percentages of each phase in the case of a multiphase crystalline material.

2.2.3 Sievert's Apparatus

Sieverts technique is a well-known method to determine the hydrogen storage properties of a material. In this work, a home-made volumetric Sievert's type apparatus was used. In this apparatus, the measurement is based on the change of pressure in a calibrated volume. The apparatus has different operational modes such as absorption and desorption kinetics, pressure composition isotherms, cycling and temperature ramp desorption.

Figure 2.7 shows a basic schematic diagram of Sieverts-type apparatus. It is made of hydrogen reservoir, valves, pressure gauge, vacuum pump and two calibrated volumes (reference and sample volumes). The device having a constant volume, the pressure difference will correspond to the amount of hydrogen absorbed or desorbed.

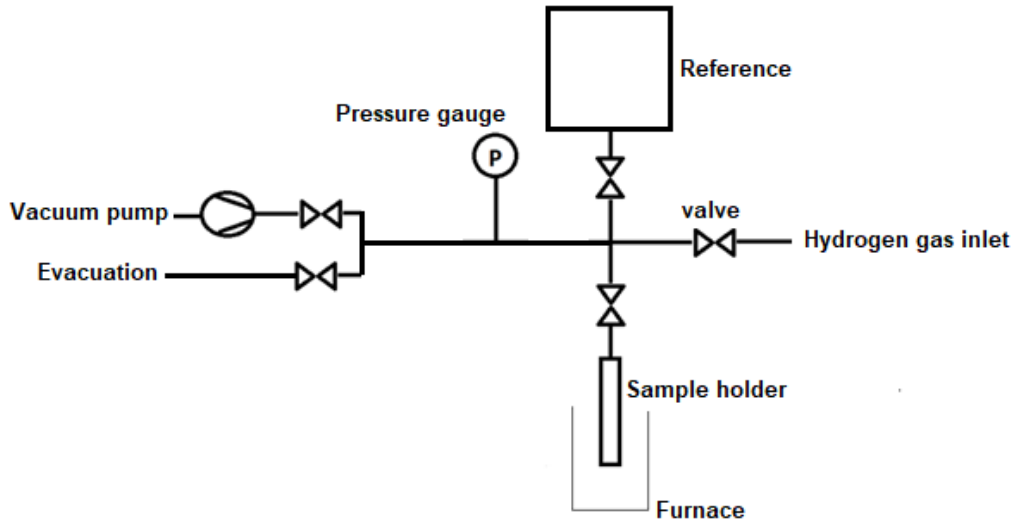


Figure 2.7 Basic schematic diagram of Sieverts-type apparatus.

The amount of gas molecules in a given volume can be calculated by using the virial expansion of second order (enough for the pressure range used in this work) of the real gas law:

$$PV = nRT \left(1 + \frac{nB}{V} \right) \quad (2.3)$$

where P is the hydrogen pressure, V is the volume filled with hydrogen, n is the number of moles of hydrogen, R is the ideal gas constant, T is the temperature of the sample and B is the second virial coefficient that is temperature dependent. The value of B was taken from reference [57].

The volume of the apparatus is constant, and the temperature is kept stable during the measurement. The number of moles of hydrogen absorbed by the sample is:

$$\Delta n = 2 \frac{V \Delta P}{RT \left(1 + \frac{B}{V} \right)} \quad (2.4)$$

where ΔP is the pressure change. The factor 2 corresponds to H atoms absorbed. It comes because the equation of state of gas is established for H_2 .

The quantity of hydrogen absorbed (in mass percentage) is calculated using the equation:

$$\% \text{ absorbed } H = \frac{\text{mass of } H}{\text{mass of (sample+H)}} \quad (2.5)$$

Chapter 3

Effect of particle size, pressure, and temperature on first hydrogenation of TiVZrHfNb high entropy alloy

3.1 Overview

This chapter describes a systematic study of the effect of particle size, pressure, and temperature on hydrogenation behaviour of TiVZrHfNb HEA. The main focus was on the kinetics of the activation. The crystallographic parameters of all samples after hydrogenation were determined. The goal was to identify the important parameters that could have some effect on activation kinetics and the hydrogen capacity of the material.

Figure 3.1 represents the summary of this work.

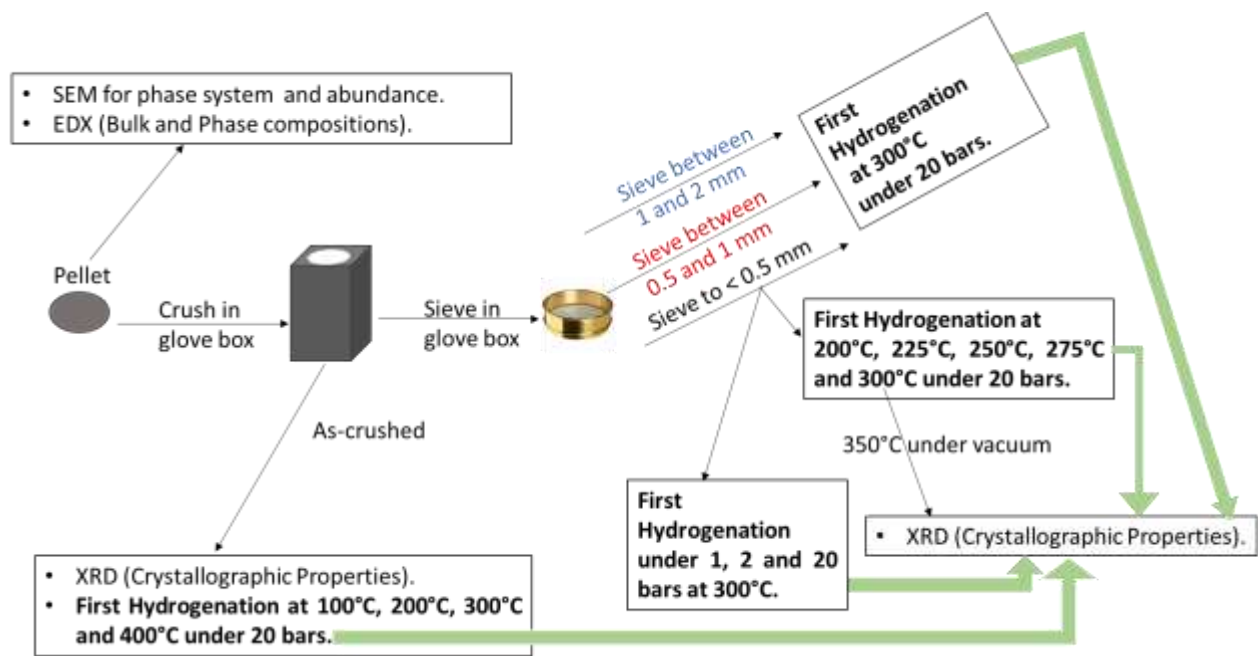


Figure 3.1 Flow chart of synthesis & characterization of TiVZrHfNb alloy.

3.2 Microstructural Study

Figure 3.2 shows backscattered electron micrograph of TiVZrHfNb alloy prepared by arc melting.

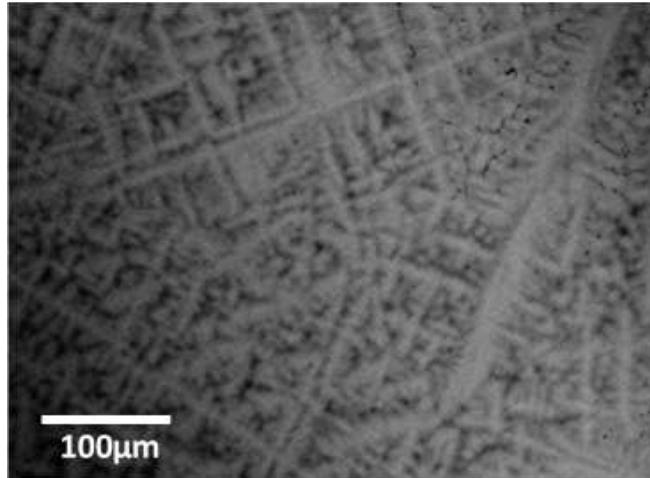
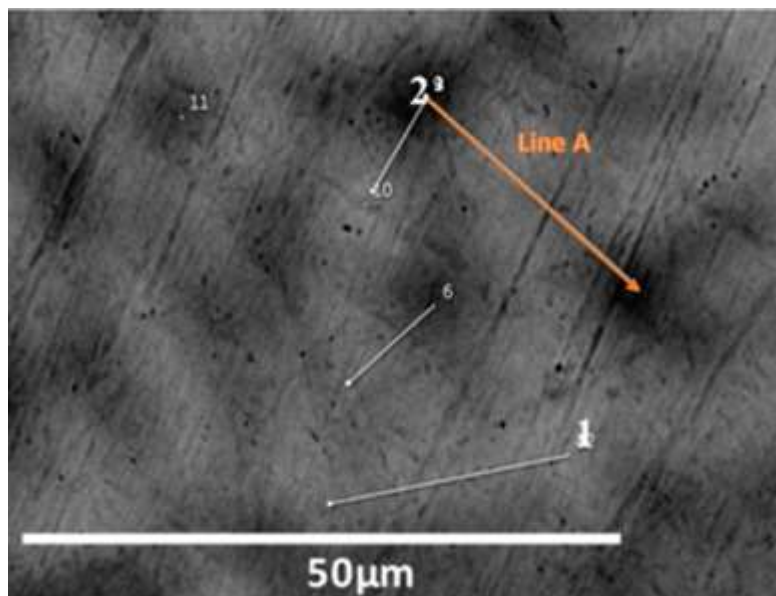


Figure 3.2 Backscattered electrons (BSE) micrograph of as-cast TiVZrHfNb alloy.

The bulk chemical composition was confirmed by EDX measurement to be equal to the nominal values. Dendrites (gray colour) with some black areas are clearly observed. Close inspection of Figure 3.2 shows that the main branch makes 90° with other branches which is an indication of a cubic structure.

Using EDX at a higher magnification, the chemical compositions in the gray and dark areas were determined. The EDX analysis was performed on the selected points presented in Figure 3.3.



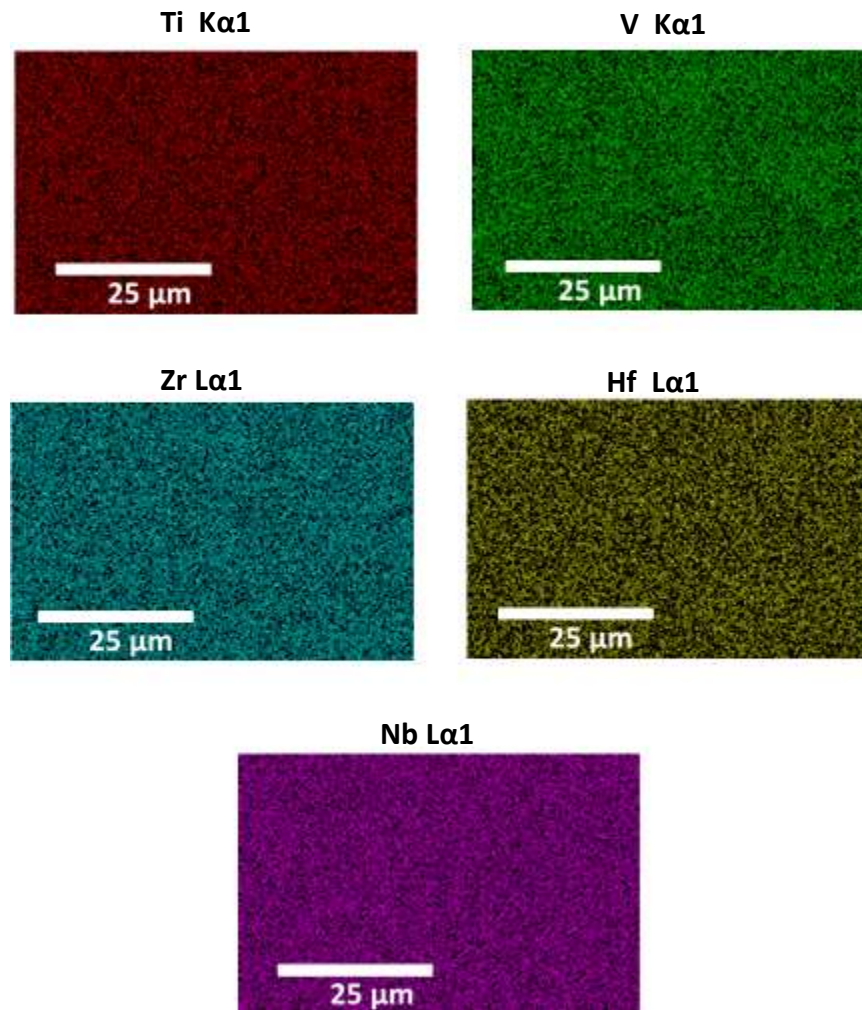


Figure 3.3 BSE micrograph of as-cast TiVZrHfNb alloy with magnification 2000 \times .

From the elements mapping, it is clear that all the elements are evenly distributed. The quantitative analysis at points 1 (gray area) and 2 (dark area) is listed in Table 3.1.

Table 3.1 EDX analysis showing the elemental composition of TiVZrHfNb alloy. Error on each value is 0.1 at.%.

Element (at.%)	Ti	V	Zr	Hf	Nb
Point 1	20.0	19.1	18.7	22.5	19.7
Point 2	20.4	22.6	21.0	18.1	17.9

From this table we see that the chemical compositions of points 1 and 2 are quite close. Also, there is no clear-cut boundary between the darker and lighter shades of gray. This indicates that there is probably a variation of composition. To confirm this, the chemical

analysis over the lines indicated in Figure 3.3 was performed. As a representative, the analysis over line A of Figure 3.3 is shown in Figure 3.4.

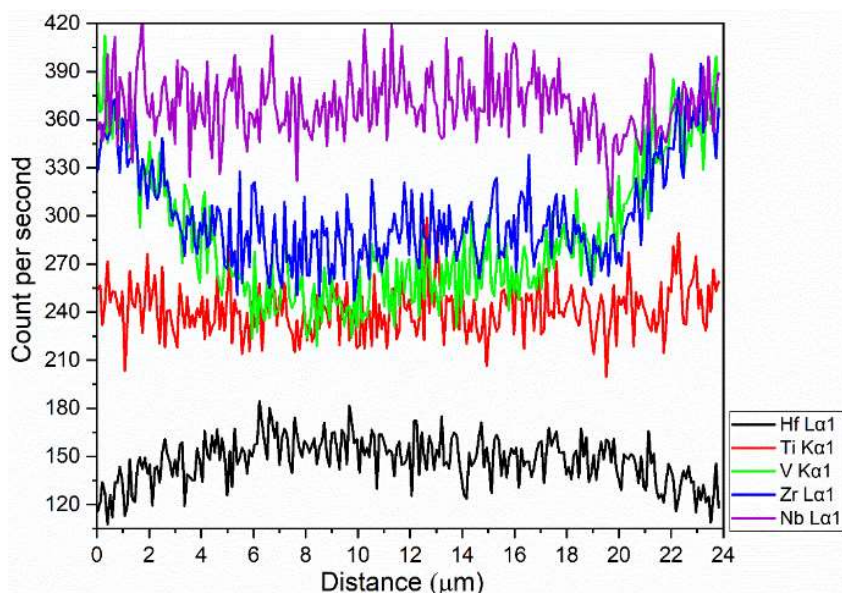


Figure 3.4 Line analysis of line A of Figure 3.3.

Figure 3.4 indicates that the amounts of Ti and Nb are almost constant over the line. The amount of Hf increases in the gray region when compared to the dark region while Zr and V decrease with the same rate. Thus, there is clearly a continuous variation of composition, but it is not random. It should also be mentioned that even if the line analysis does not show a variation in the Nb proportion, the point analysis reported in Table 3.1 indicates a slight increase between the dark and gray areas.

It is interesting to note that the two elements which have a constant or slight variation of abundance have very close atomic radii (144.8 pm for Ti and 142 pm for Nb). However, the two elements that have identical decrease of abundance, Zr and V are respectively the biggest atomic radius (160 pm for Zr) and the smallest one (132.1 pm for V). In the case of Hf which abundance increases by going from the dark to the gray areas, its atomic radius is 156.4 pm. These observations indicate that the atomic radii most probably play a role in the variation of composition. However, other factors are certainly playing a role. Because of the variation of composition, it should be pointed out that the abundances given by EDX are only an indication. From point to point, the proportion could change as seen in Figure 3.4.

3.3 Crystal Structure

Figure 3.5 presents the XRD patterns of the as-cast TiVZrHfNb alloy. The crystal structure parameters and the R_{wp} value as evaluated by Rietveld's refinement are shown in Table 3.2.

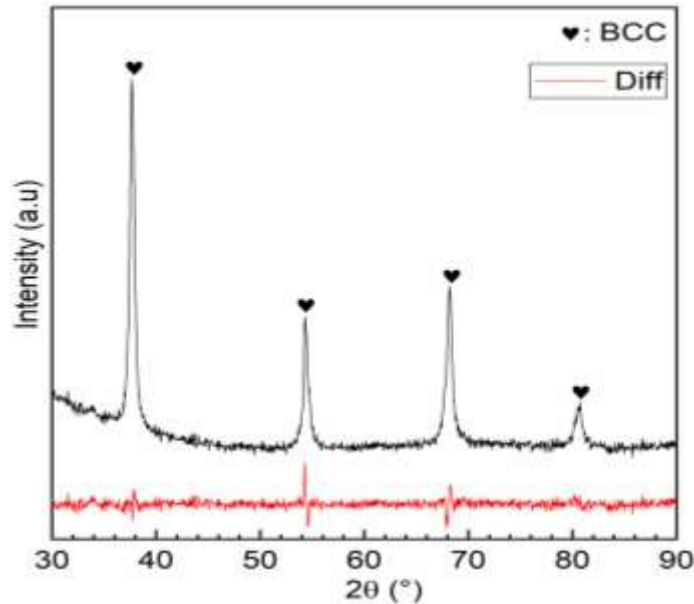


Figure 3.5 XRD patterns of the as-cast TiVZrHfNb alloy. The bottom curve is the difference between calculated and measured intensities.

Table 3.2 Crystal structure parameters and the R_{wp} value of the as-cast TiVZrHfNb alloy. Error on the last significant digit is indicated in parentheses.

Phase	Cell Volume (Å ³)	Lattice Parameter (Å)	Crystallite Size (nm)	Microstrain %	R_{wp}
BCC	38.14 (2)	3.3663 (4)	14.3 (3)	0.08 (1)	4.67

The diffraction pattern indicates that the alloy is a single-phase BCC (space group $Im\bar{3}m$). However, as the SEM investigation showed a variation in chemical composition, we could conclude that this BCC phase has a range of chemical composition. The lattice parameter of TiVZrHfNb alloy reported in Table 3.2 is in good agreement with the previous study of Sahlberg et al. (lattice parameter 3.3659 Å) [34]. The microstrain value suggests that the lattice of TiVZrHfNb alloy is slightly strained. This may be due to the inhomogeneous chemical composition which in turn gives rise to a variation of lattice parameters within the phase thus creating microstrains. Therefore, the microstrain

parameter effectively reflects the composition change within the phase. The same phenomenon was seen by Khajavi et al. for AB₂ system [58].

3.4 First Hydrogenation (Activation)

3.4.1 Effect of Particle size on activation behaviour

The activation curves at 300°C and under 20 bars of hydrogen pressure of powder with different particle sizes are shown in Figure 3.6.

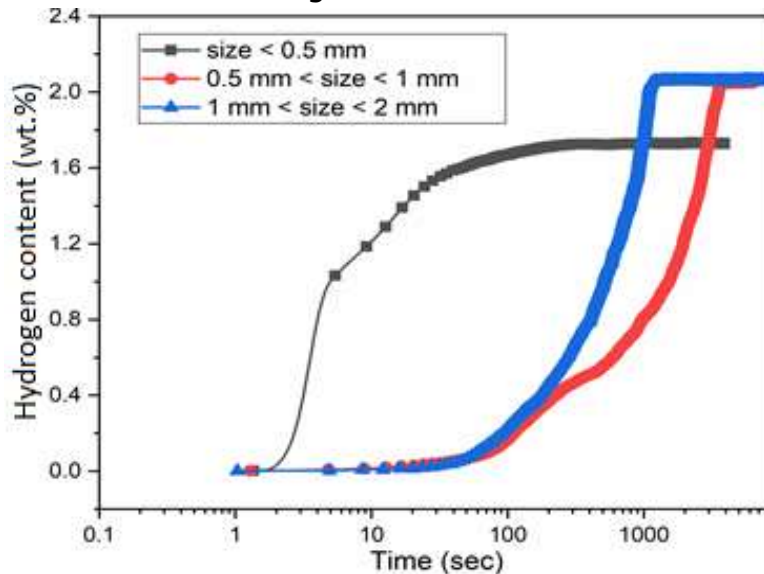


Figure 3.6 Activation curves at 300°C of TiVZrHfNb alloy for different particle size.

The fastest activation is for the smallest particle size (< 0.5 mm). Surprisingly, the kinetics of particles between 0.5 mm and 1 mm is slower than that of size between 1 mm and 2 mm. But both samples absorb hydrogen to a maximum capacity of 2.1 wt.% (1.94 H/M) where the small particle size has 1.7 wt. % (1.57 H/M) capacity. The 'maximum capacity' or 'full capacity' means the highest capacity reached by the particular sample.

Although bigger particles have a slightly faster kinetics than the intermediate size one, we could still conclude that the activation depends on the particle size. This result agrees with a previous work investigated by Kamble et al. on the BCC TiVCr system [59].

To see the impact of particle size on the crystal structure of the hydride phase, the XRD patterns were taken after reaching full hydrogenation. At the end of the absorption experiment, the sample was kept under hydrogen pressure while the temperature decreased. Sahlberg et al. have shown that under vacuum no desorption occurred at temperatures below 200°C [34]. Therefore, this procedure effectively 'quenched' the

hydride phase. Figure 3.7 presents the XRD patterns of the hydride samples with different particle size.

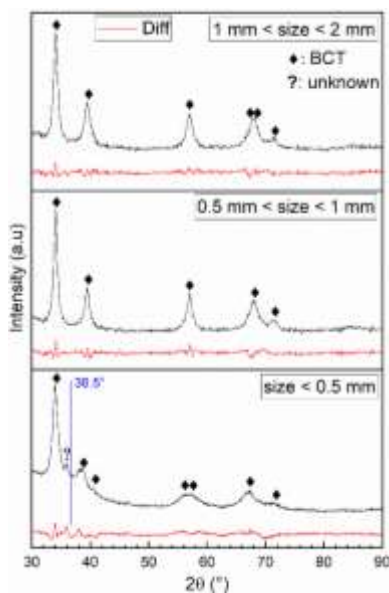


Figure 3.7 XRD patterns of different particle sizes hydrogenated at 300°C under 20 bars.

Figure 3.7 shows the X-ray diffraction patterns after first exposure to hydrogen. Both FCC and BCT structures were used for refinement but, for all patterns, the BCT structure was giving a better fit. In Table 3.3, there are the results of Rietveld's refinement of all these patterns.

Table 3.3 Crystal structure parameters of the BCT phase for different particle sizes hydrogenated at 300°C under 20 bars. Error on the last significant digit is indicated in parentheses.

Sample particle size	Cell Volume (Å ³)	Lattice parameter (Å)	Crystallite size (nm)	Micro strain (%)	Phase (%)	R _{wp}	Amorphous
Less than 0.5 mm	48.60 (7)	a= 3.301 (2) c= 4.460 (4)	5.9 (2)	0.41 (2)	77	3.95	23%
Between 0.5 and 1 mm	48.38 (4)	a= 3.260 (1) c= 4.551 (3)	10.6 (5)	0.31 (2)	100	5.06	-----
Between 1 and 2 mm	48.50 (5)	a= 3.264 (1) c= 4.552 (3)	11.2 (6)	0.41 (2)	100	4.86	-----

All the hydrogenated sizes have the BCT structure with almost same lattice parameters. However, the crystallite size decreases with decreasing particle size. This may be explained by the higher specific surface of the small particles. Also, as the small particles were produced by mechanical deformation, the fact that these particles broke down from the main ingot means that the defect density on their surface is higher than the big particles. The defects act as nucleation points for the hydride phase and more defects means that the crystallite size will be smaller.

It is well known that BCT is the monohydride structure of BCC alloys where FCC is usually the crystal structure adopted by a fully hydrided BCC alloy [60]. However, for the HEA TiVZrHfNb, Sahlberg et al. have shown that the dihydride has the BCT structure [34]. They explained the high hydrogen abundance of the BCT structure by strain in the distorted HEA lattice. This high strain enabled the occupation of both tetrahedral and octahedral sites. In situ synchrotron X-ray diffraction at temperature up to 600°C and pressure 100 bars was performed by Karlsson et al. [31]. They confirmed the BCT structure and mentioned that the room temperature data could be fitted by BCT or FCC structures. From neutron diffraction, Karlsson et al. also confirmed the occupation of both the tetrahedral and octahedral interstitial sites in the BCT structure at 500°C and 100 bars. The present results are in agreement with the conclusions of Sahlberg et al. and Karlsson et al. [31, 34]. It should be noted that the microstrain in the BCT phase is much higher than the microstrain of the as-cast BCC phase reported in Table 3.1.

For the pattern of powder less than 0.5 mm, we found a broad peak centred at 36.5°. We attributed this peak to the presence of an amorphous phase. The center of this amorphous peak is indicated by a line in Figure 3.7. From Rietveld refinement, the abundance of that phase was determined to be 23 wt.%. This may explain the lower hydrogen capacity of this sample indicated in Figure 3.6. Actually, the capacity ratio of 1.7wt.%/2.1 wt% is equal to 81% which is very close to the 77% crystallinity (BCT phase) seen in the diffraction pattern. The reason for the appearance of this amorphous phase will be discussed in the next section.

3.4.2 Effect of Temperature on activation behaviour

To study the effect of temperature, two types of samples were used, first one is as-crushed alloy without sieving and the second one is the sieved powder to particles smaller than 0.5 mm. Figure 3.8 shows the activation curves of the crushed sample at different temperatures and under 20 bars of hydrogen pressure.

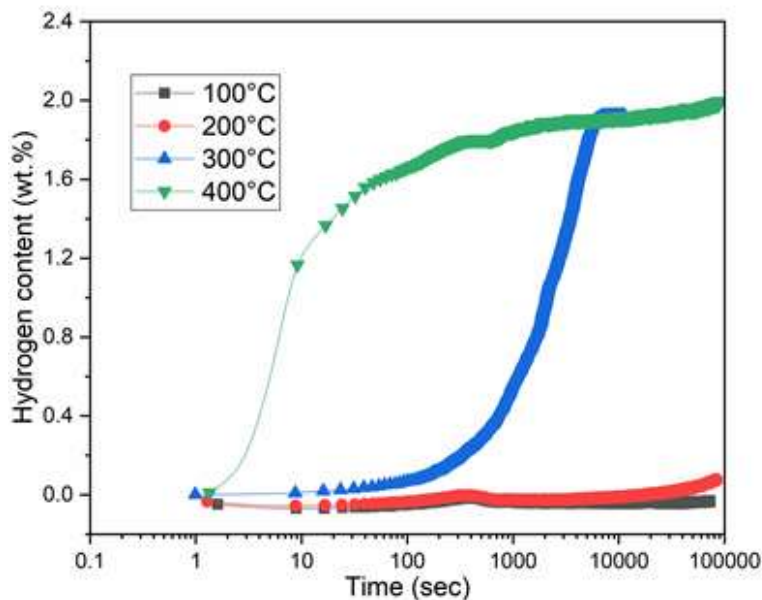


Figure 3.8 Activation curves of as-crushed TiVZrHfNb alloy at 100°C, 200°C, 300°C and 400°C under 20 bars.

The sample didn't absorb hydrogen at 100°C and 200°C even after 24 h of hydrogen exposure. At 300°C, after an incubation period of 500 s, the sample reached a maximum capacity of 1.9 wt.% (1.75 H/M) within 100 min. The activation kinetics was faster at 400°C, reaching 1.9 wt.% capacity after 33 min without incubation period. It is clear that the activation of TiVZrHfNb alloy strongly depends on temperature.

Figure 3.9 shows the XRD patterns of the as-crushed sample hydrogenated at 300°C and 400°C under 20 bars and quenched. Table 3.4 presents their crystal structure parameters as determined by Rietveld's refinement.

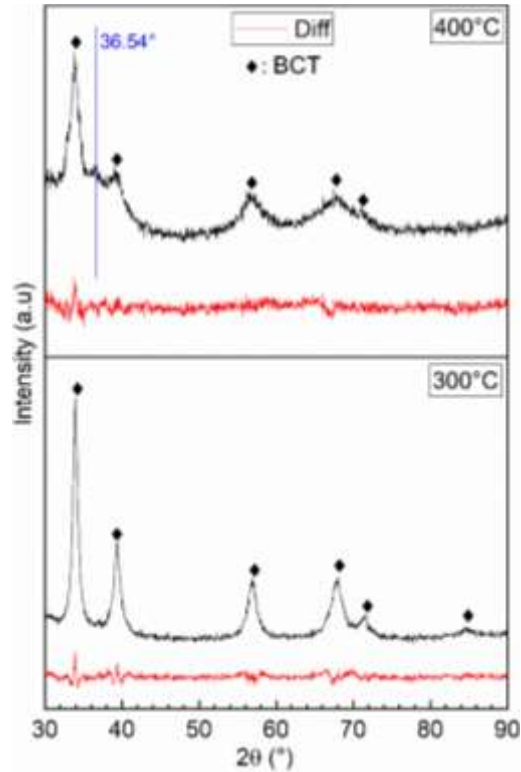


Figure 3.9 XRD patterns of as-crushed TiVZrHfNb alloy hydrogenated at 300°C and 400°C under 20 bars.

Table 3.4 Crystal structure parameters of the BCT phase for as-crushed TiVZrHfNb alloy hydrogenated at 300°C and 400°C under 20 bars. Error on the last significant digit is indicated in parentheses.

	Cell Volume (Å³)	Lattice parameter (Å)	Crystallite size (nm)	Micro strain (%)	R_{wp}	Amorphous
300°C	48.23 (3)	a= 3.257 (8) c= 4.546 (2)	9.2 (2)	0.29 (1)	4.80	-----
400°C	48.66 (9)	a= 3.287 (2) c= 4.505 (5)	3.05 (7)	-----	5.37	8%

The crystal structure of all the patterns in the hydrided state has BCT crystal structure. This is another indication that, for this alloy, the fully hydride sample could have the BCT structure. We see a large difference in the crystallite size at 300°C and 400°C. Also, the microstrain is absent in the 400°C pattern. Moreover, there seems to be a small

amorphous peak at 36.5° which is the exact position of the amorphous peak seen in the pattern of small particles shown in Figure 3.7. Taking into account this amorphous peak, the crystallinity of the 400°C pattern was estimated to be 92%.

A similar investigation was performed on small particles (size less than 0.5 mm). Figure 3.10 presents the activation curves at 200°C , 225°C , 250°C , 275°C and 300°C under 20 bars of hydrogen pressure.

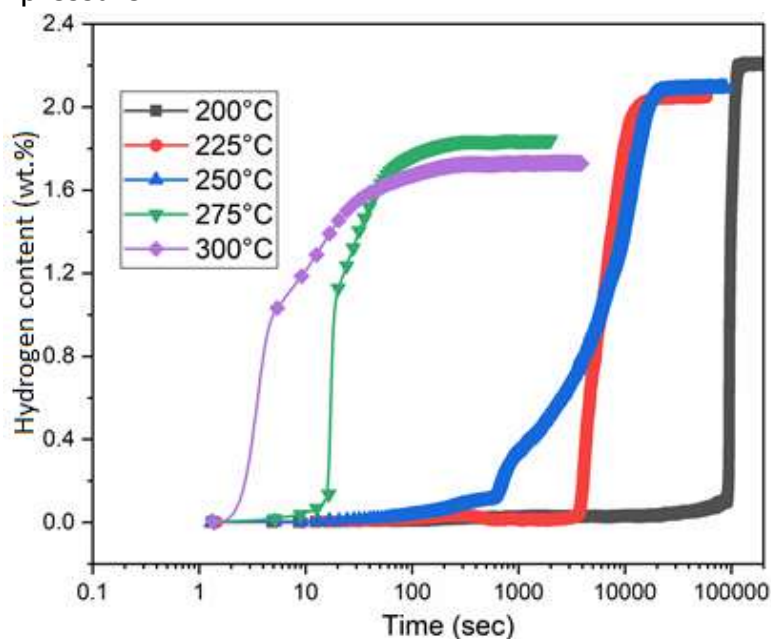


Figure 3.10 Activation curves at 200°C , 225°C , 250°C , 275°C and 300°C of particle size less than 0.5 mm.

The differences between the curves are their shape and incubation period. At 200°C , the activation curve shows a long incubation period (27 h) before starting to absorb hydrogen. However, once started, the hydrogenation is relatively fast, reaching 2.2 wt.% (2.0 H/M) capacity. Increasing the temperature to 225°C reduces drastically the incubation period. At 250°C , the full capacity is reached after 5 h. At 300°C , the kinetics is even faster, and the full hydrogenation is reached after only 5 min. Such a variation of the incubation period with temperature may suggest an Arrhenius-type mechanism. To verify this, we plotted on Figure 3.11 the incubation period ($\ln t$) as a function of $1000/T$. Using Origin software, the onset of slope t was determined by the tangents before and after the incubation.

Figure 3.11 presents the variation of $\ln t$ as a function of the inverse of temperature. It is seen that the experimental points follow a linear relationship between $1/T$ and $\ln t$.

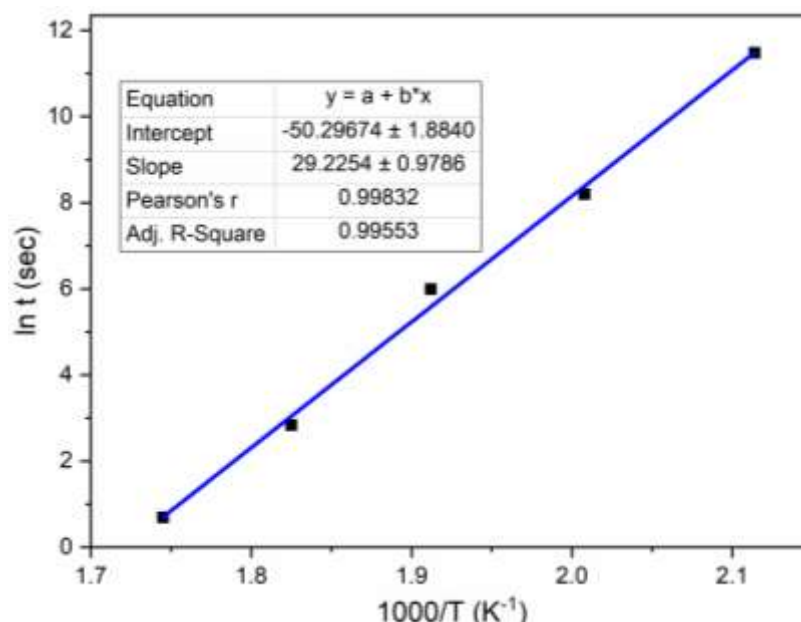


Figure 3.11 Graph of $\ln t$ as a function of $1000/T$ where t is the incubation period and T the temperature.

Figure 3.11 confirms that the incubation period follows an Arrhenius law. Arrhenius equation is expressed by:

$$\ln K = \ln A - \frac{E_A}{RT}, \quad (3.1)$$

Where K is the rate coefficient, A is the frequency factor, R is the gas constant $8.314 \text{ J}/(\text{mol}\cdot\text{K})$, E_A is the activation energy in J/mol and T is the temperature (Kelvin). At the end of the incubation period the reaction is complete, and we should have:

$$Kt = 1, \quad (3.2)$$

Thus, for the onset point (period when the incubation is complete) we have:

$$-\ln t = \ln K \quad (3.3)$$

From the fitted values of Figure 3.11, we get $E_A = 241 \pm 8 \text{ kJ}/\text{mol H}_2$.

To our knowledge, this the first time an Arrhenius mechanism is proved for incubation period of the first hydrogenation of a metal hydride. A closely related example is the amorphous phase transformation in bulk metallic glasses that also obeys Arrhenius

equation. The activation energies found in these cases range from 200 kJ/mol to 453 kJ/mol which is the same order of magnitude of the present result [61-63].

Figure 3.12 presents the XRD patterns of the small particles (size less than 0.5 mm) upon hydrogenation at different temperatures under 20 bars of hydrogen pressure. Their corresponding crystal parameters are reported in Table 3.5.

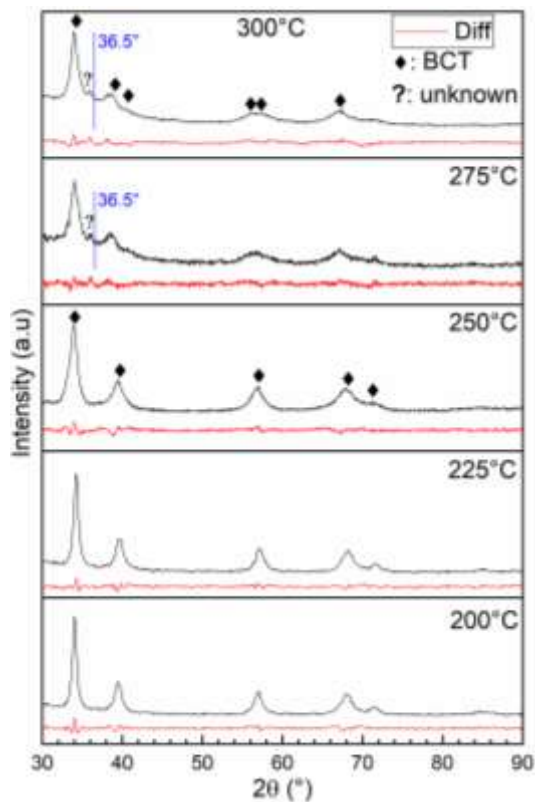


Figure 3.12 XRD patterns of particles of size less than 0.5 mm hydrogenated at 200°C, 225°C, 250°C, 275°C and 300°C.

Table 3.5 Crystal structure parameters of the BCT phase for particles of size less than 0.5 mm hydrogenated at different temperatures. Error on the last significant digit is indicated in parentheses.

	Cell Volume (Å³)	Lattice parameter (Å)	Crystallite size (nm)	Micro strain (%)	R_{wp}	Amorphous
200°C	48.05 (3)	a= 3.253 (1) c= 4.541 (2)	13.5 (6)	0.29 (1)	4.85	-----
225°C	48.23 (4)	a= 3.258 (1) c= 4.545 (2)	13.9 (7)	0.33 (1)	4.90	-----
250	48.15 (5)	a= 3.261 (3) c= 4.527 (3)	6.9 (2)	0.51 (1)	4.56	-----
275	49.2 (1)	a= 3.314 (3) c= 4.478 (6)	6.3 (5)	0.51 (3)	4.01	8%
300	48.60 (7)	a= 3.301 (2) c= 4.460 (5)	5.9 (2)	0.41 (2)	3.95	23%

It is clear that the crystal structure doesn't depend on the temperature, the hydride phase is BCT for all temperatures. All the patterns correspond to activation at 200, 225 and 250 °C have BCT crystal structure with almost same crystal parameters except for the crystallite size which decreases with increasing temperature. An amorphous phase is present in the 275 °C and 300 °C patterns. There is also a small unidentified peak at around 36°. As no reduction of capacity and absence of amorphous phase was seen for particles bigger than 0.5 mm, it seems that both particle size and temperature are factors for the appearance of amorphous phase upon hydrogenation. We saw that small particle size produces small crystallite size. At higher temperatures, the kinetic is faster and the material may not have time to mechanically adjust to the new phase and break. A smaller crystallite size means a higher proportion of grain boundaries. The grain boundary is amorphous and probably does not absorb hydrogen. Thus, the hydrogen capacity will reduce with crystallite size and thus be dependent on the particle size and hydrogenation temperature. This could also explain the features of Figure 3.9 where the amorphous content was seen only 8 wt.% for the 400 °C sample. The as-crushed sample is made of particles of all sizes. Only the smaller ones will partially transform to an amorphous phase and thus the amorphous proportion is lower than for a sample exclusively made of small particles.

3.4.3 Effect of Pressure on first hydrogenation

To study the impact of pressure in the crystal structure after hydrogen absorption, we did the activation of the small particles (less than 0.5 mm) under 1, 2, and 20 bars of hydrogen pressure at 300°C. The activation curves are shown in Figure 3.13.

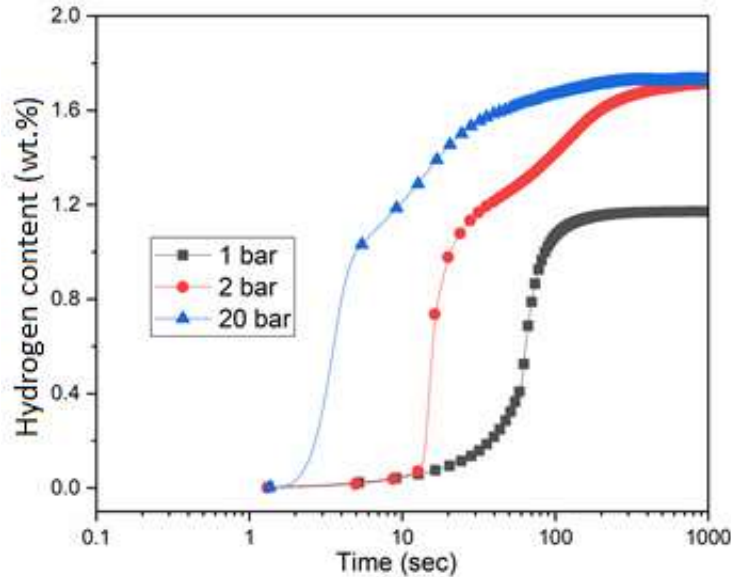


Figure 3.13 Activation curves at 300°C under 1, 2 and 20 bars of hydrogen of particles of size less than 0.5 mm.

We see that activation under 1 bar gives a capacity of around 1.2 wt.% (1.1 H/M) of hydrogen with 50 s of incubation period. As the pressure increases, the incubation period decreases. The curves of 2 and 20 bars clearly show a two-step mechanism. The first step ends at about 1.2 wt.% (1.1 H/M) and corresponds to the final capacity of the 1 bar curve.

The XRD patterns of the three samples after full hydrogenation are presented in Figure 3.14. The patterns of the 20 bars and 2 bars show a BCT structure. The pattern for the sample activated under 1 bar seems to be different than the other two samples. It looks more like a BCC phase than a BCT, so we tried to fit a BCC but the BCT gave a better fit. The unit cell parameters for each hydride BCT phase are presented in Table 3.6. It should be noted that the a parameter of the BCT phase decreases with the hydrogenation pressure while the c parameter increases. For the 1 bar hydrogenation the a and c parameters are quite close. This means that maybe a BCC phase could also fit this pattern. We therefore fitted the pattern using a BCC and compared it to the BCT fit. The R_{wp} of the BCC and BCT are respectively 6.469 and 6.632. The lattice parameter of the BCC phase is 3.463 Å, a value that is intermediate between the a and c parameters of the BCT phase. The unit cell volume of the BCC phase is 41.54 Å³, again very close to the BCT

value of 41.61 \AA^3 . Therefore, we think this structure is maybe at the transition, between a BCT and a BCC. In this discussion we will assume a BCT phase, but it should be mentioned that a BCC phase also fit this pattern.

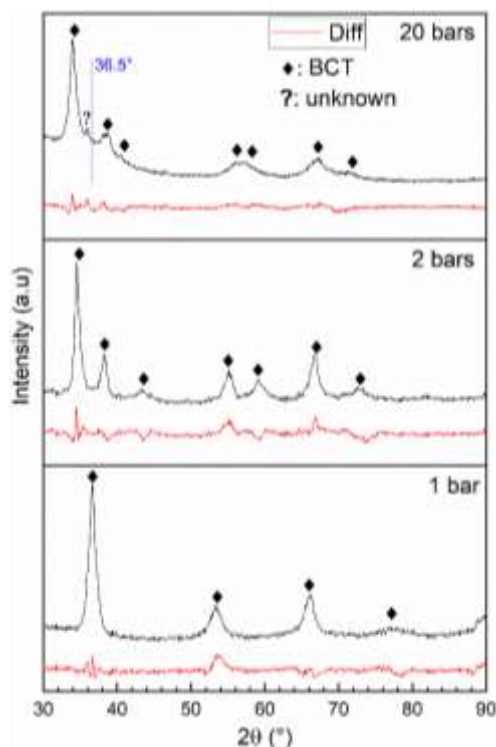


Figure 3.14 XRD patterns of size less than 0.5 mm hydrogenated at 300°C under 1, 2 and 20 bars of hydrogen.

Table 3.6 Crystal structure parameters of the BCT phase of the particles of size less than 0.5 mm hydrogenated at 300°C under 1, 2 and 20 bars of hydrogen. Error on the last significant digit is indicated in parentheses.

Pressure	Cell Volume (\AA^3)	Lattice parameter (\AA)	Crystallite size (nm)	Micro strain (%)	R_{wp}	Amorphous
1 bar	41.61 (8)	a = 3.442 (2) c = 3.512 (3)	8.3 (5)	0.38 (3)	4.23	-----
2 bars	47.01 (6)	a = 3.349 (2) c = 4.191 (3)	8.5 (5)	0.27 (2)	4.54	-----
20 bars	48.60 (7)	a = 3.301 (2) c = 4.460 (5)	5.9 (2)	0.41 (2)	3.95	23%

We see that, for the 1 bar pattern, the a and c lattice parameters are very close ($c/a=1.020$). The volume of the unit cell is 41.61 \AA^3 which gives a volume expansion of the lattice compared to the as-cast BCC of 3.47 \AA^3 . Taking into account that the volume taken by a hydrogen atom is between 2 and 3 \AA^3 , we could estimate the amount of hydrogen in the BCT hydride phase. The amount of hydrogen is between 0.6 wt.% and 0.9 wt.% which is smaller than the measured capacity in Figure 3.13. For the 2 bars sample, the volume expansion of the BCT phase is 8.87 \AA^3 that is transformed to a capacity between 1.6 wt.% to 2.4 wt.% (1.47 to 2.2 H/M) which agrees with the measured capacity (1.7 wt.% or 1.57 H/M) shown in Figure 3.13. A higher volume expansion is obtained under 20 bars. That translates to a capacity between 1.95 wt.% (1.8 H/M) to 2.9 wt.% (2.7 H/M). But as the pattern shows a degree of crystallinity of 77% then the capacity should be between 1.5 wt.% (1.38 H/M) and 2.2 wt.% (2.0 H/M) which is in the range of the measured value.

3.4.4 Study of Stability of the hydrided phase

The hydrogenated sample of particles of size less than 0.5 mm and activated under 20 bars of hydrogen pressure at 300°C were used to investigate the stability of the BCT hydride phase. After reaching full hydrogenation, the sample was subjected to vacuum for two hours at 300°C . XRD measurements (not shown) confirmed that no desorption occurred. To achieve desorption, the temperature had to be raised to 350°C and the sample kept under dynamic vacuum for two hours. In Figure 3.15, the XRD pattern of the dehydrogenated sample is shown and compared to the as-cast alloy.

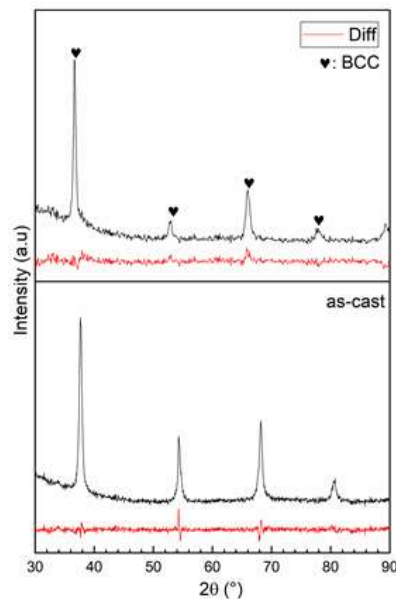


Figure 3.15 XRD patterns of particles of size less than 0.5 mm in the as-cast state and after dehydrogenation at 350°C under vacuum.

It is clear that the hydride BCT phase reverted to BCC upon dehydrogenation at 350 °C under vacuum. To check if there is still hydrogen in the retained BCC phase, the Rietveld refinement was done, and the results are reported in Table 3.7.

Table 3.7 Crystal structure parameters of particles of size less than 0.5 mm dehydrided at 350°C under vacuum as compared to the as-cast alloy. Error on the last significant digit is indicated in parentheses.

	Cell Volume (Å³)	Lattice parameter (Å)	Crystallite size (nm)	Microstrain (%)	R_{wp}
As-cast	38.14 (2)	3.3663 (4)	14.3 (3)	0.08 (1)	4.67
Desorption of activated at 300°C	41.82 (3)	3.4711 (7)	12 (1)	0.14 (2)	5.56

We see that the volume of the BCC phase is slightly larger after dehydrogenation as compared to the as-cast state. This may indicate a small amount of hydrogen is still in solid solution in the BCC phase. Again, assuming a volume of hydrogen atom between 2 and 3 Å³, the amount of hydrogen in solid solution is estimated to be between 0.63 and 0.96 hydrogen per metallic atom (H/M) which translate to a capacity between 0.7 wt.% and 1.0 wt.%. The fact that this alloy retains hydrogen even after heating under dynamic vacuum at 350°C could be explained by the very high stability of the binary hydrides of the raw elements. Amongst all these elements, vanadium has the highest plateau pressure in the range $0 < H/M < 1$ of about 10 kPa. The plateau pressure of the other pure elements ranges from 1 kPa down to a fraction of one Pascal [64]. Considering that the vacuum level in our Sieverts apparatus is of the order of a few kPa, it is reasonable to assume that the alloy is not totally dehydrided. Recently, a similar result was obtained, showing that hydrogen is trapped in a stable sites after desorption [65].

3.5 Conclusion

The effects of particle size, pressure, and temperature on the first hydrogenation of TiVZrHfNb high entropy alloy were investigated. It was found that particles smaller than 0.5 mm of diameter activate quickly but, for bigger particle size the dependence of activation time on particle size is not clear. Upon hydrogenation the BCC structure is transformed to BCT irrespective of particle size, temperature, and pressure. The temperature dependence of activation time and more particularly the incubation period is much clearer. It was found that the incubation period follows an Arrhenius relation, with $E_A = 241 \pm 8$ kJ/mol H₂. We observed that, upon hydrogenation, an amorphous

phase could be formed. This formation seems to depend on the hydrogenation temperature and particle size. Small particles get amorphized at lower temperature. However, more experimental evidences are needed to confirm this hypothesis. For example, TEM and high-resolution synchrotron may help to confirm the presence of an amorphous phase.

Chapter 4

Microstructure and hydrogen storage properties of TiHfZrNb_{1-x}V_{1+x} alloy for x=0, 0.1, 0.2, 0.4, 0.6 and 1.

4.1 Overview

This chapter describes our investigation of the effect of the substitution of Nb by V on the microstructure and hydrogen storage properties of TiHfZrNb_{1-x}V_{1+x} alloy (x= 0.1, 0.2, 0.4, 0.6 and 1). The reason for this substitution is that V is lighter than Nb but has similar chemistry. However, the atomic radius is quite different and the metallurgy not the same (different melting point). Therefore, the substitution of Nb by V is not straightforward.

Figure 4.1 represents the summary of this work.

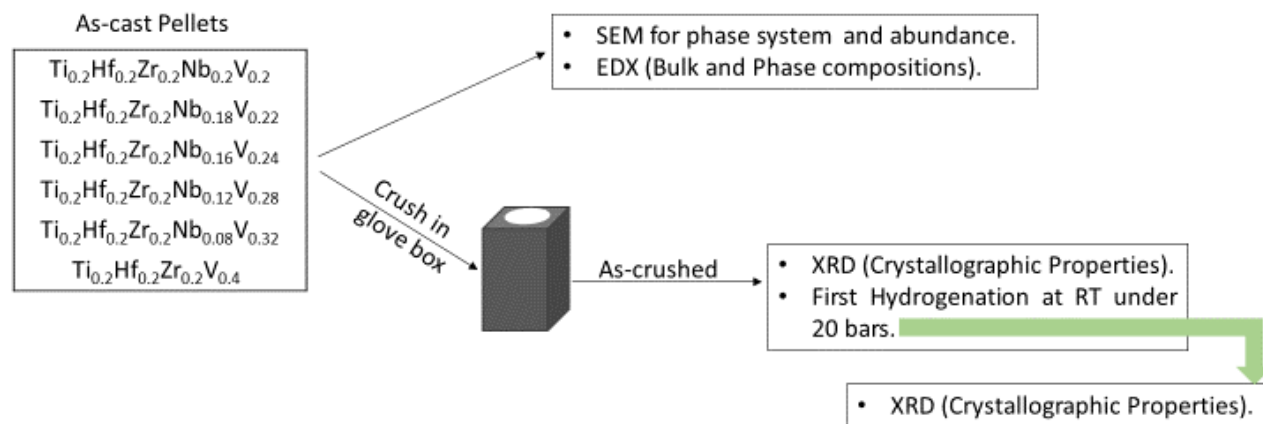


Figure 4.1 Flow chart of synthesis & characterization of TiHfZrNb_{1-x}V_{1+x} alloys for x= 0.1, 0.2, 0.4, 0.6 and 1.

4.2 Calculation of Parameters for Phase Formation Rules

The parameters ΔS_{mix} , ΔH_{mix} , Ω and δ were calculated using Equations 1.2, 1.11, 1.12 and 1.14 respectively. Their values are listed in Table 4.1. The value of VEC is 4.4 for all investigated alloys.

Table 4.1 The parameters ΔS_{mix} , ΔH_{mix} , Ω and δ for each alloy.

x value	ΔS_{mix} $\text{J.K}^{-1}\text{mol}^{-1}$	ΔH_{mix} kJ.mol^{-1}	Ω	δ %
Criteria for solid solution [66]	Maximum	-11 to 5	≥ 1.1	≤ 6.6
0	13.38	0.16	192	6.86
0.1	13.37	-0.13	235	6.99
0.2	13.31	-0.40	76	7.13
0.4	13.10	-0.97	30	7.39
0.6	12.74	-1.51	19	7.64
1	11.08	-2.56	9	8.08

We can see that ΔS_{mix} decreased with x, reaching the lowest value for the Nb-free (x= 1) alloy. ΔH_{mix} and Ω also decreased with x and their values satisfied the conditions for the formation of solid solution phases. In the case of δ , it increased with x and was the maximum for x= 1. VEC was 4.4 for all alloys and this value favours the formation of the BCC structure over the face-centred cubic (FCC) structure [44]. According to the Ω and VEC values, all the selected compositions fulfilled the conditions for the formation of the BCC phase. However, referring to δ values, the formation of intermetallic compounds is expected.

4.3 Microstructural Study

Figure 4.2 shows the backscattered electron micrograph of TiHfZrNb_{1-x}V_{1+x} alloys for x=0, 0.1, 0.2, 0.4, 0.6 and 1.

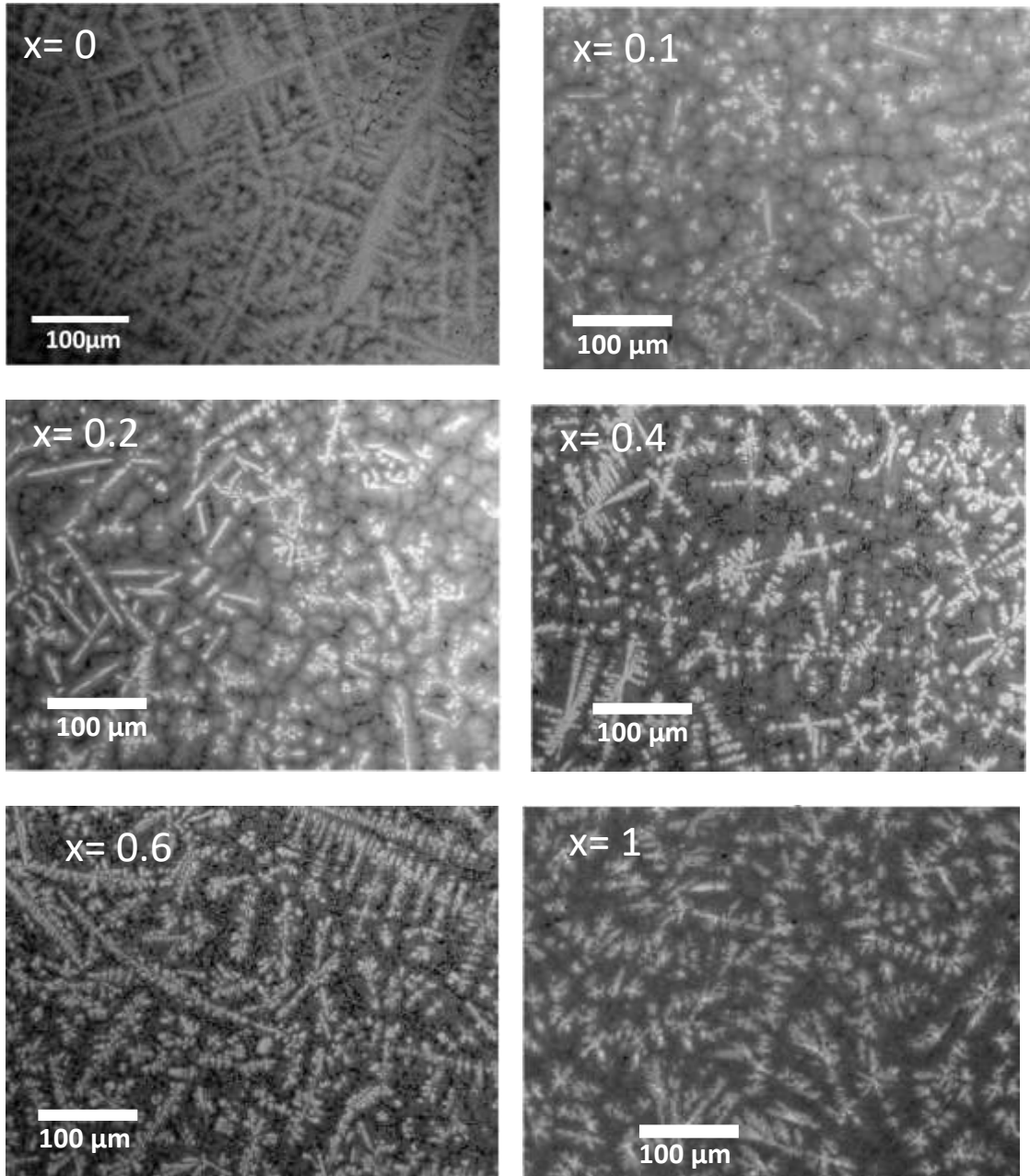


Figure 4.2 Backscattered electron (BSE) micrograph of $\text{TiHfZrNb}_{1-x}\text{V}_{1+x}$ alloys for $x=0, 0.1, 0.2, 0.4, 0.6$ and 1 .

The bulk chemical composition for each sample was confirmed by EDX measurements to be equal to the nominal values. From Figure 4.2, it is clear that all compositions had a dendritic structure, but the microstructure changed with x . The TiHfZrNbV alloy ($x=0$) was made of light grey dendrites surrounded by darker grey regions and a few darker (almost black) spots. A slight substitution of Nb by V ($x=0.1$) made the dendrites much brighter, but also smaller. All the substituted alloys were found to be multiphase, showing

a matrix, bright and dark phases. For total substitution ($x= 1$), the dark phase disappeared.

Using EDX at a higher magnification, the chemical compositions of the individual phases were measured on the selected points presented in Figure 4.3.

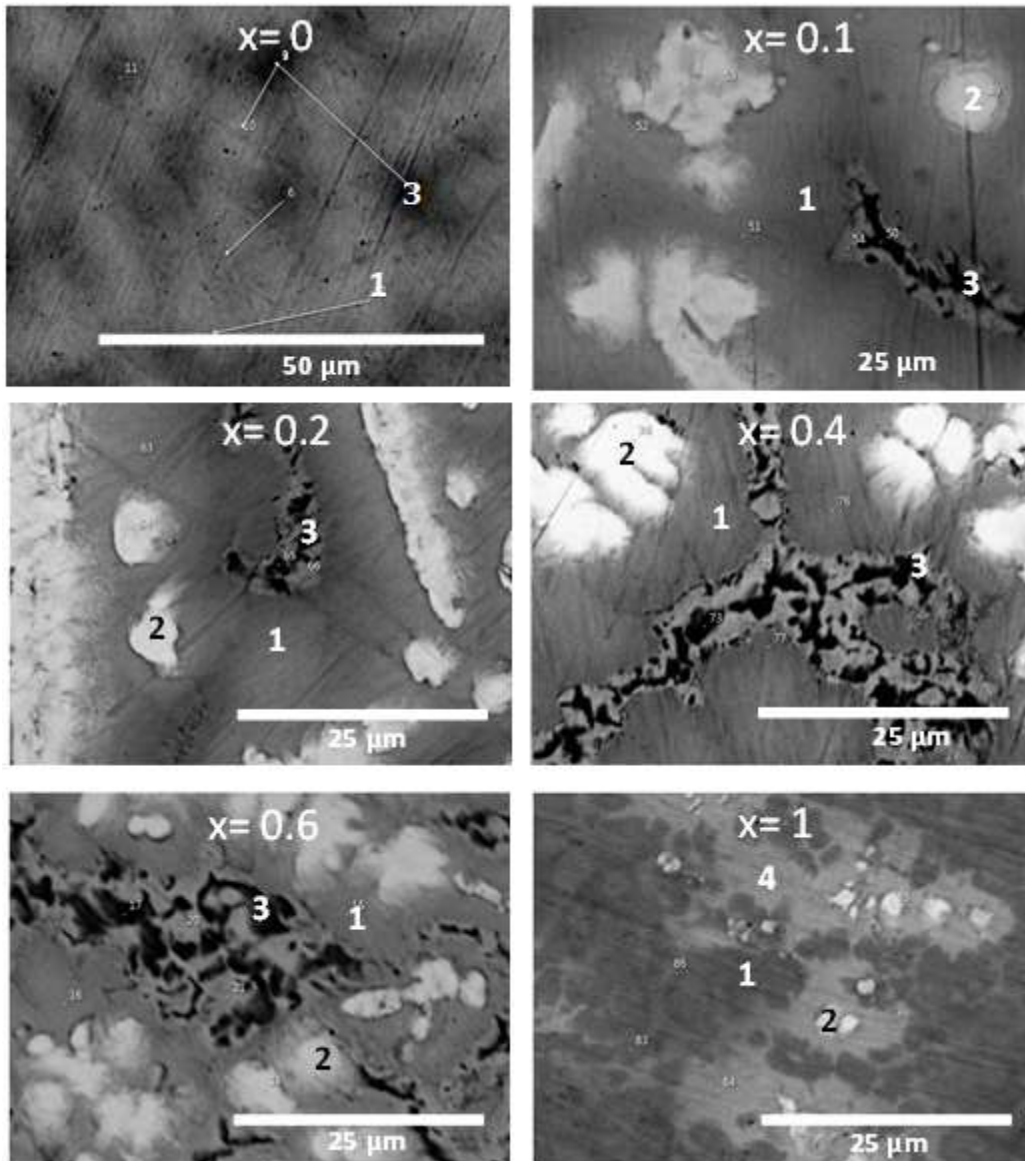


Figure 4.3 BSE micrographs of TiHfZrNb_{1-x}V_{1+x} alloys for x=0, 0.1, 0.2, 0.4, 0.6 and 1 with higher magnification.

In a previous investigation, it was shown that the equiatomic sample TiHfZrNbV is a single-phase BCC with a range of composition. This variation of composition is the origin of the change in grey shade seen in Figure 4.3 for $x= 0$ [67].

The other micrographs show that the alloys are made of a main phase, thereafter, called matrix and indicated by point number 1, a bright phase (point 2) and a dark phase (point 3). For $x= 1$, no black region was present, but there was a bright grey phase (point 4). The chemical compositions of points 1, 2 and 3 are listed in Tables 4.2, 4.3 and 4.4 respectively.

Table 4.2 EDX analysis showing the elemental composition of the matrix (point 1) of: $\text{TiHfZrNb}_{1-x}\text{V}_{1+x}$ alloys for $x= 0.1, 0.2, 0.4, 0.6$ and 1 . Error on all values is 1 at.%.

x	Ti (at.%)	Hf (at.%)	Zr (at.%)	Nb (at.%)	V (at.%)
0	20	19	19	22	20
0.1	21	18	18	20	23
0.2	21	18	18	21	22
0.4	20	17	19	14	30
0.6	23	18	20	9	30
1	12	18	16	0	54

From Table 4.2, it can be seen that for $x= 0$, the matrix had a composition very close to the nominal one. For $x= 0.1$, the composition was again very close to the nominal one. For $x= 0.2$, the composition was still very similar to the composition of $x= 0$ and 0.1 . For $x= 0.4$, we could see an important increase in vanadium content and a corresponding decrease in niobium. The other concentrations of the elements were still close to nominal. At $x= 0.6$, the matrix showed a strong depletion of niobium and an increase in titanium when compared to $x= 0.4$. Finally, for $x= 1$, the vanadium content was much higher than the nominal one and the titanium content was lower. From this, we can see that substitution of Nb by V does not result in a smooth variation of the matrix composition. Vanadium seems to be more abundant, while titanium was less abundant than what was expected from a linear variation of element's concentration with x .

The atomic compositions of the bright phase (point 2) are listed in Table 4.3. It is clear that the bright phase (point 2) was rich in Hf and Zr and depleted in Nb and V. From $x= 0.1$ to 0.6 , the composition was almost constant, but there was a slight decrease in Nb proportion and a slight increase in Zr proportion, keeping the Zr+Nb proportion constant. For $x= 1$, the proportion of vanadium was much higher than for the other compositions.

Table 4.3 EDX analysis showing the elemental composition of the bright phase (point 2) of: TiHfZrNb_{1-x}V_{1+x} alloys for x= 0.1, 0.2, 0.4, 0.6 and 1. Error on all values is 1 at %.

X	Ti (at. %)	Hf (at. %)	Zr (at. %)	Nb (at. %)	V (at. %)
0.1	15	42	36	5	2
0.2	15	40	38	5	2
0.4	14	43	37	4	2
0.6	14	41	41	2	2
1	13	38	36	0	13

The atomic compositions of the dark phase (point 3) are presented in Table 4.4. This phase was not present for x= 1. We could see that the dark phase was V-rich and its composition was nearly constant for all values of x.

Table 4.4 EDX analysis showing the elemental composition of the dark phase (point 3) of: TiHfZrNb_{1-x}V_{1+x} alloys for x= 0.1, 0.2, 0.4 and 0.6. Error on all values is 1 at %.

x	Ti (at. %)	Hf (at. %)	Zr (at. %)	Nb (at. %)	V (at. %)
0.1	14	6	7	12	61
0.2	14	7	10	12	57
0.4	14	7	8	9	62
0.6	17	8	8	8	59

For the bright grey phase (point 4, only for x= 1) of Figure 4.2, its atomic composition was 26Ti-24Hf-26Zr-24V, which was very close to the equiatomic composition.

4.4 Crystal Structure

Figure 4.4 presents the XRD patterns of all compositions in their as-cast state.

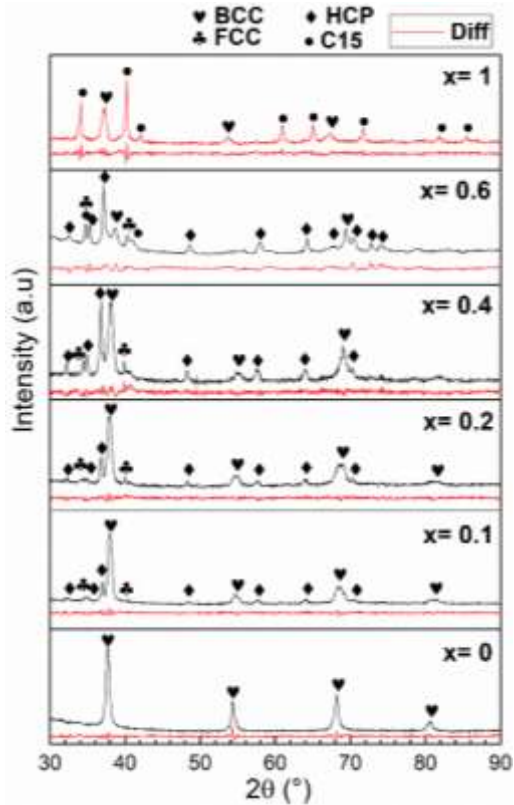


Figure 4.4 X-ray diffraction patterns of as-cast $\text{TiHfZrNb}_{1-x}\text{V}_{1+x}$ alloys for $x = 0, 0.1, 0.2, 0.4, 0.6$ and 1 . The bottom (red) line of each pattern is the residue of Rietveld refinement.

For $x = 0$, the crystal structure was pure BCC. Other phases appeared upon the substitution. The abundance of each phase as determined by Rietveld refinement is reported in Table 4.5. For $x = 0.1, 0.2$ and 0.6 , the main phase was the BCC phase along with a HCP phase and a minor amount of a FCC phase. As x increased from 0.1 to 0.6 , the abundance of the BCC phase decreased, the HCP phase increased, and the FCC phase had roughly the same abundance. At $x = 0.6$, a C15 Laves phase appeared. For complete substitution of Nb by V, C15 becomes the main phase along a BCC phase.

Table 4.5 Abundance in wt.% of each phase in $\text{TiHfZrNb}_{1-x}\text{V}_{1+x}$ alloys for $x = 0, 0.1, 0.2, 0.4, 0.6$ and 1 . The number in parentheses is the error on the last significant digit.

x	0	0.1	0.2	0.4	0.6	1
BCC	100	80 (1)	76 (2)	59 (2)	38 (3)	31 (1)
HCP	14 (1)	17 (1)	29 (2)	35 (3)
FCC	6 (1)	7 (1)	11 (1)	10 (1)
C15	16 (2)	69 (1)

The crystal structures seen in the diffraction patterns could be correlated to the chemical compositions of phases given by EDX. For $x= 0.1$ to 0.6 , we could associate the matrix (point 1) to the BCC crystal structure.

The bright phase (point 2) could be associated with the HCP crystal structure for $x= 0.1$ to 0.6 . From the chemical composition of the bright phase shown in Table 4.3, we could infer that the structure type of this HCP phase is $\text{Hf}_{0.5}\text{Zr}_{0.5}$. The phase diagram of Hf-Zr indicates that these two elements are totally miscible and have a HCP structure. The bright phase seen in the present samples was mainly made of hafnium (41% on average) and zirconium (38% on average). Therefore, the bright phase could be associated with a HCP phase of the chemical composition $0.14\text{Ti}-0.41\text{Hf}-0.38\text{Zr}-0.04\text{Nb}-0.02\text{V}$.

For the patterns $x= 0.1$ to 0.6 , a FCC phase was identified. From Figure 4.3, we can see that the dark phase is the only possibility of matching this phase. From Table 4.4, the average composition of the dark phase was $0.15\text{Ti}-0.07\text{Hf}-0.08\text{Zr}-0.1\text{Nb}-0.6\text{V}$.

For $x= 0.6$ and 1 , a C15 phase was identified in the diffraction pattern. In the case of $x= 0.6$, the only possibility was to assume that some of the dark regions in the micrographs are associated with this C15 phase and some others to a FCC phase. In fact, the $x= 0.6$ composition of the dark phase was $0.17\text{Ti}-0.08\text{Hf}-0.08\text{Zr}-0.08\text{Nb}-0.59\text{V}$. This is very close to the composition of the dark phase for $x= 0.1$ to 0.4 , but here, the atomic abundance of group 5 atoms (V and Nb) was exactly 0.67 , while the total abundance of group 4 atoms (Ti, Zr, and Hf) was 0.33 . The C15 phase had a structure AB_2 , where A is a hydride forming element and B is a non-hydride forming element. Thus, we can assign this phase to a C15 structure (space group Fd-3m) where Ti/Zr/Hf are assigned to the 8b site (A atoms) and the B atoms V/Nb are on the 16c site. It is known that Laves phases are related to BCC. For example, Hao et al. have shown by molecular dynamics that a perfect C15 cluster could be embedded in BCC iron [68].

For $x= 1$, the situation is more complex. The C15 phase is the most abundant phase in the diffraction pattern. Compared to Figure 4.3, it is most likely to be the matrix with a composition of $0.12\text{Ti}-0.18\text{Hf}-0.16\text{Zr}-0.54\text{V}$ that could be written as $\text{Ti}_{0.36}\text{Hf}_{0.54}\text{Zr}_{0.48}\text{V}_{1.62}$. This is relatively far from an AB_2 stoichiometry as most likely Ti, Zr, and Hf share the same site. The bright grey phase (point 4) seen in Figure 4.3 is associated with the BCC phase. The stoichiometry of that phase was $26\text{Ti}-0.24\text{Hf}-0.26\text{Zr}-0.24\text{V}$.

The crystal structure parameters of the BCC phase as determined by Rietveld refinement are tabulated in Table 4.6 with the average atomic radius of this phase. The chemical composition of the BCC phase was taken from the EDX measurements for each x . The BCC phase is the matrix for $x= 0.1$ to 0.6 and the bright grey phase for $x= 1$.

Table 4.6 Crystal structure parameters of the BCC phase in TiHfZrNb_{1-x}V_{1+x} alloys for x= 0, 0.1, 0.2, 0.4, 0.6 and 1. Error on the last significant digit is indicated in parentheses.

BCC	Cell Volume (Å ³)	Lattice parameter (Å)	Crystallite size (nm)	Micro strain (%)	Average radius (µm)	Ratio
0	37.99 (2)	3.362 (1)	9.9 (2)	1.01 (3)	147	2.29
0.1	37.92 (3)	3.360 (1)	30 (2)	0.31 (1)	146.1	2.30
0.2	37.51 (3)	3.347 (1)	25 (3)	0.35 (1)	146.2	2.29
0.4	37.01 (3)	3.333 (1)	10.5 (6)	0.23 (2)	145.5	2.29
0.6	36.79 (6)	3.326 (2)	4.1 (7)	145.9	2.28
1	39.81 (3)	3.415 (1)	25 (5)	0.38 (2)	148.5	2.30

The chemical composition of the BCC phase changes with x, but not in a linear fashion. However, from Table 4.6, we can see that the ratio of the average radius over the lattice parameter is practically constant.

The crystal structure parameters of the HCP phase are presented in Table 4.7. The lattice parameters of all samples were roughly constant with x. This is expected because, as shown in Table 4.3, the chemical composition for the HCP phase was almost the same for all samples.

Table 4.7 Crystal structure parameters of HCP phase in TiHfZrNb_{1-x}V_{1+x} alloys for x= 0.1, 0.2, 0.4 and 0.6. Error on the last significant digit is indicated in parentheses.

HCP	Cell Volume (Å ³)	Lattice parameter (Å)	Crystallite size (nm)	Microstrain (%)
0.1	45.57 (3)	a= 3.202 (1) c= 5.132 (2)	38 (9)	0.14 (2)
0.2	45.38 (3)	a= 3.199 (1) c= 5.121 (2)	41 (10)	0.13 (2)
0.4	45.46 (3)	a= 3.201 (1) c= 5.123 (2)	22 (2)	0.07 (2)
0.6	45.57 (3)	a= 3.203 (1) c= 5.129 (2)	21 (1)

The crystal structure parameters of the FCC phase are shown in Table 4.8. The lattice parameter of the FCC phase was almost the same for all compositions. This is consistent

with the fact that the chemical composition of this phase is constant, as shown in Table 4.4. For this phase, the microstrain was refined, but the results were always zero within the experimental error.

Table 4.8 The crystal structure parameters of the FCC phase in TiHfZrNb_{1-x}V_{1+x} alloys for x= 0.1 to 0.6. Error on the last significant digit is indicated in parentheses.

FCC	Cell Volume (Å ³)	Lattice parameter (Å)	Crystallite size (nm)
0.1	91.61 (1)	4.508 (3)	16 (3)
0.2	91.33 (1)	4.503 (2)	22 (5)
0.4	91.25 (1)	4.502 (2)	15 (2)
0.6	91.74 (6)	4.511 (1)	53 (17)

The crystal structure parameters of the C15 phase are shown in Table 4.9. The lattice parameter of C15 phase increased with x. However, the main differences were the crystallite size and microstrain. For x= 0.6, only the microstrain could be refined. All attempts to refine the crystallite size provided unrealistic numbers. This is similar to the one encountered for another AB₂ alloy [69]. It has been shown that when crystallite size is impossible to refine, the microstrain reflects a variation of chemical composition. This is also most likely the case here. Because the chemical composition varies within the dark phase, the crystal may adopt the FCC or the C15 structure. It should be pointed out that in the Rietveld refinement of the C15 phase for x= 1, the occupancy factor of vanadium was refined. The refined occupancy was 0.84, which translates to an abundance of 55 at.%. This value was very close to the measured value of 54 at.% in Table 4.2. This means that the C15 phase of x= 1 has an important number of vacancies on the B site.

Table 4.9 Crystal structure parameters of the C15 phase in TiHfZrNb_{1-x}V_{1+x} alloys for x= 0.6 and 1. Error on the last significant digit is indicated in parentheses.

C15	Cell Volume (Å ³)	Lattice parameter (Å)	Crystallite size (nm)	Microstrain (%)
0.6	397 (1)	7.350 (7)	0.63 (4)
1	412.0 (2)	7.441 (1)	21.1 (6)

4.5 First Hydrogenation

The first hydrogenation (activation) of $\text{TiHfZrNb}_{1-x}\text{V}_{1+x}$ alloys for $x=0, 0.1, 0.2, 0.4, 0.6$ and 1 was performed at room temperature under a hydrogen pressure of 20 bars without any prior heat treatment. Results are presented in Figure 4.5.

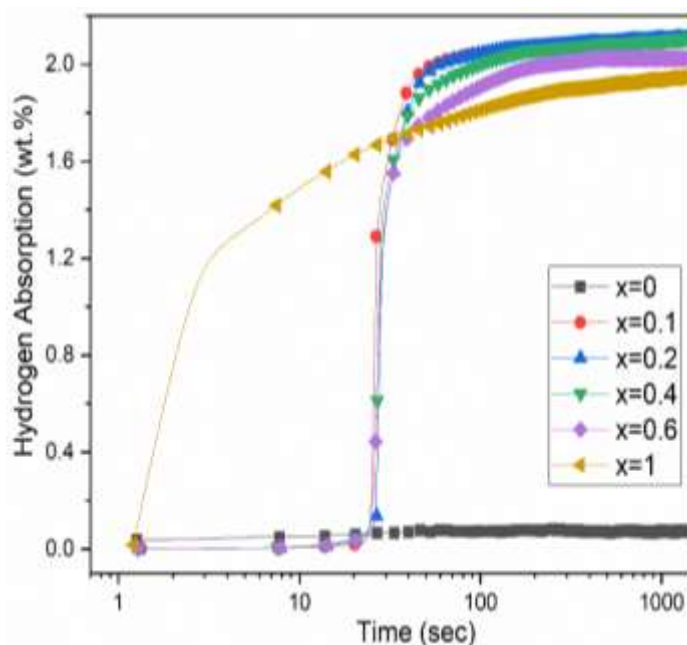


Figure 4.5 Activation curves of $\text{TiHfZrNb}_{1-x}\text{V}_{1+x}$ alloys for $x=0, 0.1, 0.2, 0.4, 0.6$ and 1 .

The first hydrogenation for $x=0$ is impossible at room temperature [34, 67]. Substituting niobium by vanadium provided a good hydrogen uptake with 25 s of incubation time and fast kinetics. Surprisingly, even if the heavy element Nb was replaced by the lighter element V, there was a slight downward trend for the capacity with increasing x . Additionally, the incubation time and kinetics were essentially the same for all substituted alloys. The TiHfZrV_2 alloy did not show any incubation time. The disappearance of the incubation time could be related to the predominant C15 phase.

The crystal structure of the hydrided alloys were investigated by XRD. The results are shown in Figure 4.6.

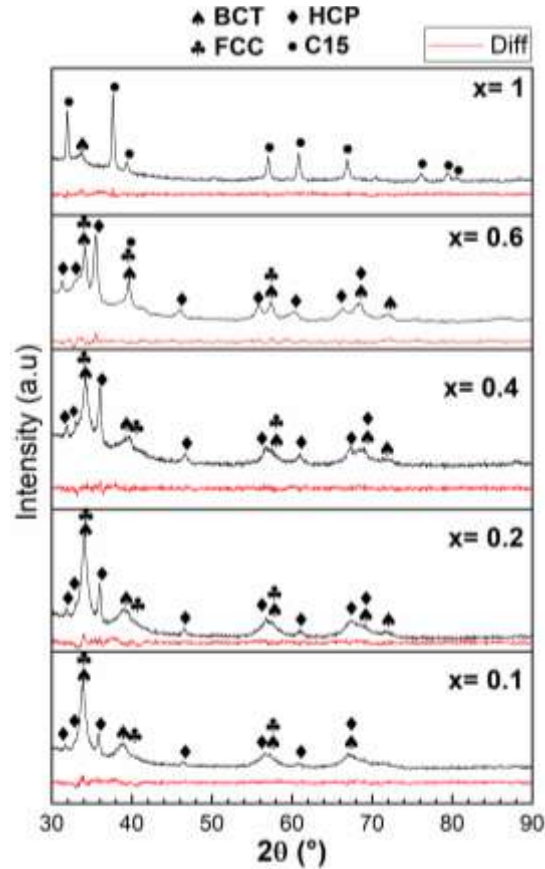


Figure 4.6 XRD patterns of $\text{TiHfZrNb}_{1-x}\text{V}_{1+x}$ alloys in the hydrogenated state for $x=0.1, 0.2, 0.4, 0.6$ and 1 . The bottom (red) line of each pattern is the residue of Rietveld refinement.

For $x=0.1, 0.2, 0.4$ and 0.6 , the crystal structure was essentially BCT with HCP and FCC as a secondary phase. It has been reported that BCT is the structure adopted by a fully hydrided BCC high entropy alloy [34, 67]. For the $x=1$ sample, the main phase was C15 and BCT was the minor phase. The crystal structure parameters and the abundance of each phase in all hydrogenated samples as determined by Rietveld's analysis are presented in Table 4.10.

Table 4.10 The crystal parameters of each phase in the hydrogenated TiHfZrNb_{1-x}V_{1+x} alloys for x= 0.1, 0.2, 0.4, 0.6 and 1. Error on the last significant digit is indicated in parentheses.

Sample	phase	Cell Volume (Å ³)	Lattice parameter (Å)	Crystallite size (nm)	Micro-strain (%)	Abundance (%)
0.1	BCT	47.90 (6)	a= 3.286 (2) c= 4.437 (3)	8.1 (5)	0.48 (2)	76 (1)
	HCP	49.88 (6)	a= 3.255 (1) c= 5.435 (2)	15 (1)	11 (1)
	FCC	95.8 (2)	4.574 (2)	0.33 (2)	13 (1)
0.2	BCT	47.35 (5)	a= 3.273 (2) c= 4.419 (3)	7.5 (6)	0.49 (2)	73 (2)
	HCP	49.43 (5)	a= 3.246 (1) c= 5.418 (2)	17 (1)	14 (1)
	FCC	94.4 (1)	4.554 (2)	0.35 (2)	13 (1)
0.4	BCT	46.86 (8)	a= 3.265 (2) c= 4.395 (5)	5.2 (4)	0.60 (4)	65 (2)
	HCP	49.55 (4)	a= 3.249 (1) c= 5.421 (2)	15 (1)	22 (1)
	FCC	93.9 (1)	4.545 (2)	0.36 (2)	13 (1)
0.6	BCT	47.47 (9)	a= 3.193 (2) c= 4.657 (7)	3.3 (2)	57 (2)
	HCP	51.33 (4)	a= 3.296 (1) c= 5.456 (2)	36 (6)	0.29 (1)	24 (2)
	FCC	93.66 (8)	4.541 (1)	43 (20)	0.15 (2)	15 (2)
	C15	434 (1)	7.574 (6)	0.31 (4)	4 (1)
1	BCT	49.0 (2)	a= 3.339 (5) c= 4.40 (1)	7 (2)	1.09 (7)	31 (2)
	C15	492.8 (1)	7.899 (1)	31 (2)	0.07 (1)	69 (2)

Basically, the same phases were present in the hydrided and as-cast patterns. From Table 4.11 and referring to Table 4.5, we can see that for x= 0.1 to 0.6 except for x= 0.4, the abundance of the FCC phase in the hydrogenated samples was higher than the abundance in the as-cast samples. For x= 0.4, the abundance of the FCC phase in the hydrogenated sample had relatively the same abundance as in the as-cast sample. From x= 0.1 to 0.2, the abundance of the HCP phase in the hydrogenated samples was close to the abundance in the as-cast samples. However, the HCP phase was less abundant in the hydrogenated samples for x= 0.4 and 0.6. The BCT phase abundance was relatively

the same abundance as the BCC phase for $x= 0.1$ and 0.2 . However, its abundance was higher than the BCC abundance for $x= 0.4$ and 0.6 . Regarding the C15 phase for $x= 0.6$, the amount of the hydrided C15 phase was much lower than that in the as-cast (4% vs. 16%).

In the case of $x= 1$, we can see that the hydrogenated alloy had a 31 wt.% BCT phase, which corresponds to the abundance of the BCC phase (31%) in the as-cast alloy. Therefore, BCC was completely transformed into BCT upon hydrogenation. For the C15 phase, similar to the as-cast state, the occupancy factor of the B site corresponded to a vanadium abundance of 57 at.%.

Concerning the HCP phase and referring to Table 4.7, we see that the crystallite size of this phase decreased upon hydrogenation for $x= 0.1$ to 0.4 , but it increased for $x= 0.6$. No microstrains were found in the hydrogenated samples of $x= 0.1$ to 0.4 , while a microstrain of 0.29% appeared for $x= 0.6$. For the C15 phase and using Table 4.9, the crystallite size in the hydrided C15 was greater than the one of the as-cast when $x= 1$.

As the unit cell volume of all phases in the hydrided state was larger than in the as-cast state, we could use the volume increase to estimate the hydrogen capacity. Considering that a hydrogen atom produces a volume expansion between 2 and 3 Å³, the estimated amount of hydrogen in each phase was determined from the volume expansion ΔV of each hydrided phase. The results are shown in Table 4.11.

Table 4.11 The variation of volume ΔV and the estimated range of hydrogen in each phase in the hydrogenated $\text{TiHfZrNb}_{1-x}\text{V}_{1+x}$ alloys for $x= 0.1, 0.2, 0.4, 0.6$ and 1 .

	ΔV of BCT (Å ³)	Estimated amount of H in BCT (wt.%)	ΔV of HCP (Å ³)	Estimated amount of H in HCP (wt.%)	ΔV of FCC (Å ³)	Estimated amount of H in FCC (wt.%)	ΔV of C15 (Å ³)	Estimated amount of H in C15 (wt.%)
0.1	9.98	1.87 to 2.8	4.31	0.6 to 0.89	4.19	0.53 to 0.79
0.2	9.84	1.83 to 2.75	4.05	0.57 to 0.85	3.07	0.37 to 0.56
0.4	9.85	1.91 to 2.88	4.09	0.56 to 0.84	2.65	0.33 to 0.5
0.6	10.68	2.09 to 3.14	5.76	0.8 to 1.2	1.92	0.24 to 0.36	37	0.76 to 1.14
1	9.19	1.68 to 2.52	80.8	1.7 to 2.55

Taking into consideration the abundance of each phase in the hydrided samples, the estimated amount of hydrogen is shown in Table 4.12.

Table 4.12 Estimated capacity of the phases in the hydrided samples.

	0.1	0.2	0.4	0.6	1
Estimated amount of H in the hydride (wt.%)	1.56 to 2.33	1.46 to 2.2	1.4 to 2.12	1.45 to 2.18	1.69 to 2.54
Measured capacity (wt.%)	2.1	2.1	2.1	2	1.95

This table clearly shows that the measured capacities of all samples were in the middle of the estimated range. We could estimate that, on average, a hydrogen atom takes a volume of 2.7 \AA^3 . This is very close to the volume expansion estimated at 2.9 \AA^3 that Peisl found for a wide range of materials [70]. Using 2.7 \AA^3 for the hydrogen volume in the crystal structure, we estimated the H/M ratio for each phase. We found that the BCT phase had a ratio close to 2, and the HCP phase had a ratio between 0.75 and 1. Surprisingly, the FCC H/M ratio for $x = 0.1, 0.2, 0.4$ and 0.6 was 0.39, 0.28, 0.24 and 0.18, respectively. We also observed that the FCC phase took up less and less hydrogen as x value increased. Regarding the C15 phase, for $x = 0.6$, the H/M is 0.57 while for $x = 1$, the H/M was 1.25.

For $x = 0.1$ to 0.6 , most of the capacity came from the BCT phase. This is because the estimated amount of hydrogen in the hydride BCT was higher than that of the hydride HCP and FCC phases and also BCT was the most abundant over the hydrided phases. For $x = 1$, the estimated amount of hydrogen in the hydride C15 phase was higher than that of BCT. Additionally, C15 had the highest abundance (69%) compared to BCT (31%). Therefore, most of the measured capacity came from the C15 phase. Referring to the activation curves of Figure 4.4, one can correlate the absence of the incubation time to the presence of the C15 phase as the main phase.

The TiHfZrV_2 alloy was selected to study its dehydrided state. The choice of this composition is because it is the total substituted sample, and its synthesis is relatively easy compared to the other samples. However, studying the stability of the other hydrided compositions is planned for a future paper. After reaching full hydrogenation, the sample was subjected to vacuum for two hours at $350 \text{ }^\circ\text{C}$. XRD measurements (not shown) confirmed that no desorption occurred. Thus, the temperature was raised to $400 \text{ }^\circ\text{C}$ and the sample kept under dynamic vacuum for two hours. The XRD pattern of the dehydrogenated sample is presented in Figure 4.7. The very high background is due to a special sample holder that kept the powder under an argon atmosphere.

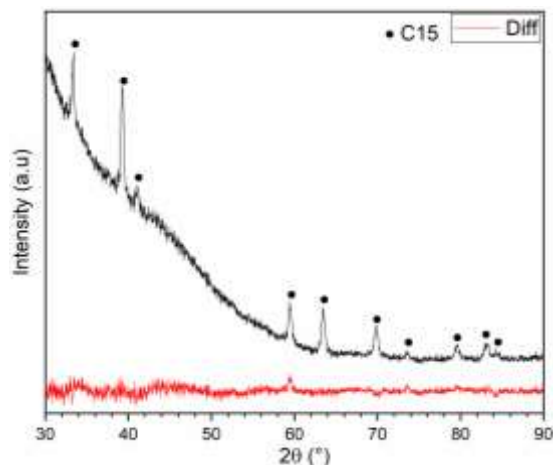


Figure 4.7 XRD pattern of TiHfZrV₂ alloy (x= 1) dehydrided at 400 °C under vacuum.

We could see that only C15 phase was present in the desorbed patterns; no BCC phase or BCT phases were seen. The reason is that BCC/BCT phases were most probably 'buried' under the high background. The volume of the C15 phase as determined by Rietveld refinement is 443.8 Å³. The volume of the C15 phase after dehydrogenation was larger than that of the C15 phase in the as-cast state (412.1 Å³). This indicates that there is still hydrogen in the C15 phase. Assuming a volume of hydrogen atom of 2.7 Å³, the hydrogen still present is 0.73 wt.% (0.49 H/M). This means that the sample is not fully desorbed even at 400°C under vacuum. This could be explained by the high stability of the binary hydrides of the raw elements where vanadium has the highest plateau pressure in the range 0 < H/M < 1 of about 10 kPa. A temperature higher than 400°C is needed for full desorption, but this is over the limit of our apparatus.

4.6 Conclusions

The effect of the substitution of Nb by V on the microstructure and hydrogen storage properties of TiHfZrNb_{1-x}V_{1+x} alloy for x= 0, 0.1, 0.2, 0.4, 0.6 and 1 was investigated. For x= 0, the alloy was pure BCC. All alloys with substitutions were multiphase. Upon substitution of niobium by vanadium, the BCC was progressively replaced with HCP and FCC phases. For high values of x, a C15 phase was present and became the main phase for x= 1. We found that the substitution of Nb by V greatly enhanced the first hydrogenation and made it possible at room temperature under 20 bars of hydrogen. The BCC phase transformed to BCT in the fully hydride state. For hydrogen storage purposes, the optimum amount of substitution seems to be the total substitution where there is no Nb in the alloy.

Chapter 5

Microstructure and Hydrogen Storage Properties of the multi-phase alloy $\text{Ti}_{0.3}\text{V}_{0.3}\text{Mn}_{0.2}\text{Fe}_{0.1}\text{Ni}_{0.1}$

5.1 Overview

This chapter describes our investigation of the crystal structure and hydrogen storage properties of a new multi-component alloy of composition $\text{Ti}_{0.3}\text{V}_{0.3}\text{Mn}_{0.2}\text{Fe}_{0.1}\text{Ni}_{0.1}$. The transition elements of period 4, Ti, V, Mn, Fe and Ni were selected. They are not all strong hydride forming elements but, not using the heavier elements of periods 5 or 6 means that potentially the gravimetric hydrogen storage capacity may be higher.

The composition was selected by taking into account the thermodynamic, geometric and electronic parameters. The thermodynamic parameter is related to the dimensionless parameter Ω , the geometric parameter is characterized by the atomic size difference δ and the electronic parameter is the valence electron concentration (VEC) of the constituent elements.

Ω was determined using Equation (1.12) and it is equal to 1.84 where ΔH_{mix} is equal to $-12.84 \text{ kJ}\cdot\text{mol}^{-1}$ (using Eq. 1.11), ΔS_{mix} is $12.51 \text{ J}\cdot\text{K}^{-1}\cdot\text{mol}^{-1}$ (using Eq. 1.2) and T_m is 1894.9 K (using Eq. 1.13). The δ value was calculated to be 5.4 % from Equation (1.14) using the atomic radii taken from reference [71]. Empirically, when $\Omega \geq 1.1$ and $\delta \leq 6.6\%$, the formation of solid solution phases are suggested [43, 72]. VEC predicts the phase selection between FCC and BCC type solid solutions [44]. It was calculated using Equation (1.16). The VECs, taken from reference [73], are 4, 5, 7, 8 and 10 respectively for Ti, V, Mn, Fe and Ni. VEC value of this alloy is 5.9. A value of VEC smaller than 6.87 means that BCC phase formation is favoured over FCC [44].

Based on the criteria Ω , δ and VEC, the BCC phase is most likely to occur in $\text{Ti}_{0.3}\text{V}_{0.3}\text{Mn}_{0.2}\text{Fe}_{0.1}\text{Ni}_{0.1}$ alloy. BCC structure is more desirable for hydrogen storage than FCC structure because it has more interstitial sites. Moreover, diffusivity of hydrogen is higher in BCC structure [74].

Figure 5.1 represents the flow chart of synthesis & characterization of $\text{Ti}_{0.3}\text{V}_{0.3}\text{Mn}_{0.2}\text{Fe}_{0.1}\text{Ni}_{0.1}$ alloy.

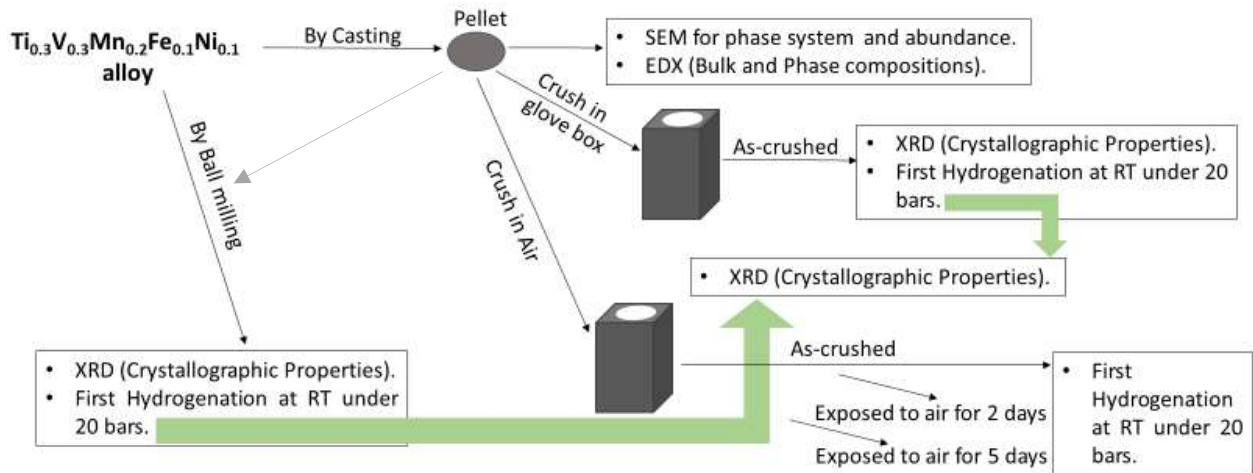


Figure 5.1 Flow chart of synthesis & characterization of $\text{Ti}_{0.3}\text{V}_{0.3}\text{Mn}_{0.2}\text{Fe}_{0.1}\text{Ni}_{0.1}$ alloy.

5.2 Microstructural Study

Figure 5.2 shows the backscattered electron micrograph of as-cast $\text{Ti}_{0.3}\text{V}_{0.3}\text{Mn}_{0.2}\text{Fe}_{0.1}\text{Ni}_{0.1}$ alloy.

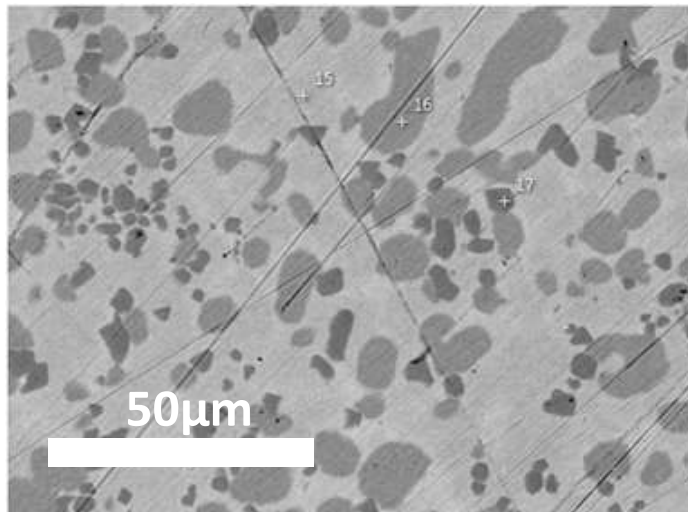


Figure 5.2 Backscattered electron (BSE) micrograph of as-cast $\text{Ti}_{0.3}\text{V}_{0.3}\text{Mn}_{0.2}\text{Fe}_{0.1}\text{Ni}_{0.1}$ alloy.

The different shades of grey indicate a multiphase alloy. Using ImageJ, the area percentages for the bright, grey, and dark grey phases were found to be, respectively

66%, 25%, and 9%. Being the dominant phase, the bright phase is thereafter called "matrix".

The chemical composition of the alloy was determined by EDX measurement. Table 5.1 shows the bulk measured atomic abundance compared to the nominal composition. We see that the bulk measured composition agrees with the nominal one.

Table 5.1 Bulk atomic abundance: nominal and as measured by EDX of as-cast $\text{Ti}_{0.3}\text{V}_{0.3}\text{Mn}_{0.2}\text{Fe}_{0.1}\text{Ni}_{0.1}$ alloy. Error on the last significant digit is indicated in parentheses.

Element (at %)	Ti	V	Mn	Fe	Ni
Nominal	30	30	20	10	10
Measured	29.4 (3)	30.8 (1)	19.1 (2)	10.4 (1)	10.3 (2)

Using EDX, we also measured the chemical composition of each phase. The EDX point analysis was performed at a higher magnification on the regions presented in Figure 5.3.

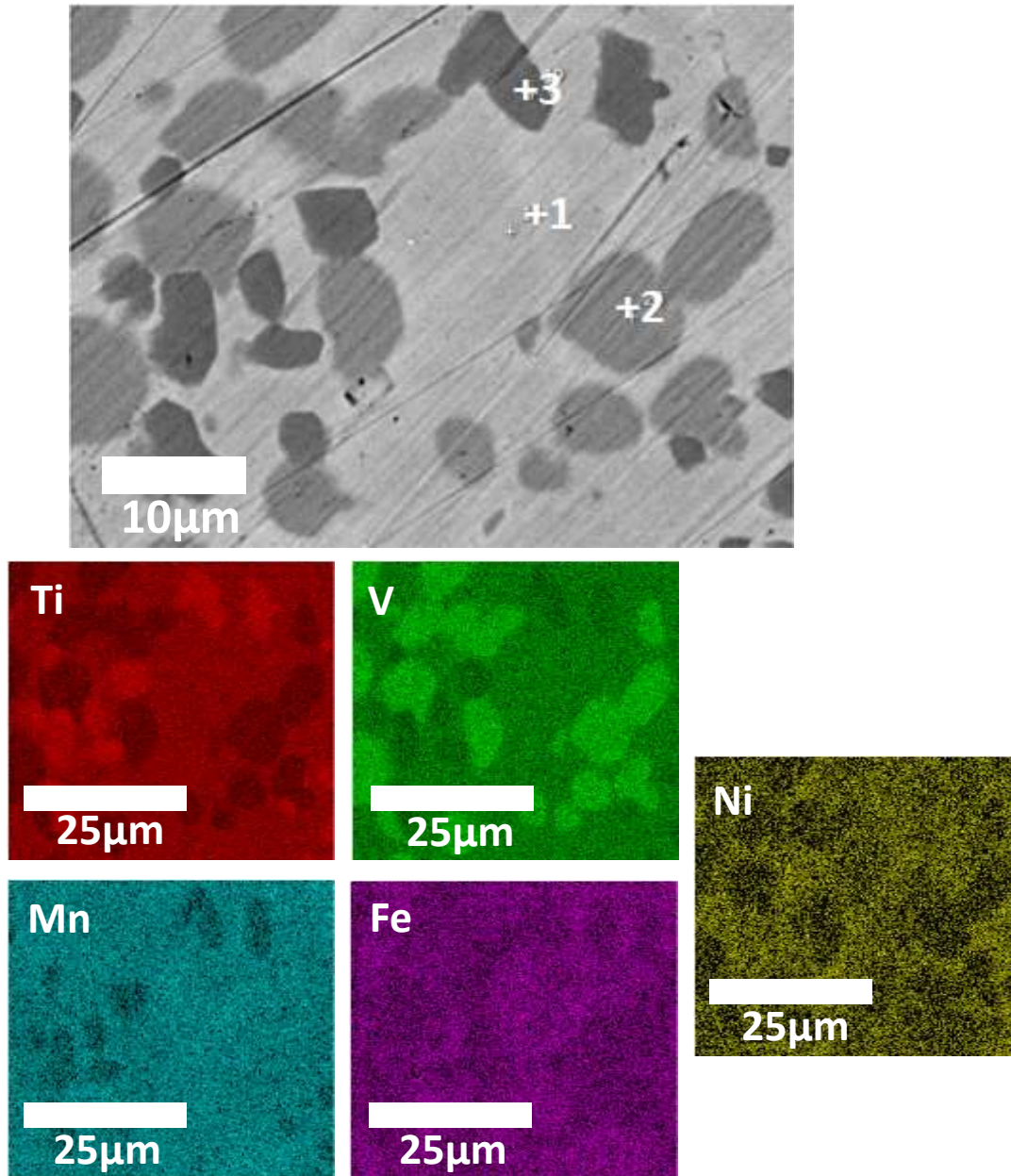


Figure 5.3 BSE micrographs with elemental mappings of as-cast $\text{Ti}_{0.3}\text{V}_{0.3}\text{Mn}_{0.2}\text{Fe}_{0.1}\text{Ni}_{0.1}$ alloy.

In the micrograph, the matrix, grey and dark grey phases are indicated by points number 1, 2 and 3 respectively. Their chemical composition is listed in Table 5.2.

Table 5.2 EDX analysis showing the elemental composition of all the phases of as-cast $Ti_{0.3}V_{0.3}Mn_{0.2}Fe_{0.1}Ni_{0.1}$ alloy. Error on all values is 1 at %.

Element (at %)	Ti	V	Mn	Fe	Ni
Matrix (Point 1)	32	23	19	11	15
Grey phase (Point 2)	16	51	21	9	3
Dark grey (Point 3)	51	13	11	11	14

The matrix is relatively close to the nominal composition, only slightly depleted in vanadium and rich in nickel. The major constituent of the grey phase is vanadium while titanium is the main element in the dark grey phase. Nickel and iron are mainly in the matrix and dark grey phase. Iron is uniformly distributed over all phases.

5.3 Crystal Structure

Figure 5.4 presents the XRD patterns of $Ti_{0.3}V_{0.3}Mn_{0.2}Fe_{0.1}Ni_{0.1}$ alloy in as-cast state. The following phases were found to give the best Rietveld refinement fit for this pattern: C14 Laves phase (space group $P6_3/mmc$, structure type $MgZn_2$), BCC phase (Space group $Im-3m$, structure type W) and Ti_2Fe type phase (space group $Fd-3m:2$, structure type Ti_2Ni). The lattice parameters and the abundance of these phases are presented in Table 5.3.

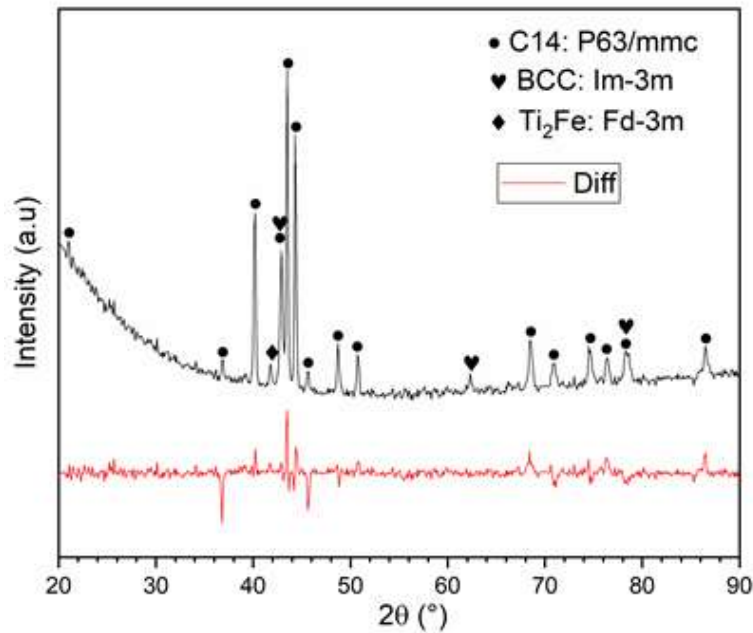


Figure 5.4 X-ray diffraction patterns of as-cast $Ti_{0.3}V_{0.3}Mn_{0.2}Fe_{0.1}Ni_{0.1}$ alloy. The bottom curve is the difference between calculated and measured intensities.

Table 5.3 Crystal parameters and abundance of each phase of as-cast $\text{Ti}_{0.3}\text{V}_{0.3}\text{Mn}_{0.2}\text{Fe}_{0.1}\text{Ni}_{0.1}$ alloy. Error on the last significant digit is indicated in parentheses.

Phase	Unit cell volume \AA^3	Lattice parameter \AA	Crystallite size nm	Micro-strain %	Abundance %
C14	164.98 (3)	a= 4.8900 (4) c= 7.9651 (9)	125 (48)	0.04 (1)	79
BCC	26.58 (1)	2.9841 (5)	31 (5)	-----	17
Ti_2Fe	1418 (3)	11.234 (8)	-----	-----	4

Correlating the abundance of the phases as measured by ImageJ software with the percentage of phases as determined by Rietveld's analysis, we see that the C14 phase may be associated with the matrix. From Table 5.2, the matrix composition could be written $\text{Ti}_{0.96}\text{V}_{0.69}\text{Mn}_{0.57}\text{Fe}_{0.33}\text{Ni}_{0.45}$. For the relatively close composition $\text{Ti}_1\text{V}_{0.64}\text{Mn}_{0.81}\text{Fe}_{0.15}\text{Ni}_{0.4}$, Song et al. found that the crystal structure was C14 [75]. Therefore, it is reasonable to associate the C14 crystal structure with the matrix phase. In their analysis, Song et al. assigned Ti to the $4f$ site and the other atoms were evenly distributed on the other two sites ($2a$ and $6h$) [75]. From the chemical composition of the matrix presented in Table 5.2, we see that the same assignation could be done here.

The abundance of the BCC phase roughly matches the abundance of the grey phase. Again, using Table 5.2 we could assume that the BCC phase has a composition $\text{Ti}_{0.16}\text{V}_{0.51}\text{Mn}_{0.21}\text{Fe}_{0.09}\text{Ni}_{0.03}$. This is supported by the fact that there is a wide range of $\text{Ti}_{1-x}\text{V}_x\text{Mn}_y$ that has the BCC structure [76-84]. The least abundant phase (dark grey) has a composition that could be written as $\text{Ti}_{1.53}\text{V}_{0.39}\text{Mn}_{0.33}\text{Fe}_{0.33}\text{Ni}_{0.42}$. The diffraction pattern indicates the presence of a Ti_2Fe -like phase which roughly matches the abundance of the dark grey phase. As Ti_2Ni is the structure type of Ti_2Fe , it is reasonable to assume that the dark grey phase has the Ti_2Fe structure with vanadium most likely substituted for Ti and Mn substituting for Ni/Fe.

According to the criteria used Ω , δ and VEC, the as-cast $\text{Ti}_{0.3}\text{V}_{0.3}\text{Mn}_{0.2}\text{Fe}_{0.1}\text{Ni}_{0.1}$ alloy should adopt a BCC phase. However, the main phase found is the C14 phase instead of BCC. One can see that Ω is 1.84 higher than the condition proposed by Yang and Zhang [43]. However, the absolute of ΔH_{mix} ($12.84 \text{ kJ}\cdot\text{mol}^{-1}$) is not small enough for the entropy effect to be the dominant term. This means that the formation of ordered intermetallic compounds with solid solution are expected to form [72].

5.4 First Hydrogenation Properties

Figure 5.5 shows the first hydrogenation (activation) curve of the as-cast alloy. The activation was performed at room temperature under hydrogen pressure of 20 bars without any prior treatment.

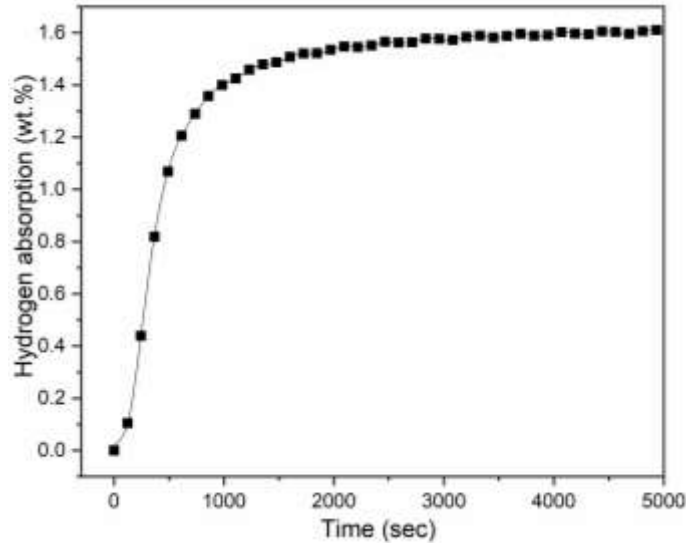


Figure 5.5 Activation curve of as-cast $\text{Ti}_{0.3}\text{V}_{0.3}\text{Mn}_{0.2}\text{Fe}_{0.1}\text{Ni}_{0.1}$ alloy.

The alloy absorbs hydrogen, reaching a maximum capacity of 1.6 wt.% within one hour. Even if the alloy is multiphase, the activation curve seems to behave as a single-phase absorption.

In an attempt to find the crystal structure of the hydride alloy, the experiment was stopped after reaching full hydrogenation and the powder immediately prepared for X-ray diffraction. The result is presented in Figure 5.6. The crystal parameters and abundance of each phase as determined by Rietveld's refinement are shown in Table 5.4.

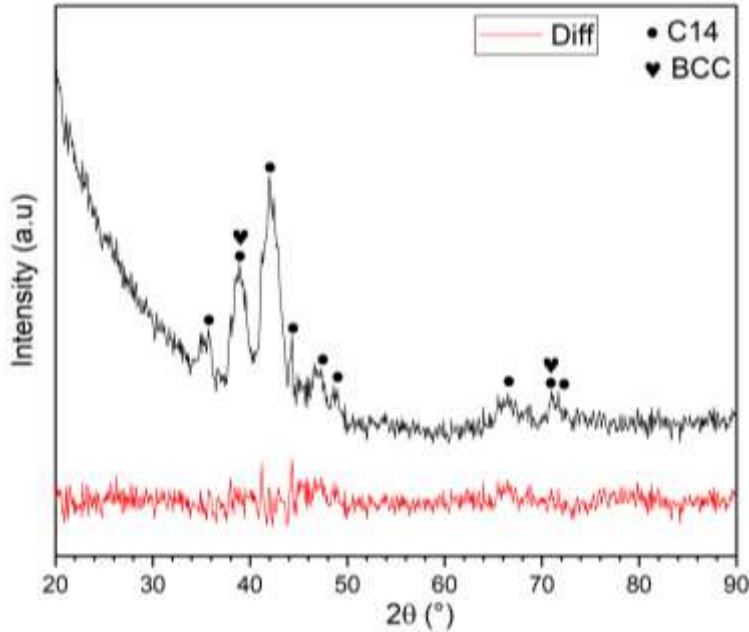


Figure 5.6 XRD patterns of the hydride sample.

Table 5.4 Crystal structure parameters and abundance of each phase in the hydride sample. Error on the last significant digit is indicated in parentheses.

Phase	Unit cell volume \AA^3	Lattice parameter \AA	Crystallite size nm	Micro-strain %	Abundance %
C14	187.85 (9)	a= 5.1091 (1) c= 8.2835 (2)	11 (3)	0.62 (3)	92
BCC	34.5 (2)	3.257 (6)	7 (2)	-----	8

Compared to the as-cast sample, the abundance of C14 increased from 79% to 92%, while the abundance of BCC phase decreased from 17% to 8%. There was no evidence of Ti_2Fe like phase in the hydride pattern. From the lattice expansion of each phase and assuming that the volume taken by a hydrogen atom is 2.9\AA^3 [70], the amount of hydrogen in each hydride phase could be estimated. Table 5.5 presents the volume expansion of the hydride phases with the estimated value of hydrogen per metallic atom (H/M) and corresponding wt.%. We see that, for the C14 phase, the H/M ratio is 2.0, which corresponds to the dihydride. In the case of the BCC phase, the H/M is 1.4. It is known that upon hydrogenation a BCC phase adopts a BCT (body centred tetragonal) structure for the monohydride and an FCC (face centered cubic) dihydride. It is therefore strange that, in the present case, the BCC phase absorbed up to H/M=1.4 but still

maintained the BCC structure. However, it has been shown that for the HEA TiVZrHfNb [31, 34] and TiVZrNbHf-based HEAs the BCT structure could have a H/M of 2. In the present case, the crystal structure is indexed to a BCC, but the broadness of the peaks and the overlap with C14 peaks makes it difficult to clearly distinguish between a BCC and BCT structure.

Table 5.5 Estimated capacity of the phases in the hydride sample.

Phase	Volume Expansion (\AA^3)	H/M	Estimated capacity of the phase (wt.%)
C14	22.9	2.0	1.2
BCC	7.9	1.4	2.6

From Table 5.5 and taking into consideration the abundance of each phase, the estimated amount of hydrogen in the hydride sample is about 1.3 wt.%. This is relatively far from the measured capacity of 1.6 wt.%. However, as the pattern was taken at room temperature and in air, there is a possibility that some desorption occurred. Therefore, we can not be absolutely certain that the pattern shown in Figure 5.6 is for a fully hydrided sample. However, this is an indication that the hydride phase is probably very stable at room temperature.

5.5 Air Exposure Effect

It is easier to handle the alloy in the air rather than in argon atmosphere. This stimulated us to study the air exposure effect on the as-cast $\text{Ti}_{0.3}\text{V}_{0.3}\text{Mn}_{0.2}\text{Fe}_{0.1}\text{Ni}_{0.1}$ alloy. Figure 5.7 shows the activation curves of the crushed alloy crushed under argon and in air. After crushing in air, the sample was also further exposed to the air for two and five days.

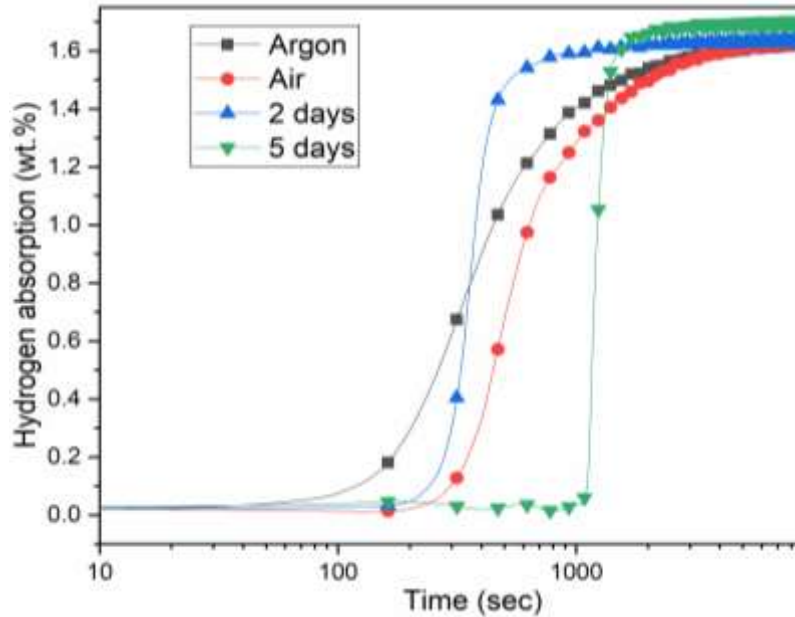


Figure 5.7 Activation curves at room temperature under 20 bars of hydrogen of as-cast $\text{Ti}_{0.3}\text{V}_{0.3}\text{Mn}_{0.2}\text{Fe}_{0.1}\text{Ni}_{0.1}$ alloy crushed in argon and air. The sample crushed in air was further exposed for two and five days.

The sample crushed in argon has 40 s incubation time while the one crushed in air needed 200 s before absorbing hydrogen. However, the intrinsic kinetic (tangent at mid capacity) was the same for the samples crushed in air or argon. Surprisingly, two days of air exposure did not change the incubation time but the intrinsic kinetic was about four times faster than the sample simply crushed in air. The sample exposed for five days has the longest incubation time of 1080 s. The intrinsic kinetic was slower than the two-day air exposed but still about three times faster than the air crushed sample. This long incubation time is probably related to the thick oxide layer caused by the long exposure to air. We have seen from the TiFe alloy that the presence of some level of oxide could speed up the intrinsic kinetics of hydrogenation [85]. The faster intrinsic kinetic of the air exposed samples may be due to the catalytic effect of TiO_2 layer on the surface. However, this has to be confirmed in a dedicated investigation. It should be noted that air exposure did not reduce the hydrogen capacity.

5.6 Synthesis by Mechanical Alloying

The $\text{Ti}_{0.3}\text{V}_{0.3}\text{Mn}_{0.2}\text{Fe}_{0.1}\text{Ni}_{0.1}$ alloy was also synthesized by mechanical alloying. To synthesize the alloy, the raw materials Ti, V, Mn, Fe and Ni were mixed in the desired proportion and milled for 1, 5 and 10 h. Figure 5.8 presents the evolution of XRD patterns of the milled powder.

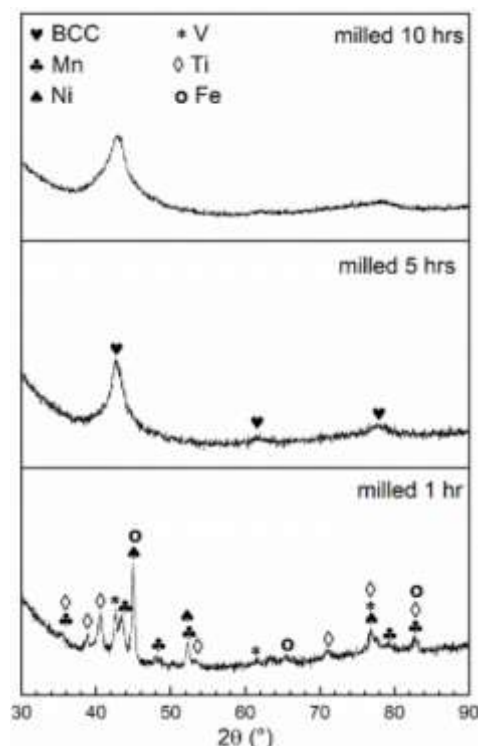


Figure 5.8 XRD patterns of Ti-V-Mn-Fe-Ni powders milled for 1, 5 and 10 h.

After one hour of milling, the Bragg peaks from all raw elements are still present. The five-hour milled pattern shows the formation of a BCC phase. Milling for 10 hours leads to further broadening of the BCC peaks. The diffraction patterns were analyzed by Rietveld's refinement and the obtained crystal parameters of the BCC phase are shown in Table 5.6.

Table 5.6 Crystal parameters of the BCC phase of the samples milled for 5 and 10 h. Error on the last significant digit is indicated in parentheses.

Milling time (hr)	Unit cell volume (\AA^3)	Lattice parameter (\AA)	Crystallite size (nm)
5	28.0 (2)	3.035 (6)	2.30 (5)
10	27.7 (4)	3.03 (1)	1.40 (2)

We see that, after the formation of a BCC phase, further milling essentially reduces the crystallite size. Actually, such a small crystallite size means that the structure is very close to be amorphous. For this reason, the first hydrogenation tests were done on the sample milled for five hours as this sample is most likely to have a true BCC structure.

5.7 Effect of Milling on As-cast Alloy

We investigated the effect of ball milling for 1, 5 and 10 h on as-cast $\text{Ti}_{0.3}\text{V}_{0.3}\text{Mn}_{0.2}\text{Fe}_{0.1}\text{Ni}_{0.1}$ alloy. The X-ray patterns are shown in Figure 5.9.

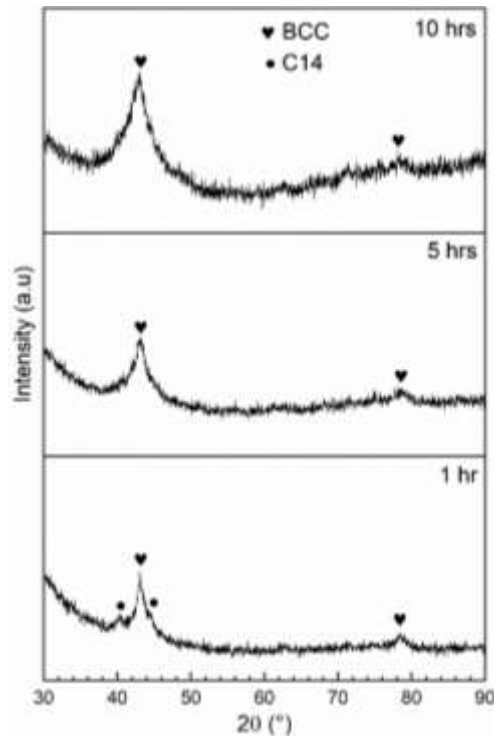


Figure 5.9 X-ray diffraction patterns of as-cast $\text{Ti}_{0.3}\text{V}_{0.3}\text{Mn}_{0.2}\text{Fe}_{0.1}\text{Ni}_{0.1}$ alloy after milling for 1, 5 and 10 h.

Before milling the $\text{Ti}_{0.3}\text{V}_{0.3}\text{Mn}_{0.2}\text{Fe}_{0.1}\text{Ni}_{0.1}$ alloy was multiphase with C14, BCC, and Ti_2Fe -type phases. After milling for one hour, the crystal structure was mainly BCC with some C14 phase. The peaks of the Ti_2Fe type phase could not be identified. After five hours milling, only broad BCC peaks were present. A similar result was obtained by Amira et al. who studied the effect of ball milling on cast TiCr_x alloys. They found that TiCr_x transforms from a mixture of C14 and C15 Laves phases to a metastable BCC phase after milling five hours under argon [86]. In the present case, as expected, further milling to 10 h had the effect of decreasing the crystallite size and thus broadening the Bragg's peaks of the BCC phase. Additionally, the Bragg's BCC peak is shifted to lower angles with milling time. This is an indication of the increasing lattice parameter of the BCC phase. Table 5.7 lists the

crystal structure parameters and the abundance of each phase in the cast alloy before and after milling as given by Rietveld's refinement.

Table 5.7 Crystal parameters and abundance of each phase in as-cast $\text{Ti}_{0.3}\text{V}_{0.3}\text{Mn}_{0.2}\text{Fe}_{0.1}\text{Ni}_{0.1}$ alloy before and after milling. Error on the last significant digit is indicated in parentheses.

Milling Time (hr)	Phase	Unit cell volume (\AA^3)	Lattice parameter (\AA)	Crystallite size (nm)	Abundance (%)
0	C14	164.98 (3)	4.8900 (4) 7.9651 (9)	125 (48)	79
	BCC	26.58 (1)	2.9841 (5)	31 (5)	17
	Ti_2Fe	1418 (3)	11.234 (8)	-----	4
1	C14	165.9 (6)	4.897 (7) 7.989 (2)	13.0 (2)	36
	BCC	27.02 (1)	3.001 (4)	4.0 (2)	64
5	BCC	27.60 (4)	3.02 (1)	1.88 (6)	100
10	BCC	28.60 (4)	3.06 (1)	1.12 (3)	100

In the case of C14 phase, milling up to 1 h doesn't significantly change the lattice parameters and the unit cell volume but it causes an important decrease in the crystallite size. For the BCC phase, with milling the lattice parameter increases and the crystallite size is reduced to approximately one nanometer after 10 h.

Milling the cast alloy produced similar results to milling the raw elements. As in the case of milling the raw elements, we selected the five-hour-milled sample to perform the hydrogenation test.

5.8 First Hydrogenation of the Milled Raw Powder and the Alloy

The first hydrogenation of both samples formed after five hours milling is shown in Figure 5.10 and compared to the as-cast alloy. The measurements were performed at room temperature under hydrogen pressure of 20 bars without any prior treatment.

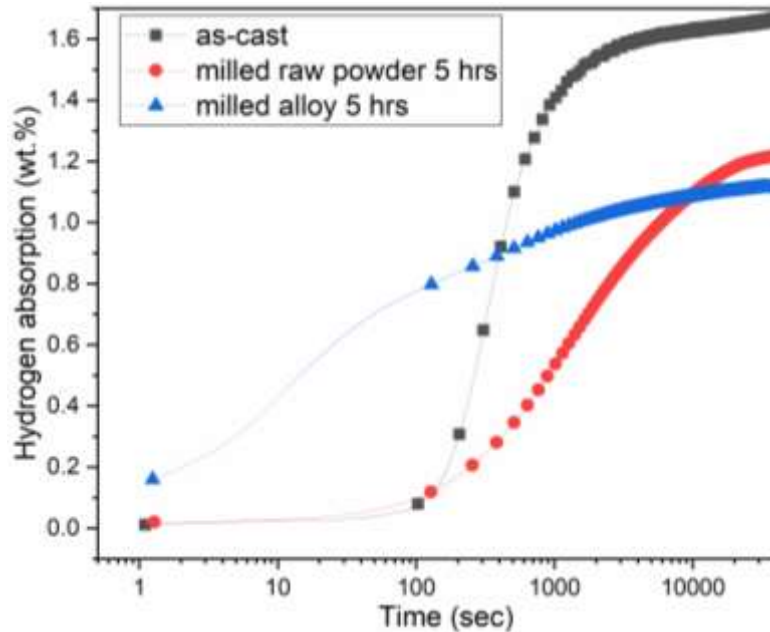


Figure 5.10 Activation curves of the milled raw powder for five hours, the as-cast alloy further milled for five hours, and the as-cast one.

The milled raw powder and the as-cast alloy have the same incubation time. The maximum capacity reached by the milled raw powder sample is 1.2 wt.% H, which is lower than the capacity of the as-cast alloy (1.6 wt.%). The reduction in capacity is most likely due to the reduction in crystallite size. Assuming that the grain boundaries are just one unit cell thick, the grain boundary volume for the five-hour ball milled materials is almost 50%. This grain boundary most probably does not store hydrogen at the same level as the BCC phase. Therefore, the total capacity is severely lowered. The same effect was seen for the TiFe alloy [87].

The milled alloy readily absorbs hydrogen without incubation time. In our apparatus, the first second of absorption is not recorded. Additionally, we see an initial capacity of 0.16 wt.%, therefore we assume that the real capacity of the milled alloy should be increased by about 0.1 wt.%. Therefore, the total capacity of this alloy is probably around 1.2 wt.%, which is the same capacity obtained with milling the raw elements for five hours. Figure 5.11 shows the XRD patterns of the hydrogenated alloys after full hydrogenation.

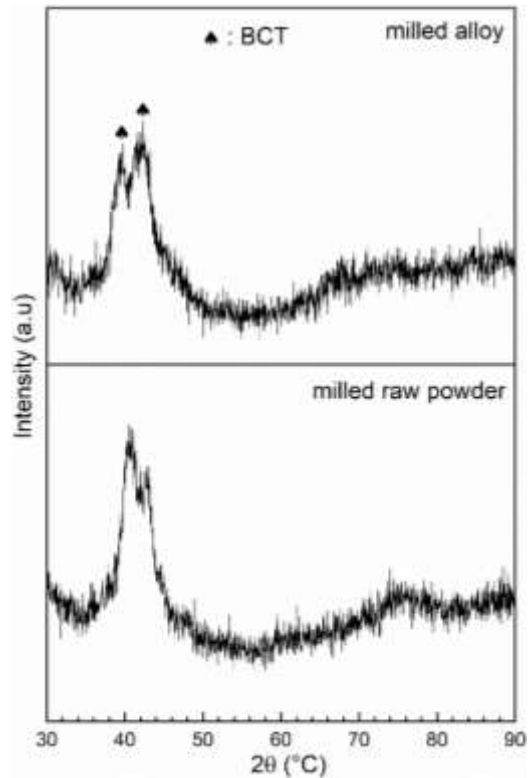


Figure 5.11 XRD patterns of the milled raw powder and milled alloy in the hydrogenated state.

Upon hydrogenation, the crystal structure of both samples is BCT of space group $I4/mmm$. It was shown by Nakamura and Akiba that the monohydride of the BCC phase has a BCT (body centered tetragonal) structure [60]. The transformation into BCT instead of the dihydride FCC could be because of a high hysteresis. From Rietveld's analysis, the crystal structure parameters of the BCT phase for milling the raw materials are the same as for the milled alloy. The unit cell volume is $30.1 (5) \text{ \AA}^3$, $a = 2.99 (2) \text{ \AA}$ and $c = 3.36 (3) \text{ \AA}$. The crystallite size is $1.51 (5) \text{ nm}$. The c/a ratio of the BCT phase is 1.12, which is in agreement with cases where the distortion of the lattice caused by hydrogen is along the c -axis [88]. Taking into account that each hydrogen atom occupies a volume of 2.9 \AA^3 , we could estimate that the BCC phase in the hydrogenated state has a capacity of around 0.7 wt.%, which is smaller than the measured capacity of 1.2 wt.%. However, as indicated above, because the X-ray diffraction was under air, there is a likelihood that the sample was partially desorbed.

5.9 Conclusions

The alloy $\text{Ti}_{0.3}\text{V}_{0.3}\text{Mn}_{0.2}\text{Fe}_{0.1}\text{Ni}_{0.1}$ was successfully synthesized by arc-melting and mechanical alloying. The arc-melted alloy has a multiphase structure, with a main C14 Laves phase matrix along with a BCC phase and a small amount of Ti_2Fe -type phase. Its maximum hydrogen storage capacity was 1.6 wt.%. Upon hydrogenation, Ti_2Fe -type phase disappeared. The initial C14 and BCC phases were converted into the C14 and BCC hydrides, respectively. The H/M value was 1.4 in the hydride BCC. Air exposure for two or five days has no impact on the hydrogen capacity but changed the kinetics.

Synthesis by mechanical alloying for five hours resulted in an alloy with BCC structure. The hydrogen capacity of the milled alloy was lower than the as-cast one. The BCC structure transforms after hydrogen absorption (under 20 bars of H_2) to monohydride phase "BCT" and not to dihydride "FCC". The effect of ball milling of the as-cast alloy was also studied. Ball milling for five hours produced a BCC structure similar to the one obtained by milling the raw elements for five hours. The first hydrogenation measurements showed that milling for five hours leads to a faster kinetics compared to the as-cast sample but with a reduced capacity. The synthesis of $\text{Ti}_{0.3}\text{V}_{0.3}\text{Mn}_{0.2}\text{Fe}_{0.1}\text{Ni}_{0.1}$ alloy by arc-melting is better than by mechanical alloying because arc-melted alloy shows a higher capacity.

Chapter 6

Enhancement of first hydrogenation of $\text{Ti}_1\text{V}_{0.9}\text{Cr}_{1.1}$ BCC alloy by cold rolling and ball milling

6.1 Overview

This chapter describes the effects of a mechanical treatment by cold rolling (CR) and ball milling (BM) on the microstructure and first hydrogenation of $\text{Ti}_1\text{V}_{0.9}\text{Cr}_{1.1}$ BCC alloy. The BCC alloys, as most of the metal hydrides, exhibit slow and difficult first hydrogenation. The aim of this work is to see if mechanical treatment could be effective for the enhancement of the first hydrogenation of $\text{Ti}_1\text{V}_{0.9}\text{Cr}_{1.1}$ alloy.

Figure 6.1 represents the summary of this work.

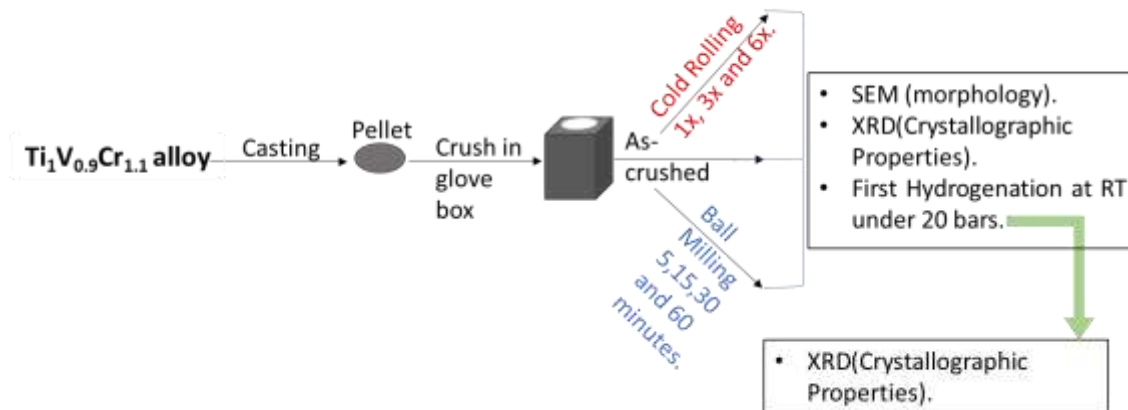


Figure 6.1 Flow chart of synthesis & characterization of $\text{Ti}_1\text{V}_{0.9}\text{Cr}_{1.1}$ alloy.

6.2 Morphology

Figure 6.2 shows the morphologies of $\text{Ti}_1\text{V}_{0.9}\text{Cr}_{1.1}$ alloy in the as-cast state after hand crushing and CR.

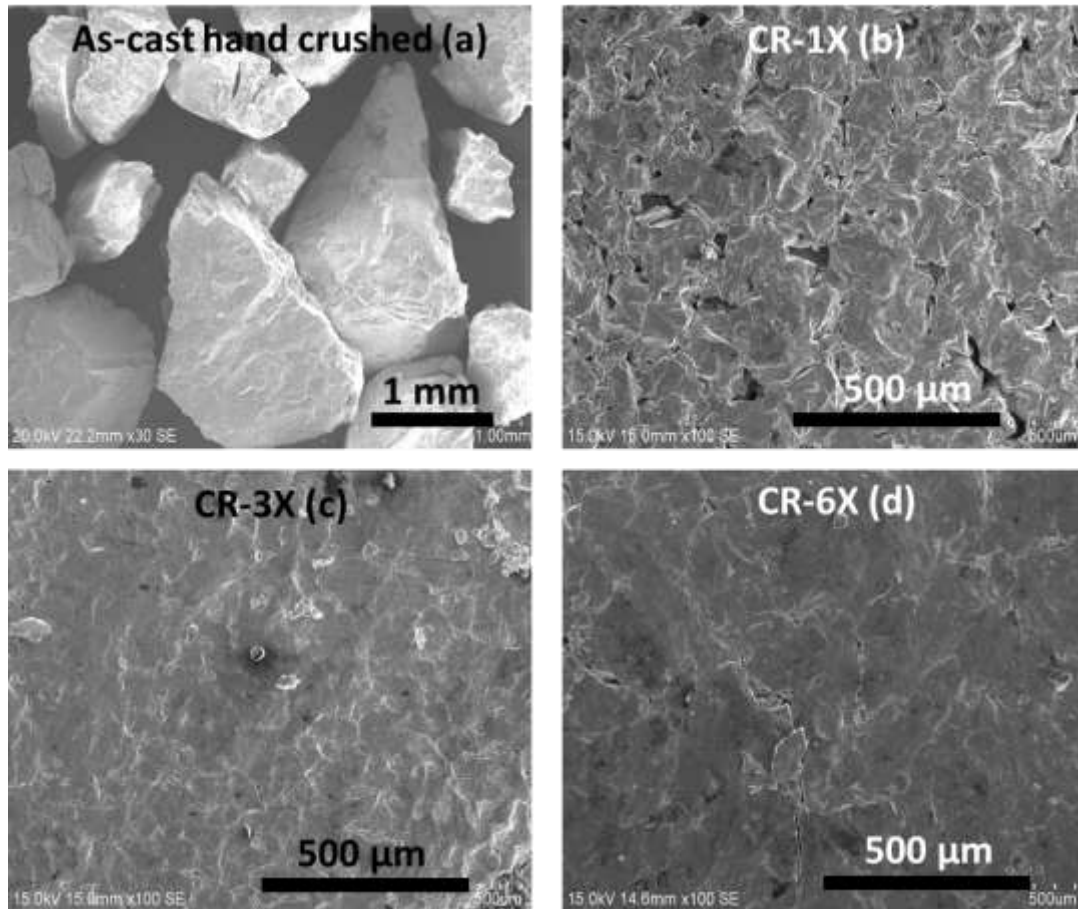


Figure 6.2 Scanning electron microscopy (SEM) micrographs of hand crushed (a), CR-1x (b), CR-3x (c), and CR-6x (d) of $Ti_1V_{0.9}Cr_{1.1}$ alloy.

The as-cast sample, after hand crushing, consisted of particles ranging from 0.65 to 2.2 mm. After CR, the sample showed consolidation of the powder. CR the sample one time agglomerated the powder into plates but with some voids, as presented in Figure 6.2b. The plates seemed to be porous. After three times of CR, the voids within the plates disappeared, but some cracks remained. With six rolling passes, the plate seemed to be more consolidated.

6.3 Crystal Structure

Figure 6.3 presents the XRD patterns of the as-cast $Ti_1V_{0.9}Cr_{1.1}$ alloy and after 1x, 3x, and 6x CR. All patterns showed a BCC structure (S.G. $Im-3m$). The crystal structure parameters and the weighted profile factor R_{wp} as evaluated by Rietveld's refinement are presented in Table 6.1.

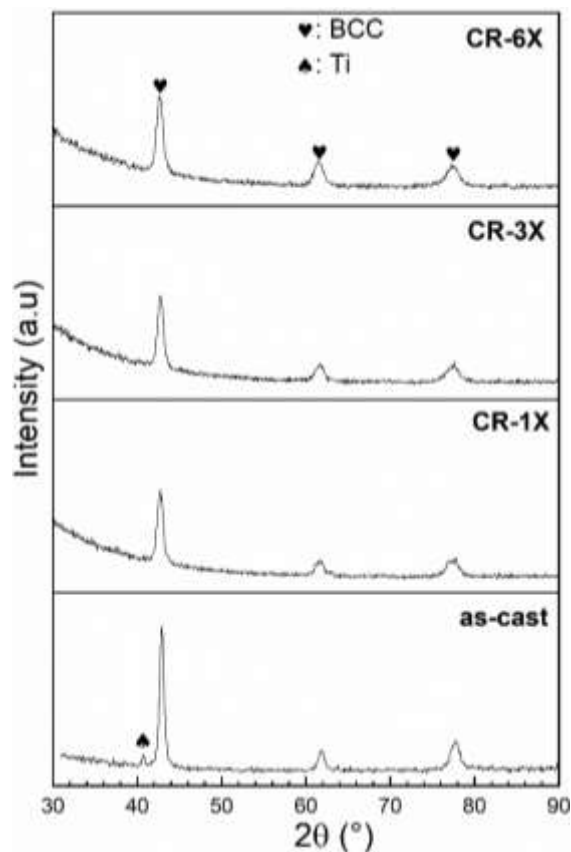


Figure 6.3 XRD patterns of the as-cast, CR-1x, CR-3x, and CR-6x of, $Ti_1V_{0.9}Cr_{1.1}$ alloy.

Table 6.1 Crystal structure parameters and the R_{wp} values of the as-cast, CR-1x, CR-3x, and CR-6x of $Ti_1V_{0.9}Cr_{1.1}$ alloy. Error on the last significant digit is indicated in parentheses.

Sample	Phase	Unit Cell Volume (\AA^3)	Lattice Parameter (\AA)	Crystallite Size (nm)	Micro strain (%)	Phase Abundance (%)	Rwp
As-cast	BCC Ti	28.04 (2) 36.25 (1)	3.0379 (9) $a = 2.961$ (4) $c = 4.773$ (1)	24 (2) 13 (2)	0.26 (1)	97 (3) 3 (3)	7.76
CR-1x	BCC	28.24 (3)	3.0453 (1)	28 (5)	0.40 (1)	100	5.95
CR-3x	BCC	28.34 (4)	3.0487 (1)	25 (4)	0.40 (1)	100	6.07
CR-6x	BCC	28.26 (4)	3.0459 (1)	21 (3)	0.42 (2)	100	6.55

As seen in Table 6.1, crystallite size did not drastically change upon rolling, whereas the microstrain slightly increased but only for the first rolling. Further rolling did not change the microstrain. The disappearance of the Ti-phase in the CR patterns after rolling occurred because the crystallite size of this phase tended to decrease and the microstrain increased. These two factors caused the peak to broaden. As the Ti phase was already at the limit of detection in the as-cast pattern (the value was $3 \pm 3\%$), as the peaks broadened, they became undistinguishable from the background.

6.4 First Hydrogenation

The first hydrogenation (activation) of the as-cast and cold rolled alloys were performed at room temperature under 20 bars of hydrogen and without any prior heat treatment. The activation kinetics are shown in Figure 6.4.

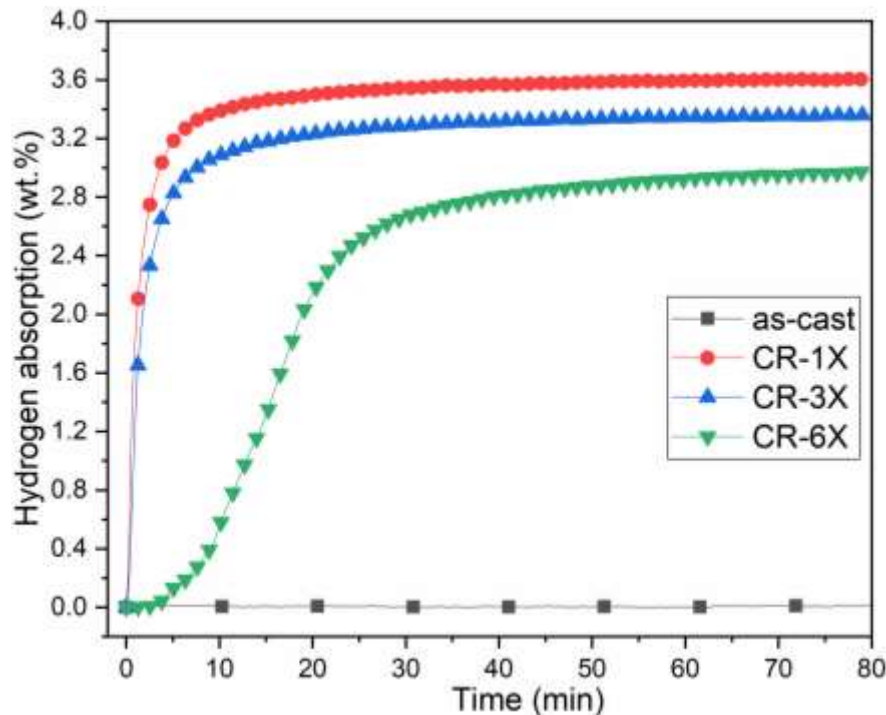


Figure 6.4 Activation curves of the as-cast, CR-1 \times , CR-3 \times , and CR-6 \times of $Ti_1V_{0.9}Cr_{1.1}$ alloy.

The as-cast $Ti_1V_{0.9}Cr_{1.1}$ alloy is hard to activate and did not absorb hydrogen even after 15 h of hydrogen exposure. Just one pass of CR made the activation possible without any incubation time and with fast kinetics. Full capacity was reached after only 12 min. The CR-3 \times sample also demonstrated good hydrogen uptake but with a slight reduction in capacity. Further rolling to 6 \times showed a 4 min incubation time followed by a slower absorption and reduced total capacity. The effectiveness of CR in activating the $Ti_1V_{0.9}Cr_{1.1}$

alloy is still unclear. Considering the crystal structure before and after CR, one rolling pass did not change the crystal structure of the alloy, and the reduction in crystallite size was relatively small. Therefore, the reason is something else. CR breaks particles in smaller pieces, thus producing new surfaces that could be active to hydrogen. However, as CR was performed in air, the newly produced surfaces would, in principle, oxidize immediately. Nevertheless, the speed of oxidation could be so slow that the freshly produced surfaces have only very thin oxide, which could be easily broken during hydrogenation.

Figure 6.4 shows that the capacity after 1, 3, and 6 CR passes are 3.6, 3.3, and 2.9 wt.%, respectively. Therefore, the loss of capacity appears to be directly proportional to the number of rolling passes. Each rolling pass decreased the capacity by about 0.1 wt.%. This decrease is most likely due to the formation of oxide as the rollings were performed in air.

The crystal structure of the full hydride samples was investigated from XRD patterns. Figure 6.5 presents the XRD patterns of the hydride samples of CR-1×, CR-3×, and CR-6× of $Ti_1V_{0.9}Cr_{1.1}$ alloy.

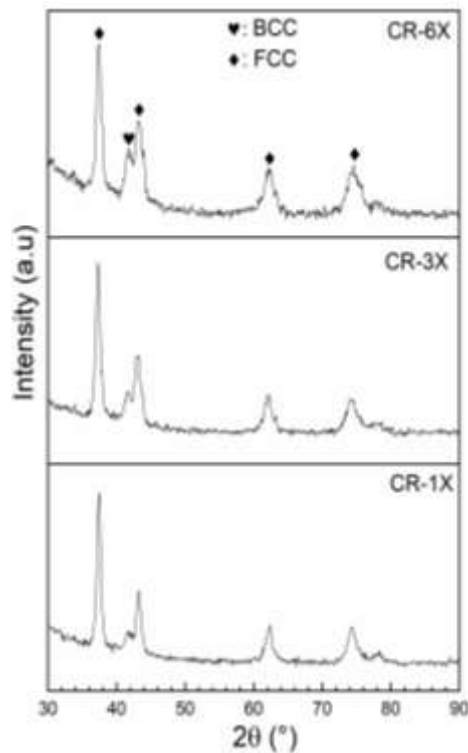


Figure 6.5 X-ray diffraction (XRD) patterns of hydrogenated of CR-1×, CR-3×, and CR-6× of $Ti_1V_{0.9}Cr_{1.1}$ alloy.

Figure 6.5 clearly shows that BCC and FCC phases were present in all patterns, but the relative intensities of both phases are different. Despite the capacity decreasing with increasing numbers of rolling passes, no oxide phase was identified in these patterns. For the 6× pattern, the proportion of oxide should be approximately 17 wt.% and should be seen in the diffraction pattern. The absence of the oxide phase in the patterns may be due to the very small crystallite size of the oxide phase. Assuming that the oxide phase is a shell around the hydride phase, the oxide's thickness is about 6% of the radius of the hydride crystallite. As seen in Table 6.2, which shows the results of Rietveld's refinement of all hydride patterns, the crystallite size of the FCC hydride phase is 30 nm; this means that the thickness of the oxide phase could be as small as 0.8 nm. Such a small crystallite size produces a diffraction pattern with very broad peaks that are effectively indistinguishable from the background.

Table 6.2 Crystal structure parameters and the R_{wp} values of all patterns after hydrogenation. Error on the last significant digit is indicated in parentheses.

Sample	Phase	Unit Cell Volume (\AA^3)	Lattice parameter (\AA)	Crystallite Size (nm)	Micro strain (%)	Phase Abundance (%)	R_{wp}
CR-1×	FCC	79.03 (1)	4.2914 (2)	20.2 (2)	0.34 (1)	84 (2)	5.34
	BCC	30.84 (8)	3.136 (3)	7 (2)	0.43 (1)	16 (2)	
CR-3×	FCC	78.90 (1)	4.289 (2)	17.3 (1)	0.40 (1)	76 (3)	5.28
	BCC	30.65 (9)	3.130 (7)	4.0 (6)	0.33 (1)	24 (3)	
CR-6×	FCC	78.61 (1)	4.284 (2)	29 (6)	0.53 (2)	72 (2)	4.93
	BCC	30.67 (7)	3.130 (2)	4.9 (6)	0.36 (8)	28 (2)	

The abundance of the phase (FCC) decreased with the number of rolls, and this seems to agree with the decreases in capacity shown in Figure 6.4. All the hydride patterns had BCC and FCC phases with almost the same lattice parameters. However, the lattice parameter of the BCC phase was much bigger than the as-cast BCC phase reported in Table 6.1. This was an indication that the BCC phase also contained hydrogen. The volume expansion of the BCC phase was about 2.6 \AA^3 . Considering that a hydrogen atom occupies a volume between 2 and 3 \AA^3 , and that there are two lattice points per unit cell, we estimated that the BCC phase contained about 0.5 hydrogen atom per metallic atom ($H/M \approx 0.5$). Since the diffraction patterns were captured in air at room temperature, it is possible that the samples experienced a partial dehydrogenation. To determine the true crystal structure in the fully hydride state, an in-situ diffraction pattern should be recorded.

6.5 Effect of ball milling on $\text{Ti}_1\text{V}_{0.9}\text{Cr}_{1.1}$ alloy

As cold rolling was found to be beneficial for activation, we wanted to determine if BM produces the same effect. For this, the as-cast alloy was milled for 5, 15, 30, and 60 min. The morphologies of the processed powders are shown in Figure 6.6.

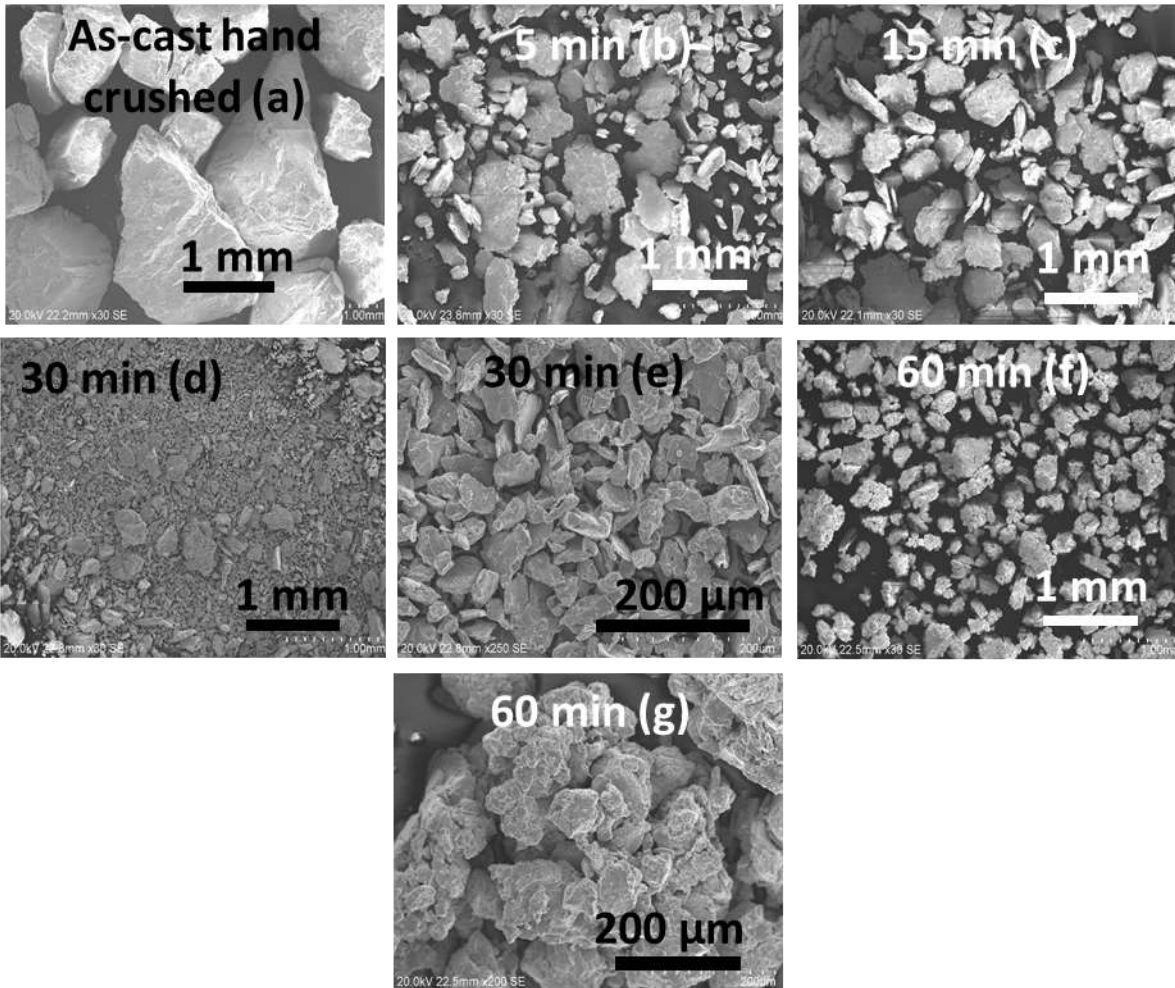


Figure 6.6 SEM micrographs of $\text{Ti}_1\text{V}_{0.9}\text{Cr}_{1.1}$ alloy before (a) and after 5 (b), 15 (c), 30 (d,e), and 60 min (f,g) of ball milling (BM).

After 5 min BM, some flat surfaces and formation of smaller particles in the range 0.2–1 mm were observed. Further milling decreased the size of the particles. Agglomeration of small particles was observed after 60 min of milling.

The XRD patterns of $\text{Ti}_1\text{V}_{0.9}\text{Cr}_{1.1}$ alloy for different BM times are presented in Figure 6.7. The crystal structure parameters and the R_{wp} , as evaluated by Rietveld's refinement, are shown in Table 6.3.

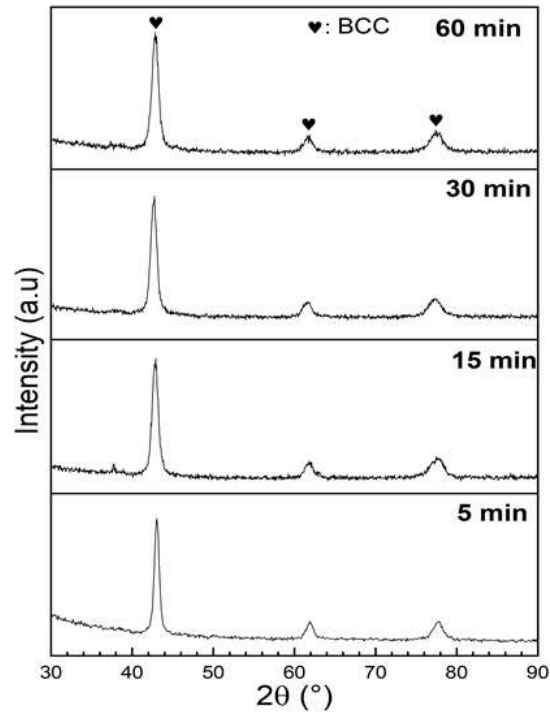


Figure 6.7 Diffraction patterns of $\text{Ti}_1\text{V}_{0.9}\text{Cr}_{1.1}$ alloy for different ball milling times.

Table 6.3 Crystal parameters and the R_{wp} values of $\text{Ti}_1\text{V}_{0.9}\text{Cr}_{1.1}$ alloy for different ball milling times compared with the as-cast sample. Error on the last significant digit is indicated in parentheses.

Sample	Phase	Unit Cell Volume (\AA^3)	Lattice Parameter (\AA)	Crystallite Size (nm)	Microstrain (%)	Phase Abundance (%)	R_{wp}
As-cast	BCC Ti	28.04 (2) 36.25 (1)	3.0379 (9) $a = 2.961(4)$ $c = 4.773 (1)$	24 (2) 13 (2)	0.26 (1)	97 (3) 3 (3)	7.76
BM 5 min	BCC	28.29 (3)	3.0471 (9)	20.5 (1)	0.30 (1)	100	5.20
BM 15 min	BCC	28.18 (3)	3.0432 (1)	16.1 (1)	0.40 (2)	100	7.84
BM 30 min	BCC	28.28 (3)	3.0468 (1)	14.5 (8)	0.40 (1)	100	7.46
BM 60 min	BCC	28.32 (3)	3.0481 (1)	12.2 (6)	0.40 (1)	100	7.30

All the ball-milled samples had a BCC crystal structure. The crystallite size decreased with milling while the microstrain remained almost constant. The microstrain in the ball-milled samples was almost identical to that in the cold rolled samples.

The activation curves of the ball-milled samples compared to the cold-rolled sample are presented in Figure 6.8.

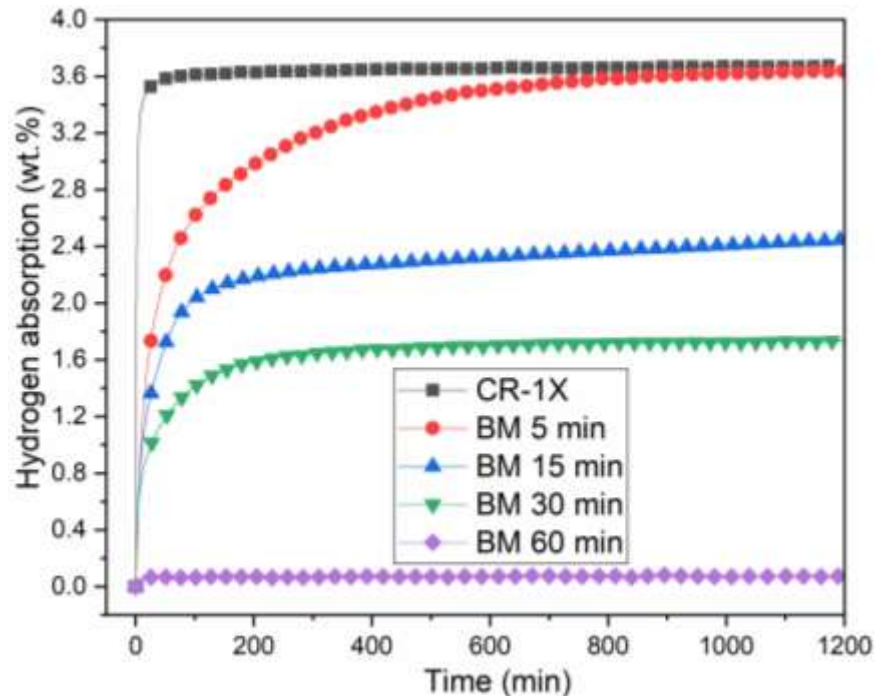


Figure 6.8 Activation curves of $Ti_1V_{0.9}Cr_{1.1}$ alloy for different BM times as compared to the 1 cold-rolled sample.

BM enabled the activation of $Ti_1V_{0.9}Cr_{1.1}$ alloy. Milling for 5 min significantly improved the kinetics with a maximum capacity of 3.6 wt.% H_2 . Further milling for 15 and 30 min reduced the capacity to 2.4 and to respectively 1.7 wt.% of hydrogen. Milling for one hour made the sample inert to hydrogen. This behavior is still unclear and suggests that, besides the sample's morphology, other parameters impact the activation. The effect of particle size in a BCC alloy was investigated by Kamble et al. [59]. For the first hydrogenation, they found that particle size affects the incubation time but has no significant effect on the capacity. Luo et al. found similar results on BCC $V_{40}(TiCr)_{51}Fe_8Mn$ alloy [89]. In their study, the particle size was 60 to 500 mesh (0.25 to 0.025 mm), but they registered the same hydrogen capacity in the first cycle with a different loss of

capacity with cycling. After 25 cycles, the best performance was obtained for the 400-mesh sample, which lost 11% of its initial capacity.

Comparing the result of CR-1× with that of BM-5 min, both are beneficial for activation of the $Ti_1V_{0.9}Cr_{1.1}$ alloy, but CR-1× is more effective since full hydrogenation occurs much faster.

In a previous investigation, we showed that an addition of 12 wt.% Zr to $Ti_1V_{0.9}Cr_{1.1}$ alloy produced fast activation kinetics, reaching a maximum capacity of 3 wt.% H_2 within 3 min [50]. Therefore, adding 12 wt.% Zr still produces faster kinetics compared to CR-1× but with reduced capacity. However, using mechanical deformation such as BM and CR does not change the chemistry. Adding other elements may increase the cost of the alloy and change the chemistry of the BCC phase. For these reasons, activation enhancement is better achieved by mechanical than by additive treatment.

We observed that the hydrogenation was complete for all BM samples, even if the total capacity was reduced. To determine the crystal structure of the ball-milled samples after hydrogenation, we performed XRD patterns, as seen in Figure 6.9. The crystal structure parameters as determined by Rietveld refinement are shown in Table 6.4.

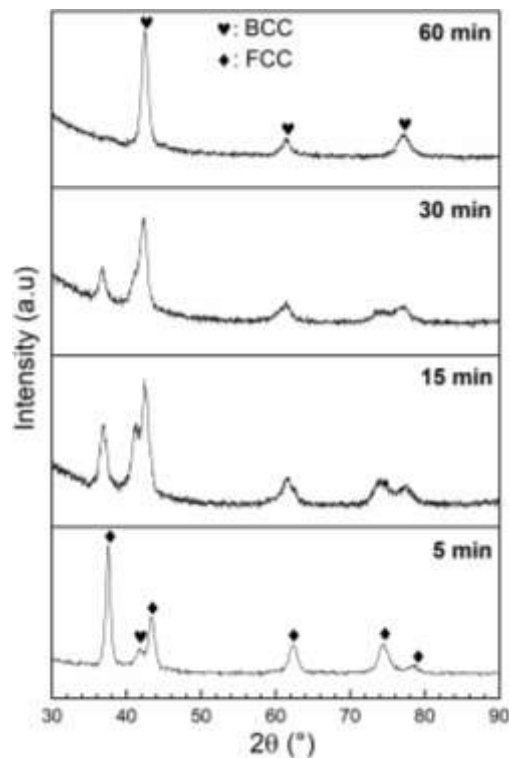


Figure 6.9 Diffraction patterns of $Ti_1V_{0.9}Cr_{1.1}$ alloy for different BM times after hydrogenation.

Table 6.4 Crystal parameters of Ti₁V_{0.9}Cr_{1.1} alloy for different ball milling times after hydrogenation. Error on the last significant digit is indicated in parentheses.

Activated BM	Phase	Unit Cell Volume (Å ³)	Lattice Parameter (Å)	Crystallite Size (nm)	Micro strain (%)	Phase Abundance (%)	Rwp
5 min	FCC	78.97 (7)	4.2903 (1)	15.4 (8)	0.35 (1)	79 (2)	4.12
	BCC	31.06 (7)	3.144 (2)	3.8 (5)	0.34 (1)	21 (2)	
15 min	FCC	78.38 (1)	4.280 (2)	15.8 (2)	0.42 (2)	36 (2)	5.12
	BCC	29.33 (5)	3.0841 (2)	8.6 (1)	1.09 (4)	64 (2)	
30 min	FCC	78.49 (2)	4.282 (3)	14.0 (2)	0.29 (3)	23 (2)	5.17
	BCC	28.75 (5)	3.0634 (2)	5.1 (3)	0.49 (3)	77 (2)	
60 min	BCC	28.15 (3)	3.0418 (9)	12.4 (6)	0.40 (1)	100	4.63

For the 60 min sample, the crystal structure was still BCC, which confirmed that this sample did not absorb hydrogen, as seen in Figure 6.8. There was no significant change in the lattice parameter and crystallite size of this BCC phase, confirming that there was no reaction with hydrogen. All the other hydride patterns had BCC and FCC phases. The abundance of the FCC phase decreased with milling time, which agrees with the reduction of hydrogen capacity seen in Figure 6.8. The unit cell volume of the FCC phase was practically identical to the FCC phase observed in the hydrogenated cold-rolled samples. However, the unit cell volume of the BCC phase showed different behavior. It progressively decreased with milling time; this means that as milling time increased, the amount of hydrogen retained in the BCC phase decreased. It seems that milling decreases the ability of the BCC phase to absorb hydrogen. The exact mechanism is not clear, but it is a subject for further research and may explain the reduction of capacity with milling time.

6.6 Conclusions

The effects of cold rolling and ball milling on the microstructure and hydrogen storage properties of Ti₁V_{0.9}Cr_{1.1} alloy were investigated. Cold-rolled samples for one, three, and six rolling passes had a BCC crystal structure. One cold roll was efficient for the first absorption kinetics. However, increasing rolling passes led to a reduction in capacity. The BCC and FCC phases were present in the cold-rolled samples after hydrogenation. Ball-milled samples for 5, 15, 30, and 60 min also maintained the original BCC crystal structure, and no other crystal structure was identified. After BM for five minutes, the first hydrogenation proceeded with relatively good kinetics. However, further milling

decreased hydrogen capacity. Milling to 60 min made the alloy inert to hydrogen. The hydrogenated samples had both BCC and FCC phases.

One cold roll and BM for five minutes were beneficial for the first hydrogenation kinetics. CR-1X was more effective than ball milling for five minutes since full hydrogenation occurred much faster. The exact mechanism responsible for the improvement of activation kinetics upon CR and BM is still unknown. Mechanical treatment, and especially CR, are more efficient, low-cost, and improve activation kinetics more than addition of other elements such as Zr.

Chapter 7

Conclusion and Future Work

In this thesis, a systematic investigation of the effect of particle size, temperature, and pressure, on the first hydrogenation of TiVZrHfNb HEA is reported. We found that smaller particles have faster hydrogenation kinetics. The activation is strongly dependent on the temperature, higher temperature drastically reducing the incubation period. It was shown that the incubation period follows an Arrhenius relationship.

After understanding the important parameters of activation kinetics, the effect of the substitution of Nb by V on the microstructure and hydrogen storage properties of TiHfZrNb_{1-x}V_{1+x} alloy (x= 0, 0.1, 0.2, 0.4, 0.6 and 1) was studied. The microstructures of all substituted samples are multiphase. Upon substitution, the BCC phase is progressively replaced by an HCP and FCC phases. For high values of x, a C15 phase is present and becomes the main phase for x= 1. We found that substitution of Nb by V greatly enhanced the first hydrogenation and makes it possible at room temperature under 20 bars of hydrogen without any prior treatment with maximum hydrogen capacity of 2 wt.%. From these results, it seems that for hydrogen storage purposes, the optimum alloy is the one without Nb.

In a way to potentially increase the gravimetric hydrogen storage capacity, a new multicomponent alloy of composition Ti_{0.3}V_{0.3}Mn_{0.2}Fe_{0.1}Ni_{0.1} was studied. The alloy was successfully synthesized by arc-melting and mechanical alloying resulting in different microstructures. The arc-melted alloy has a multiphase structure mainly C14 Laves phase while the alloy synthesized by mechanical alloying for five hours resulted in an alloy with BCC structure. Both alloys were able to absorb hydrogen at room temperature under 20 bars of hydrogen pressure without any prior treatment. The as-cast alloy had a maximum capacity of 1.6 wt.% while the milled one had 1.2 wt.%. It is worth to mention that we were able to handle the as-cast alloy in the air and even after 2 and 5 days of exposure without loss in capacity, which is an advantage for large-scale production.

Finally, we tried to solve the problem of impossible first hydrogenation of Ti₁V_{0.9}Cr_{1.1} BCC alloy by treating it by mechanical deformation. One cold roll or milling for five minutes made the activation possible. However, more rolling passes or further milling led to a reduction in capacity. We concluded that mechanical treatments, and especially cold rolling, are efficient and low-cost techniques to improve activation kinetics of metal hydrides.

As most of the studies on HEAs for hydrogen storage are based on the transition metals of heavy elements from 3d, 4d, and 5d transition groups, we propose adding light elements such as Mg or Al. Such elements could incorporate in the solid solution phase, reduce the molar mass and thereby increasing the gravimetric capacity of the HEAs. Because of low melting points of Mg/Al, that HEAs should be synthesized by mechanical alloying.

As the durability to hydrogenation/dehydrogenation cycling is a significant practical part of metal hydrides, we suggest a systematic study of cycling behaviour of the TiVZrHfNb, TiHfZrV₂ and of Ti₁V_{0.9}Cr_{1.1} alloys to be done.

With respect to the production cost of the alloys, we think that replacing vanadium by the less expensive ferrovanadium could be promising. Such a substitution could be taken into consideration towards a low-cost hydrogen storage material. We suggest studying the impact of replacement of vanadium by ferrovanadium on the crystal structure, microstructure, and hydrogen storage properties of TiHfZrV₂, Ti_{0.3}V_{0.3}Mn_{0.2}Fe_{0.1}Ni_{0.1} and of Ti₁V_{0.9}Cr_{1.1} alloys.

Since cold rolling is effective for the activation of Ti₁V_{0.9}Cr_{1.1} alloy, it would be interesting to investigate cold rolling for other BCC alloys and HEAs for easy activation. Also, the effect of rolling parameters, such as speed and force, on the cold rolling process should be investigated.

REFERENCES

- [1] <https://www.osler.com/en/resources/regulations/2020/federal-government-announces-canada-s-hydrogen-strategy>.
- [2] I. Dincer, Renewable energy and sustainable development: a crucial review, *Renewable and sustainable energy reviews*, 4 (2000) 157-175.
- [3] M. Paskevicius, D. Sheppard, K. Williamson, C. Buckley, Metal hydride thermal heat storage prototype for concentrating solar thermal power, *Energy*, 88 (2015) 469-477.
- [4] C.E. Law, M.D. Vandayburg, Hydrogen generator having a thermal actuator, in, Google Patents, 2016.
- [5] G. Majeau-Bettez, T.R. Hawkins, A.H. Strømman, Life cycle environmental assessment of lithium-ion and nickel metal hydride batteries for plug-in hybrid and battery electric vehicles, *Environmental science & technology*, 45 (2011) 4548-4554.
- [6] C.J. Quarton, O. Tlili, L. Welder, C. Mansilla, H. Blanco, H. Heinrichs, J. Leaver, N.J. Samsatli, P. Lucchese, M. Robinius, The curious case of the conflicting roles of hydrogen in global energy scenarios, *Sustainable Energy & Fuels*, 4 (2020) 80-95.
- [7] L. Schlapbach, A. Züttel, Hydrogen-storage materials for mobile applications, in: *Materials for sustainable energy: a collection of peer-reviewed research and review articles from nature publishing group*, World Scientific, 2011, pp. 265-270.
- [8] R. Krishna, E. Titus, M. Salimian, O. Okhay, S. Rajendran, A. Rajkumar, J. Sousa, A. Ferreira, J.C. Gil, J. Gracio, Hydrogen storage for energy application, in: *Hydrogen storage*, IntechOpen, 2012.
- [9] E. Rivard, M. Trudeau, K. Zaghbi, Hydrogen storage for mobility: A review, *Materials*, 12 (2019) 1973.
- [10] A. Yamashita, M. Kondo, S. Goto, N. Ogami, Development of high-pressure hydrogen storage system for the Toyota "MIRAI", in, SAE Technical Paper, 2015.
- [11] L. Schlapbach, A. Züttel, Hydrogen-storage materials for mobile applications, *Nature*, 414 (2001) 353-358.
- [12] V.A. Yartys, M.V. Lototsky, E. Akiba, R. Albert, V.E. Antonov, J.R. Ares, M. Baricco, N. Bourgeois, C.E. Buckley, J.M. Bellosta von Colbe, J.C. Crivello, F. Cuevas, R.V. Denys, M. Dornheim, M. Felderhoff, D.M. Grant, B.C. Hauback, T.D. Humphries, I. Jacob, T.R. Jensen, P.E. de Jongh, J.M. Joubert, M.A. Kuzovnikov, M. Latroche, M. Paskevicius, L. Pasquini, L. Popilevsky, V.M. Skripnyuk, E. Rabkin, M.V. Sofianos, A. Stuart, G. Walker, H. Wang, C.J. Webb, M. Zhu, Magnesium based materials for hydrogen based energy storage: Past, present and future, *International Journal of Hydrogen Energy*, 44 (2019) 7809-7859.
- [13] D.R. Leiva, J.A.M. Jorge, T.T. Ishikawa, W.J. Botta, Hydrogen Storage in Mg and Mg-Based Alloys and Composites Processed by Severe Plastic Deformation, *MATERIALS TRANSACTIONS*, 60 (2019) 1561-1570.
- [14] S.S. Srinivasan, D.E. Demirocak, Metal hydrides used for hydrogen storage, in: *Nanostructured Materials for Next-Generation Energy Storage and Conversion*, Springer, 2017, pp. 225-255.
- [15] A. Lys, J.O. Fadonougbo, M. Faisal, J.-Y. Suh, Y.-S. Lee, J.-H. Shim, J. Park, Y.W. Cho, Enhancing the Hydrogen Storage Properties of AxBy Intermetallic Compounds by Partial Substitution: A Short Review, *Hydrogen*, 1 (2020) 38-63.
- [16] E. Kouloukakis, E. I Gkanas, S. Makridis, C. Christodoulou, D. Fruchart, A. Stubos, High-temperature activated AB₂ nanopowders for metal hydride hydrogen compression, *International journal of energy research*, 38 (2014) 477-486.
- [17] F. Stein, M. Palm, G. Sauthoff, Structure and stability of Laves phases. Part I. Critical assessment of factors controlling Laves phase stability, *Intermetallics*, 12 (2004) 713-720.

- [18] L. Ouyang, J. Huang, H. Wang, J. Liu, M. Zhu, Progress of hydrogen storage alloys for Ni-MH rechargeable power batteries in electric vehicles: A review, *Materials Chemistry and Physics*, 200 (2017) 164-178.
- [19] K. Young, T. Ouchi, J. Koch, M. Fetcenko, The role of Mn in C14 Laves phase multi-component alloys for NiMH battery application, *Journal of Alloys and Compounds*, 477 (2009) 749-758.
- [20] K.-H. Young, J. Nei, C. Wan, R. Denys, V. Yartys, Comparison of C14-and C15-predominated AB₂ metal hydride alloys for electrochemical applications, *Batteries*, 3 (2017) 22.
- [21] B. Sakintuna, F. Lamari-Darkrim, M. Hirscher, Metal hydride materials for solid hydrogen storage: a review, *International journal of hydrogen energy*, 32 (2007) 1121-1140.
- [22] G. Mazzolai, B. Coluzzi, A. Biscarini, F.M. Mazzolai, A. Tuissi, F. Agresti, S. Lo Russo, A. Maddalena, P. Palade, G. Principi, Hydrogen-storage capacities and H diffusion in bcc TiVCr alloys, *Journal of Alloys and Compounds*, 466 (2008) 133-139.
- [23] S. Miraglia, P. de Rango, S. Rivoirard, D. Fruchart, J. Charbonnier, N. Skryabina, Hydrogen sorption properties of compounds based on BCC Ti_{1-x}V_{1-y}Cr_{1+x+y} alloys, *Journal of Alloys and Compounds*, 536 (2012) 1-6.
- [24] T. Tamura, T. Kazumi, A. Kamegawa, H. Takamura, M. Okada, Protium absorption properties and protide formations of Ti-Cr-V alloys, *Journal of alloys and compounds*, 356 (2003) 505-509.
- [25] W. Zhang, P.K. Liaw, Y. Zhang, Science and technology in high-entropy alloys, *Science China Materials*, (2018) 1-21.
- [26] J.W. Yeh, S.K. Chen, S.J. Lin, J.Y. Gan, T.S. Chin, T.T. Shun, C.H. Tsau, S.Y. Chang, Nanostructured high-entropy alloys with multiple principal elements: novel alloy design concepts and outcomes, *Advanced Engineering Materials*, 6 (2004) 299-303.
- [27] B. Cantor, I. Chang, P. Knight, A. Vincent, Microstructural development in equiatomic multicomponent alloys, *Materials Science and Engineering: A*, 375 (2004) 213-218.
- [28] S. Ranganathan, Alloyed pleasures: multimetallic cocktails, *Current science*, 85 (2003) 1404-1406.
- [29] X. Chang, M. Zeng, K. Liu, L. Fu, Phase Engineering of High-Entropy Alloys, *Advanced Materials*, 32 (2020) 1907226.
- [30] D. Miracle, High entropy alloys as a bold step forward in alloy development, *Nature communications*, 10 (2019) 1-3.
- [31] D. Karlsson, G. Ek, J. Cedervall, C. Zlotea, K.T. Møller, T.C. Hansen, J. Bednarcik, M. Paskevicius, M.H. Sørby, T.R. Jensen, Structure and hydrogenation properties of a HfNbTiVZr high-entropy alloy, *Inorganic chemistry*, 57 (2018) 2103-2110.
- [32] I. Kunce, M. Polanski, J. Bystrzycki, Structure and hydrogen storage properties of a high entropy ZrTiVCrFeNi alloy synthesized using Laser Engineered Net Shaping (LENS), *International Journal of Hydrogen Energy*, 38 (2013) 12180-12189.
- [33] I. Kunce, M. Polanski, J. Bystrzycki, Microstructure and hydrogen storage properties of a TiZrNbMoV high entropy alloy synthesized using Laser Engineered Net Shaping (LENS), *International journal of hydrogen energy*, 39 (2014) 9904-9910.
- [34] M. Sahlberg, D. Karlsson, C. Zlotea, U. Jansson, Superior hydrogen storage in high entropy alloys, *Scientific reports*, 6 (2016) 36770.
- [35] Y.-F. Kao, S.-K. Chen, J.-H. Sheu, J.-T. Lin, W.-E. Lin, J.-W. Yeh, S.-J. Lin, T.-H. Liou, C.-W. Wang, Hydrogen storage properties of multi-principal-component CoFeMnTi_xVyZr_z alloys, *international journal of hydrogen energy*, 35 (2010) 9046-9059.
- [36] W. Steurer, Single-phase high-entropy alloys—A critical update, *Materials Characterization*, 162 (2020) 110179.

- [37] H.-J. Lee, Molecular dynamics studies of metallic glasses, Dissertation (Ph.D.), California Institute of Technology. doi:10.7907/ZE5V-VZ33. <https://resolver.caltech.edu/CaltechETD:etd-05292003-165018>, 2003.
- [38] Y. Ye, Q. Wang, J. Lu, C. Liu, Y. Yang, The generalized thermodynamic rule for phase selection in multicomponent alloys, *Intermetallics*, 59 (2015) 75-80.
- [39] G. Mansoori, N.F. Carnahan, K. Starling, T. Leland Jr, Equilibrium thermodynamic properties of the mixture of hard spheres, *The Journal of Chemical Physics*, 54 (1971) 1523-1525.
- [40] M.C. Gao, C. Zhang, P. Gao, F. Zhang, L. Ouyang, M. Widom, J. Hawk, Thermodynamics of concentrated solid solution alloys, *Current Opinion in Solid State and Materials Science*, 21 (2017) 238-251.
- [41] Y. Yuan, Y. Wu, X. Tong, H. Zhang, H. Wang, X. Liu, L. Ma, H. Suo, Z. Lu, Rare-earth high-entropy alloys with giant magnetocaloric effect, *Acta Materialia*, 125 (2017) 481-489.
- [42] A. Takeuchi, A. Inoue, Classification of Bulk Metallic Glasses by Atomic Size Difference, Heat of Mixing and Period of Constituent Elements and Its Application to Characterization of the Main Alloying Element, *Materials Transactions*, 46 (2005) 2817-2829.
- [43] X. Yang, Y. Zhang, Prediction of high-entropy stabilized solid-solution in multi-component alloys, *Materials Chemistry and Physics*, 132 (2012) 233-238.
- [44] S. Guo, C. Ng, J. Lu, C. Liu, Effect of valence electron concentration on stability of fcc or bcc phase in high entropy alloys, *Journal of applied physics*, 109 (2011) 103505.
- [45] M. Dornheim, Thermodynamics of metal hydrides: tailoring reaction enthalpies of hydrogen storage materials, in: *Thermodynamics-Interaction Studies-Solids, Liquids and Gases*, InTech, 2011.
- [46] https://www.ctcms.nist.gov/hydrogen_storage/research_pct.html.
- [47] X. Xin, R. Johansson, M. Wolff, B. Hjörvarsson, Hydrogen in vanadium: Site occupancy and isotope effects, *Physical Review B*, 93 (2016) 134107.
- [48] E. Akiba, H. Iba, Hydrogen absorption by Laves phase related BCC solid solution, *Intermetallics*, 6 (1998) 461-470.
- [49] M. Okada, T. Kuriwa, T. Tamura, H. Takamura, A. Kamegawa, Ti-V-Cr b.c.c. alloys with high protium content, *Journal of Alloys and Compounds*, 330-332 (2002) 511-516.
- [50] S. Sleiman, J. Huot, Microstructure and Hydrogen Storage Properties of Ti1V0.9Cr1.1 Alloy with Addition of x wt % Zr (x = 0, 2, 4, 8, and 12), *Inorganics*, 5 (2017) 86.
- [51] M. Abramoff, P. Magalhaes, S. Ram, Image processing with ImageJ. *Biophotonics Int* 2004; 11 (7): 36-42, in, 2014.
- [52] A. Bruker, Topas V3: general profile and structure analysis software for powder diffraction data-user's manual; Bruker AXS, Karlsruhe; Coelho AA (2007) TOPAS academic. Coelho Software, Brisbane, in, 2005.
- [53] <https://science.howstuffworks.com/scanning-electron-microscope2.htm>.
- [54] https://serc.carleton.edu/research_education/geochemsheets/BraggsLaw.html.
- [55] R. Jenkins, X-Ray Techniques: Overview, *Encyclopedia of analytical chemistry*, (2000).
- [56] B. AXS, Topas V3: general profile and structure analysis software for powder diffraction data-user's manual; Bruker AXS, Karlsruhe; Coelho AA (2007) TOPAS academic. Coelho Software, Brisbane, in, 2005.
- [57] P. American Institute of, B.H. Billings, D.E. Gray, American Institute of Physics handbook, McGraw-Hill, New York, 1972.
- [58] S. Khajavi, M. Rajabi, J. Huot, Crystal structure of as-cast and heat-treated Ti0.5Zr0.5(Mn1-xFex)Cr1, x= 0, 0.2, 0.4, *Journal of Alloys and Compounds*, 767 (2018) 432-438.
- [59] A. Kamble, P. Sharma, J. Huot, Effect of doping and particle size on hydrogen absorption properties of BCC solid solution 52Ti-12V-36Cr, *International Journal of Hydrogen Energy*, (2017).

- [60] Y. Nakamura, E. Akiba, Hydriding properties and crystal structure of NaCl-type mono-hydrides formed from Ti–V–Mn BCC solid solutions, *Journal of Alloys and Compounds*, 345 (2002) 175-182.
- [61] Q. Cao, J. Li, P. Zhang, A. Horsewell, J. Jiang, Y. Zhou, Second amorphous-to-crystalline phase transformation in Cu₆₀Ti₂₀Zr₂₀ bulk metallic glass, *Journal of Physics: Condensed Matter*, 19 (2007) 246206.
- [62] D. Ouyang, N. Li, L. Liu, Structural heterogeneity in 3D printed Zr-based bulk metallic glass by selective laser melting, *Journal of Alloys and Compounds*, 740 (2018) 603-609.
- [63] M. Qi, H. Fecht, On the thermodynamics and kinetics of crystallization of a Zr–Al–Ni–Cu-based bulk amorphous alloy, *Materials characterization*, 47 (2001) 215-218.
- [64] E. Zuzek, J. Abriata, A. San-Martin, F. Manchester, H-Zr(hydrogen-zirconium), *Phase Diagrams of Binary Hydrogen Alloys*. ASM International, Member/Customer Service Center, Materials Park, OH 44073-0002, USA, 2000., (2000) 309-322.
- [65] M.M. Nygård, W.A. Sławiński, G. Ek, M.H. Sørby, M. Sahlberg, D.A. Keen, B.C. Hauback, Local order in high-entropy alloys and associated deuterides – a total scattering and Reverse Monte Carlo study, *Acta Materialia*, 199 (2020) 504-513.
- [66] Y. Zhang, Y.J. Zhou, J.P. Lin, G.L. Chen, P.K. Liaw, Solid-solution phase formation rules for multi-component alloys, *Advanced engineering materials*, 10 (2008) 534-538.
- [67] S. Sleiman, J. Huot, Effect of particle size, pressure and temperature on the activation process of hydrogen absorption in TiVZrHfNb high entropy alloy, *Journal of Alloys and Compounds*, 861 (2021) 158615.
- [68] H. Wang, N. Gao, G.-H. Lü, Z.-W. Yao, Effects of temperature and point defects on the stability of C15 Laves phase in iron: A molecular dynamics investigation, *Chinese physics B*, 27 (2018) 066104.
- [69] S. Khajavi, M. Rajabi, J. Huot, Crystal structure of as-cast and heat-treated Ti_{0.5}Zr_{0.5}(Mn_{1-x}Fe_x)Cr₁, x=0, 0.2, 0.4, *Journal of Alloys and Compounds*, (2018).
- [70] H. Peisl, Lattice strains due to hydrogen in metals, in: *Hydrogen in metals I*, Springer, 1978, pp. 53-74.
- [71] <http://www.crystalmaker.com/support/tutorials/atomic-radii/>.
- [72] Y. Zhang, Z. Lu, S. Ma, P. Liaw, Z. Tang, Y. Cheng, M. Gao, Guidelines in predicting phase formation of high-entropy alloys, *Mrs Communications*, 4 (2014) 57-62.
- [73] <https://www.ptable.com/>.
- [74] R. Kirchheim, A. Pundt, 25 - Hydrogen in Metals, in: D.E. Laughlin, K. Hono (Eds.) *Physical Metallurgy (Fifth Edition)*, Elsevier, Oxford, 2014, pp. 2597-2705.
- [75] S. Deying, G. Xueping, Z. Yunshi, Y. Jie, S. Panwen, Characteristics of titanium-based C14-type Laves phase alloys and their hydride electrodes, *Journal of alloys and compounds*, 206 (1994) 43-46.
- [76] S. Challet, M. Latroche, F. Heurtaux, Hydrogenation properties and crystal structure of the single BCC (Ti_{0.355}V_{0.645})_{100-x}M_x alloys with M= Mn, Fe, Co, Ni (x= 7, 14 and 21), *Journal of alloys and compounds*, 439 (2007) 294-301.
- [77] S. Couillaud, H. Enoki, S. Amira, J.-L. Bobet, E. Akiba, J. Huot, Effect of ball milling and cold rolling on hydrogen storage properties of nanocrystalline TiV_{1.6}Mn_{0.4} alloy, *Journal of Alloys and Compounds*, 484 (2009) 154-158.
- [78] A. Aleksanyan, S. Dolukhanyan, O. Ter-Galstyan, N. Mnatsakanyan, Hydride cycle formation of ternary alloys in TiVMn system and their interaction with hydrogen, *International Journal of Hydrogen Energy*, 41 (2016) 13521-13530.
- [79] T. Huang, Z. Wu, G. Sun, N. Xu, Microstructure and hydrogen storage characteristics of TiMn₂-XVX alloys, *Intermetallics*, 15 (2007) 593-598.

- [80] Y. Nakamura, J. Nakamura, K. Sakaki, K. Asano, E. Akiba, Hydrogenation properties of Ti–V–Mn alloys with a BCC structure containing high and low oxygen concentrations, *Journal of Alloys and Compounds*, 509 (2011) 1841-1847.
- [81] T. Bibienne, M. Tousignant, J.-L. Bobet, J. Huot, Synthesis and hydrogen sorption properties of TiV (2– x) Mn_x BCC alloys, *Journal of Alloys and Compounds*, 624 (2015) 247-250.
- [82] J. Huot, H. Enoki, E. Akiba, Synthesis, phase transformation, and hydrogen storage properties of ball-milled TiV_{0.9}Mn_{1.1}, *Journal of alloys and compounds*, 453 (2008) 203-209.
- [83] J. Huot, E. Akiba, Y. Ishido, Crystal structure of multiphase alloys (Zr, Ti)(Mn, V) ₂, *Journal of alloys and compounds*, 231 (1995) 85-89.
- [84] J. Huot, E. Akiba, H. Iba, Crystal structure and phase composition of alloys Zr_{1– x}Ti_x (Mn_{1– y}V_y) ₂, *Journal of alloys and compounds*, 228 (1995) 181-187.
- [85] C. Gosselin, J. Huot, Hydrogenation Properties of TiFe Doped with Zirconium, *Materials (Basel)*, 8 (2015) 7864-7872.
- [86] S. Amira, S. Santos, J. Huot, Hydrogen sorption properties of Ti–Cr alloys synthesized by ball milling and cold rolling, *Intermetallics*, 18 (2010) 140-144.
- [87] P. Lv, M.N. Guzik, S. Sartori, J. Huot, Effect of ball milling and cryomilling on the microstructure and first hydrogenation properties of TiFe+ 4 wt.% Zr alloy, *Journal of Materials Research and Technology*, 8 (2019) 1828-1834.
- [88] Y. Fukai, *The metal-hydrogen system: basic bulk properties*, Springer Science & Business Media, 2006.
- [89] L. Luo, C. Wu, S. Yang, J. Zhou, Y. Chen, F. Yang, Y. Xu, P. Liu, Decaying behaviors of V₄₀(TiCr)₅₁Fe₈Mn hydrogen storage alloys with different particle sizes, *Journal of Alloys and Compounds*, 645 (2015) S178-S183.

SECTION 2

Publications

Article 1

Journal of Alloys and Compounds 861 (2021) 158615



Contents lists available at ScienceDirect

Journal of Alloys and Compounds

journal homepage: www.elsevier.com/locate/jalcom



Effect of particle size, pressure and temperature on the activation process of hydrogen absorption in TiVZrHfNb high entropy alloy



Salma Sleiman, Jacques Huot*

Hydrogen Research Institute, Université du Québec à Trois-Rivières, 3351 des Forges, Trois-Rivières, QC G9A 5H7, Canada

ARTICLE INFO

Article history:

Received 26 September 2020

Received in revised form 23 December 2020

Accepted 3 January 2021

Available online 5 January 2021

Keywords:

Metal hydrides

First hydrogenation

Kinetics

Arrhenius equation

High Entropy alloys

ABSTRACT

The effect of particle size, pressure and temperature on the first hydrogenation of TiVZrHfNb high entropy alloy were investigated. Three particle size ranges were selected: less than 0.5 mm, between 0.5 mm and 1 mm and between 1 mm and 2 mm. The hydrogen pressure applied during the first hydrogenation was 1 bar, 2 and 20 bars. The temperature of first hydrogenation was varied from 100 °C to 400 °C. It was found that the particle size plays a role in the activation; smaller particle size having faster kinetics. Under 2 bars and 20 bars of hydrogen pressure, the activation curves have the same features. The activation is strongly dependent on the temperature: higher temperature drastically reduces the incubation period. The important parameter for the activation is the temperature rather than the particle size. It was also found that the activation process obeys an Arrhenius relationship. Upon hydrogenation, the BCC phase is transformed to a BCT phase. Also, an amorphous phase seems to be formed. This formation depends on the hydrogenation temperature and particle size.

© 2021 Elsevier B.V. All rights reserved.

1. Introduction

Solid-state storage systems based on metal hydrides are considered as a reasonable solution to store hydrogen safely, in large quantities and under moderate pressure [1–4]. In general, most of the hydride-forming metal alloys exhibit slow and difficult hydrogenation during the first exposure to hydrogen, the so-called activation process [5–9]. Typically, the surface of the metal alloys is coated with oxide layers of different thicknesses depending on the synthesis technique and the nature of the alloy. The oxide layers should be broken to permit the diffusion of gaseous hydrogen into the bare metal. Usually the activation requires high hydrogen pressure and high temperature to compel hydrogen through the oxide layer to reach the fresh metal for direct hydrogen interaction [10]. After the alloy has been activated, hydrogen absorption becomes easier and with faster kinetics. Therefore, activation is an important factor to be taken into account from a practical application point of view. It is well known that nanocrystallinity and small particle size led to a faster first hydrogenation in metal hydrides [11–14]. Huot et al. and Couillaud et al. found that ball milling can be used to improve the hydrogenation properties of Ti-V-Mn alloy [15,16]. Balcerzak reported that the nanocrystalline Ti-V BCC alloys prepared

by mechanically alloying have fast hydrogen sorption and good activation properties [17]. Kamble et al. studied the effect of particle size on the first hydrogenation of BCC alloy 52Ti-12V-36Cr. They observed that the activation time decreases with the reduction of particle size and faster kinetics corresponds to smaller particle sizes [5]. However, nanocrystallinity and decrease of particle size have a negative impact on the hydrogen storage capacity of BCC alloys [16,18].

High entropy alloys (HEAs) were recently proposed as a new class of metal hydrides [19–22]. In general, HEAs which are composed of five or more principal elements in equimolar ratios or varying from 5 to 35 at%, tend to form simple solid solutions with BCC or FCC structures [23–25]. The TiVZrHfNb alloy was reported in one of the first papers in storing hydrogen in HEAs [21]. TiVZrHfNb alloy crystallized in a BCC type structure [26] and its hydrogen storage properties were studied by Sahlberg et al. [21]. They reported that the TiVZrHfNb alloy can absorb hydrogen with a plateau pressure of 0.1 bar H₂ at 299 °C with maximum storage capacity of 2.7 wt%. In their work, the as-cast TiVZrHfNb alloy was ball milled and afterward sieved to obtain powder of size less than 0.05 mm that was used for activation at 400 °C under 20 bar H₂ [21]. As activation behavior could depend on particle size and temperature, we did a systematic study on the effect of particle size and temperature on the activation process of the TiVZrHfNb HEA.

* Corresponding author.

E-mail address: jacques.huot@trh.ca (J. Huot).

2. Experimental details

The raw materials, Ti sponge (99.95%), V pieces (99.7%), Zr sponge (99.5%), Hf sponge (99.6%) and Nb pieces (99.8%) were purchased from Alfa Aesar and used without further purification. The $Ti_{0.2}V_{0.2}Zr_{0.2}Nb_{0.2}Hf_{0.2}$ alloy was prepared by arc melting after mixing all raw elements in the desired proportion. To keep the notation simple, we will use TiVZrNbHf to identify this alloy in the rest of the manuscript. The melting was done under 0.7 bars of argon. Each pellet was melted, turned over, and remelted three times to ensure good homogeneity. The pellet was then hand crushed using a hardened steel mortar and pestle in an argon-filled glovebox. After hand crushing, the powder was sieved using sieves of size 0.5 mm, 1 mm and 2 mm. By sieving, the powder was thus divided into three populations: particles of size less than 0.5 mm, particles between 0.5 mm and 1 mm and particles between 1 mm and 2 mm. The sieving process and the preparation of samples for activation were done under argon atmosphere. Before hydrogenation experiments, the samples were always kept under argon and never exposed to the air. First hydrogenation was performed at different temperatures under 20 bars of hydrogen pressure using a homemade Sievert's apparatus. The hydrogen gas from Praxair was 99.999% pure. For some measurements, the pressure was changed to 1 bar and 2 bars of hydrogen. The crystal structure was determined by X-ray diffraction using a Bruker D8 Focus X-ray diffractometer having a Bragg-Brentano configuration with $Cu\ K\alpha$ ($\lambda_{\alpha} = 1.54\ \text{\AA}$) radiation. All the XRD measurements were done at room temperature. The scanning parameters were step size 0.07° and time per step 10 s. The as-cast diffraction pattern was made on crushed powder of size $< 0.5\ \text{mm}$. Lattice parameters and the weighted profile factor R-factor: R_{wp} were evaluated from Rietveld refinement using Topas software [27]. For each pattern presented, the residue of the Rietveld refinement is given by the curve below the pattern. The degree of crystallinity was estimated from the Topas software by taking into account the broad amorphous peak. As this calculation was not performed with an internal standard, the values obtained for the abundance of each phase should be taken with caution. Microstructure and chemical analysis were performed using a Hitachi Su1510 scanning electron microscopy (SEM) equipped with an EDX (energy-dispersive X-ray) apparatus from Oxford Instruments.

3. Results

3.1. Morphology

Fig. 1 shows backscattered electron micrograph of TiVZrHfNb alloy prepared by arc melting.

The bulk chemical composition was confirmed by EDX measurement to be equal to the nominal values. Dendrites (gray color)

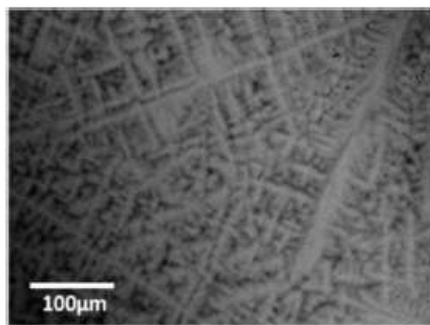


Fig. 1. Backscattered electrons (BSE) micrograph of as-cast TiVZrHfNb alloy with magnification 250 \times .

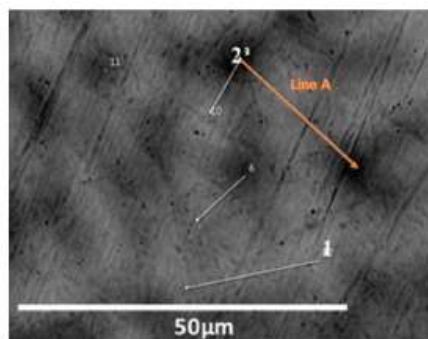


Fig. 2. BSE micrograph of as-cast TiVZrHfNb alloy with magnification 2000 \times .

with some black areas are clearly observed. Close inspection of Fig. 1 shows that the main branch makes 90° with other branches which is an indication of a cubic structure.

Using EDX at a higher magnification, the chemical compositions in the gray and dark areas were determined. The EDX analysis was performed on the selected points presented in Fig. 2.

The quantitative analysis at points 1 (gray area) and 2 (dark area) is listed in Table 1.

From this table we see that the chemical compositions of points 1 and 2 are quite close. Also, there is no clear-cut boundary between the darker and lighter shades of gray. This indicates that there is probably a variation of composition. To confirm this, the chemical analysis over the lines indicated in Fig. 2 was performed. As a representative, the analysis over line A of Fig. 2 is shown in Fig. 3.

Fig. 3 indicates that the amounts of Ti and Nb are almost constant over the line. The amount of Hf increases in the gray region when compared to the dark region while Zr and V decrease with the same rate. Thus, there is clearly a continuous variation of composition, but it is not random. It should also be mentioned that even if the line analysis does not show a variation in the Nb proportion, the point analysis reported in Table 1 indicates a slight increase between the dark and gray areas.

It is interesting to note that the two elements which have a constant or slight variation of abundance have very close atomic radii (144.8 pm for Ti and 142 pm for Nb). However, the two elements that have identical decrease of abundance, Zr and V are respectively the biggest atomic radius (160 pm for Zr) and the smallest one (132.1 pm for V). In the case of Hf which abundance increases by going from the dark to the gray areas, its atomic radius is 156.4 pm. These observations indicate that the atomic radii most probably play a role in the variation of composition. However other factors are certainly playing a role. Because of the variation of composition, it should be pointed out that the abundances given by EDS are only an indication. From point to point, the proportion could change as seen in Fig. 3.

3.2. Crystal structure

Fig. 4 presents the XRD patterns of the as-cast TiVZrHfNb alloy. The crystal structure parameters as evaluated by Rietveld's refinement are shown in Table 2.

Table 1

EDX analysis showing the elemental composition of TiVZrHfNb alloy. Error on each value is 0.1 at%.

Element (at%)	Ti	V	Zr	Hf	Nb
Point 1	20.0	19.1	18.7	22.5	19.7
Point 2	20.4	22.6	21.0	18.1	17.9

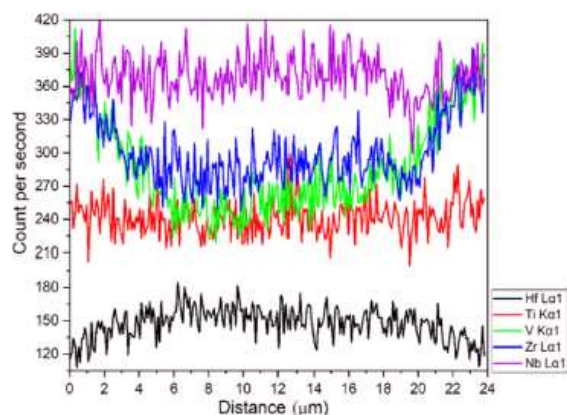


Fig. 3. Line analysis of line A of Fig. 2.

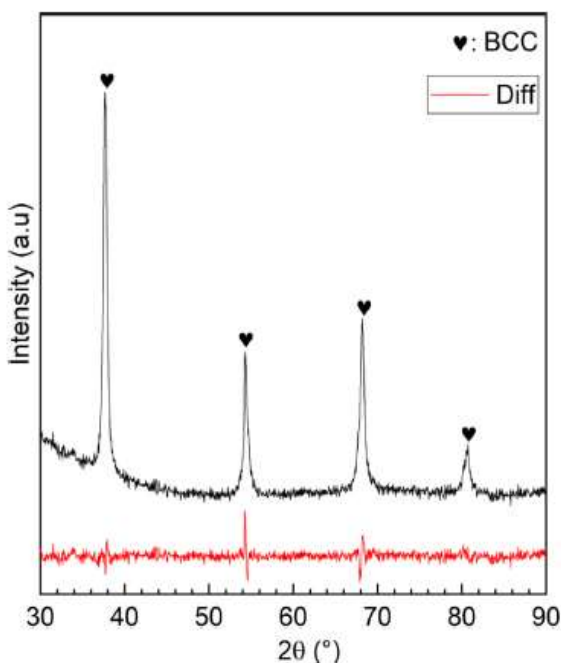


Fig. 4. XRD patterns of the as-cast TiVZrHfNb alloy.

The diffraction pattern indicates that the alloy is single phase BCC (space group $Im-3m$). However, as the SEM investigation showed a variation in chemical composition, we could conclude that this BCC phase has a range of chemical composition. The lattice parameter of TiVZrHfNb alloy reported in Table 2 is in good agreement with the previous study of Sahlberg et al. (lattice parameter 3.3659 Å) [21]. The microstrain value suggests that the lattice of TiVZrHfNb alloy is slightly strained. This may be due to the inhomogeneous chemical composition which in turn gives rise to a variation of lattice parameters within the phase thus creating microstrains. Therefore, the microstrain parameter effectively reflects the composition change within the phase. The same phenomenon was seen by Khajavi et al. for AB_2 system [28].

Table 2

Crystal structure parameters of the as-cast TiVZrHfNb alloy. Error on the last significant digit is indicated in parentheses.

Phase	Cell Volume (Å ³)	Lattice Parameter (Å)	Crystallite Size (nm)	Microstrain %	R _{wp}
BCC	38.14 (2)	3.3663 (4)	14.3 (3)	0.08 (1)	4.67

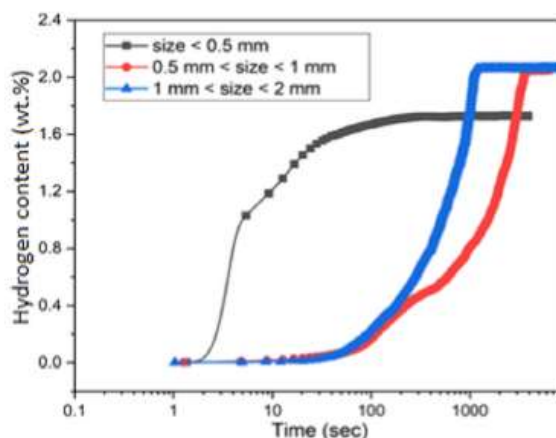


Fig. 5. Activation curves at 300 °C of TiVZrHfNb alloy for different particle size.

3.3. First hydrogenation (activation)

3.3.1. Effect of particle size on activation behavior

The activation curves of powder with different particle size done at 300 °C and under 20 bars of hydrogen pressure are shown in Fig. 5.

The fastest activation is for the smallest particle size (< 0.5 mm). Surprisingly, the kinetics of particles between 0.5 mm and 1 mm is slower than that of size between 1 mm and 2 mm. But both samples absorb hydrogen to a maximum capacity of 2.1 wt% (1.94 H/M) where the small particle size has 1.7 wt% (1.57 H/M) capacity. In the remaining of this paper 'maximum capacity' or 'full capacity' means the highest capacity reached by the particular sample.

Although bigger particles have a slightly faster kinetics than the intermediate size one, we could still conclude that the activation depends on the particle size. This result agrees with a previous work investigated by Kamble et al. on the BCC TiVCr system [5].

To see the impact of particle size on the crystal structure of the hydride phase, the XRD patterns were taken after reaching full hydrogenation. At the end of the absorption experiment, the sample was kept under hydrogen pressure while the temperature decreased. Sahlberg et al. have shown that under vacuum no desorption occurred at temperatures below 200 °C [21]. Therefore, this procedure effectively 'quenched' the hydride phase. Fig. 6 presents the XRD patterns of the hydride samples with different particle size.

Fig. 6 shows the X-ray diffraction patterns after first exposure to hydrogen. Both FCC and BCT structures were used for refinement but, for all patterns, the BCT structure was giving a better fit. A justification is presented in the supplementary file. In Table 3, there are the results of Rietveld's refinement of all these patterns.

All the hydrogenated sizes have the BCT structure with almost same lattice parameters. However, the crystallite size decreases with decreasing particle size. This may be explained by the higher specific surface of the small particles. Also, as the small particles were produced by mechanical deformation, the fact that these particles broke down from the main ingot means that the defect density on their surface is higher than the big particles. The defects act as nucleation points for the hydride phase and more defects means that the crystallite size will be smaller.

It is well known that BCT is the monohydride structure of BCC alloys where FCC is usually the crystal structure adopted by a fully

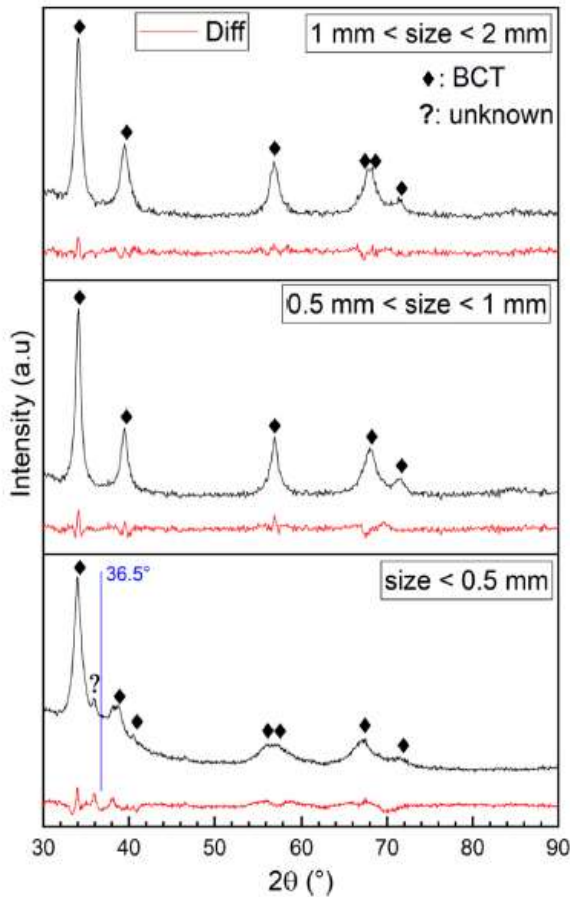


Fig. 6. XRD patterns of different particle sizes hydrogenated at 300 °C under 20 bars.

hydrided BCC alloy [29]. However, for the HEA TiVZrHfNb, Sahlberg et al. have shown that the dihydride has the BCT structure [21]. They explained the high hydrogen abundance of the BCT structure by strain in the distorted HEA lattice. This high strain enabled the occupation of both tetrahedral and octahedral sites. In situ synchrotron X-ray diffraction at temperature up to 600 °C and pressure 100 bars was performed by Karlsson et al. [30]. They confirmed the BCT structure and mentioned that the room temperature data could be fitted by BCT or FCC structures. From neutron diffraction, Karlsson et al. also confirmed the occupation of both the tetrahedral and octahedral interstitial sites in the BCT structure at 500 °C and 100 bars. The present results are in agreement with the conclusions of Sahlberg et al. and Karlsson et al. [21,30]. It should be noted that the microstrain in the BCT phase is much higher than the microstrain of the as-cast BCC phase reported in Table 1.

For the pattern of powder less than 0.5 mm, we found a broad peak centered at 36.5°. We attributed this peak to the presence of an amorphous phase. The center of this amorphous peak is indicated by

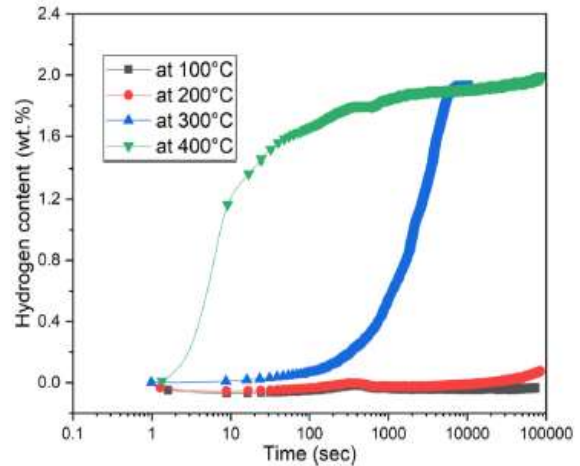


Fig. 7. Activation curves of as-crushed TiVZrHfNb alloy at 100 °C, 200 °C, 300 °C and 400 °C under 20 bars.

a line in Fig. 6. From Rietveld refinement, the abundance of that phase was determined to be 23 wt%. This may explain the lower hydrogen capacity of this sample indicated in Fig. 5. Actually, the capacity ratio of 1.7 wt%/2.1 wt% is equal to 81% which is very close to the 77% crystallinity (BCT phase) seen in the diffraction pattern. The reason for the appearance of this amorphous phase will be discussed in the next section.

3.3.2. Effect of temperature on activation behavior

To study the effect of temperature, two types of samples were used, first one is as-crushed alloy without sieving and the second one is the sieved powder to particles smaller than 0.5 mm. Fig. 7 shows the activation curves of the crushed sample at different temperatures and under 20 bars of hydrogen pressure. The reproducibility of these measurements is shown in the supplementary file.

The sample didn't absorb hydrogen at 100 °C and 200 °C even after 24 h of hydrogen exposure. At 300 °C, after an incubation period of 500 s the sample reached a maximum capacity of 1.9 wt% (1.75 H/M) within 100 min. The activation kinetics was even faster at 400 °C, reaching 1.9 wt% capacity after 33 min without incubation period. It is clear that the activation of TiVZrHfNb alloy strongly depends on temperature.

Fig. 8 shows the XRD patterns of the as-crushed sample hydrogenated at 300 °C and 400 °C under 20 bars and quenched. Table 4 presents their crystal parameters as determined by Rietveld's refinement.

The crystal structure of all the patterns in the hydrided state has BCT crystal structure. This is another indication that, for this alloy, the fully hydride sample could have the BCT structure. We see a large difference in the crystallite size at 300 °C and 400 °C. Also, the microstrain is absent in the 400 °C pattern. Moreover, there seems to be a small amorphous peak at 36.5° which is the exact position of the amorphous peak seen in the pattern of small particles shown in

Table 3

Crystal structure parameters of the BCT phase for different particle sizes hydrogenated at 300 °C under 20 bars. Error on the last significant digit is indicated in parentheses.

Sample particle size	Cell Volume (\AA^3)	Lattice parameter (\AA)	Crystallite size (nm)	Micro strain (%)	Phase (%)	R_{wp}	Amorphous
Less than 0.5 mm	48.60 (7)	$a = 3.301$ (2) $c = 4.460$ (4)	5.9 (2)	0.41 (2)	77	3.95	23%
Between 0.5 and 1 mm	48.38 (4)	$a = 3.260$ (1) $c = 4.551$ (3)	10.6 (5)	0.31 (2)	100	5.06	–
Between 1 and 2 mm	48.50 (5)	$a = 3.264$ (1) $c = 4.552$ (3)	11.2 (6)	0.41 (2)	100	4.86	–

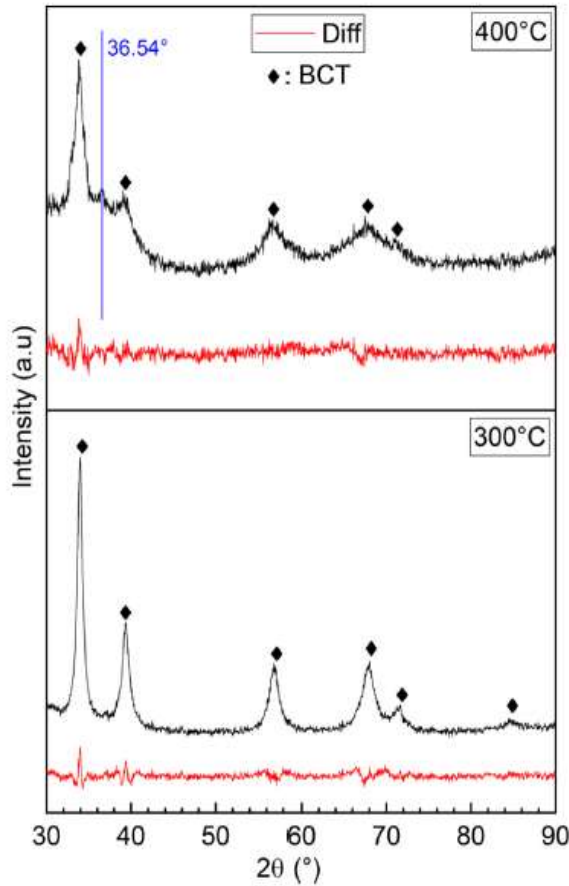


Fig. 8. XRD patterns of as-crushed TiVZrHfNb alloy hydrogenated at 300 °C and 400 °C under 20 bars.

Fig. 6. Taking into account this amorphous peak, the crystallinity of the 400 °C pattern was estimated to be 92%.

A similar investigation was performed on small particles (size less than 0.5 mm). Fig. 9 presents the activation curves at 200 °C, 225 °C, 250 °C, 275 °C and 300 °C under 20 bars of hydrogen pressure.

The differences between the curves are their shape and incubation period. At 200 °C, the activation curve shows a long incubation period (27 h) before starting to absorb hydrogen. However, once started, the hydrogenation is relatively fast, reaching 2.2 wt% (2.0 H/M) capacity. Increasing the temperature to 225 °C reduces drastically the incubation period. At 250 °C, the full capacity is reached after 5 h. At 300 °C, the kinetics is even faster, and the full hydrogenation is reached after only 5 min. Such a variation of incubation period with temperature may suggest an Arrhenius-type mechanism. To verify this, we plotted on Fig. 10 the incubation period as a function of $1000/T$. The procedure to determine the incubation period is explained in the [supplementary file](#).

Table 4

Crystal structure parameters of the BCT phase for as-crushed TiVZrHfNb alloy hydrogenated at 300 °C and 400 °C under 20 bars. Error on the last significant digit is indicated in parentheses.

Temperature (°C)	Cell Volume (Å ³)	Lattice parameter (Å)	Crystallite size (nm)	Microstrain (%)	R_{wp}	Amorphous
300	48.23 (3)	$a = 3.257$ (8) $c = 4.546$ (2)	9.2 (2)	0.29 (1)	4.80	–
400	48.66 (9)	$a = 3.287$ (2) $c = 4.505$ (5)	3.05 (7)	–	5.37	8%

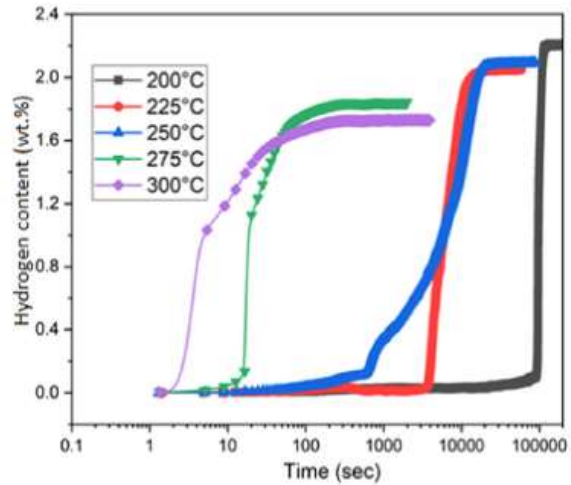


Fig. 9. Activation curves at 200 °C, 225 °C, 250 °C, 275 °C and 300 °C of particle size less than 0.5 mm.

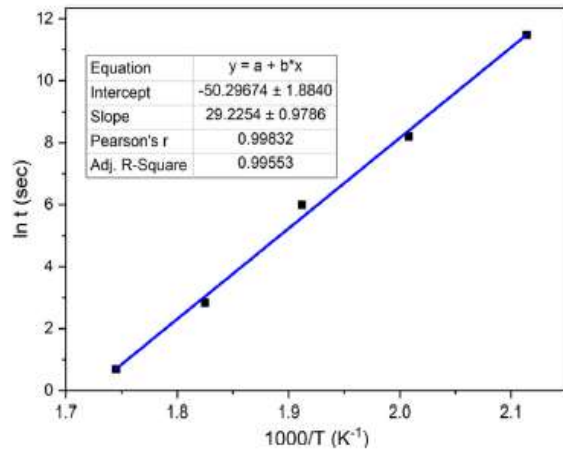


Fig. 10. Graph of $\ln t$ as function of $1000/T$ where t is the incubation period and T the temperature.

Fig. 10 presents the variation of $\ln t$ (incubation period) as function of the inverse of temperature. It is seen that the experimental points follow a linear relationship between $1/T$ and $\ln t$.

Fig. 10 confirms that the incubation period follows an Arrhenius law. Arrhenius equation is expressed by:

$$\ln K = \ln A - \frac{E_A}{RT} \quad (1)$$

Where K is the rate coefficient, A is the frequency factor, R is the gas constant 8.314 J/(mol K), E_A is the activation energy in J/mol and T is the temperature (Kelvin). At the end of the incubation period the reaction is complete, and we should have:

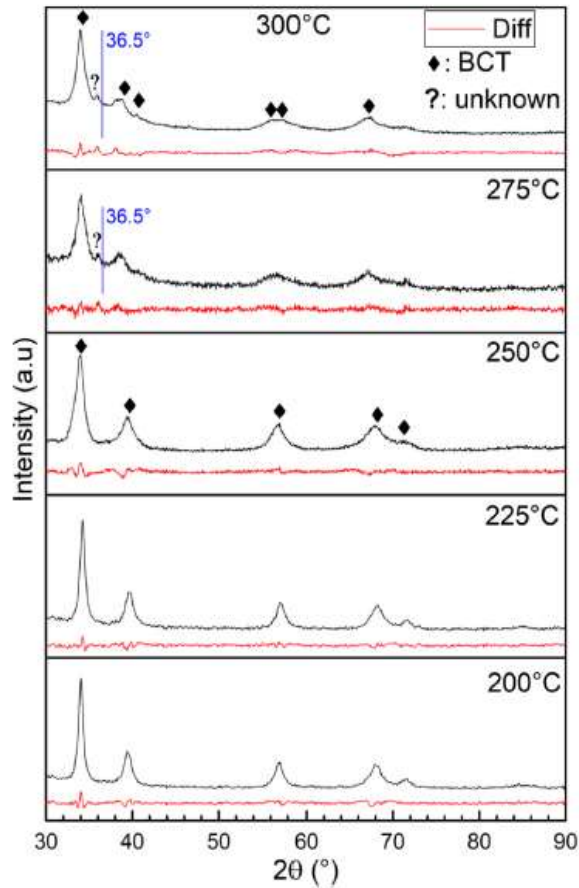


Fig. 11. XRD patterns of particles of size less than 0.5 mm hydrogenated at 200 °C, 225 °C, 250 °C, 275 °C and 300 °C.

$$Kt = 1, \quad (2)$$

Thus, for the onset point (period when the incubation is complete) we have:

$$- \ln t = \ln K \quad (3)$$

From the fitted values of Fig. 10, we get $E_A = 241 \pm 8$ kJ/mol H_2 .

To our knowledge, this is the first time an Arrhenius mechanism is proved for incubation period of the first hydrogenation of a metal hydride. A closely related example is the amorphous phase transformation in bulk metallic glasses that also obeys Arrhenius equation. The activation energies found in these cases range from 200 kJ/

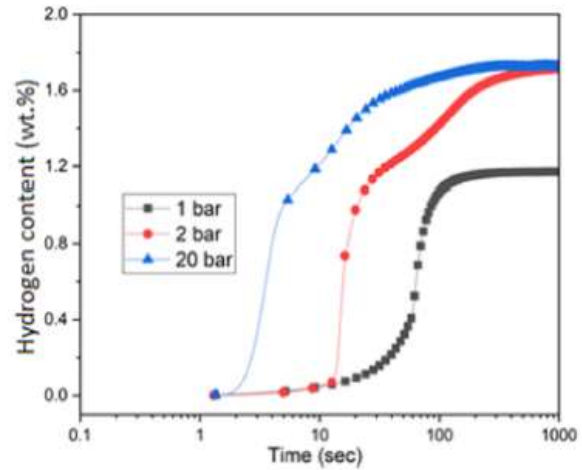


Fig. 12. Activation curves at 300 °C under 1, 2 and 20 bars of hydrogen of particles of size less than 0.5 mm.

mol to 453 kJ/mol which is the same order of magnitude of the present result [31–33].

Fig. 11 presents the XRD patterns of the small particles (size less than 0.5 mm) upon hydrogenation at different temperatures under 20 bars of hydrogen pressure. Their corresponding crystal parameters are reported in Table 5.

It is clear that the crystal structure doesn't depend on the temperature, the hydride phase is BCT for all temperatures. All the patterns correspond to activation at 200, 225 and 250 °C have BCT crystal structure with almost same crystal parameters except for the crystallite size which decreases with increasing temperature. An amorphous phase is present in the 275 °C and 300 °C patterns. There is also a small unidentified peak at around 36°. As no reduction of capacity and absence of amorphous phase was seen for particles bigger than 0.5 mm, it seems that both particle size and temperature are factors for the appearance of amorphous phase upon hydrogenation. We saw that small particle size produces small crystallite size. At higher temperatures, the kinetic is faster and the material may not have time to mechanically adjust to the new phase and break. A smaller crystallite size means a higher proportion of grain boundaries. The grain boundary is amorphous and probably does not absorb hydrogen. Thus, the hydrogen capacity will reduce with crystallite size and thus be dependent on the particle size and hydrogenation temperature. This could also explain the features of Fig. 8 where the amorphous content was seen only 8 wt% for the 400 °C sample. The as-crushed sample is made of particles of all sizes. Only the smaller ones will partially transform to an amorphous phase and thus the amorphous proportion is lower than for a sample exclusively made of small particles.

Table 5

Crystal structure parameters of the BCT phase for particles of size less than 0.5 mm hydrogenated at different temperatures. Error on the last significant digit is indicated in parentheses.

Temperature (°C)	Cell Volume (Å ³)	Lattice parameter (Å)	Crystallite size (nm)	Microstrain (%)	R_{wp}	Amorphous
200	48.05 (3)	a= 3.253 (1) c= 4.541 (2)	13.5 (6)	0.29 (1)	4.85	–
225	48.23 (4)	a= 3.258 (1) c= 4.545 (2)	13.9 (7)	0.33 (1)	4.90	–
250	48.15 (5)	a= 3.261 (3) c= 4.527 (3)	6.9 (2)	0.51 (1)	4.56	–
275	49.2 (1)	a= 3.314 (3) c= 4.478 (6)	6.3 (5)	0.51 (3)	4.01	8%
300	48.60 (7)	a= 3.301 (2) c= 4.460 (5)	5.9 (2)	0.41 (2)	3.95	23%

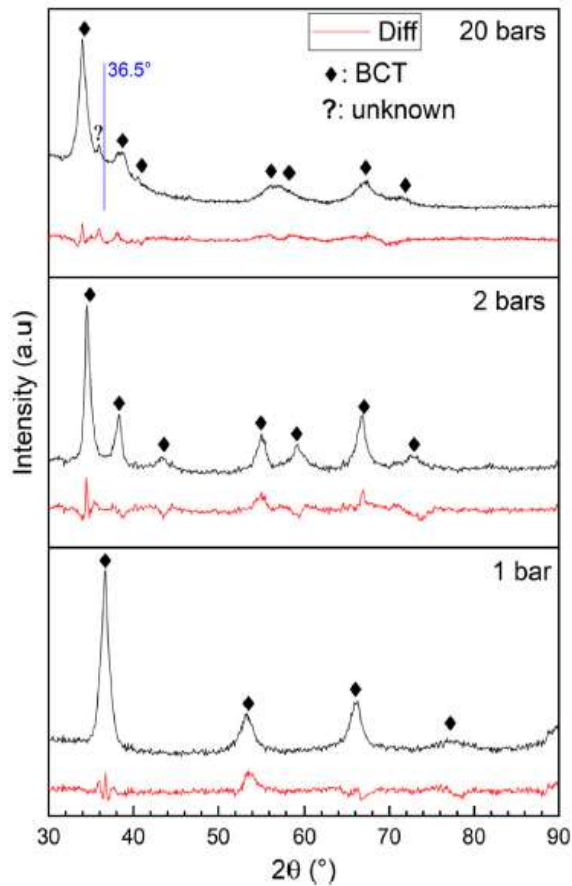


Fig. 13. XRD patterns of size less than 0.5 mm hydrogenated at 300 °C under 1, 2 and 20 bars of hydrogen.

3.3.3. Effect of pressure on first hydrogenation

To study the impact of pressure in the crystal structure after hydrogen absorption, we did the activation of the small particles (less than 0.5 mm) under 1, 2, and 20 bars of hydrogen pressure at 300 °C. The activation curves are shown in Fig. 12.

We see that activation under 1 bar gives a capacity around 1.2 wt% (1.1 H/M) of hydrogen with 50 s of incubation period. As the pressure increases, the incubation period decreases. The curves of 2 and 20 bars clearly show a two-step mechanism. The first step ends at about 1.2 wt% (1.1 H/M) and corresponds to the final capacity of the 1 bar curve.

The XRD patterns of the three samples after full hydrogenation are presented in Fig. 13. The patterns of the 20 bars and 2 bars show a BCT structure. The pattern for the sample activated under 1 bar seems to be different than the other two samples. It looks more like a BCC phase than a BCT, so we tried to fit a BCC but the BCT gave a

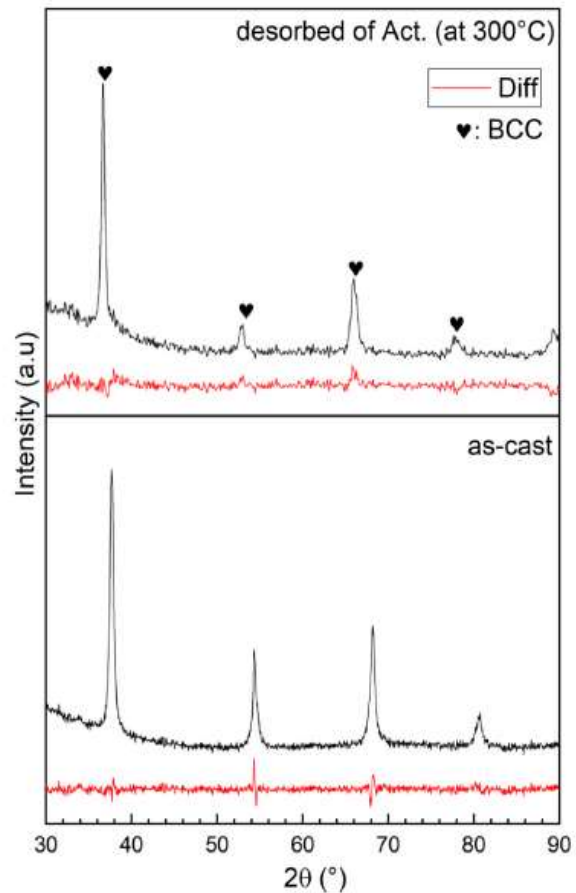


Fig. 14. XRD patterns of particles of size less than 0.5 mm dehydrided at 350 °C under vacuum as compared to the as-cast alloy.

better fit. The unit cell parameters for each hydride BCT phase are presented in Table 6. It should be noted that the a parameter of the BCT phase decreases with the hydrogenation pressure while the c parameter increases. For the 1 bar hydrogenation the a and c parameters are quite close. This means that maybe a BCC phase could also fit this pattern. We therefore fitted the pattern using a BCC and compared it to the BCT fit. The R_{wp} of the BCC and BCT are respectively 6.469 and 6.632. the lattice parameter of the BCC phase is 3.463 Å, a value that is intermediate between the a and c parameters of the BCT phase. The unit cell volume of the BCC phase is 41.54 \AA^3 , again very close to the BCT value of 41.61 \AA^3 . Therefore, we think this structure is maybe at the 'transition, between a BCT and a BCC. In this discussion we will assume a BCT phase but it should be mention that a BCC phase also fit this pattern.

We see that, for the 1 bar pattern, the a and c lattice parameters are very close ($c/a = 1.020$). The volume of the unit cell is 41.61 \AA^3

Table 6

Crystal structure parameters of the BCT phase of the particles of size less than 0.5 mm hydrogenated at 300 °C under 1, 2 and 20 bars of hydrogen. Error on the last significant digit is indicated in parentheses.

Pressure	Cell Volume (\AA^3)	Lattice parameter (\AA)	Crystallite size (nm)	Microstrain (%)	Rwp	Amorphous
1 bar	41.61 (8)	$a = 3.442$ (2) $c = 3.512$ (3)	8.3 (5)	0.38 (3)	4.23	–
2 bars	47.01 (6)	$a = 3.349$ (2) $c = 4.191$ (3)	8.5 (5)	0.27 (2)	4.54	–
20 bars	48.60 (7)	$a = 3.301$ (2) $c = 4.460$ (5)	5.9 (2)	0.41 (2)	3.95	23%

Table 7

Crystal structure parameters of particles of size less than 0.5 mm dehydrogenated at 350 °C under vacuum as compared to the as-cast alloy. Error on the last significant digit is indicated in parentheses.

	Cell Volume (\AA^3)	Lattice parameter (\AA)	Crystallite size (nm)	Microstrain (%)	R_{wp}
As-cast	38.14 (2)	3.36	14.3 (3)	0.08 (1)	4.67
Desorption of activated at 300 °C	41.82 (3)	3.3663 (4) 2 (1) 3.4711 (7)	12 (1)	0.14 (2)	5.56

which gives a volume expansion of the lattice compared to the as-cast BCC of 3.47\AA^3 . Taking into account that the volume taken by a hydrogen atom is between 2 and 3\AA^3 , we could estimate the amount of hydrogen in the BCT hydride phase. The amount of hydrogen is between 0.6 wt% and 0.9 wt% which is smaller than the measured capacity in Fig. 12. For the 2 bars sample, the volume expansion of the BCT phase is 8.87\AA^3 that is transformed to a capacity between 1.6 wt% and 2.4 wt% (1.47–2.2 H/M) which agrees with the measured capacity (1.7 wt% or 1.57 H/M) shown in Fig. 12. A higher volume expansion is obtained under 20 bars. That translates to a capacity between 1.95 wt% (1.8 H/M) to 2.9 wt% (2.7 H/M). But as the pattern shows a degree of crystallinity of 77% then the capacity should be between 1.5 wt% (1.38 H/M) and 2.2 wt% (2.0 H/M) which is in the range of the measured value.

3.3.4. Study of stability of the hydride phase

The hydrogenated sample of particles of size less than 0.5 mm and activated under 20 bars of hydrogen pressure 300 °C were used to investigate the stability of the BCT hydride phase. After reaching full hydrogenation, the sample was subjected to vacuum for two hours at 300 °C. XRD measurements (not shown) confirmed that no desorption occurred. To achieve desorption, the temperature had to be raised to 350 °C and the sample kept under dynamic vacuum for two hours. In Fig. 14, the XRD pattern of the dehydrogenated sample is shown and compared to the as-cast alloy.

It is clear that the hydride BCT phase reverted to BCC upon dehydrogenation at 350 °C under vacuum. To check if there is still hydrogen in the retained BCC phase, the Rietveld refinement was done, and the results are reported in Table 7.

We see that the volume of the BCC phase is slightly larger after dehydrogenation as compared to the as-cast state. This may indicate a small amount of hydrogen is still in solid solution in the BCC phase. Again, assuming a volume of hydrogen atom between 2 and 3\AA^3 , the amount of hydrogen in solid solution is estimated to be between 0.63 and 0.96 hydrogen per metallic atom (H/M) which translate to a capacity between 0.7 wt% and 1.0 wt%. The fact that this alloy retains hydrogen even after heating under dynamic vacuum at 350 °C could be explained by the very high stability of the binary hydrides of the raw elements. Amongst all these elements, vanadium has the highest plateau pressure in the range $0 < \text{H/M} < 1$ of about 10 kPa. The plateau pressure of the other pure elements ranges from 1 kPa down to a fraction of one Pascal [34]. Considering that the vacuum level in our Sieverts apparatus is of the order of a few kPa, it is reasonable to assume that the alloy is not totally dehydrogenated. Recently, a similar result was obtained, showing that hydrogen is trapped in a stable sites after desorption [35].

4. Conclusion

The effects of particle size, pressure and temperature on the first hydrogenation of TiVZrHfNb high entropy alloy were investigated. It was found that particles smaller than 0.5 mm of diameter activate quickly but, for bigger particle size the dependence of activation time on particle size is not clear. Upon hydrogenation the BCC structure is transformed to BCT irrespective of particle size, temperature and pressure. The temperature dependence of activation

time and more particularly the incubation period is much clearer. It was found that the incubation period follows an Arrhenius relation, with $E_A = 241 \pm 8 \text{ kJ/mol H}_2$. We observed that, upon hydrogenation, an amorphous phase could be formed. This formation seems to depend on the hydrogenation temperature and particle size. Small particles get amorphized at lower temperature. However, more experimental evidences are needed to confirm this hypothesis. For example TEM and high resolution synchrotron may help to confirm the presence of an amorphous phase.

CRedit authorship contribution statement

Salma Sleiman: Investigation, formal analysis, writing-original draft. **Jacques Huot:** Conceptualization, Validation, formal analysis, writing review & Editing.

Declaration of Competing Interest

The authors declare no conflict of interest.

Acknowledgments

We would like to thank A. Lejeune for electron microscopy experiments. This investigation was supported in part by a discovery grant from the Natural Sciences and Engineering Research Council of Canada.

Author contributions

All experiments, except electron microscopy, were performed by S. Sleiman under the supervision of J. Huot.

Appendix A. Supporting information

Supplementary data associated with this article can be found in the online version at doi:10.1016/j.jallcom.2021.158615.

References

- [1] R. Prabhukhot Prachi, M. Wagh Mahesh, A review on solid state hydrogen storage material, *Adv. Energy Power* 4 (2016) 11–22.
- [2] N.A.A. Rusman, M. Dahari, A review on the current progress of metal hydrides material for solid-state hydrogen storage applications, *Int. J. Hydrog. Energy* 41 (2016) 12108–12126.
- [3] B. Sakintuna, F. Lamari-Darkrim, M. Hirscher, Metal hydride materials for solid hydrogen storage: a review, *Int. J. Hydrog. Energy* 32 (2007) 1121–1140.
- [4] A. Züttel, A. Remhof, A. Borgschulte, O. Friedrichs, Hydrogen: the future energy carrier, *Philos. Trans. R. Soc. Lond. A Math. Phys. Eng. Sci.* 368 (2010) 3329–3342.
- [5] A. Kamble, P. Sharma, J. Huot, Effect of doping and particle size on hydrogen absorption properties of BCC solid solution $52\text{Ti}-^{12}\text{V}-^{36}\text{Cr}$, *Int. J. Hydrog. Energy* 42 (2017) 11523–11527.
- [6] D. Khan, J. Zou, M. Pan, Z. Ma, W. Zhu, T. Huang, X. Zeng, W. Ding, Hydrogen storage properties of nanostructured $2\text{MgH}_2\text{Co}$ powders: the effect of high-pressure compression, *Int. J. Hydrog. Energy* 44 (2019) 15146–15158.
- [7] P. Lv, J. Huot, Hydrogenation improvement of TiFe by adding ZrMn₂, *Energy* 138 (2017) 375–382.
- [8] S. Sleiman, J. Huot, Microstructure and hydrogen storage properties of Ti1V0.9Cr1.1 Alloy with Addition of x wt%Zr (x = 0, 2, 4, 8, and 12), *Inorganics* 5 (2017) 86.

- [9] C. Zhang, Y. Wu, L. You, X. Cao, Z. Lu, X. Song, Investigation on the activation mechanism of hydrogen absorption in TiZrNbTa high entropy alloy, *J. Alloy. Compd.* 781 (2019) 613–620.
- [10] J. Huot, Kinetics and Thermodynamics, in: A. Léon (Ed.), *Hydrogen Technology: Mobile and Portable Applications*, Springer Berlin Heidelberg, Berlin, Heidelberg, 2008, pp. 471–500.
- [11] A. Schneemann, J.L. White, S. Kang, S. Jeong, L.F. Wan, E.S. Cho, T.W. Heo, D. Prendergast, J.J. Urban, B.C. Wood, M.D. Allendorf, V. Stavila, Nanostructured metal hydrides for hydrogen storage, *Chem. Rev.* 118 (2018) 10775–10839.
- [12] X. Yu, Z. Tang, D. Sun, L. Ouyang, M. Zhu, Recent advances and remaining challenges of nanostructured materials for hydrogen storage applications, *Prog. Mater. Sci.* 88 (2017) 1–48.
- [13] J. Zhang, Y. Zhu, H. Lin, Y. Liu, Y. Zhang, S. Li, Z. Ma, L. Li, Metal hydride nanoparticles with ultrahigh structural stability and hydrogen storage activity derived from microencapsulated nanoconfinement, *Adv. Mater.* 29 (2017) 1700760.
- [14] M. Balcerzak, Hydrogenation properties of nanocrystalline TiVMn body-centered-cubic alloys, *Int. J. Hydrog. Energy* (2019).
- [15] S. Couillaud, H. Enoki, S. Amira, J.-L. Bobet, E. Akiba, J. Huot, Effect of ball milling and cold rolling on hydrogen storage properties of nanocrystalline TiV1.6Mn0.4 alloy, *J. Alloy. Compd.* 484 (2009) 154–158.
- [16] J. Huot, H. Enoki, E. Akiba, Synthesis, phase transformation, and hydrogen storage properties of ball-milled TiV0.9Mn1.1, *J. Alloy. Compd.* 453 (2008) 203–209.
- [17] M. Balcerzak, Structure and hydrogen storage properties of mechanically alloyed Ti-V alloys, *Int. J. Hydrog. Energy* 42 (2017) 23698–23707.
- [18] B.K. Singh, G. Shim, S.-W. Cho, Effects of mechanical milling on hydrogen storage properties of Ti0.32Cr0.43V0.25 alloy, *Int. J. Hydrog. Energy* 32 (2007) 4961–4965.
- [19] J. Hu, H. Shen, M. Jiang, H. Gong, H. Xiao, Z. Liu, G. Sun, X. Zu, A DFT study of hydrogen storage in high-entropy alloy TiZrHfScMo, *Nanomaterials* 9 (2019) 461.
- [20] I. Kuncce, M. Polanski, J. Bystrzycki, Structure and hydrogen storage properties of a high entropy ZrTiVCrFeNi alloy synthesized using Laser Engineered Net Shaping (LENS), *Int. J. Hydrog. Energy* 38 (2013) 12180–12189.
- [21] M. Sahlberg, D. Karlsson, C. Zlotea, U. Jansson, Superior hydrogen storage in high entropy alloys, *Sci. Rep.* 6 (2016) 36770.
- [22] C. Zlotea, M.A. Sow, G. Ek, J.P. Couzinié, L. Perrière, I. Guillot, J. Bourgon, K.T. Møller, T.R. Jensen, E. Akiba, M. Sahlberg, Hydrogen sorption in TiZrNbHTa high entropy alloy, *J. Alloy. Compd.* 775 (2019) 667–674.
- [23] D.B. Miracle, O.N. Senkov, A critical review of high entropy alloys and related concepts, *Acta Mater.* 122 (2017) 448–511.
- [24] O.N. Senkov, D.B. Miracle, K.J. Chaput, J.-P. Couzinié, Development and exploration of refractory high entropy alloys—A review, *J. Mater. Res.* 33 (2018) 3092–3128.
- [25] W. Zhang, P.K. Liaw, Y. Zhang, Science and technology in high-entropy alloys, *Sci. China Mater.* 61 (2018) 2–22.
- [26] E. Fazakas, V. Zadorozhnyy, L. Varga, A. Inoue, D. Louzguine-Luzgin, F. Tian, L. Vitos, Experimental and theoretical study of Ti20Zr20Hf20Nb20×20 (X= V or Cr) refractory high-entropy alloys, *Int. J. Refract. Metal Hard Mater.* 47 (2014) 131–138.
- [27] A. Bruker, *Topas V3: general profile and structure analysis software for powder diffraction data—user's manual*; Bruker AXS, Karlsruhe; Coelho AA (2007) TOPAS academic, Coelho Software, Brisbane, in, 2005.
- [28] S. Khajavi, M. Rajabi, J. Huot, Crystal structure of as-cast and heat-treated Ti0.5Zr0.5(Mn1-xFex)Cr1, x= 0, 0.2, 0.4, *J. Alloy. Compd.* 767 (2018) 432–438.
- [29] Y. Nakamura, E. Akiba, Hydriding properties and crystal structure of NaCl-type mono-hydrides formed from Ti–V–Mn BCC solid solutions, *J. Alloy. Compd.* 345 (2002) 175–182.
- [30] D. Karlsson, G. Ek, J. Cedervall, C. Zlotea, K.T. Møller, T.C. Hansen, J. Bednarcik, M. Paskevicius, M.H. Sørby, T.R. Jensen, Structure and hydrogenation properties of a HfNbTiVZr high-entropy alloy, *Inorg. Chem.* 57 (2018) 2103–2110.
- [31] Q. Cao, J. Li, P. Zhang, A. Horswell, J. Jiang, Y. Zhou, Second amorphous-to-crystalline phase transformation in Cu60Ti20Zr20 bulk metallic glass, *J. Phys. Condens. Matter* 19 (2007) 246206.
- [32] D. Ouyang, N. Li, L. Liu, Structural heterogeneity in 3D printed Zr-based bulk metallic glass by selective laser melting, *J. Alloy. Compd.* 740 (2018) 603–609.
- [33] M. Qi, H. Fecht, On the thermodynamics and kinetics of crystallization of a Zr–Al–Ni–Cu-based bulk amorphous alloy, *Mater. Charact.* 47 (2001) 215–218.
- [34] E. Zuzek, J. Abriata, A. San-Martin, F. Manchester, H-Zr(hydrogen-zirconium), Phase Diagrams of Binary Hydrogen Alloys, ASM International, Member/ Customer Service Center, Materials Park, OH 44073-0002, USA, 2000, pp. 309–322.
- [35] M.M. Nygård, W.A. Sławiński, G. Ek, M.H. Sørby, M. Sahlberg, D.A. Keen, B.C. Hauback, Local order in high-entropy alloys and associated deuterides – a total scattering and Reverse Monte Carlo study, *Acta Mater.* 199 (2020) 504–513.

Article

Microstructure and First Hydrogenation Properties of TiHfZrNb_{1-x}V_{1+x} Alloy for x = 0, 0.1, 0.2, 0.4, 0.6 and 1

Salma Sleiman and Jacques Huot *

Hydrogen Research Institute, Université du Québec à Trois-Rivières, 3351 des Forges, Trois-Rivières, QC G9A 5H7, Canada; salma.sleiman@irh.ca

* Correspondence: jacques.huot@uqtr.ca; Tel.: +1-819-376-5011 (ext. 3576)

Abstract: The effect of the substitution of Nb by V on the microstructure and hydrogen storage properties of TiHfZrNb_{1-x}V_{1+x} alloys (x = 0.1, 0.2, 0.4, 0.6 and 1) was investigated. For x = 0, the alloy was pure BCC and upon the substitution of niobium by vanadium, the BCC was progressively replaced by HCP and FCC phases. For x = 0.6, a C15 phase was also present and becomes the main phase for x = 1. The substitution greatly enhanced the first hydrogenation and makes it possible at room temperature under 20 bars of hydrogen. The capacity of all substituted alloys was around 2 wt.%.

Keywords: metal hydrides; high entropy alloys; BCC; V substitution; kinetics

Citation: Sleiman, S.; Huot, J. Microstructure and First Hydrogenation Properties of TiHfZrNb_{1-x}V_{1+x} Alloy for x = 0, 0.1, 0.2, 0.4, 0.6 and 1. *Molecules* **2022**, *27*, 1054. <https://doi.org/10.3390/molecules27031054>

Academic Editor: Ewa C.E. Rönnebro

Received: 4 January 2022

Accepted: 2 February 2022

Published: 4 February 2022

Publisher's Note: MDPI stays neutral with regard to jurisdictional claims in published maps and institutional affiliations.



Copyright: © 2022 by the authors. Licensee MDPI, Basel, Switzerland. This article is an open access article distributed under the terms and conditions of the Creative Commons Attribution (CC BY) license (<https://creativecommons.org/licenses/by/4.0/>).

1. Introduction

Metal hydrides are known as one of the most practical solutions of hydrogen storage as they store hydrogen safely with high volumetric density under mild temperature and pressure [1]. Recently, high entropy alloys (HEAs) have attracted attention as novel materials for hydrogen storage. HEAs are multiple principal elements as described by Cantor et al. [2] and Yeh et al. [3]. The random distribution of the elements in HEAs provides a large diversity of local environments for hydrogen. The vastness of compositions in HEAs offers a large opportunity to tune their properties to practical applications [4,5].

One of the earliest studies of HEA-based metal hydrides was conducted by Kao and al. [6]. They carried out a systematic investigation of the effects of different x, y, and z values on the hydrogen properties of CoFeMnTi_xV_yZr_z alloys (0.5 ≤ x ≤ 2, 0.4 ≤ y ≤ 3.0, and 0.4 ≤ z ≤ 3.0). All samples had a C14 Laves phase structure and could absorb hydrogen at room temperature after a prior heat treatment. After heat treatment at 400 °C, the CoFeMnTiVZr_{2.5} alloy had a maximum capacity of 1.79 wt.% at room temperature under 9.8 bars of hydrogen. The hydrogen absorption kinetics was greatly enhanced for the alloys with higher amounts of Ti and Zr. This enhancement was explained by the large atomic radii of Ti and Zr compared to that of V. Adding more Ti or Zr enlarges the size of the interstitial sites, and in turn, the lattice expansion that facilitates the hydrogen diffusion [6]. Chen et al. investigated the C14-Cr₀Fe_vMn_wTi_xV_yZr_z alloys [7]. A heat treatment at 400 °C was performed before the kinetic measurements. The kinetic measurements were conducted for each composition at different temperatures of 5, 25, and 80 °C under 9.8 bars of hydrogen. The Fe-free alloy CrMnTiVZr showed the highest maximum capacity of 2.23 wt.% at 5 °C [7]. The alloys V₃₅Ti₃₀Cr₂₅Mn₁₀, V₃₅Ti₃₀Cr₂₅Fe₅Mn₅, and V₃₅Ti₃₀Cr₂₅Fe₁₀ were studied by Liu et al. [8]. The samples had mainly a body-centered cubic (BCC) structure. The V₃₅Ti₃₀Cr₂₅Mn₁₀ readily absorbed hydrogen at room temperature after heating at 100 °C, but the other alloys showed an incubation time [8]. Yang et al. systematically studied the (VFe)₆₀(TiCrCo)_{40-x}Zr_x alloys for x = 0, 1, and 2 [9]. All alloys were able to absorb hydrogen at room temperature, reaching a full capacity of 3.5 wt.% in 15 min, without prior heat

treatment [9]. Sahlberg et al. showed that the BCC TiVZrNbHf alloy has a hydrogen storage capacity of 2.5 H/M (2.7 wt.%) at 300 °C [10]. Such capacity was explained by hydrogen occupancy in both tetrahedral and octahedral sites in the fully hydrided body centered tetragonal (BCT) structure [10]. Ek et al. investigated 21 alloys with compositions related to TiVZrNbHf [11]. After heating at 340 °C for 2 h in a dynamic vacuum, most of these alloys absorbed hydrogen at room temperature under 40 bars of pressure, reaching a full capacity of H/M = 2. However, when V was partially or completely removed, the kinetics became too slow. After several days of hydrogen exposure of 40 bars at room temperature, TiV_{0.5}ZrNbHf reached only H/M of 1.3. TiZrNbHf, TiZrNb, TiNbHf, TiZrHf, and ZrNbHf alloys required heating at 500 °C instead of 340 °C and hydrogenation at 300 °C instead of room temperature [11]. We see that, in all these previous investigations, a heat treatment was needed before the first hydrogenation. However, for practical purposes, it would be preferable to perform the first hydrogenation at room temperature.

Recently, we investigated the effect of the particle size, hydrogenation temperature, and hydrogenation pressure on the kinetics absorption of the TiVZrNbHf alloy [12]. The sieving of particles to a size less than 0.5 mm made the alloy absorb hydrogen below 300 °C. At 200 °C, a long incubation period of 27 h was needed before the alloy started to absorb hydrogen. However, once started, the hydrogenation was relatively fast, reaching a 2.2 wt.% (2.0 H/ M) capacity. In another work, we selected the transition elements of period 4 to synthesize the Ti_{0.3}V_{0.3}Mn_{0.2}Fe_{0.1}Ni_{0.1} alloy [13]. Two synthesis methods were used: arc melting and ball milling. Irrespective of the synthesis method, the alloy absorbed hydrogen at room temperature under 20 bars of hydrogen without any prior heat treatment.

In this study, we substituted Nb by V in the TiHfZrNb_{1-x}V_{1+x} alloy. The reason for this substitution is that V is lighter than Nb. Thus, the hydride could potentially have a higher gravimetric hydrogen storage capacity. Here, we report the investigation of the crystal structure and hydrogen storage properties of TiHfZrNb_{1-x}V_{1+x} alloys (x = 0.1, 0.2, 0.4, 0.6, and 1).

For each alloy, we calculated the thermodynamic, geometric, and electronic parameters for phase formation rules. The thermodynamic parameter is characterized by the ratio of the entropy of mixing over the enthalpy of mixing ($\Omega = T \Delta S_{\text{mix}} / \Delta H_{\text{mix}}$) of the alloys. The geometric parameter δ is a function of the atomic size difference of the constituent elements. The electronic parameter VEC gives the valence electron concentration of the alloy. The expression for each parameter is given in [14]. Table 1 lists the values of ΔS_{mix} , ΔH_{mix} , Ω , and δ for each investigated alloy. The value of VEC was 4.4 for all investigated alloys.

Table 1. The parameters ΔS_{mix} , ΔH_{mix} , Ω , and δ for the TiHfZrNb_{1-x}V_{1+x} alloys (x = 0, 0.1, 0.2, 0.4, 0.6, and 1).

x Value	ΔS_{mix} J.K ⁻¹ mol ⁻¹	ΔH_{mix} kJ.mol ⁻¹	Ω	δ %
Criteria for solid solution [15]	Maximum	-11 to 5	≥1.1	≤6.6
0	13.38	0.16	192	6.86
0.1	13.37	-0.13	235	6.99
0.2	13.31	-0.40	76	7.13
0.4	13.10	-0.97	30	7.39
0.6	12.74	-1.51	19	7.64
1	11.08	-2.56	9	8.08

We can see that ΔS_{mix} decreased with x, reaching the lowest value for the Nb-free (x = 1) alloy. ΔH_{mix} and Ω also decreased with x and their values satisfied the conditions for the formation of solid solution phases. In the case of δ , it increased with x and was the maximum for x = 1. VEC was 4.4 for all alloys and this value favors the formation of the BCC structure over the face-centered cubic (FCC) structure [16]. According to the Ω and

VEC values, all the selected compositions fulfilled the conditions for the formation of the BCC phase. However, referring to δ values, the formation of intermetallic compounds is expected.

2. Results and Discussions

2.1. Microstructural Study

Figure 1 shows the backscattered electron micrograph of TiHfZrNb_{1-x}V_{1+x} alloys for $x = 0, 0.1, 0.2, 0.4, 0.6,$ and 1 .

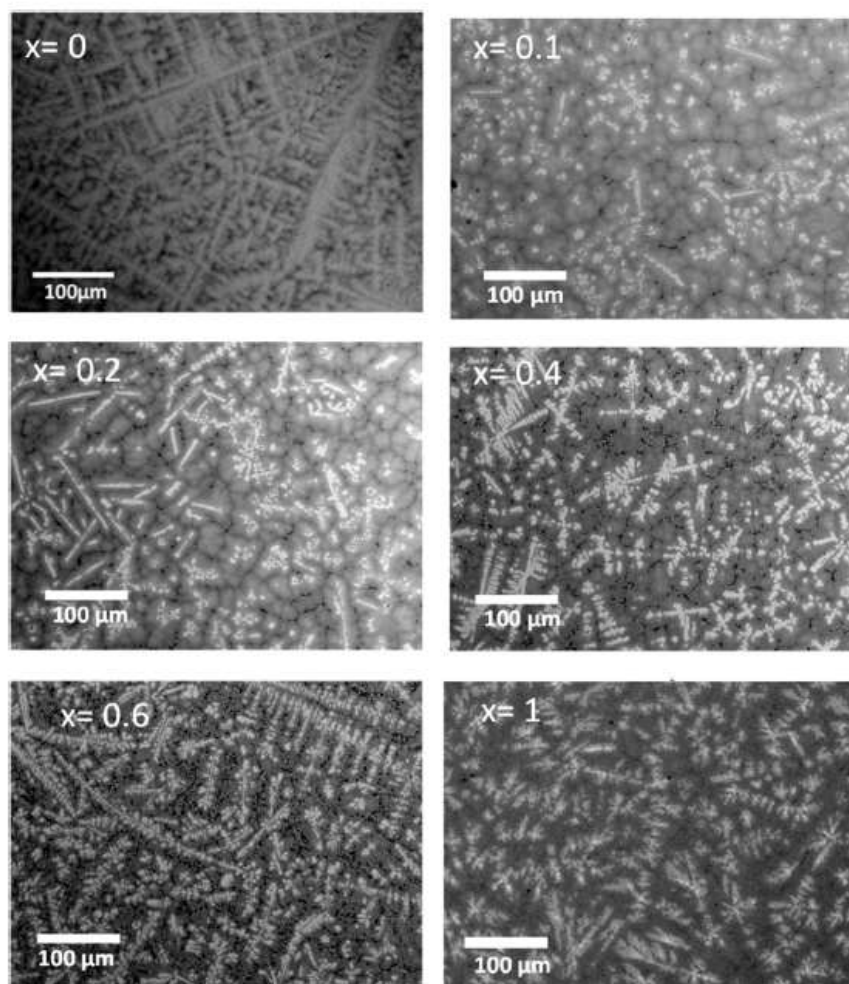


Figure 1. Backscattered electron (BSE) micrograph of the TiHfZrNb_{1-x}V_{1+x} alloys for $x = 0, 0.1, 0.2, 0.4, 0.6,$ and 1 .

The bulk chemical composition for each sample was confirmed by EDX measurements to be equal to the nominal values. From Figure 1, it is clear that all compositions had a dendritic structure, but the microstructure changed with x . The TiHfZrNbV alloy ($x = 0$) was made of light grey dendrites surrounded by darker grey regions and a few darker (almost black) spots. A slight substitution of Nb by V ($x = 0.1$) made the dendrites much brighter, but also smaller. All the substituted alloys were found to be multiphase, showing a matrix with bright and dark phases. For total substitution ($x = 1$), the dark phase disappeared.

Using EDX at a higher magnification, the chemical compositions of the individual phases were measured on the selected points presented in Figure 2.

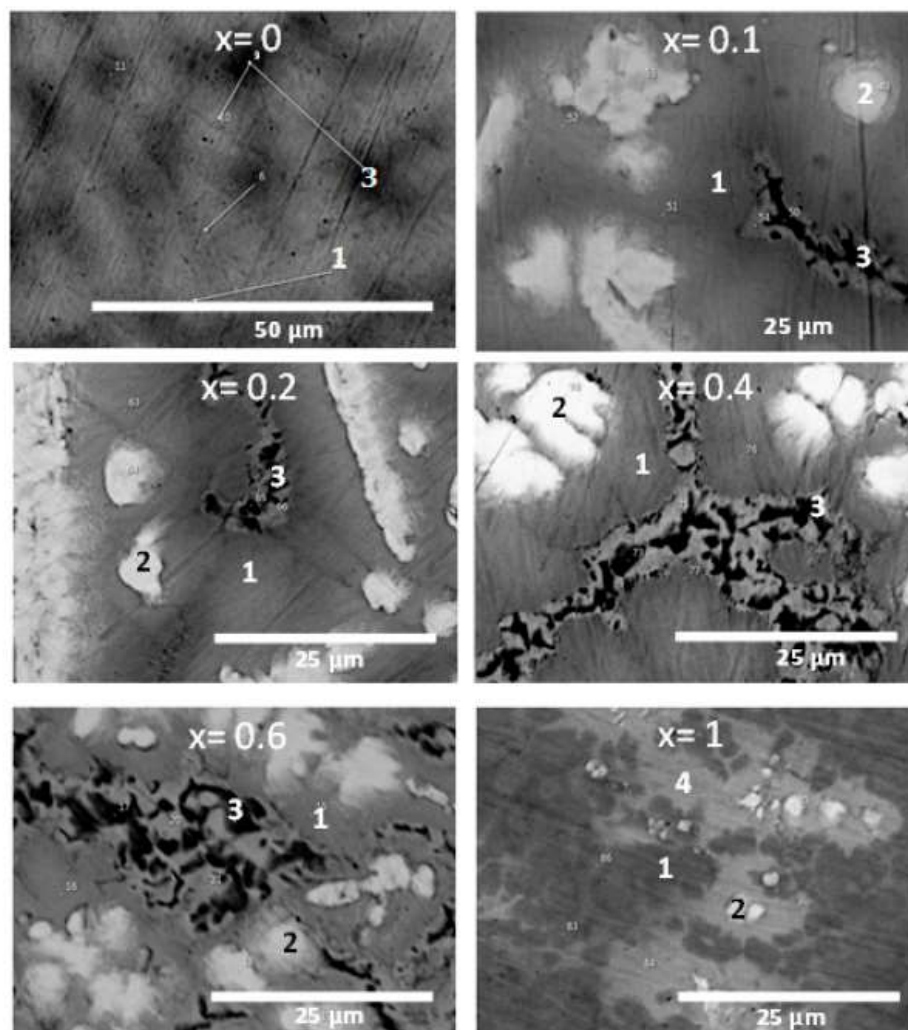


Figure 2. BSE micrographs of the $\text{TiHfZrNb}_{1-x}\text{V}_x$ alloys for $x = 0, 0.1, 0.2, 0.4, 0.6,$ and 1 with higher magnification. $x = 0$ is from [12] with permission.

In a previous investigation, it was shown that the equiatomic sample TiHfZrNbV is a single phase BCC with a range of composition. This variation of composition is the origin of the change in grey shade seen in Figure 2 for $x = 0$ [12].

The other micrographs show that the alloys are made of a main phase, thereafter, called the matrix and indicated by point number 1, a bright phase (point 2), and a dark phase (point 3). For $x = 1$, no black region was present, but there was a bright grey phase (point 4). The chemical compositions of points 1, 2, and 3 are listed in Tables 2, 3, and 4, respectively.

Table 2. EDX analysis showing the elemental composition of the matrix (point 1) of the TiHfZrNb_{1-x}V_{1+x} alloys for x = 0, 0.1, 0.2, 0.4, 0.6, and 1. Error on all values was 1 at.%.

x	Ti (at.%)	Hf (at.%)	Zr (at.%)	Nb (at.%)	V (at.%)
0	20	19	19	22	20
0.1	21	18	18	20	23
0.2	21	18	18	21	22
0.4	20	17	19	14	30
0.6	23	18	20	9	30
1	12	18	16	0	54

From Table 2, it can be seen that for x = 0, the matrix had a composition very close to the nominal one. For x = 0.1, the composition was again very close to the nominal one. For x = 0.2, the composition was still very similar to the composition of x = 0 and 0.1. For x = 0.4, we could see an important increase in vanadium content and a corresponding decrease in niobium. The other concentrations of the elements were still close to nominal. At x = 0.6, the matrix showed a strong depletion of niobium and an increase in titanium when compared to x = 0.4. Finally, for x = 1, the vanadium content was much higher than the nominal one and the titanium content was lower. From this, we can see that substitution of Nb by V does not result in a smooth variation of the matrix composition. Vanadium seems to be more abundant, while titanium was less abundant than what was expected from a linear variation of the element's concentration with x.

The atomic compositions of the bright phase (point 2) are listed in Table 3. It is clear that the bright phase (point 2) was rich in Hf and Zr and depleted in Nb and V. From x = 0.1 to 0.6, the composition was almost constant, but there was a slight decrease in Nb proportion and a slight increase in Zr proportion, keeping the Zr + Nb proportion constant. For x = 1, the proportion of vanadium was much higher than for the other compositions.

Table 3. EDX analysis showing the elemental composition of the bright phase (point 2) of: TiHfZrNb_{1-x}V_{1+x} alloys for x = 0.1, 0.2, 0.4, 0.6, and 1. Error on all values was 1 at.%.

x	Ti (at.%)	Hf (at.%)	Zr (at.%)	Nb (at.%)	V (at.%)
0.1	15	42	36	5	2
0.2	15	40	38	5	2
0.4	14	43	37	4	2
0.6	14	41	41	2	2
1	13	38	36	0	13

The atomic compositions of the dark phase (point 3) are presented in Table 4. This phase was not present for x = 1. We could see that the dark phase was V-rich and its composition was nearly constant for all values of x.

Table 4. EDX analysis showing the elemental composition of the dark phase (point 3) of: HfZrNb_{1-x}V_{1+x} alloys for x = 0.1, 0.2, 0.4, and 0.6. Error on all values was 1 at.%.

x	Ti (at.%)	Hf (at.%)	Zr (at.%)	Nb (at.%)	V (at.%)
0.1	14	6	7	12	61
0.2	14	7	10	12	57
0.4	14	7	8	9	62
0.6	17	8	8	8	59

For the bright grey phase (point 4, only for x = 1) of Figure 2, its atomic composition was 26Ti–24Hf–26Zr–24V, which was very close to the equiatomic composition.

2.2. Crystal Structure

Figure 3 presents the XRD patterns of all compositions in their as-cast state.

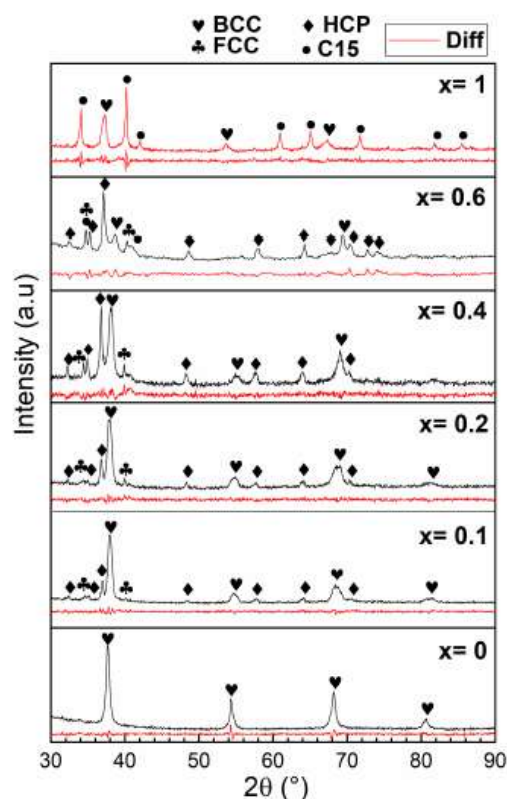


Figure 3. X-ray diffraction patterns of the as-cast $\text{TiHfZrNb}_{1-x}\text{V}_{1+x}$ alloys for $x = 0, 0.1, 0.2, 0.4, 0.6,$ and 1 . The bottom (red) line of each pattern is the residue of Rietveld refinement.

For $x = 0$, the crystal structure was pure BCC. Other phases appeared upon the substitution. The abundance of each phase as determined by Rietveld refinement is reported in Table 5. For $x = 0.1, 0.2,$ and 0.6 , the main phase was the BCC phase along with a HCP phase and a minor amount of a FCC phase. As x increased from 0.1 to 0.6 , the abundance of the BCC phase decreased, the HCP phase increased, and the FCC phase had roughly the same abundance. At $x = 0.6$, a C15 Laves phase appeared. For complete substitution of Nb by V, C15 becomes the main phase along a BCC phase.

Table 5. Abundance in wt.% of each phase in the $\text{TiHfZrNb}_{1-x}\text{V}_{1+x}$ alloys for $x = 0, 0.1, 0.2, 0.4, 0.6,$ and 1 . The number in parentheses is the error on the last significant digit.

x	0	0.1	0.2	0.4	0.6	1
BCC	100	80 (1)	76 (2)	59 (2)	38 (3)	31 (1)
HCP	14 (1)	17 (1)	29 (2)	35 (3)
FCC	6 (1)	7 (1)	11 (1)	10 (1)
C15	16 (2)	69 (1)

The crystal structures seen in the diffraction patterns could be correlated to the chemical compositions of phases given by EDX. For $x = 0.1$ to 0.6 , we could associate the matrix (point 1) to the BCC crystal structure.

The bright phase (point 2) could be associated with the HCP crystal structure for $x = 0.1$ to 0.6 . From the chemical composition of the bright phase shown in Table 3, we could infer that the structure type of this HCP phase was $\text{Hf}_{0.5}\text{Zr}_{0.5}$. The phase diagram of Hf–Zr indicates that these two elements are totally miscible and have a HCP structure. The bright phase seen in the present samples was mainly made of hafnium (41% on average) and zirconium (38% on average). Therefore, the bright phase could be associated with a HCP phase of the chemical composition $0.14\text{Ti}-0.41\text{Hf}-0.38\text{Zr}-0.04\text{Nb}-0.02\text{V}$.

For the patterns $x = 0.1$ to 0.6 , a FCC phase was identified. From Figure 2, we can see that the dark phase is the only possibility of matching this phase. From Table 4, the average composition of the dark phase was $0.15\text{Ti}-0.07\text{Hf}-0.08\text{Zr}-0.1\text{Nb}-0.6\text{V}$.

For $x = 0.6$ and 1 , a C15 phase was identified in the diffraction pattern. In the case of $x = 0.6$, the only possibility was to assume that some of the dark regions in the micrographs are associated with this C15 phase and some others to a FCC phase. In fact, the $x = 0.6$ composition of the dark phase was $0.17\text{Ti}-0.08\text{Hf}-0.08\text{Zr}-0.08\text{Nb}-0.59\text{V}$. This is very close to the composition of the dark phase for $x = 0.1$ to 0.4 , but here, the atomic abundance of group 5 atoms (V and Nb) was exactly 0.67 , while the total abundance of group 4 atoms (Ti, Zr, and Hf) was 0.33 . The C15 phase had a structure of AB_2 , where A is a hydride forming element and B is a non-hydride forming element. Thus, we can assign this phase to a C15 structure (space group Fd-3m) where Ti/Zr/Hf are assigned to the 8b site (A atoms) and the B atoms V/Nb are on the 16c site. It is known that Laves phases are related to BCC. For example, Hao et al. have shown by molecular dynamics that a perfect C15 cluster could be embedded in BCC iron [17].

For $x = 1$, the situation is more complex. The C15 phase is the most abundant phase in the diffraction pattern. Compared to Figure 2, it is most likely to be the matrix with a composition of $0.12\text{Ti}-0.18\text{Hf}-0.16\text{Zr}-0.54\text{V}$ that could be written as $\text{Ti}_{0.36}\text{Hf}_{0.54}\text{Zr}_{0.48}\text{V}_{1.62}$. This is relatively far from an AB_2 stoichiometry as most likely Ti, Zr, and Hf share the same site. The bright grey phase (point 4) seen in Figure 2 is associated with the BCC phase. The stoichiometry of that phase was $26\text{Ti}-0.24\text{Hf}-0.26\text{Zr}-0.24\text{V}$.

The crystal structure parameters of the BCC phase as determined by Rietveld refinement are tabulated in Table 6 with the average atomic radius of this phase. The chemical composition of the BCC phase was taken from the EDX measurements for each x . The BCC phase is the matrix for $x = 0.1$ to 0.6 and the bright grey phase for $x = 1$.

Table 6. Crystal structure parameters of the BCC phase in the $\text{TiHfZrNb}_{1-x}\text{V}_{1+x}$ alloys for $x = 0, 0.1, 0.2, 0.4, 0.6$, and 1 . Error on the last significant digit is indicated in parentheses.

BCC	Cell Volume (\AA^3)	Lattice Parameter (\AA)	Crystallite Size (nm)	Microstrain (%)	Average Radius (pm)	Ratio
0	37.99 (2)	3.362 (1)	9.9 (2)	1.01 (3)	147	2.29
0.1	37.92 (3)	3.360 (1)	30 (2)	0.31 (1)	146.1	2.30
0.2	37.51 (3)	3.347 (1)	25 (3)	0.35 (1)	146.2	2.29
0.4	37.01 (3)	3.333 (1)	10.5 (6)	0.23 (2)	145.5	2.29
0.6	36.79 (6)	3.326 (2)	4.1 (7)	145.9	2.28
1	39.81 (3)	3.415 (1)	25 (5)	0.38 (2)	148.5	2.30

The chemical composition of the BCC phase changes with x , but not in a linear fashion. However, from Table 6, we can see that the ratio of the average radius over the lattice parameter was practically constant.

The crystal structure parameters of the HCP phase are presented in Table 7. The lattice parameters of all samples were roughly constant with x . This is expected because, as shown in Table 3, the chemical composition for the HCP phase was almost the same for all samples.

Table 7. Crystal structure parameters of the HCP phase in the TiHfZrNb_{1-x}V_{1+x} alloys for x = 0.1, 0.2, 0.4, and 0.6. Error on the last significant digit is indicated in parentheses.

HCP	Cell Volume (Å ³)	Lattice Parameter (Å)	Crystallite Size (nm)	Microstrain (%)
0.1	45.57 (3)	a = 3.202 (1) c = 5.132 (2)	38 (9)	0.14 (2)
0.2	45.38 (3)	a = 3.199 (1) c = 5.121 (2)	41 (10)	0.13 (2)
0.4	45.46 (3)	a = 3.201 (1) c = 5.123 (2)	22 (2)	0.07 (2)
0.6	45.57 (3)	a = 3.203 (1) c = 5.129 (2)	21 (1)

The crystal structure parameters of the FCC phase are shown in Table 8. The lattice parameter of the FCC phase was almost the same for all compositions. This is consistent with the fact that the chemical composition of this phase is constant, as shown in Table 4. For this phase, the microstrain was refined, but the results were always zero within the experimental error.

Table 8. The crystal structure parameters of the FCC phase in the TiHfZrNb_{1-x}V_{1+x} alloys for x = 0.1 to 0.6. Error on the last significant digit is indicated in parentheses.

FCC	Cell Volume (Å ³)	Lattice Parameter (Å)	Crystallite Size (nm)
0.1	91.61 (1)	4.508 (3)	16 (3)
0.2	91.33 (1)	4.503 (2)	22 (5)
0.4	91.25 (1)	4.502 (2)	15 (2)
0.6	91.74 (6)	4.511 (1)	53 (17)

The crystal structure parameters of the C15 phase are shown in Table 9. The lattice parameter of C15 phase increased with x. However, the main differences were the crystallite size and microstrain. For x = 0.6, only the microstrain could be refined. All attempts to refine the crystallite size provided unrealistic numbers. This is similar to the one encountered for another AB₂ alloy [18]. It has been shown that when crystallite size is impossible to refine, the microstrain reflects a variation of chemical composition. This is also most likely the case here. Because the chemical composition varies within the dark phase, the crystal may adopt the FCC or the C15 structure. It should be pointed out that in the Rietveld refinement of the C15 phase for x = 1, the occupancy factor of vanadium was refined. The refined occupancy was 0.84, which translates to an abundance of 55 at.%. This value was very close to the measured value of 54 at.% in Table 2. This means that the C15 phase of x = 1 has an important number of vacancies on the B site.

Table 9. Crystal structure parameters of the C15 phase in the TiHfZrNb_{1-x}V_{1+x} alloys for x = 0.6 and 1. Error on the last significant digit is indicated in parentheses.

C15	Cell Volume (Å ³)	Lattice parameter (Å)	Crystallite size (nm)	Microstrain (%)
0.6	397 (1)	7.350 (7)	0.63 (4)
1	412.0 (2)	7.441 (1)	21.1 (6)

2.3. First Hydrogenation

The first hydrogenation (activation) of the $\text{TiHfZrNb}_{1-x}\text{V}_{1+x}$ alloys for $x = 0, 0.1, 0.2, 0.4, 0.6,$ and 1 was performed at room temperature under a hydrogen pressure of 20 bars without any prior heat treatment. Results are presented in Figure 4.

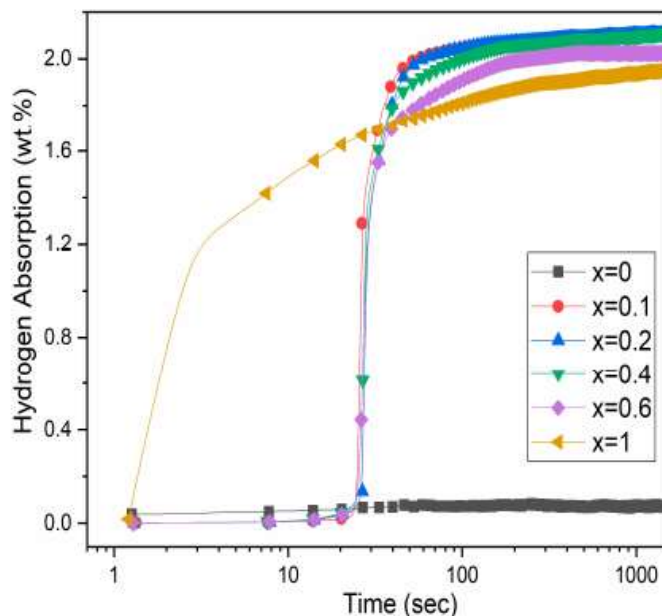


Figure 4. Activation curves of the $\text{TiHfZrNb}_{1-x}\text{V}_{1+x}$ alloys for $x = 0, 0.1, 0.2, 0.4, 0.6,$ and 1 .

The first hydrogenation for $x = 0$ is impossible at room temperature [10,12]. Substituting niobium by vanadium provided a good hydrogen uptake with 25 s of incubation time and fast kinetics. Surprisingly, even if the heavy element Nb was replaced by the lighter element V, there was a slight downward trend for the capacity with increasing x . Additionally, the incubation time and kinetics were essentially the same for all substituted alloys. The TiHfZrV_2 alloy did not show any incubation time. The disappearance of the incubation time could be related to the predominant C15 phase.

The crystal structure of the hydrided alloys were investigated by XRD. The results are shown in Figure 5.

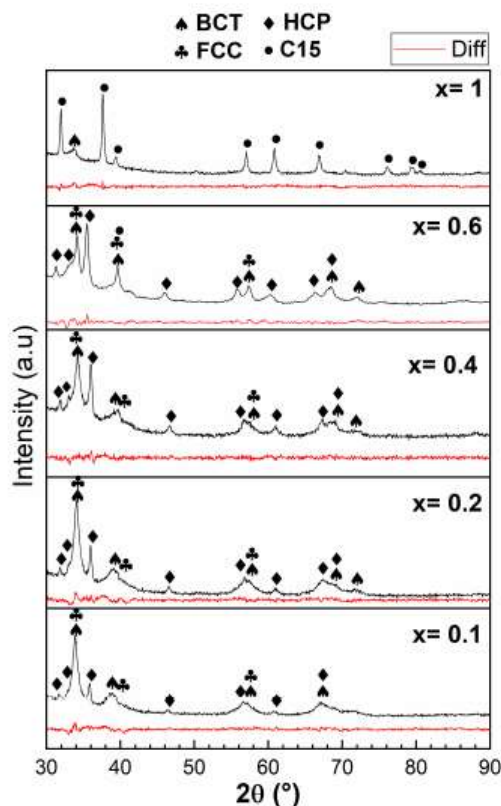


Figure 5. XRD patterns of the $\text{TiHfZrNb}_{1-x}\text{V}_{1+x}$ alloys in the hydrogenated state for $x = 0.1, 0.2, 0.4, 0.6,$ and 1 . The bottom (red) line of each pattern is the residue of Rietveld refinement.

For $x = 0.1, 0.2, 0.4,$ and 0.6 , the crystal structure was essentially BCT with HCP and FCC as a secondary phase. It has been reported that BCT is the structure adopted by a fully hydrided BCC high entropy alloy [10,12]. For the $x = 1$ sample, the main phase was C15 and BCT was the minor phase. The crystal structure parameters and the abundance of each phase in all hydrogenated samples as determined by Rietveld's analysis are presented in Table 10. To show the relative contribution of each phase to the pattern, Figure 6 shows the details of the pattern with the most phases present ($x = 0.6$).

Table 10. The crystal parameters of each phase in the hydrogenated $\text{TiHfZrNb}_{1-x}\text{V}_{1+x}$ alloys for $x = 0.1, 0.2, 0.4, 0.6,$ and 1 . Error on the last significant digit is indicated in parentheses.

Sample	Phase	Cell Volume (\AA^3)	Lattice Parameter (\AA)	Crystallite Size (nm)	Micro-Strain (%)	Abundance (%)
0.1	BCT	47.90 (6)	$a = 3.286$ (2) $c = 4.437$ (3)	8.1 (5)	0.48 (2)	76 (1)
	HCP	49.88 (6)	$a = 3.255$ (1) $c = 5.435$ (2)	15 (1)	11 (1)
	FCC	95.8 (2)	4.574 (2)	0.33 (2)	13 (1)
0.2	BCT	47.35 (5)	$a = 3.273$ (2) $c = 4.419$ (3)	7.5 (6)	0.49 (2)	73 (2)
	HCP	49.43 (5)	$a = 3.246$ (1) $c = 5.418$ (2)	17 (1)	14 (1)

	FCC	94.4 (1)	4.554 (2)	0.35 (2)	13 (1)
	BCT	46.86 (8)	a = 3.265 (2) c = 4.395 (5)	5.2 (4)	0.60 (4)	65 (2)
0.4	HCP	49.55 (4)	a = 3.249 (1) c = 5.421 (2)	15 (1)	22 (1)
	FCC	93.9 (1)	4.545 (2)	0.36 (2)	13 (1)
	BCT	47.47 (9)	a = 3.193 (2) c = 4.657 (7)	3.3 (2)	57 (2)
0.6	HCP	51.33 (4)	a = 3.296 (1) c = 5.456 (2)	36 (6)	0.29 (1)	24 (2)
	FCC	93.66 (8)	4.541 (1)	43 (20)	0.15 (2)	15 (2)
	C15	434 (1)	7.574 (6)	0.31 (4)	4 (1)
1	BCT	49.0 (2)	a = 3.339 (5) c = 4.40 (1)	7 (2)	1.09 (7)	31 (2)
	C15	492.8 (1)	7.899 (1)	31 (2)	0.07 (1)	69 (2)

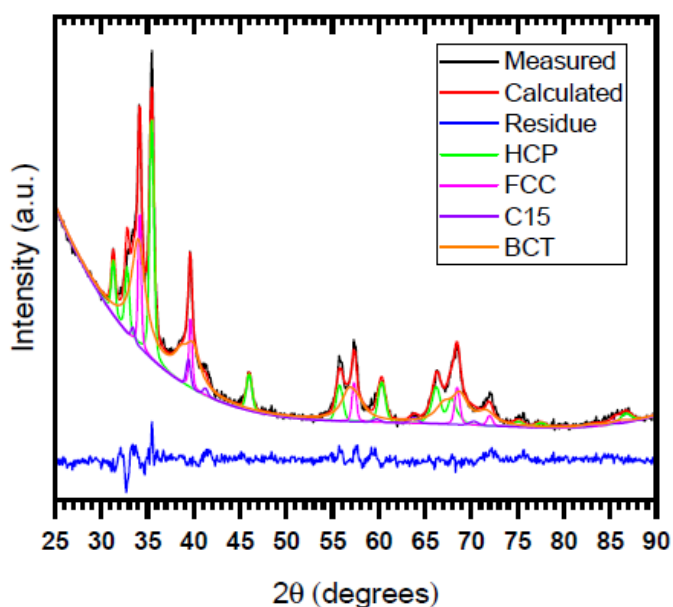


Figure 6. Rietveld refinement details of the XRD pattern of the hydrogenated TiHfZrNb_{0.4}V_{1.6} alloy.

Basically, the same phases were present in the hydrided and as-cast patterns. From Table 10 and referring to Table 5, we can see that for $x = 0.1$ to 0.6 , except for $x = 0.4$, the abundance of the FCC phase in the hydrogenated samples was higher than the abundance in the as-cast samples. For $x = 0.4$, the abundance of the FCC phase in the hydrogenated sample had relatively the same abundance as in the as-cast sample. From $x = 0.1$ to 0.2 , the abundance of the HCP phase in the hydrogenated samples was close to the abundance in the as-cast samples. However, the HCP phase was less abundant in the hydrogenated samples for $x = 0.4$ and 0.6 . The BCT phase abundance was relatively the same abundance as the BCC phase for $x = 0.1$ and 0.2 . However, its abundance was higher than the BCC abundance for $x = 0.4$ and 0.6 . Regarding the C15 phase for $x = 0.6$, the amount of the hydrided C15 phase was much lower than that in the as-cast (4% vs. 16%).

In the case of $x = 1$, we can see that the hydrogenated alloy had a 31 wt.% BCT phase, which corresponds to the abundance of the BCC phase (31%) in the as-cast alloy. Therefore, BCC was completely transformed into BCT upon hydrogenation. For the C15 phase, similar to the as-cast state, the occupancy factor of the B site corresponded to a vanadium abundance of 57 at.%.

Concerning the HCP phase and referring to Table 7, we can see that the crystallite size of this phase decreased upon hydrogenation for $x = 0.1$ to 0.4, but it increased for $x = 0.6$. No microstrains were found in the hydrogenated samples of $x = 0.1$ to 0.4, while a microstrain of 0.29% appeared for $x = 0.6$. For the C15 phase and using Table 9, the crystallite size in the hydrided C15 was greater than that of the as-cast when $x = 1$.

As the unit cell volume of all phases in the hydrided state was larger than in the as-cast state, we could use the volume increase to estimate the hydrogen capacity. Considering that a hydrogen atom produces a volume expansion between 2 and 3 Å³, the estimated amount of hydrogen in each phase was determined from the volume expansion ΔV of each hydrided phase. The results are shown in Table 11.

Table 11. The variation of volume ΔV and the estimated range of hydrogen in each phase in the hydrogenated TiHfZrNb_{1-x}V_{1+x} alloys for $x = 0.1, 0.2, 0.4, 0.6$, and 1.

	ΔV of BCT (Å ³)	Estimated Amount of H in BCT (wt.%)	ΔV of HCP (Å ³)	Estimated Amount of H in HCP (wt.%)	ΔV of FCC (Å ³)	Estimated Amount of H in FCC (wt.%)	ΔV of C15 (Å ³)	Estimated Amount of H in C15 (wt.%)
0.1	9.98	1.87 to 2.8	4.31	0.6 to 0.89	4.19	0.53 to 0.79
0.2	9.84	1.83 to 2.75	4.05	0.57 to 0.85	3.07	0.37 to 0.56
0.4	9.85	1.91 to 2.88	4.09	0.56 to 0.84	2.65	0.33 to 0.5
0.6	10.68	2.09 to 3.14	5.76	0.8 to 1.2	1.92	0.24 to 0.36	37	0.76 to 1.14
1	9.19	1.68 to 2.52	80.8	1.7 to 2.55

Taking into consideration the abundance of each phase in the hydrided samples, the estimated amount of hydrogen is shown in Table 12.

Table 12. Estimated capacity of the phases in the hydrided samples.

	0.1	0.2	0.4	0.6	1
Estimated amount of H in the hydride (wt.%)	1.56 to 2.33	1.46 to 2.2	1.4 to 2.12	1.45 to 2.18	1.69 to 2.54
Measured capac- ity (wt.%)	2.1	2.1	2.1	2	1.95

This table clearly shows that the measured capacities of all samples were in the middle of the estimated range. We could estimate that, on average, a hydrogen atom takes a volume of 2.7 Å³. This is very close to the volume expansion of estimation of 2.9 Å³ that Peisl found for a wide range of materials [19]. Using 2.7 Å³ for the hydrogen volume in the crystal structure, we estimated the H/M ratio for each phase. We found that the BCT phase had a ratio close to 2, and the HCP phase had a ratio between 0.75 and 1. Surprisingly, the FCC H/M ratio for $x = 0.1, 0.2, 0.4$, and 0.6 was 0.39, 0.28, 0.24 and 0.18, respectively. We also observed that the FCC phase took up less and less hydrogen as x value increased. Regarding the C15 phase, for $x = 0.6$, the H/M was 0.57 while for $x = 1$, the H/M was 1.25.

For $x = 0.1$ to 0.6, most of the capacity came from the BCT phase. This is because the estimated amount of hydrogen in the hydride BCT was higher than that of the hydride

HCP and FCC phases and also because BCT was the most abundant over the hydrided phases. For $x = 1$, the estimated amount of hydrogen in the hydride C15 phase was higher than that of BCT. Additionally, C15 had the highest abundance (69%) compared to BCT (31%). Therefore, most of the measured capacity came from the C15 phase. Referring to the activation curves of Figure 4, one can correlate the absence of the incubation time to the presence of the C15 phase as the main phase.

The TiHfZrV₂ alloy was selected to study its dehydrided state. The choice of this composition is because it is the total substituted sample, and its synthesis is relatively easy compared to the other samples. However, studying the stability of the other hydrided compositions is planned for a future paper. After reaching full hydrogenation, the sample was subjected to vacuum for two hours at 350 °C. XRD measurements (not shown) confirmed that no desorption occurred. Thus, the temperature was raised to 400 °C and the sample kept under dynamic vacuum for two hours. The XRD pattern of the dehydrogenated sample is presented in Figure 7. The very high background is due to a special sample holder that kept the powder under an argon atmosphere.

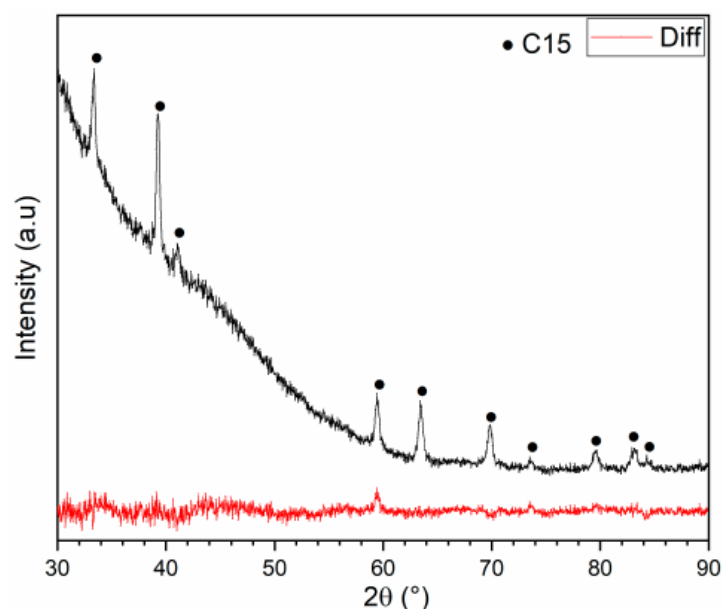


Figure 7. XRD pattern of the TiHfZrV₂ alloy ($x = 1$) dehydrided at 400 °C under vacuum.

We could see that only the C15 phase was present in the desorbed patterns; no BCC or BCT phases were seen. The reason is that the BCC/BCT phases were most probably ‘buried’ under the high background. The volume of the C15 phase as determined by Rietveld refinement was 443.8 Å³. The volume of the C15 phase after dehydrogenation was larger than that of the C15 phase in the as-cast state (412.1 Å³). This indicates that there is still hydrogen in the C15 phase. Assuming a volume of hydrogen atom of 2.7 Å³, the hydrogen still present is 0.73 wt.% (0.49 H/M). This means that the sample is not fully desorbed even at 400 °C under vacuum. This could be explained by the high stability of the binary hydrides of the raw elements where vanadium has the highest plateau pressure in the range $0 < H/M < 1$ of about 10 kPa. A temperature higher than 400 °C is needed for full desorption, but this is over the limit of our apparatus.

3. Materials and Methods

All the raw materials, Ti sponge (99.95%), Hf sponge (99.6%), Zr sponge (99.5%), Nb pieces (99.8%), and V pieces (99.7%) were purchased from Alfa Aesar (Tewksbury, USA).

and used as received. After mixing all raw elements in the desired proportion, each alloy was prepared by arc melting under 0.7 bars of argon. Each pellet was melted, turned over, and remelted three times to ensure good homogeneity. Before the hydrogenation measurements, the as-cast alloy was hand-crushed under an argon atmosphere using a hardened steel mortar and pestle. The first hydrogenation of all alloys was measured at room temperature under 20 bar hydrogen pressure on a homemade Sievert's apparatus. The powder was filled in the reactor and kept under dynamic vacuum for one hour at room temperature before the measurement. The crystal structure was determined by X-ray diffraction using a Bruker D8 Focus with Cu K α radiation. Lattice parameters were evaluated from Rietveld refinement using Topas software [20]. Microstructure and chemical analysis were performed using a Hitachi Su1510 scanning electron microscope (SEM) (Hitachi, Mississauga, Canada) equipped with an EDX (energy dispersive X-ray) apparatus from Oxford Instruments (Abingdon, UK).

4. Conclusions

The effect of the substitution of Nb by V on the microstructure and hydrogen storage properties of the TiHfZrNb_{1-x}V_x alloy for x = 0, 0.1, 0.2, 0.4, 0.6, and 1 was investigated. For x = 0, the alloy was pure BCC. All alloys with substitutions were multiphase. Upon substitution of niobium by vanadium, the BCC was progressively replaced with HCP and FCC phases. For high values of x, a C15 phase was present and became the main phase for x = 1. We found that substitution of Nb by V greatly enhanced the first hydrogenation and made it possible at room temperature under 20 bars of hydrogen. The BCC phase transformed to BCT in the fully hydrided state. For hydrogen storage purposes, the optimum amount of substitution seems to be the total substitution where there is no Nb in the alloy.

Author Contributions: All experiments, except electron microscopy, were performed by S.S. under the supervision of J.H. J.H. and S.S. analyzed the results and wrote the paper. All authors have read and agreed to the published version of the manuscript.

Funding: This research was funded in part by a discovery grant from the Natural Sciences and Engineering Research Council of Canada.

Institutional Review Board Statement: Not applicable.

Informed Consent Statement: Not applicable.

Data Availability Statement: Data available by contacting the authors.

Acknowledgments: We would like to thank A. Lejeune for the electron microscopy experiments.

Conflicts of Interest: The authors declare no conflict of interest.

Sample Availability: Samples of all the compounds are available from the authors.


References

1. Von Colbe, J.B.; Ares, J.-R.; Barale, J.; Baricco, M.; Buckley, C.; Capurso, G.; Gallandat, N.; Grant, D.M.; Guzik, M.N.; Jacob, I. Application of hydrides in hydrogen storage and compression: Achievements, outlook and perspectives. *Int. J. Hydrogen Energy* **2019**, *44*, 7780–7808.
2. Cantor, B.; Chang, I.; Knight, P.; Vincent, A. Microstructural development in equiatomic multicomponent alloys. *Mater. Sci. Eng.: A* **2004**, *375*, 213–218.
3. Yeh, J.W.; Chen, S.K.; Lin, S.J.; Gan, J.Y.; Chin, T.S.; Shun, T.T.; Tsau, C.H.; Chang, S.Y. Nanostructured high-entropy alloys with multiple principal elements: Novel alloy design concepts and outcomes. *Adv. Eng. Mater.* **2004**, *6*, 299–303.
4. Ding, Q.; Zhang, Y.; Chen, X.; Fu, X.; Chen, D.; Chen, S.; Gu, L.; Wei, F.; Bei, H.; Gao, Y. Tuning element distribution, structure and properties by composition in high-entropy alloys. *Nature* **2019**, *574*, 223–227.
5. Felderhoff, M.; Marques, F.; Balcerzak, M.; Winkelmann, F.; Zepon, G. Review and outlook on high-entropy alloys for hydrogen storage. *Energy Environ. Sci.* **2021**, *14*, 5191–5227.
6. Kao, Y.-F.; Chen, S.-K.; Sheu, J.-H.; Lin, J.-T.; Lin, W.-E.; Yeh, J.-W.; Lin, S.-J.; Liou, T.-H.; Wang, C.-W. Hydrogen storage properties of multi-principal-component CoFeMnTi_xVyZr_z alloys. *Int. J. Hydrogen Energy* **2010**, *35*, 9046–9059.

7. Chen, S.-K.; Lee, P.-H.; Lee, H.; Su, H.-T. Hydrogen storage of $C14-CrFeV_{0.5}MnW_{0.5}Ti_{0.5}V_{0.5}Zr_{0.5}$ alloys. *Mater. Chem. Phys.* **2018**, *210*, 336–347.
8. Liu, J.; Xu, J.; Sleiman, S.; Chen, X.; Zhu, S.; Cheng, H.; Huot, J. Microstructure and hydrogen storage properties of Ti–V–Cr based BCC-type high entropy alloys. *Int. J. Hydrogen Energy* **2021**, *46*, 28709–28718.
9. Yang, S.; Yang, F.; Wu, C.; Chen, Y.; Mao, Y.; Luo, L. Hydrogen storage and cyclic properties of (VFe)₆₀(TiCrCo)_{40-x}Zrx (0 ≤ x ≤ 2) alloys. *J. Alloys Compd.* **2016**, *663*, 460–465.
10. Sahlberg, M.; Karlsson, D.; Zlotea, C.; Jansson, U. Superior hydrogen storage in high entropy alloys. *Sci. Rep.* **2016**, *6*, 36770.
11. Ek, G.; Nygård, M.M.; Pavan, A.F.; Montero, J.; Henry, P.F.; Sørby, M.H.; Witman, M.; Stavila, V.; Zlotea, C.; Hauback, B.C. Elucidating the effects of the composition on hydrogen sorption in TiVZrNbHf-based high-entropy alloys. *Inorg. Chem.* **2020**, *60*, 1124–1132.
12. Sleiman, S.; Huot, J. Effect of particle size, pressure and temperature on the activation process of hydrogen absorption in TiVZrHfNb high entropy alloy. *J. Alloys Compd.* **2021**, *861*, 158615. <https://doi.org/10.1016/j.jallcom.2021.158615>.
13. Sleiman, S.; Moussa, M.; Huot, J. Microstructure and Hydrogen Storage Properties of the Multiphase Ti_{0.3}V_{0.3}Mn_{0.2}Fe_{0.1}Ni_{0.1} Alloy. *Reactions* **2021**, *2*, 287–300.
14. Zhang, Y.; Lu, Z.; Ma, S.; Liaw, P.; Tang, Z.; Cheng, Y.; Gao, M. Guidelines in predicting phase formation of high-entropy alloys. *Mrs Commun.* **2014**, *4*, 57–62.
15. Zhang, Y.; Zhou, Y.J.; Lin, J.P.; Chen, G.L.; Liaw, P.K. Solid-solution phase formation rules for multi-component alloys. *Adv. Eng. Mater.* **2008**, *10*, 534–538.
16. Guo, S.; Ng, C.; Lu, J.; Liu, C. Effect of valence electron concentration on stability of fcc or bcc phase in high entropy alloys. *J. Appl. Phys.* **2011**, *109*, 103505.
17. Wang, H.; Gao, N.; Lü, G.-H.; Yao, Z.-W. Effects of temperature and point defects on the stability of C15 Laves phase in iron: A molecular dynamics investigation. *Chin. Phys. B* **2018**, *27*, 066104.
18. Khajavi, S.; Rajabi, M.; Huot, J. Crystal structure of as-cast and heat-treated Ti_{0.5}Zr_{0.5}(Mn_{1-x}Fe_x)Cr₁, x = 0, 0.2, 0.4. *J. Alloys Compd.* **2018**, *767*, 432–438.
19. Peisl, H. Lattice strains due to hydrogen in metals. In *Hydrogen in Metals I*; Springer: Berlin/Heidelberg, Germany, 1978; pp. 53–74.
20. Bruker, A. *Topas V3: General Profile and structure ANALYSIS Software for Powder Diffraction Data—User's Manual*; Bruker AXS, Karlsruhe; Coelho AA (2007) TOPAS Academic: Coelho Software, Brisbane, Australia, 2005.

Article

Microstructure and Hydrogen Storage Properties of the Multiphase $\text{Ti}_{0.3}\text{V}_{0.3}\text{Mn}_{0.2}\text{Fe}_{0.1}\text{Ni}_{0.1}$ Alloy

Salma Sleiman, Maria Moussa and Jacques Huot * 

Hydrogen Research Institute, Université du Québec à Trois-Rivières, 3351 des Forges, Trois-Rivières, QC G9A 5H7, Canada; salma.sleiman@irh.ca (S.S.); maria.moussa@irh.ca (M.M.)
 * Correspondence: jacques.huot@irh.ca; Tel.: +1-819-376-5011 (ext. 3576)

Abstract: The hydrogen storage properties of a multi-component alloy of composition $\text{Ti}_{0.3}\text{V}_{0.3}\text{Mn}_{0.2}\text{Fe}_{0.1}\text{Ni}_{0.1}$ were investigated. The alloy was synthesized by arc melting and mechanical alloying, resulting in different microstructures. It was found that the as-cast alloy is multiphase, with a main C14 Laves phase matrix along with a BCC phase and a small amount of Ti_2Fe -type phase. The maximum hydrogen storage capacity of the alloy was 1.6 wt.%. We found that the air-exposed samples had the same capacity as the as-cast sample but with a longer incubation time. Synthesis by mechanical alloying for five hours resulted in an alloy with only BCC structure. The hydrogen capacity of the milled alloy was 1.2 wt.%, lower than the as-cast one. The effect of ball milling of the as-cast alloy was also studied. Ball milling for five hours produced a BCC structure similar to the one obtained by milling the raw materials for the same time.

Keywords: hydrogen storage; C14 Laves phase; mechanical alloying; kinetics



Citation: Sleiman, S.; Moussa, M.; Huot, J. Microstructure and Hydrogen Storage Properties of the Multiphase $\text{Ti}_{0.3}\text{V}_{0.3}\text{Mn}_{0.2}\text{Fe}_{0.1}\text{Ni}_{0.1}$ Alloy. *Reactions* **2021**, *2*, 287–300. <https://doi.org/10.3390/reactions2030018>

Academic Editors: Valérie Meille, Sibudjing Kawi, Francesco Frusteri and Luis M. Gandía

Received: 31 July 2021

Accepted: 20 August 2021

Published: 23 August 2021

Publisher's Note: MDPI stays neutral with regard to jurisdictional claims in published maps and institutional affiliations.



Copyright © 2021 by the authors. Licensee MDPI, Basel, Switzerland. This article is an open access article distributed under the terms and conditions of the Creative Commons Attribution (CC BY) license (<https://creativecommons.org/licenses/by/4.0/>).

1. Introduction

Hydrogen is considered an attractive energy vector for renewable energies. However, its storage in a safe, compact, and inexpensive way is still an important issue. A variety of hydrogen storage systems are possible: liquid, compressed gas, physisorption on high specific surface area materials, and metal hydrides [1–3]. Among these techniques, metal hydrides in which hydrogen forms a chemical bond with the metal atoms are attractive due to the high volumetric density and moderate operation conditions [4].

In 2004, Cantor et al. [5] and Yeh et al. [6] independently proposed the concept of high entropy alloys (HEAs). HEAs are an advanced type of multi-component alloy system [7]. The definition of HEAs is usually based on composition or configurational entropy. From the composition-based definition, HEAs contain at least five principal elements, each with an atomic abundance between 5 and 35%. Based on entropy, HEAs are alloys having configurational entropies greater than or equal to $1.5R$, where R is the gas constant. An alloy fitting one of these two definitions could be considered a HEA. However, these definitions should be considered guidelines and not laws. Because of the nature of HEAs, they have interesting properties such as high thermal stability, good ductility, high strength, good corrosion resistance, etc., [8].

Recently, HEAs have been considered for hydrogen storage [9–12]. Kuncce et al. studied the high entropy alloy ZrTiVCrFeNi prepared by laser engineered net shaping (LENS). This alloy was mainly C14 Laves phase with small amount of $\alpha\text{-Ti}$ phase. After heat treatment at $500\text{ }^\circ\text{C}$, the maximum hydrogen capacity was found to be 1.8 wt.% under 100 bars of hydrogen at $50\text{ }^\circ\text{C}$. Additional heat treatment at $1000\text{ }^\circ\text{C}$ had no effect on the crystal structure but reduced the capacity to 1.56 wt.% under the same absorption conditions [9]. Kuncce et al. also examined another high entropy alloy TiZrNbMoV [10]. Depending on LENS synthesis conditions, this alloy exhibited different phase compositions. The predominant BCC TiZrNbMoV alloy absorbed only 0.59 wt.% under 85 bar at $50\text{ }^\circ\text{C}$ without prior heat treatment [10]. However, the multiphase alloy prepared with a higher laser

power absorbed 2.3 wt.% of hydrogen in less than 25 min under the same hydrogenation conditions [10]. Sahlberg et al. investigated the alloy TiZrHfNbV and found that it could absorb 2.7 wt.% of hydrogen at 300 °C [12]. They pointed out that hydrogen desorbed completely at 500 °C under vacuum [13]. Kao et al. prepared by arc melting CoFeMnTi_xV_yZr_z alloys which have a single C14 Laves phase. The maximum capacity was 1.8 wt.% at room temperature with prior heat treatment at 400 °C [14]. Zepon et al. synthesized by high energy ball milling a nanocrystalline MgZrTiFe_{0.5}Co_{0.5}Ni_{0.5} HEA with a single BCC phase. This BCC alloy absorbed 1.2 wt.% at 350 °C under 20 bars of hydrogen [15]. These results indicate that HEAs have interesting hydrogen storage properties.

In the present work, the transition elements of period 4, Ti, V, Mn, Fe, and Ni, were selected. They are not all strong hydride forming elements, but not using the heavier elements of periods 5 or 6 means that the gravimetric hydrogen storage capacity may be higher. The composition was selected by taking into account the thermodynamic, geometric, and electronic parameters.

The phase formation is thermodynamically controlled by the Gibbs free energy ΔG . ΔG can be determined by Equation (1):

$$\Delta G_{\text{mix}} = \Delta H_{\text{mix}} - T\Delta S_{\text{mix}}, \quad (1)$$

where ΔH_{mix} is the enthalpy of mixing, ΔS_{mix} is the entropy of mixing of the alloys and T is the absolute temperature. ΔS_{mix} and ΔH_{mix} are calculated according to Formulas (2) and (3), respectively [6,16]:

$$\Delta S_{\text{mix}} = -R \sum_{i=1}^N C_i \ln C_i, \quad (2)$$

where R is the gas constant ($8.314 \text{ J} \cdot \text{mol}^{-1} \cdot \text{K}^{-1}$), N is the number of elements of the alloy, and C_i is the percentage of each element of the alloy.

$$\Delta H_{\text{mix}} = \sum_{i=1, i \neq j}^N 4\Delta H_{\text{AB}}^{\text{mix}} C_i C_j, \quad (3)$$

where $\Delta H_{\text{AB}}^{\text{mix}}$ is the binary enthalpy of equiatomic AB alloy taken from [17].

Yang and Zhang proposed a dimensionless parameter Ω that combines the effects of ΔS_{mix} and ΔH_{mix} [18]. Ω is defined as:

$$\Omega = \frac{T_m \Delta S_{\text{mix}}}{|\Delta H_{\text{mix}}|}, \quad (4)$$

where T_m is the melting temperature of the alloy determined by the rule of mixtures:

$$T_m = \sum_{i=1}^N C_i (T_m)_i, \quad (5)$$

where $(T_m)_i$ is the melting temperature of the i^{th} element.

The geometric parameter is characterized by the atomic size difference δ of the constituent elements. δ is calculated using the following relation [19]:

$$\delta\% = 100\% \sqrt{\sum_{i=1}^N C_i \left(1 - \frac{r_i}{\sum_{i=1}^N C_i r_i}\right)^2}, \quad (6)$$

where r_i is the atomic radius of element i .

Empirically, it was found that when $\Omega \geq 1.1$ and $\delta \leq 6.6\%$, the formation of solid solution phases are suggested [18].

The electronic parameter is the valence electron concentration (VEC) of the constituent elements. VEC predicts the phase selection between FCC and BCC type solid solutions [20]. It is given by Equation (7):

$$VEC = \sum_{i=1}^N C_i(VEC)_i, \quad (7)$$

where $(VEC)_i$ is the VEC for the i th element, which is the number of total electrons in the valence band including d electrons. The VECs of for Ti, V, Mn, Fe, and Ni are, respectively 4, 5, 7, 8, and 10. A value of VEC smaller than 6.87 means that BCC phase formation is favored over FCC [20].

Based on the criteria Ω , δ , and VEC, we selected the composition $Ti_{0.3}V_{0.3}Mn_{0.2}Fe_{0.1}Ni_{0.1}$. For this composition, ΔH_{mix} is equal to $-12.84 \text{ kJ}\cdot\text{mol}^{-1}$ and ΔS_{mix} is $12.51 \text{ J}\cdot\text{K}^{-1}\cdot\text{mol}^{-1}$, giving $\Omega = 1.84$. δ was calculated to be 5.4% using the atomic radii taken from [21]. VEC value was found to be 5.9 (data taken from [22]), which means that the BCC phase is most likely to occur. The aim of this investigation was to study the crystal structure and hydrogen storage properties of $Ti_{0.3}V_{0.3}Mn_{0.2}Fe_{0.1}Ni_{0.1}$ alloy synthesized by arc melting and ball milling. The effect of ball milling the as-cast alloy was also examined.

2. Materials and Methods

All raw materials, Ti sponge (99.9%), V pieces (99.9%), Mn chunks (99.9%), Fe pieces (99.9%), and Ni pieces (99%) were purchased from Alfa Aesar. The $Ti_{0.3}V_{0.3}Mn_{0.2}Fe_{0.1}Ni_{0.1}$ alloys were prepared by arc melting and by mechanical alloying after mixing all raw elements at the desired proportions. The subscripts mean the mole fractions of the constituent elements. The melting was done under 0.7 bars of argon. Each pellet was melted, turned over, and remelted three times to ensure good homogeneity. The as-cast alloys were hand-crushed using a hardened steel mortar and pestle. Ball milling was carried out on a SPEX high energy mill 8000 M in a hardened steel crucible and balls. The ball-to-metal mass ratio was 10 and milling was done for 1, 5, and 10 h. The crucible was loaded in an argon-filled glovebox. The hydrogen sorption properties were measured using a homemade Sievert's apparatus. The powder was filled in a reactor and kept under dynamic vacuum for one hour at room temperature before its exposure to hydrogen. The crystal structure was determined by X-ray powder diffraction using a Bruker D8 Focus with Cu $K\alpha$ radiation. Crystal structure parameters were evaluated from Rietveld refinement using Topas software [23]. Microstructure and chemical analysis were performed using a Hitachi Su1510 scanning electron microscopy (SEM) equipped with an EDX (energy-dispersive X-ray) apparatus from Oxford Instruments. The relative abundance of each phase was evaluated from micrographs using ImageJ software [24].

3. Results and Discussions

3.1. Microstructural Study

Figure 1 shows the backscattered electron micrograph of as-cast $Ti_{0.3}V_{0.3}Mn_{0.2}Fe_{0.1}Ni_{0.1}$ alloy.

The different shades of grey indicate a multiphase alloy. Using ImageJ, the area percentages for the bright, grey, and dark grey phases were found to be, respectively 66%, 25%, and 9%. Being the dominant phase, the bright phase is thereafter called "matrix".

The chemical composition of the alloy was determined by EDX measurement. Table 1 shows the bulk measured atomic abundance compared to the nominal composition. We see that the bulk measured composition agrees with the nominal one.

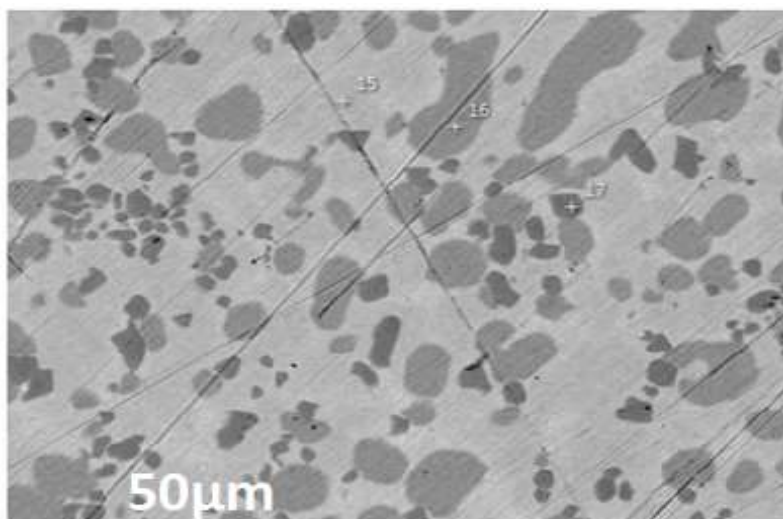


Figure 1. Backscattered electron (BSE) micrograph of as-cast $\text{Ti}_{0.3}\text{V}_{0.3}\text{Mn}_{0.2}\text{Fe}_{0.1}\text{Ni}_{0.1}$ alloy.

Table 1. Bulk atomic abundance: nominal and as measured by EDX of as-cast $\text{Ti}_{0.3}\text{V}_{0.3}\text{Mn}_{0.2}\text{Fe}_{0.1}\text{Ni}_{0.1}$ alloy. Error on the last significant digit is indicated in parentheses.

Element (at.%)	Ti	V	Mn	Fe	Ni
Nominal	30	30	20	10	10
Measured	29.4 (3)	30.8 (1)	19.1 (2)	10.4 (1)	10.3 (2)

Using EDX, we also measured the chemical composition of each phase. The EDX point analysis was performed at a higher magnification on the regions presented in Figure 2.

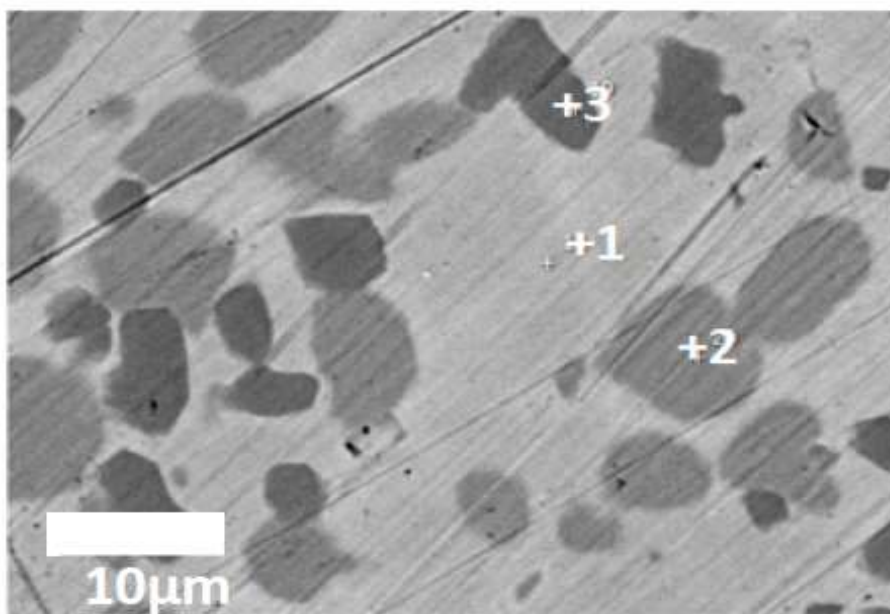


Figure 2. BSE micrograph of as-cast $\text{Ti}_{0.3}\text{V}_{0.3}\text{Mn}_{0.2}\text{Fe}_{0.1}\text{Ni}_{0.1}$ alloy.

In this micrograph, the matrix, grey, and dark grey phases are indicated by points number 1, 2, and 3, respectively. Their chemical composition is listed in Table 2.

Table 2. EDX analysis showing the elemental composition of all the phases of as-cast $\text{Ti}_{0.3}\text{V}_{0.3}\text{Mn}_{0.2}\text{Fe}_{0.1}\text{Ni}_{0.1}$ alloy. Error on all values is 1 at.%.

Element (at.%)	Ti	V	Mn	Fe	Ni
Matrix (Point 1)	32	23	19	11	15
Grey phase (Point 2)	16	51	21	9	3
Dark grey (Point 3)	51	13	11	11	14

The matrix is relatively close to the nominal composition, only slightly depleted in vanadium and rich in nickel. The major constituent of the grey phase is vanadium while titanium is the main element in the dark grey phase. Nickel and iron are mainly in the matrix and dark grey phase. Iron is uniformly distributed over all phases.

3.2. Crystal Structure

Figure 3 presents the XRD patterns of $\text{Ti}_{0.3}\text{V}_{0.3}\text{Mn}_{0.2}\text{Fe}_{0.1}\text{Ni}_{0.1}$ alloy in as-cast state. The following phases were found to give the best Rietveld refinement fit for this pattern: C14 Laves phase (space group $P6_3/mmc$, structure type MgZn_2), BCC phase (space group $Im-3m$, structure type W), and Ti_2Fe type phase (space group $Fd-3m:2$, structure type Ti_2Ni). The lattice parameters and the abundance of these phases are presented in Table 3.

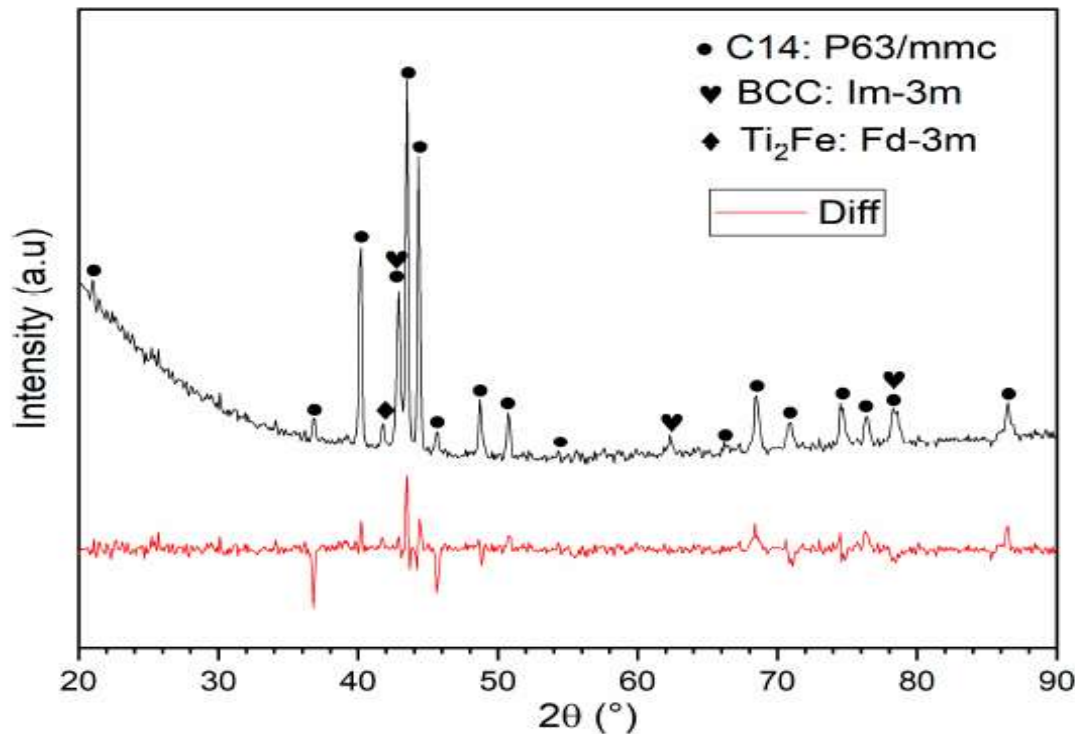


Figure 3. X-ray diffraction patterns of as-cast $\text{Ti}_{0.3}\text{V}_{0.3}\text{Mn}_{0.2}\text{Fe}_{0.1}\text{Ni}_{0.1}$ alloy. The bottom curve is the difference between calculated and measured intensities.

Table 3. Crystal parameters and abundance of each phase of as-cast $\text{Ti}_{0.3}\text{V}_{0.3}\text{Mn}_{0.2}\text{Fe}_{0.1}\text{Ni}_{0.1}$ alloy. Error on the last significant digit is indicated in parentheses.

Phase	Unit Cell Volume Å^3	Lattice Parameter Å	Crystallite Size nm	Micro-Strain %	Abundance %
C14	164.98 (3)	a = 4.8900 (4) c = 7.9651 (9)	125 (48)	0.04 (1)	79
BCC	26.58 (1)	2.9841 (5)	31 (5)	—	17
Ti_2Fe	1418 (3)	11.234 (8)	—	—	4

Correlating the abundance of the phases as measured by ImageJ software with the percentage of phases as determined by Rietveld's analysis, we see that the C14 phase may be associated with the matrix. From Table 2, the matrix composition could be written $Ti_{0.96}V_{0.69}Mn_{0.57}Fe_{0.33}Ni_{0.45}$. For the relatively close composition $Ti_1V_{0.64}Mn_{0.81}Fe_{0.15}Ni_{0.4}$, Song et al. found that the crystal structure was C14 [25]. Therefore, it is reasonable to associate the C14 crystal structure with the matrix phase. In their analysis, Song et al. assigned Ti to the 4*f* site and the other atoms were evenly distributed on the other two sites (2*a* and 6*h*) [25]. From the chemical composition of the matrix presented in Table 2, we see that the same assignation could be done here.

The abundance of the BCC phase roughly matches the abundance of the grey phase. Again, using Table 2 we could assume that the BCC phase has a composition of $Ti_{0.16}V_{0.51}Mn_{0.21}Fe_{0.09}Ni_{0.03}$. This is supported by the fact that there is a wide range of $Ti_{1-x}V_xMn_y$ that has the BCC structure [26–34]. The least abundant phase (dark grey) has a composition that could be written as $Ti_{1.53}V_{0.39}Mn_{0.33}Fe_{0.33}Ni_{0.42}$. The diffraction pattern indicates the presence of a Ti_2Fe -like phase, which roughly matches the abundance of the dark grey phase. As Ti_2Ni is the structure type of Ti_2Fe , it is reasonable to assume that the dark grey phase has the Ti_2Fe structure with vanadium most likely substituted for Ti and Mn substituting for Ni/Fe.

According to the criteria used for Ω , δ , and VEC, the as-cast $Ti_{0.3}V_{0.3}Mn_{0.2}Fe_{0.1}Ni_{0.1}$ alloy should adopt a BCC phase. However, the main phase found is the C14 phase instead of BCC. One can see that Ω is 1.84 higher than the condition proposed by Yang and Zhang [18]. However, the absolute of ΔH_{mix} ($12.84 \text{ kJ}\cdot\text{mol}^{-1}$) is not small enough for the entropy effect to be the dominant term. This means that the formation of ordered intermetallic compounds with solid solution are expected to form [19].

3.3. First Hydrogenation Properties

Figure 4 shows the first hydrogenation (activation) curve of the as-cast alloy. The activation was performed at room temperature under a hydrogen pressure of 20 bars without any prior treatment.

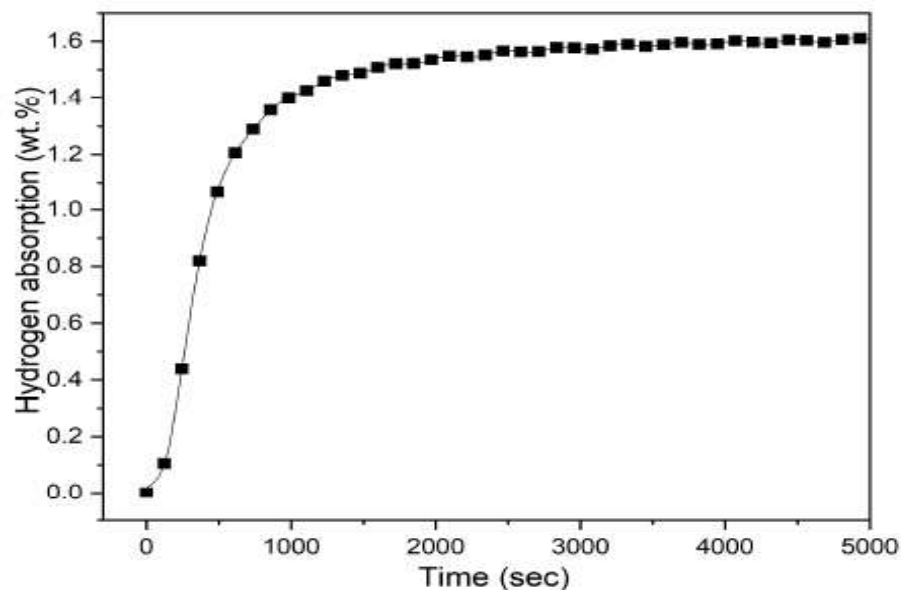


Figure 4. Activation curve of as-cast $Ti_{0.3}V_{0.3}Mn_{0.2}Fe_{0.1}Ni_{0.1}$ alloy.

The alloy absorbs hydrogen, reaching a maximum capacity of 1.6 wt.% within one hour. Even if the alloy is multiphase, the activation curve seems to behave as a single-phase absorption.

In an attempt to find the crystal structure of the hydride alloy, the experiment was stopped after reaching full hydrogenation and the powder immediately prepared for X-ray diffraction. The result is presented in Figure 5. The crystal parameters and abundance of each phase as determined by Rietveld's refinement are shown in Table 4.

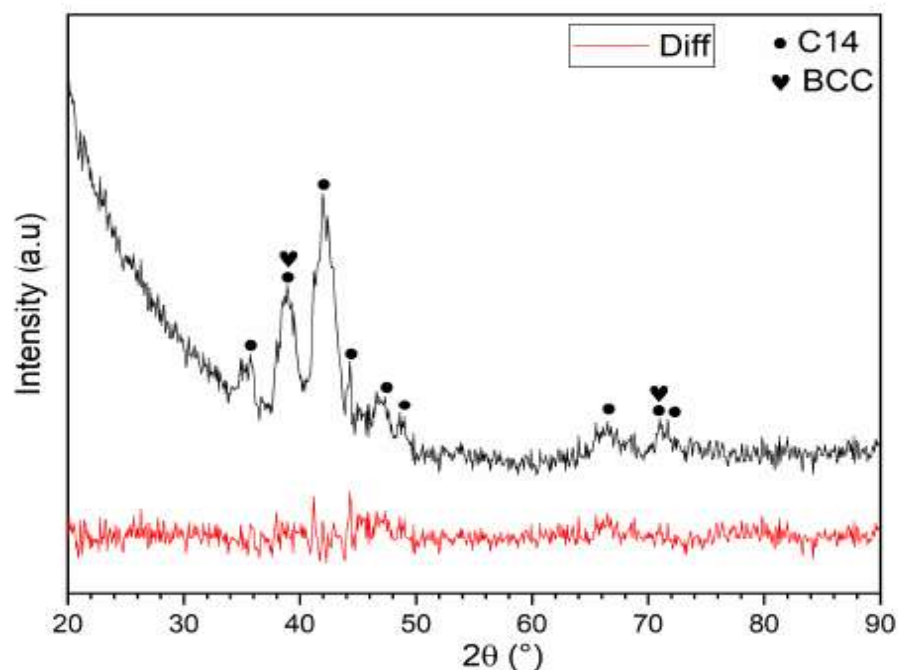


Figure 5. XRD patterns of the hydride sample.

Table 4. Crystal structure parameters and abundance of each phase in the hydride sample. Error on the last significant digit is indicated in parentheses.

Phase	Unit Cell Volume \AA^3	Lattice Parameter \AA	Crystallite Size nm	Micro-Strain %	Abundance %
C14	187.85 (9)	a = 5.1091 (1) c = 8.2835 (2)	11 (3)	0.62 (3)	92
BCC	34.5 (2)	3.257 (6)	7 (2)	—	8

Compared to the as-cast sample, the abundance of C14 increased from 79% to 92%, while the abundance of BCC phase decreased from 17% to 8%. There was no evidence of Ti_2Fe like phase in the hydride pattern. From the lattice expansion of each phase and assuming that the volume taken by a hydrogen atom is 2.9 \AA^3 [35], the amount of hydrogen in each hydride phase could be estimated. Table 5 presents the volume expansion of the hydride phases with the estimated value of hydrogen per metallic atom (H/M) and corresponding wt.%. We see that, for the C14 phase, the H/M ratio is 2.0, which corresponds to the dihydride. In the case of the BCC phase, the H/M is 1.4. It is known that upon hydrogenation a BCC phase adopts a BCT (body centered tetragonal) structure for the monohydride and an FCC (face centered cubic) dihydride. It is therefore strange that, in the present case, the BCC phase absorbed up to H/M 1.4 but still maintained the BCC structure. However, it has been shown that for the HEA TiVZrHfNb [12,13] and TiVZrNbHf-based HEAs the BCT structure could have a H/M of 2. In the present case, the crystal structure is indexed to a BCC, but the broadness of the peaks and the overlap with C14 peaks makes it difficult to clearly distinguish between a BCC and BCT structure.

Table 5. Estimated capacity of the phases in the hydrided sample.

Phase	Volume Expansion (\AA^3)	H/M	Estimated Capacity of the Phase (wt.%)
C14	22.9	2.0	1.2
BCC	7.9	1.4	2.6

From Table 5 and taking into consideration the abundance of each phase, the estimated amount of hydrogen in the hydride sample is about 1.3 wt.%. This is relatively far from the measured capacity of 1.6 wt.%. However, as the pattern was taken at room temperature and in air, there is a possibility that some desorption occurred. Therefore, we can not be absolutely certain that the pattern shown in Figure 5 is for a fully hydride sample. However, this is an indication that the hydride phase is probably very stable at room temperature.

3.4. Air Exposure Effect

It is easier to handle the alloy in the air rather than in argon atmosphere. This stimulated us to study the air exposure effect on the as-cast $\text{Ti}_{0.3}\text{V}_{0.3}\text{Mn}_{0.2}\text{Fe}_{0.1}\text{Ni}_{0.1}$ alloy. Figure 6 shows the activation curves of the crushed alloy crushed under argon and in air. After crushing in air, the sample was also further exposed to the air for two and five days.

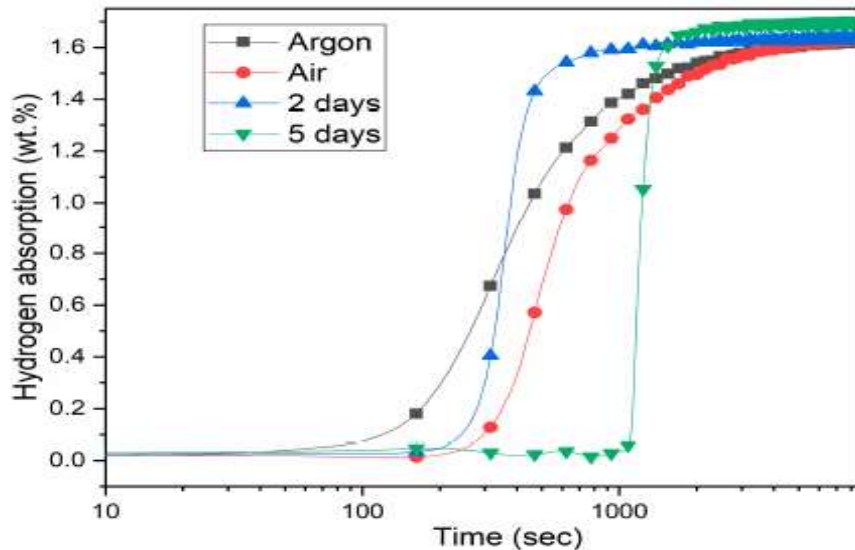


Figure 6. Activation curves at room temperature under 20 bars of hydrogen of as-cast $\text{Ti}_{0.3}\text{V}_{0.3}\text{Mn}_{0.2}\text{Fe}_{0.1}\text{Ni}_{0.1}$ alloy crushed in argon and air. The sample crushed in air was further exposed for two and five days.

The sample crushed in argon has 40 s incubation time while the one crushed in air needed 200 s before absorbing hydrogen. However, the intrinsic kinetic (tangent at mid capacity) was the same for the samples crushed in air or argon. Surprisingly, two days of air exposure did not change the incubation time but the intrinsic kinetic was about four times faster than the sample simply crushed in air. The sample exposed for five days has the longest incubation time of 1080 s. The intrinsic kinetic was slower than the two-day air exposed but still about three times faster than the air crushed sample. This long incubation time is probably related to the thick oxide layer caused by the long exposure to air. We have seen from the TiFe alloy that the presence of some level of oxide could speed up the intrinsic kinetics of hydrogenation [36]. The faster intrinsic kinetic of the air exposed samples may be due to the catalytic effect of the TiO_2 layer on the surface. However, this has to be confirmed in a dedicated investigation. It should be noted that air exposure did not reduce the hydrogen capacity.

3.5. Synthesis by Mechanical Alloying

The $\text{Ti}_{0.3}\text{V}_{0.3}\text{Mn}_{0.2}\text{Fe}_{0.1}\text{Ni}_{0.1}$ alloy was also synthesized by mechanical alloying. To synthesize the alloy, the raw materials Ti, V, Mn, Fe and Ni were mixed in the desired proportion and milled for 1, 5, and 10 h. Figure 7 presents the evolution of XRD patterns of the milled powder.

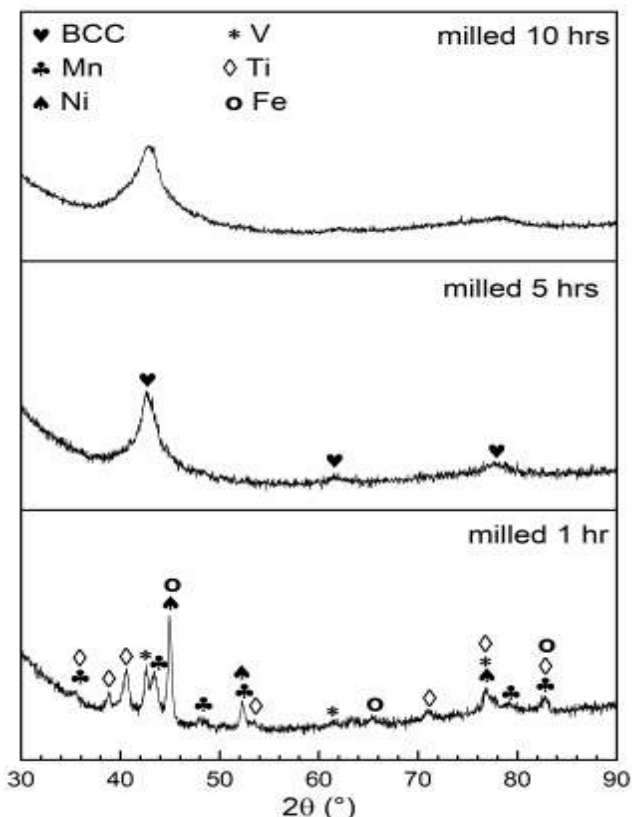


Figure 7. XRD patterns of Ti-V-Mn-Fe-Ni powders milled for 1, 5, and 10 h.

After one hour of milling, the Bragg peaks from all raw elements are still present. The five-hour milled pattern shows the formation of a BCC phase. Milling for 10 h leads to further broadening of the BCC peaks. The diffraction patterns were analyzed by Rietveld's refinement and the obtained crystal parameters of the BCC phase are shown in Table 6.

Table 6. Crystal parameters of the BCC phase of the samples milled for 5 and 10 h. Error on the last significant digit is indicated in parentheses.

Milling Time (hr)	Unit Cell Volume (\AA^3)	Lattice Parameter (\AA)	Crystallite Size (nm)
5	28.0 (2)	3.035 (6)	2.30 (5)
10	27.7 (4)	3.03 (1)	1.40 (2)

We see that after the formation of a BCC phase, further milling essentially reduces the crystallite size. Actually, such a small crystallite size means that the structure is very close to amorphous. For this reason, the first hydrogenation tests were done on the sample milled for five hours as this sample is most likely to have a true BCC structure. It should be noted that the lattice parameter of the BCC phase of the ball milled sample is bigger than the BCC phase of the as-cast alloy by around 1.7%. This may be explained by the fact that the milled BCC has the exact nominal composition while the BCC formed by arc melting

is slightly depleted in vanadium (the biggest atomic radius) and enriched in nickel (the smallest atomic radius).

3.6. Effect of Milling on As-Cast Alloy

We investigated the effect of ball milling for 1, 5, and 10 h on as-cast $\text{Ti}_{0.3}\text{V}_{0.3}\text{Mn}_{0.2}\text{Fe}_{0.1}\text{Ni}_{0.1}$ alloy. The X-ray patterns are shown in Figure 8.

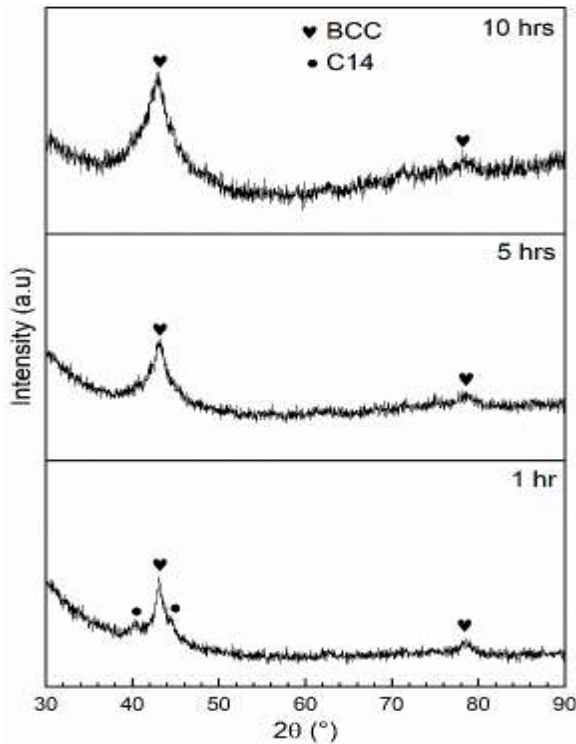


Figure 8. X-ray diffraction patterns of as-cast $\text{Ti}_{0.3}\text{V}_{0.3}\text{Mn}_{0.2}\text{Fe}_{0.1}\text{Ni}_{0.1}$ alloy before and after milling for 1, 5, and 10 h.

Before milling, the $\text{Ti}_{0.3}\text{V}_{0.3}\text{Mn}_{0.2}\text{Fe}_{0.1}\text{Ni}_{0.1}$ alloy was multiphase with C14, BCC, and Ti_2Fe -type phases. After milling for one hour, the crystal structure was mainly BCC with some C14 phase. The peaks of the Ti_2Fe type phase could not be identified. After five hours of milling, only broad BCC peaks were present. A similar result was obtained by Amira et al. who studied the effect of ball milling on cast TiCr_x alloys. They found that TiCr_x transforms from a mixture of C14 and C15 Laves phases to a metastable BCC phase after milling five hours under argon [37]. In the present case, as expected, further milling to 10 h had the effect of decreasing the crystallite size and thus broadening the Bragg's peaks of the BCC phase. Additionally, the Bragg's BCC peak is shifted to lower angles with milling time. This is an indication of the increasing lattice parameter of the BCC phase. Table 7 lists the crystal structure parameters and the abundance of each phase in the cast alloy before and after milling as given by Rietveld's refinement.

In the case of C14 phase, milling up to 1 h does not significantly change the lattice parameters and the unit cell volume but it causes an important decrease in the crystallite size. For the BCC phase, with milling the lattice parameter increases and the crystallite size is reduced to approximately one nanometer after 10 h.

Milling the cast alloy produced similar results to milling the raw elements. As in the case of milling the raw elements, we selected the five-hour-milled sample to perform the hydrogenation test.

Table 7. Crystal parameters and abundance of each phase in as-cast $\text{Ti}_{0.3}\text{V}_{0.3}\text{Mn}_{0.2}\text{Fe}_{0.1}\text{Ni}_{0.1}$ alloy before and after milling. Error on the last significant digit is indicated in parentheses.

Milling Time (hr)	Phase	Unit Cell Volume (\AA^3)	Lattice Parameter (\AA)	Crystallite Size (nm)	Abundance (%)
0	C14	164.98 (3)	a = 4.8900 (4) c = 7.9651 (9)	125 (48)	79
	BCC	26.58 (1)	2.9841 (5)	31 (5)	17
	Ti_2Fe	1418 (3)	11.234 (8)	—	4
1	C14	165.9 (6)	4.897 (7) 7.989 (2)	13.0 (2)	36
	BCC	27.02 (1)	3.001 (4)	4.0 (2)	64
5	BCC	27.60 (4)	3.02 (1)	1.88 (6)	100
10	BCC	28.60 (4)	3.06 (1)	1.12 (3)	100

3.7. First Hydrogenation of the Milled Raw Powder and the Alloy

The first hydrogenation of both samples formed after five hours of milling is shown in Figure 9 and compared to the as-cast alloy. The measurements were performed at room temperature under a hydrogen pressure of 20 bars without any prior treatment.

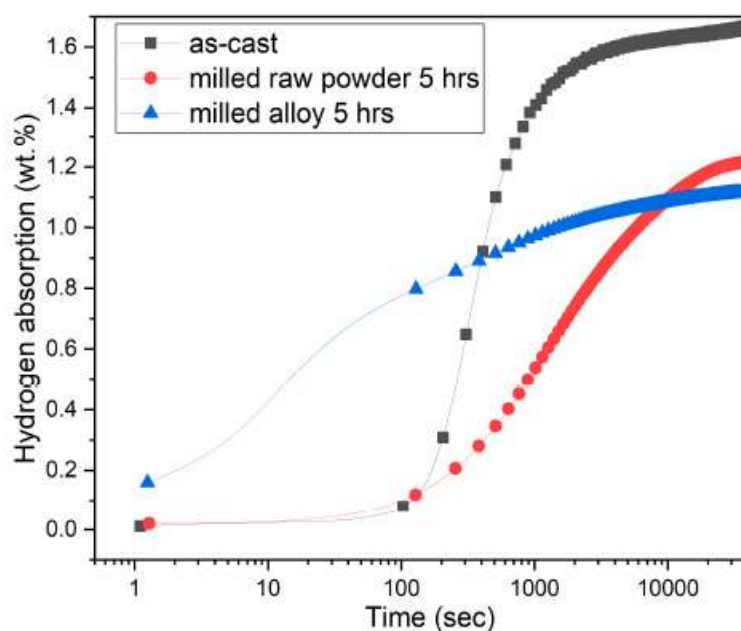


Figure 9. Activation curves of the milled raw powder for five hours, the as-cast alloy further milled for five hours, and the as-cast one.

The milled raw powder and the as-cast alloy have the same incubation time. The maximum capacity reached by the milled raw powder sample is 1.2 wt.% H, which is lower than the capacity of the as-cast alloy (1.6 wt.%). The reduction in capacity is most likely due to the reduction in crystallite size. Assuming that the grain boundaries are just one unit cell thick, the grain boundary volume for the five-hour ball milled materials is almost 50%. This grain boundary most probably does not store hydrogen at the same level as the BCC phase. Therefore, the total capacity is severely lowered. The same effect was seen for the TiFe alloy [38].

The milled alloy readily absorbs hydrogen without incubation time. In our apparatus, the first second of absorption is not recorded. Additionally, we see an initial capacity of 0.16 wt.%, therefore we assume that the real capacity of the milled alloy should be increased

by about 0.1 wt.%. Therefore, the total capacity of this alloy is probably around 1.2 wt.%, which is the same capacity obtained by milling the raw elements for five hours. Figure 10 shows the XRD patterns of the hydrogenated alloys after full hydrogenation.

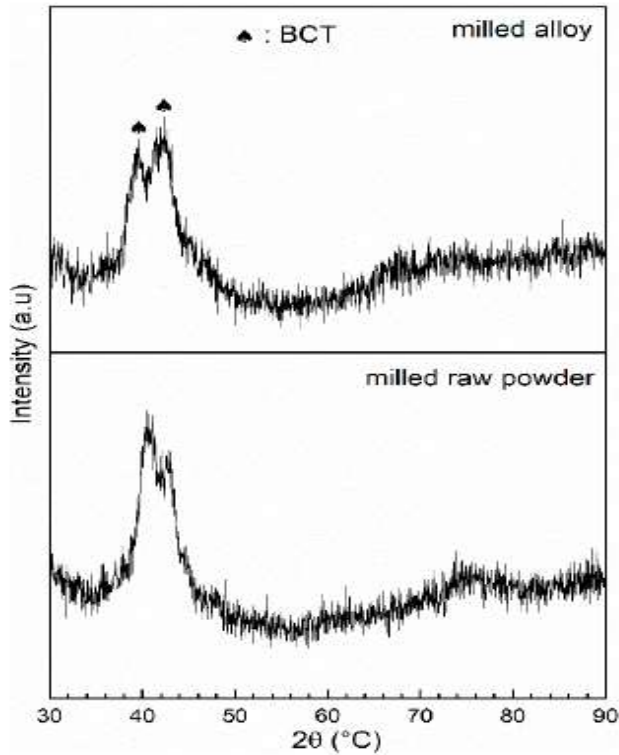


Figure 10. XRD patterns of the milled raw powder and milled alloy in the hydrogenated state.

Upon hydrogenation, the crystal structure of both samples is BCT of space group $I4/mmm$. It was shown by Nakamura and Akiba that the monohydride of the BCC phase has a BCT (body centered tetragonal) structure [39]. The transformation into BCT instead of the dihydride FCC could be because of a high hysteresis. From Rietveld's analysis, the crystal structure parameters of the BCT phase for milling the raw materials are the same as for the milled alloy. The unit cell volume is $30.1 (5) \text{ \AA}^3$, $a = 2.99 (2) \text{ \AA}$ and $c = 3.36 (3) \text{ \AA}$. The crystallite size is $1.51 (5) \text{ nm}$. The c/a ratio of the BCT phase is 1.12, which is in agreement with cases where the distortion of the lattice caused by hydrogen is along the c -axis [40]. Taking into account that each hydrogen atom occupies a volume of 2.9 \AA^3 , we could estimate that the BCC phase in the hydrogenated state has a capacity of around 0.7 wt.%, which is smaller than the measured capacity of 1.2 wt.%. However, as indicated above, because the X-ray diffraction was under air, there is a likelihood that the sample partially desorbed.

4. Conclusions

The alloy $\text{Ti}_{0.3}\text{V}_{0.3}\text{Mn}_{0.2}\text{Fe}_{0.1}\text{Ni}_{0.1}$ was successfully synthesized by arc-melting and mechanical alloying. The arc-melted alloy has a multiphase structure, with a main C14 Laves phase matrix along with a BCC phase and a small amount of Ti_2Fe -type phase. Its maximum hydrogen storage capacity was 1.6 wt.%. Upon hydrogenation, the Ti_2Fe -type phase disappeared. The initial C14 and BCC phases were converted into the C14 and BCC hydrides, respectively. The H/M value was 1.4 in the hydride BCC. Air exposure for two or five days has no impact on the hydrogen capacity but changed the kinetics.

Synthesis by mechanical alloying for five hours resulted in an alloy with BCC structure. The hydrogen capacity of the milled alloy was lower than the as-cast one. The BCC structure

transforms after hydrogen absorption (under 20 bars of H₂) to monohydride phase “BCT” and not to dihydride “FCC”. The effect of ball milling of the as-cast alloy was also studied. Ball milling for five hours produced a BCC structure similar to the one obtained by milling the raw elements for five hours. The first hydrogenation measurements showed that milling for five hours leads to a faster kinetics compared to the as-cast sample but with a reduced capacity. The synthesis of Ti_{0.3}V_{0.3}Mn_{0.2}Fe_{0.1}Ni_{0.1} by arc-melting is better than by mechanical alloying because arc-melted alloy shows a higher capacity.

Author Contributions: All experiments, except electron microscopy, were performed by S.S. and M.M. under the supervision of J.H. J.H. and S.S. analyzed the results and wrote the paper. All authors have read and agreed to the published version of the manuscript.

Funding: This research was funded in part by an NSERC Discovery grant RGPIN-2017-06637.

Acknowledgments: We would like to thank Agnes Lejeune for performing the electron microscopy experiments.

Conflicts of Interest: The authors declare no conflict of interest.



References

1. Anstrom, J. Hydrogen as a fuel in transportation. In *Advances in Hydrogen Production, Storage and Distribution*; Basile, A., Lulianelli, A., Eds.; Elsevier: Amsterdam, The Netherlands, 2014; pp. 499–524.
2. Schlapbach, L.; Züttel, A. Hydrogen-storage materials for mobile applications. In *Materials for Sustainable Energy*; Co-Published with Macmillan Publishers Ltd.: London, UK, 2012; pp. 265–270. [CrossRef]
3. Züttel, A.; Remhof, A.; Borgschulte, A.; Friedrichs, O. Hydrogen: The future energy carrier. *Philos. Trans. R. Soc. Lond. A Math. Phys. Eng. Sci.* **2010**, *368*, 3329–3342. [CrossRef] [PubMed]
4. Reilly, J. Metal hydride technology. *Z. Für Phys. Chem.* **1979**, *117*, 155–184. [CrossRef]
5. Cantor, B.; Chang, I.; Knight, P.; Vincent, A. Microstructural development in equiatomic multicomponent alloys. *Mater. Sci. Eng. A* **2004**, *375*, 213–218. [CrossRef]
6. Yeh, J.W.; Chen, S.K.; Lin, S.J.; Gan, J.Y.; Chin, T.S.; Shun, T.T.; Tsau, C.H.; Chang, S.Y. Nanostructured high-entropy alloys with multiple principal elements: Novel alloy design concepts and outcomes. *Adv. Eng. Mater.* **2004**, *6*, 299–303. [CrossRef]
7. Gao, M.C.; Yeh, J.-W.; Liaw, P.K.; Zhang, Y. *High-Entropy Alloys: Fundamentals and Applications*; Springer: Berlin/Heidelberg, Germany, 2016.
8. Zhang, W.; Liaw, P.K.; Zhang, Y. Science and technology in high-entropy alloys. *Sci. China Mater.* **2018**, *61*, 1–21. [CrossRef]
9. Kunce, I.; Polanski, M.; Bystrzycki, J. Structure and hydrogen storage properties of a high entropy ZrTiVCrFeNi alloy synthesized using Laser Engineered Net Shaping (LENS). *Int. J. Hydrogen Energy* **2013**, *38*, 12180–12189. [CrossRef]
10. Kunce, I.; Polanski, M.; Bystrzycki, J. Microstructure and hydrogen storage properties of a TiZrNbMoV high entropy alloy synthesized using Laser Engineered Net Shaping (LENS). *Int. J. Hydrogen Energy* **2014**, *39*, 9904–9910. [CrossRef]
11. Kunce, I.; Polański, M.; Czujko, T. Microstructures and hydrogen storage properties of LaNiFeVMn alloys. *Int. J. Hydrogen Energy* **2017**, *42*, 27154–27164. [CrossRef]
12. Sahlberg, M.; Karlsson, D.; Zlotea, C.; Jansson, U. Superior hydrogen storage in high entropy alloys. *Sci. Rep.* **2016**, *6*, 36770. [CrossRef]
13. Karlsson, D.; Ek, G.; Cedervall, J.; Zlotea, C.; Möller, K.T.; Hansen, T.C.; Bednarcik, J.; Paskevicius, M.; Sørby, M.H.; Jensen, T.R. Structure and hydrogenation properties of a HfNbTiVZr high-entropy alloy. *Inorg. Chem.* **2018**, *57*, 2103–2110. [CrossRef]
14. Kao, Y.-F.; Chen, S.-K.; Sheu, J.-H.; Lin, J.-T.; Lin, W.-E.; Yeh, J.-W.; Lin, S.-J.; Liou, T.-H.; Wang, C.-W. Hydrogen storage properties of multi-principal-component CoFeMnTi_xV_yZr_z alloys. *Int. J. Hydrogen Energy* **2010**, *35*, 9046–9059. [CrossRef]
15. Zepon, G.; Leiva, D.; Strozi, R.; Bedoch, A.; Figueroa, S.; Ishikawa, T.; Botta, W. Hydrogen-induced phase transition of MgZrTiFe 0.5 Co 0.5 Ni 0.5 high entropy alloy. *Int. J. Hydrogen Energy* **2018**, *43*, 1702–1708. [CrossRef]
16. Zhang, Y.; Zhou, Y.J.; Lin, J.P.; Chen, G.L.; Liaw, P.K. Solid-solution phase formation rules for multi-component alloys. *Adv. Eng. Mater.* **2008**, *10*, 534–538. [CrossRef]
17. Takeuchi, A.; Inoue, A. Classification of Bulk Metallic Glasses by Atomic Size Difference, Heat of Mixing and Period of Constituent Elements and Its Application to Characterization of the Main Alloying Element. *Mater. Trans.* **2005**, *46*, 2817–2829. [CrossRef]
18. Yang, X.; Zhang, Y. Prediction of high-entropy stabilized solid-solution in multi-component alloys. *Mater. Chem. Phys.* **2012**, *132*, 233–238. [CrossRef]
19. Zhang, Y.; Lu, Z.; Ma, S.; Liaw, P.; Tang, Z.; Cheng, Y.; Gao, M. Guidelines in predicting phase formation of high-entropy alloys. *Mrs Commun.* **2014**, *4*, 57–62. [CrossRef]
20. Guo, S.; Ng, C.; Lu, J.; Liu, C. Effect of valence electron concentration on stability of fcc or bcc phase in high entropy alloys. *J. Appl. Phys.* **2011**, *109*, 103505. [CrossRef]
21. Elements, Atomic Radii and the Periodic Table. Available online: <http://www.crystallmaker.com/support/tutorials/atomic-radii/> (accessed on 12 February 2021).

22. Ptable. Available online: <https://www.ptable.com/> (accessed on 12 February 2021).
23. Bruker, A. Topas V3: General profile and structure analysis software for powder diffraction data–user’s manual. In *Coelho Software*; TOPAS Academic: Brisbane, Australia, 2005.
24. Collins, T.J. ImageJ for microscopy. *Biotechniques* **2007**, *43*, 25–30. [[CrossRef](#)] [[PubMed](#)]
25. Deying, S.; Xueping, G.; Yunshi, Z.; Jie, Y.; Panwen, S. Characteristics of titanium-based C14-type Laves phase alloys and their hydride electrodes. *J. Alloys Compd.* **1994**, *206*, 43–46. [[CrossRef](#)]
26. Challet, S.; Latroche, M.; Heurtaux, F. Hydrogenation properties and crystal structure of the single BCC (Ti_{0.355}V_{0.645})_{100–x}M_x alloys with M = Mn, Fe, Co, Ni (x = 7, 14 and 21). *J. Alloys Compd.* **2007**, *439*, 294–301. [[CrossRef](#)]
27. Couillaud, S.; Enoki, H.; Amira, S.; Bobet, J.-L.; Akiba, E.; Huot, J. Effect of ball milling and cold rolling on hydrogen storage properties of nanocrystalline TiV_{1.6}Mn_{0.4} alloy. *J. Alloys Compd.* **2009**, *484*, 154–158. [[CrossRef](#)]
28. Aleksanyan, A.; Dolukhanyan, S.; Ter-Galstyan, O.; Mnatsakanyan, N. Hydride cycle formation of ternary alloys in TiVMn system and their interaction with hydrogen. *Int. J. Hydrogen Energy* **2016**, *41*, 13521–13530. [[CrossRef](#)]
29. Huang, T.; Wu, Z.; Sun, G.; Xu, N. Microstructure and hydrogen storage characteristics of TiMn_{2–x}V_x alloys. *Intermetallics* **2007**, *15*, 593–598. [[CrossRef](#)]
30. Nakamura, Y.; Nakamura, J.; Sakaki, K.; Asano, K.; Akiba, E. Hydrogenation properties of Ti–V–Mn alloys with a BCC structure containing high and low oxygen concentrations. *J. Alloys Compd.* **2011**, *509*, 1841–1847. [[CrossRef](#)]
31. Bibienne, T.; Tousignant, M.; Bobet, J.-L.; Huot, J. Synthesis and hydrogen sorption properties of TiV (2–x) Mn_x BCC alloys. *J. Alloys Compd.* **2015**, *624*, 247–250. [[CrossRef](#)]
32. Huot, J.; Enoki, H.; Akiba, E. Synthesis, phase transformation, and hydrogen storage properties of ball-milled TiV_{0.9}Mn_{1.1}. *J. Alloys Compd.* **2008**, *453*, 203–209. [[CrossRef](#)]
33. Huot, J.; Akiba, E.; Ishido, Y. Crystal structure of multiphase alloys (zr, ti)(mn, v) 2. *J. Alloys Compd.* **1995**, *231*, 85–89. [[CrossRef](#)]
34. Huot, J.; Akiba, E.; Iba, H. Crystal structure and phase composition of alloys Zr_{1–x}Ti_x(Mn_{1–y}V_y)₂. *J. Alloys Compd.* **1995**, *228*, 181–187. [[CrossRef](#)]
35. Peisl, H. Lattice strains due to hydrogen in metals. In *Hydrogen in Metals I*; Springer: Berlin/Heidelberg, Germany, 1978; pp. 53–74.
36. Gosselin, C.; Huot, J. Hydrogenation properties of tife doped with zirconium. *Materials* **2015**, *8*, 7864–7872. [[CrossRef](#)]
37. Amira, S.; Santos, S.; Huot, J. Hydrogen sorption properties of Ti–Cr alloys synthesized by ball milling and cold rolling. *Intermetallics* **2010**, *18*, 140–144. [[CrossRef](#)]
38. Lv, P.; Guzik, M.N.; Sartori, S.; Huot, J. Effect of ball milling and cryomilling on the microstructure and first hydrogenation properties of tife+ 4 wt.% zr alloy. *J. Mater. Res. Technol.* **2019**, *8*, 1828–1834. [[CrossRef](#)]
39. Nakamura, Y.; Akiba, E. Hydriding properties and crystal structure of nacl-type mono-hydrides formed from ti–v–mn bcc solid solutions. *J. Alloys Compd.* **2002**, *345*, 175–182. [[CrossRef](#)]
40. Fukai, Y. *The Metal-Hydrogen System: Basic Bulk Properties*; Springer Science & Business Media: Berlin/Heidelberg, Germany, 2006; Volume 21.

Article

Enhancement of First Hydrogenation of $\text{Ti}_1\text{V}_{0.9}\text{Cr}_{1.1}$ BCC Alloy by Cold Rolling and Ball Milling

Salma Sleiman ¹, Anis Aliouat ²  and Jacques Huot ^{1,*} 

¹ Hydrogen Research Institute, Université du Québec à Trois-Rivières, 3351 des Forges, Trois-Rivières, QC G9A 5H7, Canada; salma.sleiman@uqtr.ca

² Faculty of Sciences, Université de Poitiers, 15, rue de l'Hôtel Dieu—TSA 71117, 86073 Poitiers CEDEX 9, France; aliouat.anis78@gmail.com

* Correspondence: jacques.huot@irh.ca or jacques.huot@uqtr.ca; Tel.: +1-819-376-5011 (ext. 3576)

Received: 27 May 2020; Accepted: 4 July 2020; Published: 12 July 2020



Abstract: In this study, we evaluated the effects of a mechanical treatment by cold rolling (CR) and ball milling (BM) on the first hydrogenation of $\text{Ti}_1\text{V}_{0.9}\text{Cr}_{1.1}$ alloy. The as-cast alloy has a body-centered cubic (BCC) crystal structure, and the first hydrogenation at room temperature under 20 bars of hydrogen is practically impossible. However, the samples mechanically activated by CR or BM readily absorbed hydrogen. The sample cold-rolled for one pass exhibited faster kinetics than the sample ball-milled for five minutes, but both samples reached the same storage capacity of 3.6 wt % hydrogen. Increasing the amount of rolling or the milling time decreased the hydrogen capacity. CR is considered the best and most efficient method for the activation of $\text{Ti}_1\text{V}_{0.9}\text{Cr}_{1.1}$ alloy.

Keywords: BCC alloys; kinetics; cold rolling; ball milling; hydrogen storage

1. Introduction

Metal hydrides are considered reliable and safe materials for storing hydrogen at a reasonable temperature and pressure, with relatively low cost and high hydrogen storage volumetric density [1–3]. Among them, the Ti–V–Cr system has been intensively studied as an attractive material for hydrogen storage due to its relatively high absorption capacity of up to 3.7 wt % in mild conditions [4–6]. The Ti–V–Cr system has tunable hydrogen sorption properties due to the wide range of possible chemical compositions [7–9]. For instance, the cyclic performance of $\text{Ti}_{21.5}\text{V}_{40}\text{Cr}_{38.5}$ alloy was found to be more durable than that of $\text{Ti}_{32}\text{V}_{20}\text{Cr}_{48}$ [8]. Lin et al. found that the $\text{Ti}_{0.8}\text{Cr}_{1.2}\text{V}$ alloy have better cyclic hydrogen properties than TiCrV alloy [10]. Another example is $(\text{TiCr}_{1.8})_{0.6}\text{V}_{0.4}$, which has the highest reversible hydrogen capacity among the series of $(\text{TiCr}_{1.8})_{1-x}\text{V}_x$ alloys with $x = 0.2, 0.6,$ and 0.8 [9]. However, the Ti–V–Cr system shows slow hydrogen sorption kinetics, and the first hydrogenation is usually difficult [11]. From a practical point of view, the first hydrogenation (also called activation) is an important aspect. It may require high pressure and temperature and thus increases the cost of the hydride. The sluggish first hydrogenation is usually explained by the presence of a surface oxide that blocks hydrogen diffusion. Generally, to force hydrogen through the oxide layers, activation at high temperature and high hydrogen pressure is needed [12,13]. There is no formal method to determine the temperature and pressure of activation. For this reason, we decided to conduct the first hydrogenation at room temperature and 20 bars of hydrogen. These are the usual working conditions of the alloys.

Alloying Ti–V–Cr alloys with Zr [14–16] or $\text{Zr}_7\text{Ni}_{10}$ [17,18] results in improvement of the activation and kinetics of absorption. This improvement has been explained by the appearance of a secondary phase, which acts as a gateway for hydrogen to reach the main phase. Heat treatment could also enhance the first hydrogenation by changing the alloy's microstructure [19–21]. Nanocrystallinity, achieved by ball milling (BM), improves the activation kinetics [22–24], potentially related to the

increase in interfaces and the specific surface area [25]. Small particle size also beneficial affects activation [26]. In a theoretical investigation, Shelyapina et al. showed that the disordered BCC solid solution is more stable than the ordered AB₂ compound [27]. Thus, we expected that our Ti–V–Cr alloy would have the BCC structure, and the full hydride phase would be the face-centered cubic (FCC) structure.

Mechanical deformation techniques including BM, cold rolling (CR), high-pressure torsion (HPT), and equal channel angular pressure (ECAP) are efficient in reducing crystallite size and introducing defects in materials, which improve the hydrogenation kinetics [28]. Among these deformation techniques, CR can be considered more promising from an industrial point of view due to its simplicity and easy scalability [29–32]. In addition, CR is an efficient method for regenerating air-exposed samples [33,34].

In a previous investigation, we showed that Ti₁V_{0.9}Cr_{1.1} alloy can be easily activated when a small amount of Zr (4 wt %) is added to the melt. This easy activation was attributed to the presence of a Zr-rich secondary phase [14]. Here, we aimed to see if mechanical treatment could be as effective as the addition of Zr for the enhancement of first hydrogenation. Thus, the Ti₁V_{0.9}Cr_{1.1} alloy was processed using CR and BM, and the effects of mechanical deformation on the first hydrogenation and microstructure investigated.

2. Materials and Methods

The raw materials Ti sponge (99.95%), V pieces (99%), and Cr pieces (99%) were purchased from Alfa-Aesar and used without further purification. The alloy was prepared by arc melting after mixing all the raw elements in the desired proportion. The melting was performed under 0.7 bars of argon. Each pellet was melted, turned over, and melted three times again to ensure homogeneity. The pellet was then hand crushed using a hardened steel mortar and pestle in an argon-filled glovebox. The CR apparatus used was a Durston DRM 130 (High Wycombe, UK) that was modified so the powder samples could be rolled vertically. Rolling experiments were performed in air by inserting the powder obtained from hand crushing between two 316 stainless steel plates to prevent contamination from the rolls. Rolling was performed once, three times, and six times. After the first roll, the powder consolidated on a plate. The thickness of the plate was about 0.5 mm. This plate was then folded in two and rolled again to the final number of rollings. Thus, a thickness reduction of around 50% was obtained after each pass.

BM was carried out on a Spex 8000 high energy ball mill (SPEX SamplePrep, Metuchen, NJ, USA) in a hardened 55 cc steel crucible and balls with a powder-to-ball mass ratio of 1/10. All loadings and unloading of powder in the crucible were performed in an argon-filled glove box. BM was performed for 5, 15, 30, and 60 min (BM 5min, BM 15min, BM 30min, and BM 60 min, respectively) with a vibration frequency of 1060 cycles per minute. After the milling process, the powders were removed from the crucible in the glove box. The crystal structure was determined by X-ray diffraction (XRD) using a Bruker D8 Focus (Bruker AXS LLC, Madison, WI, USA) with Cu-K α radiation. Lattice parameters were evaluated from Rietveld refinement using Topas software (V6.0, Bruker AXS LLC, Madison, WI, USA) [35]. Microstructure was investigated using a Hitachi Su1510 scanning electron microscopy (Hitachi High-Tech America, Dallas, TX, USA). First, hydrogenation was performed at room temperature (25 °C) under 20 bars of hydrogen pressure using a homemade Sievert's apparatus. The samples were filled in the reactor and kept under a dynamic vacuum at room temperature for 1 h before the measurement. After reaching full hydrogenation, the absorption experiment was stopped, keeping the sample under hydrogen pressure. After that, the sample was taken for XRD measurement in the air at room temperature and atmospheric pressure.

3. Results and Discussion

3.1. Morphology

Figure 1 shows the morphologies of $\text{Ti}_1\text{V}_{0.9}\text{Cr}_{1.1}$ alloy in the as-cast state after hand crushing and CR.

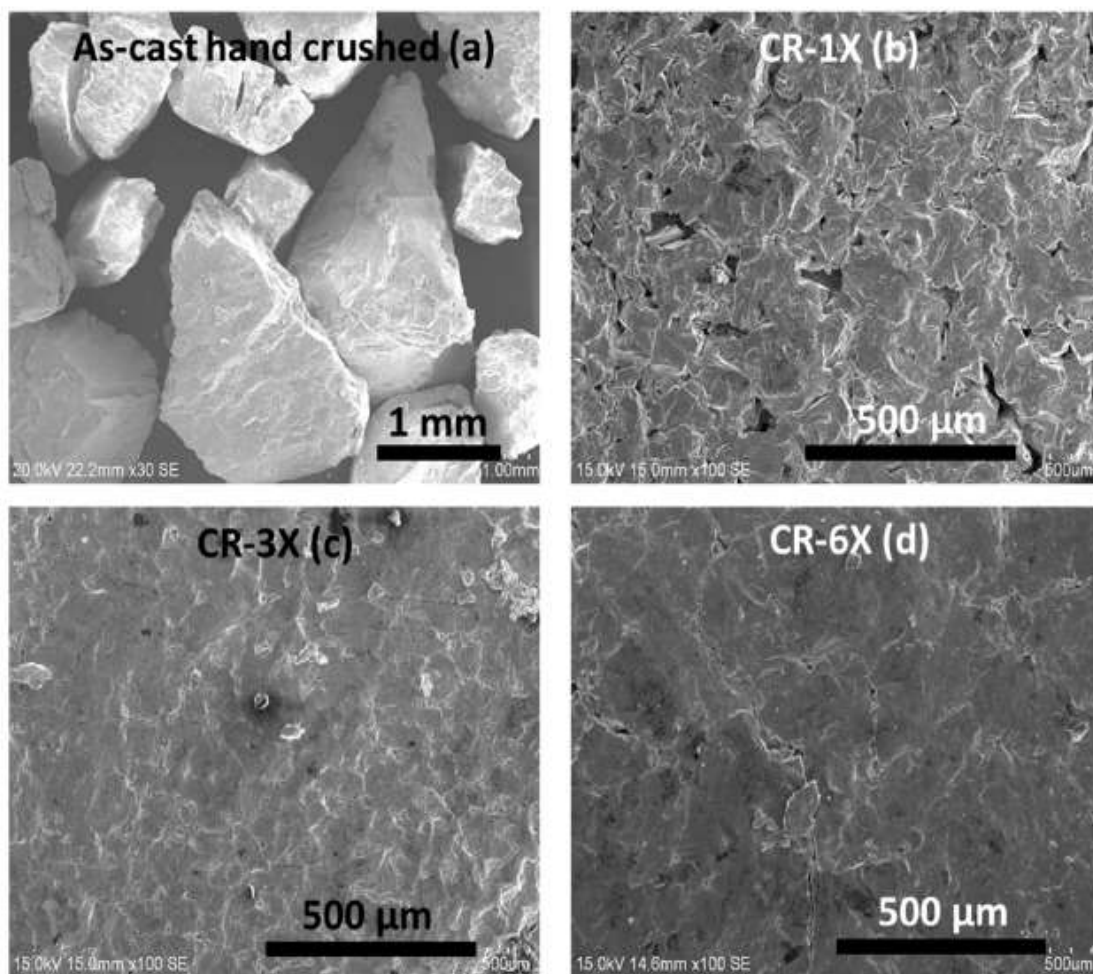


Figure 1. Scanning electron microscopy (SEM) micrographs of hand crushed (a), CR-1X (b), CR-3X (c), and CR-6X (d) of $\text{Ti}_1\text{V}_{0.9}\text{Cr}_{1.1}$ alloy.

The as-cast sample, after hand crushing, consisted of particles ranging from 0.65 to 2.2 mm. After CR, the sample showed consolidation of the powder. CR the sample one time agglomerated the powder into plates but with some voids, as presented in Figure 1b. The plates seemed to be porous. After three times of CR, the voids within the plates disappeared, but some cracks remained. With six rolling passes, the plate seemed to be more consolidated.

3.2. Crystal Structure

Figure 2 presents the XRD patterns of the as-cast $\text{Ti}_1\text{V}_{0.9}\text{Cr}_{1.1}$ alloy and after 1X, 3X, and 6X CR. All patterns showed a BCC structure (S.G. $Im-3m$). The crystal structure parameters and the weighted profile factor R_{wp} as evaluated by Rietveld's refinement, are presented in Table 1.

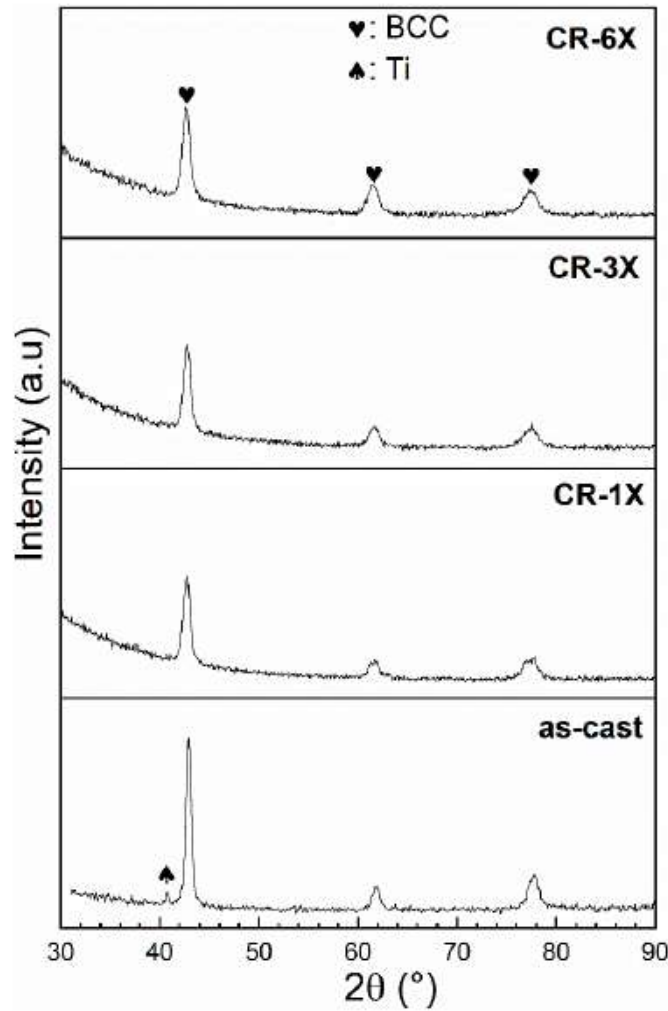


Figure 2. XRD patterns of the as-cast, CR-1X, CR-3X, and CR-6X of $\text{Ti}_1\text{V}_{0.9}\text{Cr}_{1.1}$ alloy.

Table 1. Crystal structure parameters and the R_{wp} values of the as-cast, CR-1X, CR-3X, and CR-6X of $\text{Ti}_1\text{V}_{0.9}\text{Cr}_{1.1}$ alloy. Error on the last significant digit is indicated in parentheses.

Sample	Phase	Unit Cell Volume (\AA^3)	Lattice Parameter (\AA)	Crystallite Size (nm)	Microstrain (%)	Phase Abundance (%)	R_{wp}
As-cast	BCC	28.04 (2)	3.0379 (9)	24 (2)	0.26 (1)	97 (3)	7.76
	Ti	36.25 (1)	a = 2.961 (4) c = 4.773 (1)	13 (2)		3 (3)	
CR-1X	BCC	28.24 (3)	3.0453 (1)	28 (5)	0.40 (1)	100	5.95
CR-3X	BCC	28.34 (4)	3.0487 (1)	25 (4)	0.40 (1)	100	6.07
CR-6X	BCC	28.26 (4)	3.0459 (1)	21 (3)	0.42 (2)	100	6.55

As seen in Table 1, crystallite size did not drastically change upon rolling, whereas the microstrain slightly increased but only for the first rolling. Further rolling did not change the microstrain. The disappearance of the Ti-phase in the CR patterns after rolling occurred because the crystallite size of this phase tended to decrease and the microstrain increased. These two factors caused the peak to broaden. As the Ti phase was already at the limit of detection in the as-cast pattern (the value was $3 \pm 3\%$), as the peaks broadened, they became undistinguishable from the background.

3.3. First Hydrogenation

The first hydrogenation (activation) of the as-cast and cold rolled alloys was performed at room temperature under 20 bars of hydrogen and without any prior heat treatment. The activation kinetics are shown in Figure 3.

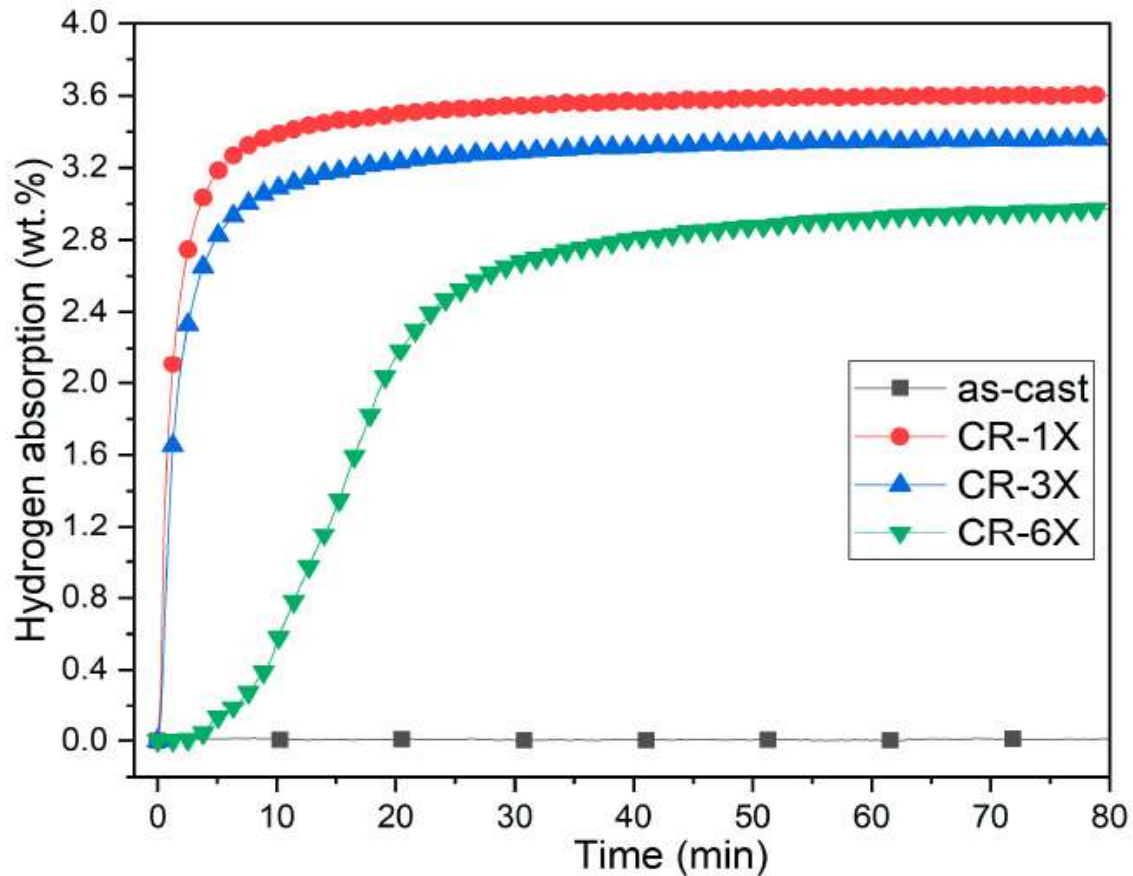


Figure 3. Activation curves of the as-cast, CR-1X, CR-3X, and CR-6X of $Ti_1V_{0.9}Cr_{1.1}$ alloy.

The as-cast $Ti_1V_{0.9}Cr_{1.1}$ alloy is hard to activate and did not absorb hydrogen even after 15 h of hydrogen exposure. Just one pass of CR made the activation possible without any incubation time and with fast kinetics. Full capacity was reached after only 12 min. The CR-3X sample also demonstrated good hydrogen uptake but with a slight reduction in capacity. Further rolling to 6X showed a 4 min incubation time followed by a slower absorption and reduced total capacity. The effectiveness of CR in activating the $Ti_1V_{0.9}Cr_{1.1}$ alloy is still unclear. Considering the crystal structure before and after CR, one rolling pass did not change the crystal structure of the alloy, and the reduction in crystallite size was relatively small. Therefore, the reason is something else. CR breaks particles in smaller pieces, thus producing new surfaces that could be active to hydrogen. However, as CR was performed in air, the newly produced surfaces would, in principle, oxidize immediately. Nevertheless, the speed of oxidation could be so slow that the freshly produced surfaces have only very thin oxide, which could be easily broken during hydrogenation. Figure 3 shows that the capacity after 1, 3, and 6 CR passes are 3.6, 3.3, and 2.9 wt %, respectively. Therefore, the loss of capacity appears to be directly proportional to the number of rolling passes. Each rolling pass decreased the capacity by about 0.1 wt %. This decrease is most likely the formation of oxide as the rollings were performed in air.

The crystal structure of the full hydride samples was investigated from XRD patterns. Figure 4 presents the XRD patterns of the hydride samples of CR-1X, CR-3X, and CR-6X of $Ti_1V_{0.9}Cr_{1.1}$ alloy.

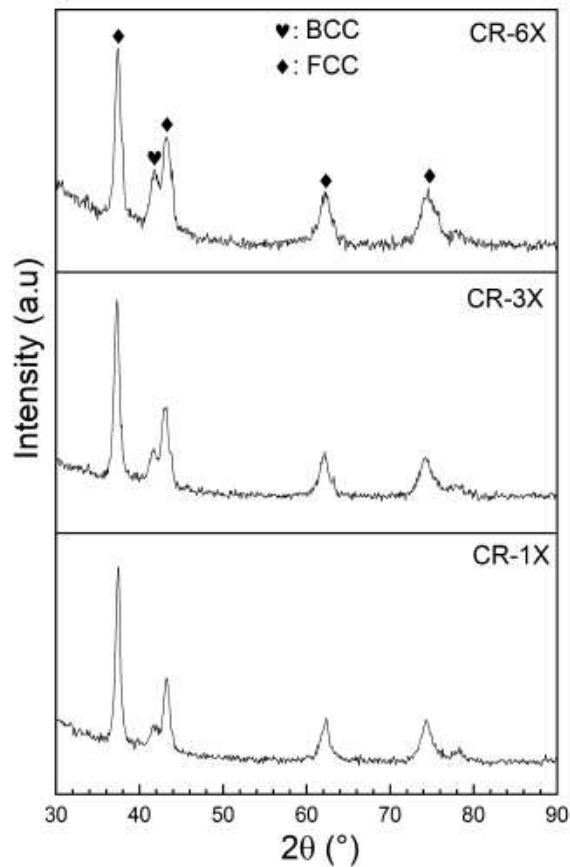


Figure 4. X-ray diffraction (XRD) patterns of hydrogenated of CR-1X, CR-3X, and CR-6X of $Ti_1V_{0.9}Cr_{1.1}$ alloy.

Figure 4 clearly shows that BCC and FCC phases were present in all patterns, but the relative intensities of both phases are different. Despite the capacity decreasing with increasing number of rolling passes, no oxide phase was identified in these patterns. For the 6X pattern, the proportion of oxide should be approximately 17 wt % and should be seen in the diffraction pattern. The absence of the oxide phase in the patterns may be due to the very small crystallite size of the oxide phase. Assuming that the oxide phase is a shell around the hydride phase, the oxide's thickness is about 6% of the radius of the hydride crystallite. As seen in Table 2, which shows the results of Rietveld's refinement of all hydride patterns, the crystallite size of the FCC hydride phase is 30 nm; this means that the thickness of the oxide phase could be as small as 0.8 nm. Such a small crystallite size produces a diffraction pattern with very broad peaks that are effectively indistinguishable from the background.

Table 2. Crystal structure parameters and the R_{wp} values of all patterns after hydrogenation. Error on the last significant digit is indicated in parentheses.

Sample	Phase	Unit Cell Volume (\AA^3)	Lattice parameter (\AA)	Crystallite Size (nm)	Microstrain (%)	Phase Abundance (%)	R_{wp}
CR-1X	FCC	79.03 (1)	4.2914 (2)	20.2 (2)	0.34 (1)	84 (2)	5.34
	BCC	30.84 (8)	3.136 (3)	7 (2)	0.43 (1)	16 (2)	
CR-3X	FCC	78.90 (1)	4.289 (2)	17.3 (1)	0.40 (1)	76 (3)	5.28
	BCC	30.65 (9)	3.130 (7)	4.0 (6)	0.33 (1)	24 (3)	
CR-6X	FCC	78.61 (1)	4.284 (2)	29 (6)	0.53 (2)	72 (2)	4.93
	BCC	30.67 (7)	3.130 (2)	4.9 (6)	0.36 (8)	28 (2)	

The abundance of the phase (FCC) decreased with the number of rolls, and this seems to agree with the decreases in capacity shown in Figure 3. All the hydride patterns had BCC and FCC phases with almost the same lattice parameters. However, the lattice parameter of the BCC phase was much bigger than the as-cast BCC phase reported in Table 1. This was an indication that the BCC phase also contained hydrogen. The volume expansion of the BCC phase was about 2.6 \AA^3 . Considering that a hydrogen atom occupies a volume between 2 and 3 \AA^3 , and that there are two lattice points per unit cell, we estimated that the BCC phase contained about 0.5 hydrogen atom per metallic atom ($H/M \approx 0.5$). Since the diffraction patterns were captured in air at room temperature, it is possible that the samples experienced a partial dehydrogenation. To determine the true crystal structure in the fully hydrided state, an in-situ diffraction pattern should be recorded.

3.4. Effect of Ball Milling on $Ti_1V_{0.9}Cr_{1.1}$ Alloy

As CR was found to be beneficial for activation, we wanted to determine if BM produces the same effect. For this, the as-cast alloy was milled for 5, 15, 30, and 60 min. The morphologies of the processed powders are shown in Figure 5.

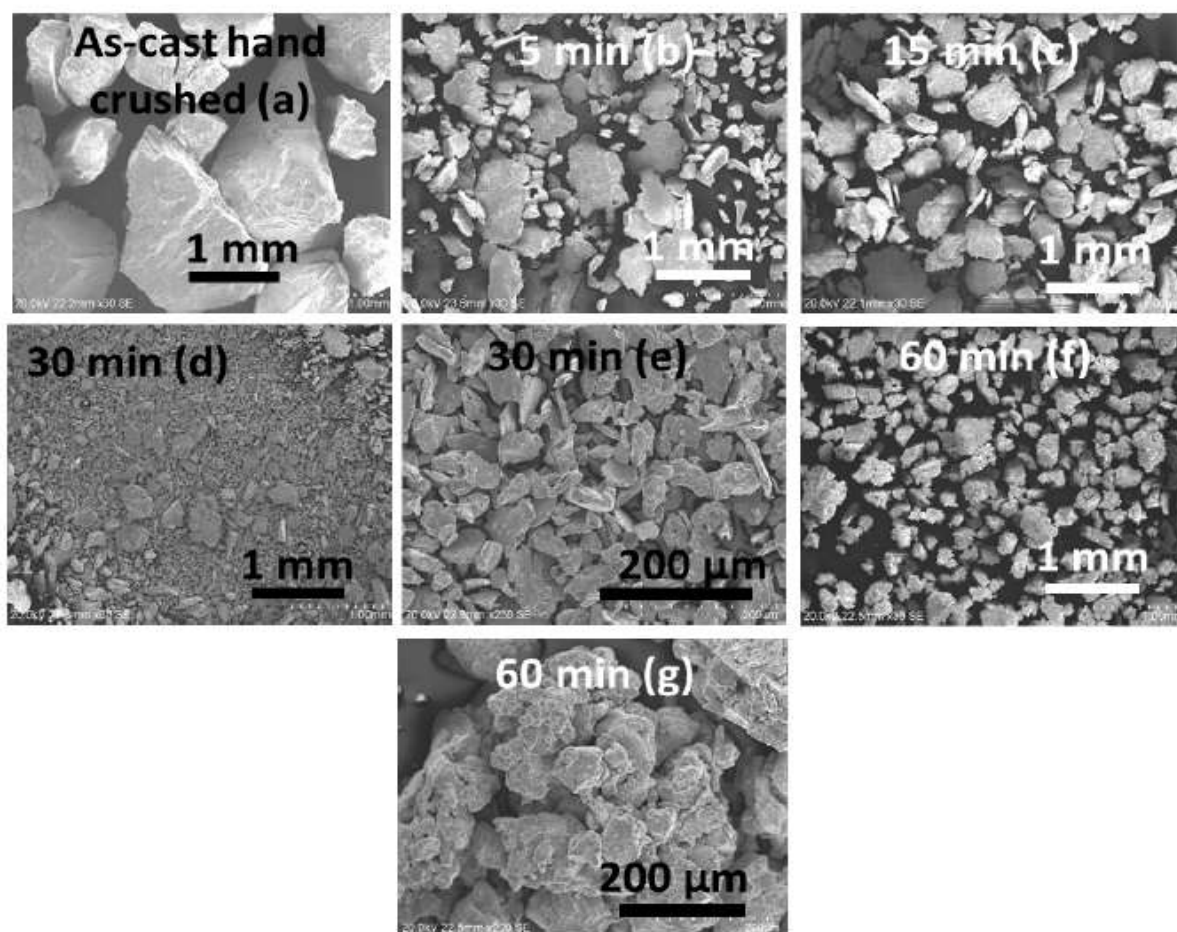


Figure 5. SEM micrographs of $Ti_1V_{0.9}Cr_{1.1}$ alloy before (a) and after 5 (b), 15 (c), 30 (d,e), and 60 min (f,g) of ball milling (BM).

After 5 min BM, some flat surfaces and formation of smaller particles in the range 0.2–1 mm were observed. Further milling decreased the size of the particles. Agglomeration of small particles was observed after 60 min of milling.

The XRD patterns of $\text{Ti}_1\text{V}_{0.9}\text{Cr}_{1.1}$ alloy for different BM times are presented in Figure 6. The crystal structure parameters and the R_{wp} , as evaluated by Rietveld's refinement, are shown in Table 3.

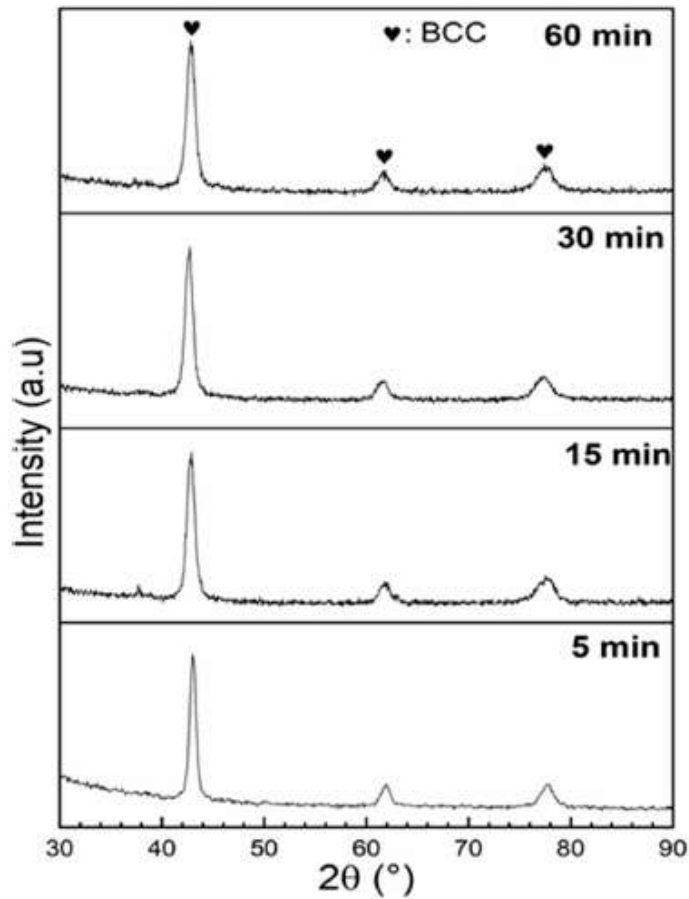


Figure 6. Diffraction patterns of $\text{Ti}_1\text{V}_{0.9}\text{Cr}_{1.1}$ alloy for different BM times.

Table 3. Crystal parameters and the R_{wp} values of $\text{Ti}_1\text{V}_{0.9}\text{Cr}_{1.1}$ alloy for different ball milling times compared with the as-cast sample. Error on the last significant digit is indicated in parentheses.

Sample	Phase	Unit Cell Volume (\AA^3)	Lattice Parameter (\AA)	Crystallite Size (nm)	Microstrain (%)	Phase Abundance (%)	R_{wp}
As-cast	BCC	28.04 (2)	3.0379 (9)	24 (2)	0.26 (1)	97 (3)	7.76
	Ti	36.25 (1)	a = 2.961(4) c = 4.773 (1)	13 (2)		3 (3)	
BM 5 min	BCC	28.29 (3)	3.0471 (9)	20.5 (1)	0.30 (1)	100	5.20
BM 15 min	BCC	28.18 (3)	3.0432 (1)	16.1 (1)	0.40 (2)	100	7.84
BM 30 min	BCC	28.28 (3)	3.0468 (1)	14.5 (8)	0.40 (1)	100	7.46
BM 60 min	BCC	28.32 (3)	3.0481 (1)	12.2 (6)	0.40 (1)	100	7.30

All the ball-milled samples had a BCC crystal structure. The crystallite size decreased with milling while the microstrain remained almost constant. The microstrain in the ball-milled samples was almost identical to that in the cold rolled samples.

The activation curves of the ball-milled samples compared to the cold-rolled sample are presented in Figure 7.

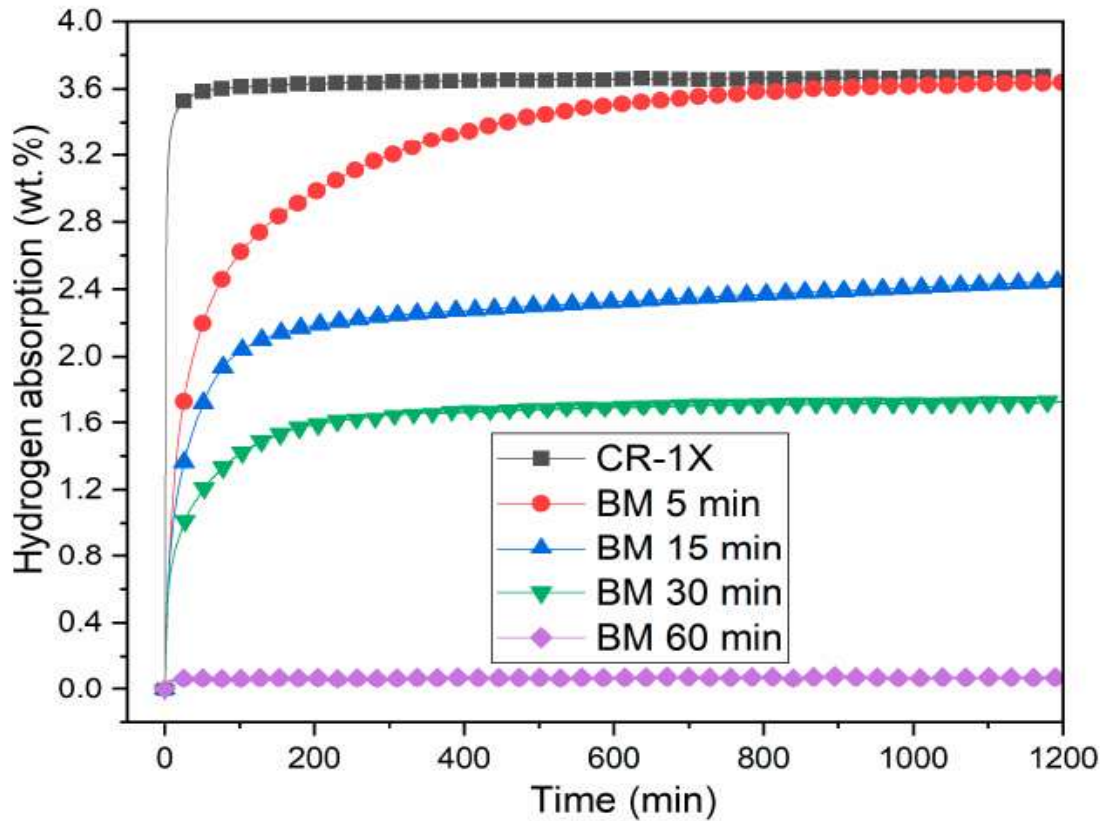


Figure 7. Activation curves of $\text{Ti}_1\text{V}_{0.9}\text{Cr}_{1.1}$ alloy for different BM times as compared to the 1 cold-rolled sample.

BM enabled the activation of $\text{Ti}_1\text{V}_{0.9}\text{Cr}_{1.1}$ alloy. Milling for 5 min significantly improved the kinetics with a maximum capacity of 3.6 wt % H_2 . Further milling for 15 and 30 min reduced the capacity to 2.4 and to respectively 1.7 wt % of hydrogen. Milling for one hour made the sample completely inert to hydrogen. This behavior is still unclear and suggests that, besides the sample's morphology, other parameters impact the activation. The effect of particle size in a BCC alloy was investigated by Kamble et al. [15]. For the first hydrogenation, they found that particle size affects the incubation time but has no significant effect on the capacity. Lou et al. found similar results on BCC $\text{V}_{40}(\text{TiCr})_{51}\text{Fe}_8\text{Mn}$ alloy [36]. In their study, the particle size was 60 to 500 mesh (0.25 to 0.025 mm) but they also registered the same hydrogen capacity in the first cycle with a different loss of capacity with cycling. After 25 cycles, the best performance was obtained for the 400-mesh sample, which lost 11% of its initial capacity.

Comparing the result of CR-1X with that of BM-5 min, both are beneficial for activation of the $\text{Ti}_1\text{V}_{0.9}\text{Cr}_{1.1}$ alloy, but CR-1X is more effective since full hydrogenation occurs much faster.

In a previous investigation, we showed that an addition of 12 wt % Zr to $\text{Ti}_1\text{V}_{0.9}\text{Cr}_{1.1}$ alloy produced fast activation kinetics, reaching a maximum capacity of 3 wt % H_2 within 3 min [14]. Therefore, adding 12 wt % Zr still produces faster kinetics compared to CR-1X but with reduced capacity. However, using mechanical deformation such as BM and CR does not change the chemistry. Adding other elements may increase the cost of the alloy and change the chemistry of the BCC phase. For these reasons, activation enhancement is better achieved by mechanical than by additive treatment.

We observed that the hydrogenation was complete for all BM samples, even if the total capacity was reduced. To determine the crystal structure of the ball-milled samples after hydrogenation, we performed XRD patterns, as seen in Figure 8. The crystal structure parameters and the R_{wp} values as determined by Rietveld refinement, are shown in Table 4.

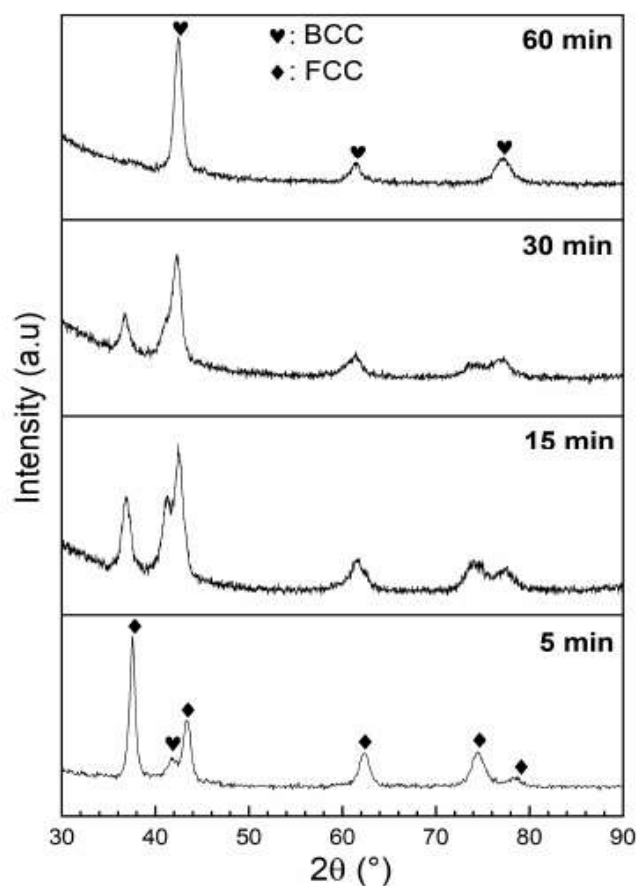


Figure 8. Diffraction patterns of $\text{Ti}_1\text{V}_{0.9}\text{Cr}_{1.1}$ alloy for different BM times after hydrogenation.

Table 4. Crystal parameters and the R_{WP} values of $\text{Ti}_1\text{V}_{0.9}\text{Cr}_{1.1}$ alloy for different ball milling times after hydrogenation. Error on the last significant digit is indicated in parentheses.

Activated BM	Phase	Unit Cell Volume (\AA^3)	Lattice Parameter (\AA)	Crystallite Size (nm)	Microstrain (%)	Phase Abundance (%)	R_{WP}
5 min	FCC	78.97 (7)	4.2903 (1)	15.4 (8)	0.35 (1)	79 (2)	4.12
	BCC	31.06 (7)	3.144 (2)	3.8 (5)	0.34 (1)	21 (2)	
15 min	FCC	78.38 (1)	4.280 (2)	15.8 (2)	0.42 (2)	36 (2)	5.12
	BCC	29.33 (5)	3.0841 (2)	8.6 (1)	1.09 (4)	64 (2)	
30 min	FCC	78.49 (2)	4.282 (3)	14.0 (2)	0.29 (3)	23 (2)	5.17
	BCC	28.75 (5)	3.0634 (2)	5.1 (3)	0.49 (3)	77 (2)	
60 min	BCC	28.15 (3)	3.0418 (9)	12.4 (6)	0.40 (1)	100	4.63

For the 60 min sample, the crystal structure was still BCC, which confirmed that this sample did not absorb hydrogen, as seen in Figure 7. There was no significant change in the lattice parameter and crystallite size of this BCC phase, confirming that there was no reaction with hydrogen. All the other hydride patterns had BCC and FCC phases. The abundance of the FCC phase decreased with milling time, which agrees with the reduction of hydrogen capacity seen in Figure 7. The unit cell volume of the FCC phase was practically identical to the FCC phase observed in the hydrogenated cold-rolled samples. However, the unit cell volume of the BCC phase showed different behavior. It progressively decreased with milling time; this means that as milling time increased, the amount of hydrogen retained in the BCC phase decreased. It seems that milling decreases the ability of the BCC phase to absorb hydrogen. The exact mechanism is not clear, but it is a subject for further research and may explain the reduction of capacity with milling time.

4. Conclusions

In this paper, the effects of CR and BM on the microstructure and hydrogen storage properties of $Ti_1V_{0.9}Cr_{1.1}$ alloy were reported. Cold-rolled samples for one, three, and six rolling passes had a BCC crystal structure. One cold roll was efficient for the first absorption kinetics. However, increasing rolling passes led to a reduction in capacity. The BCC and FCC phases were present in the cold-rolled samples after hydrogenation. Ball-milled samples for 5, 15, 30, and 60 min also maintained the original BCC crystal structure, and no other crystal structure was identified. After BM for five minutes, the first hydrogenation proceeded with relatively good kinetics. However, further milling decreased hydrogen capacity. Milling to 60 min made the alloy inert to hydrogen. The hydrogenated samples had both BCC and FCC phases.

One cold roll and BM for five minutes were beneficial for the first hydrogenation kinetics. CR-1X was more effective than ball milling for five minutes since full hydrogenation occurred much faster. The exact mechanism responsible for the improvement of activation kinetics upon CR and BM is still unknown. Mechanical treatment, and especially CR, are more efficient, low-cost, and improve activation kinetics more than addition of other elements such as Zr.

Author Contributions: All experiments, except electron microscopy, were performed by S.S. and A.A. under the supervision of J.H. J.H. and S.S. analyzed the results and wrote the paper. All authors have read and agreed to the published version of the manuscript.

Funding: This research received no external funding.

Acknowledgments: We would like to thank Agnes Lejeune for electron microscopy experiments.

Conflicts of Interest: The authors declare no conflict of interest.

References

1. Von Colbe, J.B.; Ares, J.-R.; Barale, J.; Baricco, M.; Buckley, C.; Capurso, G.; Gallandat, N.; Grant, D.M.; Guzik, M.N.; Jacob, I.; et al. Application of hydrides in hydrogen storage and compression: Achievements, outlook and perspectives. *Int. J. Hydrogen Energy* **2019**, *44*, 7780–7808. [[CrossRef](#)]
2. Rusman, N.A.A.; Dahari, M. A review on the current progress of metal hydrides material for solid-state hydrogen storage applications. *Int. J. Hydrogen Energy* **2016**, *41*, 12108–12126. [[CrossRef](#)]
3. Shelyapina, M.G. Metal hydrides for energy storage. In *Handbook of Ecomaterials*; Martínez, L.M.T., Kharissova, O.V., Kharisov, B.I., Eds.; Springer: Cham, Switzerland, 2017; pp. 1–36. [[CrossRef](#)]
4. Mazzolai, G.; Coluzzi, B.; Biscarini, A.; Mazzolai, F.M.; Tuissi, A.; Agresti, F.; Lo Russo, S.; Maddalena, A.; Palade, P.; Principi, G. Hydrogen-storage capacities and H diffusion in bcc TiVCr alloys. *J. Alloys Compd.* **2008**, *466*, 133–139. [[CrossRef](#)]
5. Miraglia, S.; de Rango, P.; Rivoirard, S.; Fruchart, D.; Charbonnier, J.; Skryabina, N. Hydrogen sorption properties of compounds based on BCC $Ti_{1-x}V_{1-y}Cr_{1+x+y}$ alloys. *J. Alloys Compd.* **2012**, *536*, 1–6. [[CrossRef](#)]
6. Tamura, T.; Kazumi, T.; Kamegawa, A.; Takamura, H.; Okada, M. Protium absorption properties and protide formations of Ti–Cr–V alloys. *J. Alloys Compd.* **2003**, *356*, 505–509. [[CrossRef](#)]
7. Kuriwa, T.; Maruyama, T.; Kamegawa, A.; Okada, M. Effects of V content on hydrogen storage properties of V–Ti–Cr alloys with high desorption pressure. *Int. J. Hydrogen Energy* **2010**, *35*, 9082–9087. [[CrossRef](#)]
8. Selvaraj, S.; Jain, A.; Kumar, S.; Zhang, T.; Isobe, S.; Miyaoka, H.; Kojima, Y.; Ichikawa, T. Study of cyclic performance of V-Ti-Cr alloys employed for hydrogen compressor. *Int. J. Hydrogen Energy* **2018**, *43*, 2881–2889. [[CrossRef](#)]
9. Shelyapina, M.G.; Skryabina, N.E.; Surova, L.S.; Dost, A.; Ievlev, A.V.; Privalov, A.F.; Fruchart, D. Proton NMR study of hydrogen mobility in $(TiCr_{1.8})_{1-x}V_x$ hydrides. *J. Alloys Compd.* **2019**, *778*, 962–971. [[CrossRef](#)]
10. Lin, H.C.; Lin, K.M.; Wu, K.C.; Hsiung, H.H.; Tsai, H.K. Cyclic hydrogen absorption–desorption characteristics of TiCrV and $Ti_{0.8}Cr_{1.2}V$ alloys. *Int. J. Hydrogen Energy* **2007**, *32*, 4966–4972. [[CrossRef](#)]
11. Itoh, H.; Arashima, H.; Kubo, K.; Kabutomori, T. The influence of microstructure on hydrogen absorption properties of Ti–Cr–V alloys. *J. Alloys Compd.* **2002**, *330–332*, 287–291. [[CrossRef](#)]
12. Huot, J. Kinetics and thermodynamics. In *Hydrogen Technology: Mobile and Portable Applications*; Léon, A., Ed.; Springer: Berlin/Heidelberg, Germany, 2008; pp. 471–500. [[CrossRef](#)]

13. Hirose, K. *Handbook of Hydrogen Storage: New Materials for Future Energy Storage*; John Wiley & Sons: Hoboken, NJ, USA, 2010.
14. Sleiman, S.; Huot, J. Microstructure and Hydrogen Storage Properties of $\text{Ti}_1\text{V}_{0.9}\text{Cr}_{1.1}$ Alloy with Addition of x wt % Zr ($x = 0, 2, 4, 8,$ and 12). *Inorganics* **2017**, *5*, 86. [[CrossRef](#)]
15. Kamble, A.; Sharma, P.; Huot, J. Effect of doping and particle size on hydrogen absorption properties of BCC solid solution $52\text{Ti}-12\text{V}-36\text{Cr}$. *Int. J. Hydrogen Energy* **2017**, *42*, 11523–11527. [[CrossRef](#)]
16. Bellon, D.; Martinez, A.; Barreneche, D.; dos Santos, D. A structural study of the hydrogen absorption properties by replacing vanadium with zirconium in metal alloys. *J. Phys. Conf. Ser.* **2016**, *687*, 012057. [[CrossRef](#)]
17. Shelyapina, M.; Dost, A.; Skryabina, N.; Privalov, A.; Vogel, M.; Fruchart, D. Effect of $\text{Zr}_7\text{Ni}_{10}$ additive on hydrogen mobility in $(\text{TiCr}_{1.8})_{1-x}\text{V}_x$ ($x = 0.2, 0.4, 0.6, 0.8$): An ^1H NMR SFG study. *Int. J. Hydrogen Energy* **2020**, *45*, 7929–7937. [[CrossRef](#)]
18. Skryabina, N.E.; Fruchart, D.; Medvedeva, N.A.; de Rango, P.; Mironova, A.A. Correlation between the Hydrogen Absorption Properties and the Vanadium Concentration of Ti-V-Cr Based Alloys. In *Solid State Phenomena*; Trans Tech Publications Ltd.: Bäch, Switzerland, 2017; Volume 257, pp. 165–172.
19. Kamble, A.G.; Sharma, P.; Huot, J. Investigation of crystal structure, microstructure and hydrogenation behavior of heat-treated $\text{Ti}_{52}\text{V}_{12}\text{Cr}_{36}$ alloy. *ACS Appl. Energy Mater.* **2019**, *3*, 794–799. [[CrossRef](#)]
20. Zhou, H.Y.; Wang, F.; Wang, J.; Wang, Z.M.; Yao, Q.R.; Deng, J.Q.; Tang, C.Y.; Rao, G.H. Hydrogen storage properties and thermal stability of $\text{V}_{35}\text{Ti}_{20}\text{Cr}_{45}$ alloy by heat treatment. *Int. J. Hydrogen Energy* **2014**, *39*, 14887–14895. [[CrossRef](#)]
21. Rong, M.; Wang, F.; Wang, J.; Wang, Z.; Zhou, H. Effect of heat treatment on hydrogen storage properties and thermal stability of $\text{V}_{68}\text{Ti}_{20}\text{Cr}_{12}$ alloy. *Prog. Nat. Sci. Mater. Int.* **2017**, *27*, 543–549. [[CrossRef](#)]
22. Couillaud, S.; Enoki, H.; Amira, S.; Bobet, J.-L.; Akiba, E.; Huot, J. Effect of ball milling and cold rolling on hydrogen storage properties of nanocrystalline $\text{TiV}_{1.6}\text{Mn}_{0.4}$ alloy. *J. Alloys Compd.* **2009**, *484*, 154–158. [[CrossRef](#)]
23. Huot, J.; Enoki, H.; Akiba, E. Synthesis, phase transformation, and hydrogen storage properties of ball-milled $\text{TiV}_{0.9}\text{Mn}_{1.1}$. *J. Alloys Compd.* **2008**, *453*, 203–209. [[CrossRef](#)]
24. Singh, B.K.; Shim, G.; Cho, S.-W. Effects of mechanical milling on hydrogen storage properties of $\text{Ti}_{0.32}\text{Cr}_{0.43}\text{V}_{0.25}$ alloy. *Int. J. Hydrogen Energy* **2007**, *32*, 4961–4965. [[CrossRef](#)]
25. Varin, R.A.; Czujko, T.; Wronski, Z.S. *Nanomaterials for Solid State Hydrogen Storage*; Springer Science & Business Media: Berlin/Heidelberg, Germany, 2009.
26. Sleiman, S.; Huot, J. Effect of particle size, pressure and temperature on the activation mechanism of hydrogen absorption in TiVZrHfNb high entropy alloy. Unpublished work.
27. Shelyapina, M.; Fruchart, D.; De Rango, P.; Charbonnier, J.; Rivoirard, S.; Skryabina, N.; Miraglia, S.; Hlil, E.; Wolfers, P. First-Principles Investigation of the Stability of the Ti-V-Cr Ternary Alloys and Their Related Hydrides. In *AIP Conference Proceedings*; American Institute of Physics: College Park, MD, USA, 2006; Volume 837, pp. 104–111.
28. Huot, J. *Enhancing Hydrogen Storage Properties of Metal Hydrides: Enhancement by Mechanical Deformations*; Springer: Cham, Switzerland, 2016.
29. Vega, L.E.R.; Leiva, D.R.; Leal Neto, R.M.; Silva, W.B.; Silva, R.A.; Ishikawa, T.T.; Kiminami, C.S.; Botta, W.J. Mechanical activation of TiFe for hydrogen storage by cold rolling under inert atmosphere. *Int. J. Hydrogen Energy* **2018**, *43*, 2913–2918. [[CrossRef](#)]
30. De Araujo-Silva, R.A.; Jorge, A.M., Jr.; Vega, L.E.R.; Leal Neto, R.M.; Leiva, D.R.; Botta, W.J. Hydrogen desorption/absorption properties of the extensively cold rolled β Ti-40Nb alloy. *Int. J. Hydrogen Energy* **2019**, *44*, 20133–20144. [[CrossRef](#)]
31. Tousignant, M.; Huot, J. Hydrogen sorption enhancement in cold rolled LaNi_5 . *J. Alloys Compd.* **2014**, *595*, 22–27. [[CrossRef](#)]
32. Patselov, A.; Rybin, V.; Greenberg, B.; Mushnikov, N. Hydrogen absorption in as-cast bcc single-phase Ti-Al-Nb alloys. *J. Alloys Compd.* **2010**, *505*, 183–187. [[CrossRef](#)]
33. Khajavi, S.; Rajabi, M.; Huot, J. Effect of cold rolling and ball milling on first hydrogenation of $\text{Ti}_{0.5}\text{Zr}_{0.5}(\text{Mn}_{1-x}\text{Fe}_x)\text{Cr}_1$, $x = 0, 0.2, 0.4$. *J. Alloys Compd.* **2019**, *775*, 912–920. [[CrossRef](#)]
34. Manna, J.; Tougas, B.; Huot, J. Mechanical activation of air exposed TiFe + 4 wt% Zr alloy for hydrogenation by cold rolling and ball milling. *Int. J. Hydrogen Energy* **2018**, *43*, 20795–20800. [[CrossRef](#)]

35. Bruker AXS. *Topas V6: General Profile and Structure Analysis Software for Powder Diffraction Data—User's Manual*; Bruker AXS: Karlsruhe, Germany, 2017.
36. Luo, L.; Wu, C.; Yang, S.; Zhou, J.; Chen, Y.; Yang, F.; Xu, Y.; Liu, P. Decaying behaviors of $V_{40}(TiCr)_{51}Fe_8Mn$ hydrogen storage alloys with different particle sizes. *J. Alloys Compd.* **2015**, *645*, S178–S183. [[CrossRef](#)]



© 2020 by the authors. Licensee MDPI, Basel, Switzerland. This article is an open access article distributed under the terms and conditions of the Creative Commons Attribution (CC BY) license (<http://creativecommons.org/licenses/by/4.0/>).